Correlating Magnetic Damping and Microstructure in “Half Metal” Thin Films

Christopher James Love

PhD

University of York

Physics

September 2018

Abstract

Highly spin-polarised materials show great promise in applied spintronics as spin-filters and spin transfer torque magnetic random-access memory devices for data storage. However, controllable magnetisation switching requires materials with a low Gilbert damping parameter and stable magnetic properties at room temperature. Two highly spin-polarised magnetic materials with critical temperatures well above room temperature are characterised using a series of structural and magnetic analysis techniques. Correlation between the magnetic damping and microstructure is observed in both Fe_3O_4 and $Co_2FeAl_{0.5}Si_{0.5}$ samples and both are seen to improve structurally and show more favourable damping parameters with annealing.

Annealing Fe_3O_4 in CO/CO_2 is shown to reduce the antiphase boundary density and decrease the two-magnon scattering-like extrinsic damping effects. The quality of the sample structure and the stoichiometry is also seen to improve considerably after the annealing although the defects are not completely eliminated. An anomalous peak in the damping of the annealed film is observed at 10GHz

$Co_2FeAl_{0.5}Si_{0.5}$ grown on germanium and silicon substrates is seen to also improve with thermal annealing. The Gilbert damping is seen to be lower in the as-grown scheme using the silicon substrate but greater reduction of damping post-annealing is seen on germanium. In both cases the B_2 order is observed in the $Co_2FeAl_{0.5}Si_{0.5}$ thin films, and intermixing between the sample and substrate observed above 500^oC is sufficient to disrupt the crystal structure and introduce significant extrinsic damping effects which increase the total damping. This prevents the $Co_2FeAl_{0.5}Si_{0.5}$ from reaching the more desirable L_{21} structure.

Contents

Abstract iii
Contents iv
List of Tables viii
List of Figures ix
Acknowledgements xv
Declaration xvi
List of Publications xvii

Chapter 1: Introduction **1**
1.1 Project Introduction 1
1.2 Thesis Structure 3

Chapter 2: Background Theory **4**
2.1 Introduction 4
2.2 Ferromagnetism 4
2.2.1 The Exchange Interaction 4
2.2.2 Anti-Ferromagnetism and Ferrimagnetism 6
2.2.3 Superexchange 8
2.2.3.1 Goodenough-Kanamori-Anderson Rules 9
2.2.4 Double Exchange 10
2.3 Contributions to the Magnetic Free Energy 11
2.3.1 The Magnetic Free Energy Equation 11
2.3.1.1 Zeeman Energy 12
2.3.1.2 Crystal Field Effects 12
2.3.1.3 Magnetocrystalline Energy 13
2.3.1.4 Magnetostatic Energy 14
2.3.2 The Magnetic Free Energy of a Cubic Crystal Structure 16
2.4 Magnetisation Dynamics 18
2.4.1 The Landau-Lifshitz-Gilbert Equation 19
2.5 Ferromagnetic Resonance 19
2.5.1 The Classical Picture 20

2.5.2 The Quantum Picture 20
2.5.3 The Kittel Equation 21
2.5.4 FMR Damping 23
2.5.4.1 Intrinsic Damping Mechanisms 23
2.5.4.2 Two-Magnon Scattering 25
2.6 Materials 26
2.6.1 Magnetite 26
2.6.1.1 Antiphase Boundaries 28
2.6.2 $Co_2FeAl_{0.5}Si_{0.5}$ (CFAS) 29

Chapter 3: Experimental Methods **32**
3.1 Introduction 32
3.2 Structural Characterisation Techniques 32
3.2.1 XRD 32
3.2.1.1 2Theta/Omega Scans 35
3.2.1.2 Rocking Curves 36
3.2.1.3 X-Ray Reflectivity 36
3.2.1.4 Pole Figures 39
3.2.4 HAADF-STEM 40
3.2.4.1 EELS 41
3.2.4.2 SAED 41
3.3 Magnetic Characterisation Techniques 42
3.3.1 Vibrating Sample Magnetometry 42
3.3.2 Ferromagnetic Resonance Spectroscopy 46
3.3.2.1 Vector Network Analyser FMR 47
3.3.2.2 Modulation FMR 49
3.4 X-Ray Absorption Spectroscopy 51
3.5 XMCD 53
3.5.1 Synchrotron X-ray Generation 69
3.5.2 The XMCD Sum Rules 56
3.5.3 Atomic Multiplet Calculations 58

Chapter 4: The FMR Spectrometer **59**
4.1 Introduction 59

4.2 Spectrometer Design 59
4.3 The Co-Planar Waveguide 66
4.4 RF Generation Methods 68
4.4.1 The VNA-FMR Technique 68
4.4.2 The Modulation FMR Technique 70
4.5 Equipment Calibration 71
4.6 Test Sample Measurements 76
4.7 Spectrometer Control Program 79
4.8 Further Development 80

Chapter 5: Fe_3O_4 on YSZ(111) **83**
5.1 Introduction 83
5.2 Growth and Annealing 83
5.3 Structural Characterisation 84
5.3.1 X- Ray Diffraction 84
5.3.2 XAS and XMCD 89
5.3.3 HAADF-STEM 92
5.4 Magnetic Characterisation 95
5.4.1 VSM 95
5.4.2 Ferromagnetic Resonance Spectroscopy 98
5.4.2.1 Anisotropy 101
5.4.2.2. Damping 103
5.5 Conclusions 106

Chapter 6: CFAS Heusler Alloys **108**
6.1 Introduction 108
6.2 Sample Growth and Annealing 108
6.3 Structural Characterisation (CFAS/Ge(111)) 109
6.3.1 X-Ray Diffraction 109
6.3.2 HAADF-STEM 112
6.4 Magnetic Characterisation (CFAS/Ge(111)) 114
6.4.1 VSM 114
6.4.2 Ferromagnetic Resonance Spectroscopy 115
6.4.2.1 Anisotropy Measurements 118

6.4.2.2 Damping Measurements....120
6.5 Structural Characterisation (CFAS/Si(111))....122
6.5.1 X-Ray Diffraction....122
6.5.2 HAADF-STEM....126
6.6 Magnetic Characterisation (CFAS/Si(111))....128
6.6.1 VSM....128
6.6.2 Ferromagnetic Resonance Spectroscopy....130
6.6.2.1 Anisotropy Measurements....130
6.6.2.2 Damping Measurements....134
6.7 Conclusions....136

Chapter 7: Conclusions....138
7.1 Conclusions....138
7.2 Further Work....139
7.2.1 The FMR Spectrometer....139
7.2.2 Fe_3O_4/YSZ(111)....139
7.2.3 $Co_2FeAl_{0.5}Si_{0.5}$....140

Appendix A: FMR Spectrometer Control Code....142
A.1 Introduction....142
A.2 VNA-FMR Control Program....142
A.3 Modulation FMR Modifications....146
A.3.1 Frequency Control Program....146
A.3.2 Data Acquisition Software....148

Appendix B: FMR Anisotropy Fit Equation in Field Space....150

List of Symbols....153
List of Abbreviations....154
Bibliography....155

List of Tables

Table 6.1. Data table containing the magnetic parameters $\mathbf{H_{cubic}}$, $\mathbf{H_u}$, $\mathbf{M_s}$ and α for the CFAS/Ge(111) as a function of anneal temperature

Table 6.2. Data table containing the magnetic parameters $\mathbf{H_{cubic}}$, $\mathbf{H_u}$, $\mathbf{M_s}$ and α for the CFAS/Si(111) as a function of anneal temperature

Table 6.3. Data table comparing the magnetic parameters from the CFAS/Ge(111) and CFAS/Si(111) samples as a function of anneal temperature

List of Figures

Figure 2.1 A schematic diagram of electron spin moments aligned in a) ferromagnetic, b) anti-ferromagnetic and c) ferrimagnetic order. In each case, the magnitude of the spin moment is proportional to the size of the arrow.

Figure 2.2 A schematic diagram of the different arrangements of simple cubic antiferromagnetic lattice, including the a) A-Type, b) C-type, c) G-type and d) E-type order

Figure 2.3 A schematic diagram of the body-centred cubic antiferromagnetic lattices

Figure 2.4 A schematic representation of the electron state combination in a metal-interstitial-metal ion system in (i) the antiferromagnetic and (ii) the ferromagnetic electron arrangement. The arrows represent the spin states (up or down) of the electrons contributed by the metal (blue) and interstitial (orange) ions.

Figure 2.5 A Schematic diagram of the superexchange effect between the unpaired 3-d electrons in two transition metal ions (M) and the p-orbitals of a non-magnetic interstitial ion (I)

Figure 2.6 A schematic diagram of the Goodenough-Kanamori-Anderson rules, showing a) the first, b) the second and c) the third of the GKA rules governing Superexchange coupling in ionic solids

Figure 2.7 A schematic of the geometry relating **M**, θ_M, ϕ_M, θ_H and ϕ_H in a general model of magnetisation dynamics

Figure 2.8 A schematic of the energy level splitting in (tetrahedral) lattice sites arising from the crystal field

Figure 2.9 A model of the magnetic free energy surface for a cubic crystal with a) a negative K_c and b) a positive K_c

Figure 2.10 A comparison of the magnetic free energy surfaces at various polar angles for a 111-aligned cubic crystal with a) a negative Kc and b) a positive K_c

Figure 2.11 A schematic representation of the FMR effect in a sample subject to a magnetic field $\mathbf{H}_{eff}$ and a transverse RF excitation $\mathbf{H}_{rf}$. The precession is driven by **M** x $\mathbf{H}_{eff}$ at the frequency ω

Figure 2.12 A schematic representation of the Larmor precession in the classical picture of FMR

Figure 2.13 A schematic diagram of the FMR excitation in the quantum mechanical model, where m_s is the spin magnetic moment of the electron

Figure 2.14 An example of a typical Kittel Curve in frequency as a function of applied magnetic field, measured from an FeGa test sample using VNA-FMR

Figure 2.15. A simplified schematic diagram of one quarter of the structure of magnetite viewed from a) a 3D perspective and b) in the 2D elevation only. The structure of the individual sites are shown in c) the tetrahedral and d) the octahedral arrangements. The unit cell structure is achieved by stacking four such units in a cubic arrangement, mirroring each adjacent unit

Figure 2.16 The Full Heusler X_2YZ Structure, with the X (red), Y (green) and Z (blue) sites highlighting the L_{21} Order. In B_2 order, the Y and Z sites are disordered and the green and blue sites become interchangeable

Figure 3.1. A schematic diagram of Bragg reflected x-rays from a series of crystal lattice planes

Figure 3.2. A schematic diagram of alternate XRD geometries. a) The grazing incidence XRD geometry with the incident and specular beams shown in red and the diffracted beam in blue. b) The in-plane XRD geometry

Figure 3.3 A schematic diagram of the X-Ray diffractometer

Figure 3.4 A schematic diagram of the X-Ray Goniometer, showing the angles φ_{XRD} and χ_{XRD}

Figure 3.5. A typical XRD Rocking Curve, with the FWHM indicated in red

Figure 3.6. A typical X-ray Reflectivity trace measured using an X-ray diffractometer

Figure 3.7. A schematic diagram of a single crystal sample under XRR

Figure 3.8. An example XRD Pole figure recorded from the Fe_3O_4 (111) peak in an Fe_3O_4/YSZ(111) sample. The central (111) peak is clearly observed in red, and the ($\bar{1}11$), ($1\bar{1}1$) and ($11\bar{1}$) peaks are observed in the pole figure spaced equally around the central peak

Figure 3.9. A schematic diagram of the HAADF-STEM Technique, with the electron path shown in red

Figure 3.10. A schematic diagram of a typical VSM system

Figure 3.11. A typical VNA-FMR linescan from a CFAS/Si sample, showing S_{21} as a function of the applied RF frequency at a fixed field of 1500 Oe

Figure 3.12. A typical VNA-FMR linescan of ΔS_{21} as a function of the applied magnetic field at a fixed frequency

Figure 3.13. A typical modulation FMR trace from a single crystal ferromagnet with the peak-to-peak linewidth ($\Delta\mathbf{H}_{PP}$) and resonance field ($\mathbf{H}_r$) parameters indicated

Figure 3.14. A schematic diagram of X-ray absorption in a material with spin-split density of states

Figure 3.15. A schematic diagram of the x-ray photon generation process in an undulator. The photon wavelength is dictated in the laboratory reference frame by λ_{lab}

Figure 3.16. A typical XMCD measured at the iron L-Edges including a schematic displaying the sum rules parameters

Figure 4.1. A schematic diagram of the FMR Spectrometer operating in VNA-FMR mode

Figure 4.2. Calibration data from the Bruker PSU showing the magnetic field induced as a function of the voltage applied by the DAQ unit output

Figure 4.3 A spatial map of the bias field output by the electromagnet coils. Little deviation from the 5kOe maximum is observed around the centre, but the field is observed to decay quickly as the distance from the origin increases. Every second dataset (+/-5mm, +/-15mm) is removed for clarity

Figure 4.4 A comparison of the magnetic field over 30mm around the centre of the Helmholtz coils in the FMR spectrometer in the a) x- b) y- and c) z-axes, where ΔN denotes the distance from the centre of the coils in the relevant axis

Figure 4.5. Temperature data logged over one day in the spectrometer laboratory

Figure 4.6. A photograph of the custom-built sample mount system in the FMR spectrometer, including the two-axis stage, SMA bulkheads and mounting cradle, including the CPW, between the coils of the electromagnet

Figure 4.7. A schematic representation of the planar field $\mathbf{H}_{rf}$ induced by a current $\mathbf{I}_{rf}$ through a Coplanar Waveguide

Figure 4.8. A photograph of the co-planar waveguide used in the FMR spectrometer

Figure 4.9. A calibration curve showing the AC field output of the modulation coils as a function of input current at low-amplification output from the EP2000 signal amplifier

Figure 4.10 Calibration curve showing modulation FMR resonance from a Py/MgO test sample at a fixed frequency of 10GHz as a function of varying lock-in amplifier time constant settings

Figure 4.11. A measurement of the background FMR signal from the empty CPW measured in a) modulation FMR mode and b) VNA-FMR mode

Figure 4.12. An example of low-intensity FMR signal responses measured from Fe_3O_4 using the modulation FMR mode. The raw data (black) is similar in magnitude to the background (red) and therefore the FMR response (blue) can only be extracted for fitting by background subtraction

Figure 4.13. Modulation FMR from a Py/MgO test sample at a fixed frequency of 10GHz

Figure 4.14. Modulation FMR from the permalloy test sample at a fixed frequency of 10GHz over a range of azimuthal angles (θ) relative to a perpendicular configuration between the bias field and the applied RF field

Figure 4.15. A set of 5 subsequent modulation FMR scans from a Py test sample at 9GHz. Good overlap between subsequent scans shows that the data is repeatable

Figure 4.16. A modulation FMR dataset (blue) at 10GHz fixed frequency compared with corresponding VNA-FMR linescan (red). These scans overlap closely at $\mathbf{H}_r$, showing consistency between data collected in both operation modes

Figure 5.1. A comparison between the 2θ/ω out-of-plane XRD data from a) the as-grown and b) the annealed Fe_3O_4/YSZ(111) samples. The (111) peaks of the Fe_3O_4 material are marked with their respective h,k,l values

Figure 5.2. 2θ/ω XRD scan from the post-annealed Fe_3O_4/YSZ(111) with the additional K_β and L_α peaks removed by the monochromator. The remaining K_α peaks from the substrate and sample are clearly observed

Figure 5.3. An XRD Rocking curve over the Fe_3O_4 (111) peak from (a) the non-annealed and (b) the annealed Fe_3O_4/YSZ(111)

Figure 5.4. XRD Pole figures from the Fe_3O_4 (111) peaks from a) non-annealed and b) post-annealed Fe_3O_4/YSZ(111)

Figure 5.5. Normalised XRR from a) non-annealed and b) annealed Fe_3O_4/YSZ(111) samples. Data is shown in blue with the fit calculated using GlobalFIt shown in red

Figure 5.6. The a) XAS and b) XMCD from the averaged XAS of the non-annealed Fe_3O_4/YSZ(111) sample at 300K

Figure 5.7. The a) XAS and b) XMCD from the averaged XAS of the sample of annealed Fe_3O_4/YSZ(111) at 300K

Figure 5.8. A comparison of SAED Patterns observed in Fe_3O_4/YSZ(111) from a) the non-annealed and b) the post-annealed samples

Figure 5.9. A comparison of a) Low-magnification and b) high-magnification HAADF-STEM images observed in Fe_3O_4/YSZ(111) from the non-annealed sample

Figure 5.10. A comparison of a) Low-magnification and b) high-magnification HAADF-STEM images observed in Fe_3O_4/YSZ(111) from the post-annealed sample

Figure 5.11. A comparison of **M**(**H**) VSM recorded using the SQUID magnetometer (blue) and the Model 10 VSM (red)

Figure 5.12. In-plane **M**(**H**) recorded from as-grown (red) and post-anneal (blue) Fe_3O_4/(111) VSM at T = 300K

Figure 5.13. A comparison of **M**(T) VSM recorded from Fe_3O_4/YSZ(111) using the SQUID magnetometer in ZFC (blue) and FC (red) modes

Figure 5.14. The temperature dependent VSM **M**(T) recorded in ZFC at 400 Oe from the a) as-grown and b) post-annealed Fe_3O_4/YSZ(111), showing the magnetisation as a function of temperature (black) and the first derivative with respect to temperature (red)

Figure 5.15. A direct comparison of the Modulation FMR field sweep at 10GHz from the as-grown (blue) and annealed (red) Fe_3O_4/YSZ(111)

Figure 5.16. The resonance frequency as a function of field in the a) as-grown and b) post-annealed Fe_3O_4/YSZ(111), extracted from the ferromagnetic resonance spectroscopy data. Fits to the data are highlighted in red

Figure 5.17. Polar plots of the resonance field as a function of azimuthal angle from (a) the non-annealed and (b) annealed Fe_3O_4/YSZ(111)

Figure 5.18. Graphs of the total linewidth Δ**H** as a function of frequency in a) the non-annealed and b) the post-annealed Fe_3O_4/YSZ(111)

Figure 5.19. The calculated dependence of the 2-magnon scattering damping behaviour as a function of fixed RF frequency for different polar angles (designated ϕ_M in the figure, corresponding to θ in this thesis) reproduced from Landeros et. al. [227]

Figure 5.20 The calculated Free energy surface in ϕ for the MCA, Zeeman and demagnetisation effects in the (111) plane of a cubic crystal in a 1kOe applied field. A comparison of the entire free energy surface between perfectly in-plane (red) and 2.4^o out of plane (black) shows a minimum in the tilted data

Figure 5.21 A close-up of the free energy surface minimum over a narrow range in ϕ, with U calculated at a range of different angles. A minimum in **U** occurs at θ = 2.4^o

Figure 6.1. A schematic diagram of the incident x-ray plane relative to the CFAS surface in χ, where χ=0^o (blue) and χ =54.7^o (red) correspond to the (111) and (100) axes respectively

Figure 6.2. An example XRD 2θ/ω scan from the 450^{o}C annealed CFAS/Ge(111) with the 2-bounce monochromator installed

Figure 6.3. A close-up of the 2θ/ω scan from the 450^{o}C annealed CFAS/Ge(111) at the (222) peak position

Figure 6.4. HAADF-STEM images recorded from the as-grown CFAS/Ge(111). a) a low-magnification image used to determine the sample thickness. b) a SAED pattern from the interface between the crystal (red) and substrate (blue). c) A high magnification HAADF-STEM image along the [1$\bar{1}$0] axis at the crystal/substrate interface. The CFAS structure (red/white) is characteristic of the B_2 phase

Figure 6.5. Paired figures presenting the HAADF-STEM images (greyscale) and EELS chemical maps (coloured) from the CFAS/Ge(111) interface in the a) as-grown and annealed at b) 350^{o}C and c) 500^{o}C. In each image, the CFAS $L_{2,3}$ edges occupy the upper (red) layer and the Ge $L_{2,3}$ edges are the lower (green) layer

Figure 6.6. A comparison of the **M**(**H**) hysteresis loops collected from the CFAS/Ge(111) VSM. Data from the 350^{o}C annealed sample is omitted for clarity

Figure 6.7. Data derived from the VSM from CFAS/Ge(111) series, showing the magnetization (black) and the coercive field (red) as a function of anneal temperature

Figure 6.8. Easy axis Kittel curves measured from the as-grown CFAS/Ge(111) at T_{an} = a) as-grown, b) 350°C, c) 450°C and) 500°C. The red line is included as a guide to the fit. (a) Inset) The fixed-frequency linescan at 10GHz (blue) including the asymmetric lorentzian fit (red)

Figure 6.9. A schematic diagram showing the relative orientation of the scratch perpendicular to the $11\bar{2}$ axis of the sample (shown in black) and the CPW in the '0 degrees' position. The bias field direction is shown in dark blue

Figure 6.10. $H_r(\varphi)$ extracted from VNA-FMR data from the CFAS/Ge(111) samples at T_{an} = a) as-grown, b) 350°C, c) 450°C and d) 500°C. A uniaxial anisotropy is observed, with an easy axis at 60 degrees to the $\bar{1}10$ at zero degrees

Figure 6.11. The total (black), cubic (red) and uniaxial (blue) anisotropy field contributions extracted from the CFAS/Ge(111) VNA-FMR polar plots

Figure 6.12. A comparison of $\Delta\mathbf{H}(f)$ in CFAS/Ge(111) (a) as-grown and annealed at (b) 350°C, (c) 450°C and (d) 500°C

Figure 6.13. α as a function of annealing temperature for the CFAS/Ge(111) sample series

Figure 6.14. An example $2\theta/\omega$ XRD scan from the 450°C annealed CFAS/Si(111) with the monochromator installed

Figure 6.15. XRD analysis over the in CFAS/Si(111) series. a) The $2\theta/\omega$ scan from the CFAS (222) peak. A comparison of b) peak position, c) lorentzian linewidth and d) integrated peak intensity as a function of anneal temperature

Figure 6.16. XRR data (blue) from the CFAS/Si samples annealed at a) as-grown b) 350°C c) 450°C and d) 500°C. Fits to each dataset (red) performed using GlobatFit allow the extraction of the film thickness

Figure 6.17. Low-magnification TEM from the CFAS/Si(111) 350°C annealed sample. A narrow interface region (red) is observed between the CFAS region (darker) and the substrate (lighter)

Figure 6.18. Low-magnification TEM image of the CFAS/Si(111) 500°C annealed sample. A mixing region is observed between the substrate and CFAS layers

Figure 6.19. Low magnification TEM image from the CFAS/Si(111) 500°C annealed sample

Figure 6.20. Low-magnification TEM from the CFAS/Si 500°C anneal sample, showing a step in the interface region between CFAS and Si

Figure 6.21. A comparison of the hysteresis loops recorded from VSM performed on the CFAS/Si(111) samples

Figure 6.22. A comparison of $\mathbf{H}_{coer}$ and $\mathbf{M}_s$ from VSM on CFAS/Si(111) as a function of anneal temperature

Figure 6.23. The easy-axis VNA-FMR Kittel curves from the CFAS/Si(111) samples at T_{an} = a) as-grown, b) 350°C, c) 450°C and d) 500°C. (a Inset). Fits are included (red) as a guide

Figure 6.24. $H_r(\varphi)$ extracted from VNA-FMR data from the CFAS/Si(111) samples at T_{an} = a) as-grown b) 350°C c) 450°C and d) 500°C. A uniaxial anisotropy is observed, with an easy axis at +30 degrees to the $11\bar{2}$ at zero degrees

Figure 6.25. The total (black), cubic (red) and uniaxial (blue) anisotropy field contributions as a function of anneal temperature extracted from the CFAS/Si(111) VNA-FMR polar plots

Figure 6.26. Plots of the in-plane anisotropy of a) CFAS/Ge(111) and b) CFAS/Si(111) at a fixed frequency of 10GHz

Figure 6.27. A comparison of Δ**H(**f) in CFAS/Si(111) (a) as-grown and annealed at (b) 350^{o}C, (c) 450^{o}C and (d) 500^{o}C

Figure 6.28. α as a function of anneal temperature in the CFAS/Si(111) sample series

Figure A.1 The LabVIEW frontend for the VNA-FMR Data Acquisition Program, operating in the primary Field-Frequency-Phi Sweep mode

Figure A.2 The LabVIEW frontend for the Frequency Control Program, designed for the modulation FMR experiment

Figure A.3 The LabVIEW frontend for the Modulation FMR Data Acquisition Program, operating in the primary azimuthal Angular (Phi) Sweep mode

Acknowledgements

First and foremost I would like to thank my PhD project supervisors, Dr. S. Cavill and Prof. G. van der Laan, without whom this work would not have been possible. Thank you for your support and encouragement over the last four years, and for giving me the opportunity to explore some fascinating physics.

I would like to express my appreciation to all the other PhD students who have supported me during my time at York: it's been a pleasure to work with you all. Special thanks to J. Beevers , I. Azaceta and O. Alsager for discussions of physics, sharing their experience and doing their best to keep me sane. My thanks also go to B. Kuerbanjiang, who performed the HAADF-STEM microscopy and liaised with the sample growth teams for this project. Your enthusiasm for, and knowledge of the physics and techniques involved in this project have been invaluable.

My gratitude is also extended to the support staff at the York Physics department, especially the mechanical workshop, electronic engineering and computer support teams, all of whom have gone above and beyond to help me realise this project.

To my friends far and wide, without whom I could never have come this far, thank you for your support, and for your patience. I can't really put into words how grateful I am. For all the good times so far, and all of those yet to come, you have my thanks. Special thanks to Josh, Matt, Sam, Jim, James and Laura, who have borne the brunt of the less positive bits, and put up with far more than I could have asked from them. I owe you guys big time.

Last, but by no means least, a big thank you to my long suffering parents, who have provided care and support through the best and worst of times over the last few years. I know it's been difficult at times, but your support means the world to me.

Declaration

I declare that this thesis is a presentation of original work and I am the sole author. This work has not previously been presented for an award at this, or any other, University. All sources are acknowledged as references. This work was jointly funded by the University of York and Diamond Light Source.

Data from chapters 5 and 6 of this thesis have been submitted for publication in papers which are currently under review. These publications are listed in the section 'List of Publications'.

Data from the CFAS/Ge(111) VSM and all HAADF-STEM data have been provided by our collaborators at the University of York, Dr. V. Lazarov and Dr. B. Kuerbanjiang. This data has been published previously in reference [121].

The CFAS samples presented in this work were grown by Prof. K. Hamaya at Osaka University.

All the Fe_3O_4 samples were grown by K. Matsuzaki at the Secure Materials Centre at the Tokyo Institute for Technology.

Author: Christopher Love

…….

List of Publications

Published

Effect of Annealing on Structure and Magnetic Properties of $Co_2FeAl_{0.5}Si_{0.5}$ Thin Films on Ge(111), B. Kuerbanjiang, C. Love, D. Kepaptsoglou, Z. Nedelkoski, S. Tear, A. Ghasemi, Q. M. Ramasse, K. Hamaya, S. A. Cavill and V. K. Lazarov, Journal of Alloys and Compounds **748** (2018)

Submitted for Review

Anomalous Magnetic Damping in Epitaxial Fe_3O_4 Films Grown on YSZ(111) Substrates, C. Love, B. Kuerbanjiang, A. Ghasemi, K. Hamaya, R. Fan, S. S. Dhesi, V.K. Lazarov, G. van der Laan and S. A. Cavill

Substrate Dependent Reduction of Gilbert Damping in Annealed $Co_2FeAl_{0.5}Si_{0.5}$ Thin Films Grown on Group IV Semiconductors, C. Love, B. Kuerbanjiang, A. Ghasemi, K. Hamaya, G. van der Laan, V.K. Lazarov and S. A. Cavill

Other Publications

Ansiotropic Absorption of Pure Spin Currents, A.A. Baker, A.I. Figueroa, C.J. Love, S.A. Cavill, T. Hesjedal and G. van der Laan, Phys. Rev. Lett. **116** (2016) 047201

Optically Excited Spin Pumping Mediating Collective Magnetization Dynamics in a Spin Valve Structure, A.P. Danilov, A.V. Scherbakov, B.A. Glavin, T.L. Linnik, A.M. Kalashnikova, L.A. Shelukhin, D.P. Pattnaik, A.W. Rushforth, C.J. Love, S.A. Cavill, D.R. Yakovlev, and M. Bayerm, Phys. Rev. B **98** 060406(R) (2018)

Enhanced Magnetoelectric Effect in M-type Hexaferrites by Co Substitution into Trigonal Bi-Pyramidal Sites, J.E. Beevers, C.J. Love, V. Lazarov, S.A. Cavill, H. Izadkhah, C. Vittoria, R. Fan, G. van der Laan and S.S. Dhesi, Appl. Phys. Lett. **112** 082401 (2018)

Chapter 1: Introduction

1.1 Project Introduction

In recent years, the field of spintronics has shown great promise in the development of highly efficient spin-based electronic devices. Highly spin-polarised materials are predicted to be useful in realising these next-generation data storage and computational devices. The original spintronic device, the spin-valve [1], opened the door for spin-transfer devices. This simple GMR based device comprises two ferromagnetic (FM) layers separated by a non-magnetic spacer. One FM layer is left 'free', able to be re-oriented relative to the other 'pinned' FM layer. In the parallel alignment, spin-up electrons can pass between the layers due to low resistivity, while in the anti-parallel state the scattering is observed in both spin-up and spin-down electrons, resulting in a high-resistivity state.

Recently, a variety of other devices have been proposed which are based on this principle of spin-transfer electronics. Magnetic tunnel junctions, spin-filters and spin-current generators are theoretically highly energy- and scale-efficient compared to modern charge-based electronics, potentially allowing the transfer of information using a spin-current rather than a charge current [2,3]. Spin-transfer within magnetic multilayer systems offers a promising candidate for next generation electronics, with high efficiency, low-power consumption and rapid spin-switching being highly desirable. Spin-transfer torque devices are a field of great interest for this purpose. Spin-polarised current switching has been proposed for use in STT-MRAM, driving the switching of the magnetic free layer in order to change the bit state. Fast, efficient switching using an applied current rather than an applied field would be ideal for this type of application. As such, investigation into controlling spin reversal behaviour using techniques like ferromagnetic resonance has seen progress in recent years [4,5,6].

In each of these applications, fine control of the spin-switching though magnetisation dynamics is crucial to the development of the next generation. Materials research is therefore an important step in developing these technologies, since thorough understanding of the magnetic behaviour is required before practical application can be achieved. Two possible candidates for this type of application are the well-known ferrimagnet magnetite (Fe_3O_4) and the recently developed quaternary Heusler Alloy $Co_2FeAl_{0.5}Si_{0.5}$ (CFAS). Both of these materials display so-called 'Half-Metal' behaviour, with a theoretical 100% spin-polarisation at the Fermi level as a result of a spin-split density of states [7,8,9,10]. This property makes both of these materials ideal for application to spin-filtering and spin-current generation. Whether or not magnetite is a true half metal is still a matter of some debate, although its high predicted spin polarisation is of great interest for practical spintronic applications.

While naturally abundant and cheap to produce, the practical application of magnetite has been hindered by its tendency to develop defects like antiphase boundaries [11,12], which render the saturation of the magnetisation difficult and induce large damping effects. The recently developed CFAS also shows promise, and has also been observed to form significant defects during growth, although in less significant quantities relative to magnetite [13]. Further investigation of this new material and its interaction with technologically relevant substrates is required before a complete understanding can be reached. The purpose of the work presented

here is to better understand the magnetisation dynamics of these highly spin-polarised metals, and to examine how the crystal structure affects the magnetic properties in systems analogous to technologically relevant applications.

In order to induce spin-flipping in a free magnetic layer, a critical current density (j_c) must be achieved [14] which is governed by the Jullière equation (equation 1.1). As the critical current density is lowered, the spin-flip process can be driven more energy-efficiently. For the purposes of this thesis, the key term is in $\frac{\alpha}{P}$ where α is the damping and P the spin polarisation. The remaining parameters are either tied to local parameters or intrinsic to the material. The critical current density can be lowered by minimising the damping or maximising the spin-polarisation (P). Given the theoretical 100% spin polarisation of both Fe_3O_4 and CFAS, P is expected to be maximised in these materials. The next step in minimising j_c is therefore to reduce the damping.

$$j_c = \left(\frac{2e}{\hbar}\right)\left(\frac{\alpha_T t}{P}\right)\mu_0 \boldsymbol{M}_s \left(\boldsymbol{H} + \boldsymbol{H}_{an} + \frac{\boldsymbol{M}_{eff}}{2}\right) \quad (1.1)$$

where e Is the electron charge, α_T is the total damping, t is the thickness of the free magnetic layer, P is the spin polarisation, μ_0 is the vacuum permeability, $\mathbf{M}_s$ is the saturation magnetisation, H is the magnetic field strength, $\mathbf{H}_{an}$ is the shape anisotropy field, and $\mathbf{M}_{eff}$ is the effective magnetisation. The effective magnetisation is given by [15]

$$\boldsymbol{M}_{eff} = \boldsymbol{M}_S - \frac{2K_u}{\mu_0 \boldsymbol{M}_S} \quad (1.2)$$

where K_u is the out of plane anisotropy constant.

The damping of the magnetisation dynamics is therefore key to the understanding of these materials, and to applying them to practical spintronics. In a highly damped system, increased energy is required to flip the spin states and this is inefficient. If the system is overdamped, the spin-flip may not occur. Conversely, if the system is underdamped, the precessional behaviour risks changing spin states continuously upon excitation, which gives rise to instability in the system. For data storage applications in particular, this instability risks the corruption and loss of data. An understanding of the damping behaviour is therefore crucial in the development of devices. The application to devices is beyond the scope of this thesis but highly spin-polarised materials will play a significant role in the next generation of spin-driven technologies. In order to understand the behaviour of these highly spin-polarised materials, thin films of Fe_3O_4 and CFAS have been grown in UHV conditions and annealed. A series of experiments have been performed to ascertain the magnetic and structural properties of each sample.

The work presented in this thesis concerns the observation of the correlation between the microstructure of a series of thin film samples and their magnetic behaviour. Fe_3O_4 is improved by a recently published annealing process [16] and this improvement is observed in both the microstructure and the magnetic behaviour of the sample. The post-annealed structure shows improvement in the damping as a result of the decreased defect density, which is confirmed by a reduction in the extrinsic damping. Fitting values to this data is difficult, however: the broad nature of the resonance peak in the non-annealed sample makes fitting to data measured at frequencies below 7GHz impossible. Anomalous behaviour in the annealed film also makes fitting

this data using conventional methods difficult. The defects are not completely eliminated by annealing, as the post-annealed film still shows a dominant extrinsic damping behaviour.

In the CFAS, it is observed that the damping is dominated by the intrinsic effects in the as-grown samples, and that it is improved with annealing up to around 500^{o}C. At this temperature, intermixing between the substrate and the thin film is observed, which distorts the crystal structure and increases the damping considerably. The increase in damping arises due to the introduction of two-magnon scattering- like behaviour from the sample defects. While the as-grown CFAS samples show better damping on the silicon substrate (α = 4.4x10^{-3} in CFAS/Si, compared to 5.6x10^{-3} in CFAS/Ge), greater improvement is observed in the post-anneal samples grown on the germanium substrate (α = 2.8x10^{-3} in CFAS/Ge annealed at 350^{o}C, compared to 4.1x10^{-3} in the CFAS/Si annealed at 450^{o}C).

1.2 Thesis Structure

This thesis is separated into seven chapters, including this introduction. Chapter 2 focuses on the physics behind the project, and the effects which give rise to the data presented in this thesis. This section of the work discusses the principles of magnetism, the physics required to understand the data presented in the later chapters and a discussion of the well understood features of materials examined in this thesis.

The techniques used to examine these materials are discussed in chapter 3. A variety of well-known experimental techniques have been used to examine both the structural and magnetic properties of the thin films in this thesis. Each of these techniques is outlined here, including a description of the physics behind each experiment, and an explanation of the useful data which can be extracted from each.

Chapter 4 presents the design, construction and testing of a bespoke Ferromagnetic Resonance Spectrometer, which is key for the acquisition of some of the key data presented in this thesis. A discussion of the practical application of each component is provided, as well as test data from the apparatus which confirms that not only is the equipment functioning correctly, but that the data collected shows good consistency with both repeated measurements from the equipment and the values recorded in the literature.

The fifth section of this thesis presents the data acquired from a series of magnetite thin films, discussing both the structural and magnetic analysis and how the two are correlated. The effects of annealing this material on the structure are also explored, and a comparison of the pre- and post-annealed samples is presented.

Chapter 6 provides a discussion of the magnetic and structural properties of a series of CFAS thin films grown on both germanium and silicon substrates. The differences between the two are compared both in the as-grown state and after annealing over a series of different temperatures.

The final section of this thesis is chapter 7, which includes a discussion of the outcomes of each experiment and how this data fits into the wider context of applied spintronic materials. A discussion of further work is also presented, considering where the project might be taken next and discussing possible follow-up experiments that might widen the communal understanding of these highly spin-polarised materials.

Chapter 2: Background Theory

2.1 Introduction

In this chapter, a discussion of the background theory behind this project is presented. Particular focus is given to ferromagnetism and magnetisation dynamics, and their role in Ferromagnetic Resonance.

2.2 Ferromagnetism

Magnetism appears in specific materials as a result of the quantum mechanical interactions between unpaired electrons in neighbouring atoms [17]. A net magnetic moment (μ) arises from the orbital and spin angular momenta of each of these electrons. In most paramagnetic materials, these spins are randomly oriented as a result of thermal effects unless an external magnetic field is applied. However, in certain materials such as iron, cobalt and nickel, as well as some of the heavy rare-earth metals, the spin moments can align in parallel, giving rise to non-zero spontaneous magnetisation even in a zero applied field. This behaviour is known as *Ferromagnetism* (figure 2.1.a) [18,19].

2.2.1 The Exchange Interaction

Two electrons with spins S_1 and S_2 and individual wavefunctions (ψ_1, ψ_2) can be expressed as a product of the individual wavefunctions when the two overlap [18,20,21,22]. The total wavefunction of the system must be antisymmetric for fermions. In this simple two-electron model, each electron is assigned a spatial co-ordinate r_n. The state of each electron is described as $\psi_n(r_n)$ electron states, and the combined state of two electrons can be written as the product of the individual states $\psi_n(r_n)\psi_m(r_m)$. Given that exchange symmetry must hold true, two possibilities arise: either the wavefunctions are spatially symmetric resulting in a singlet state with zero spin(Ψ_S), in which case the spatial component of the total wavefunction is additive (equation 2.1), or the alignment is spatially antisymmetric, giving rise to a triplet state with a total spin of 1 (Ψ_T) and the total spatial component is subtractive (equation 2.2).

$$\Psi_S = \frac{1}{\sqrt{2}}[\psi_1(r_1)\psi_2(r_2) + \psi_2(r_1)\psi_1(r_2)]\chi_S \tag{2.1}$$

$$\Psi_T = \frac{1}{\sqrt{2}}[\psi_1(r_1)\psi_2(r_2) - \psi_2(r_1)\psi_1(r_2)]\chi_T \tag{2.2}$$

where χ_n describes the spin of the corresponding electron state n. The electrons each induce a Coulomb repulsion as a result of their charges, and they each occupy non-degenerate quantum states as a consequence of the Pauli exclusion principle. The local charge distribution and subsequent spin arrangement are governed by the resulting electrostatic energy difference, known as the *exchange energy*. For simplicity it is easier to think of the exchange energy as arising from an effective interaction between two spins.

In this approach, the exchange parameter J is an energy term which is defined such that

$$\boldsymbol{U}_{Exchange} = -2J\overline{\boldsymbol{S}}_a \cdot \overline{\boldsymbol{S}}_b \tag{2.3}$$

When a series of electrons are used instead of a single pair, this energy can be generalised to the sum over local pairs i and j in the Heisenberg model (equation 2.4). It is well known, however, that this exchange effect is localised between spin pairs and doesn't have a strong effect beyond the nearest neighbouring electrons. Assuming that this is the case, and that the lattice in a given material is uniform (and therefore the exchange is isotropic throughout) this interaction can be simplified further (equation 2.5) [18].

$$\boldsymbol{U}_{Exchange} = -\sum_{i,j} J_{i,j} \overline{\boldsymbol{S}}_i \cdot \overline{\boldsymbol{S}}_j \tag{2.4}$$

$$\boldsymbol{U}_{Exchange} = -J \sum_{<i,j>} \overline{\boldsymbol{S}}_i \cdot \overline{\boldsymbol{S}}_j \tag{2.5}$$

The effect of each exchange is local, but each exchange pair will have an effect on their neighbours, resulting in a long-range ordering of all of the spin moments throughout the material. When J is positive, the spins align parallel and the material is ferromagnetic, with all the electron spin moments aligned in parallel even when no magnetic field is applied (figure 2.1.a). This differentiates it from paramagnetic materials which only align as a consequence of externally applied magnetic fields [19].

Instead of treating many spins at once, it is convenient to work with a single vector representing the sum total of moments. This is represented using the moment per unit volume, known as the *magnetisation* (**M**). If all the spins are perfectly parallel, M takes the value of the *saturation magnetisation* ($\mathbf{M_s}$) [19]. In ferromagnetic materials, the parallel alignment of all the spin moments throughout the material gives a uniform alignment across the whole sample. The long and short range interactions often overlap to a point where distinguishing between them is difficult. It is therefore convenient to model the system using a continuum approximation in which the total magnetisation is treated as one uniform magnetisation such that

$$\overline{\boldsymbol{M}}(\bar{r}) = \boldsymbol{M_s} \overline{\boldsymbol{m}}(\bar{r}) \tag{2.6}$$

where $\overline{\boldsymbol{m}}$ is a unit vector in the direction of the magnetisation (known as the reduced magnetisation) and $\bar{\boldsymbol{r}}$ denotes the position vector within the crystal structure. Assuming a uniform density of the crystal structure, a volume integral can be used to describe the exchange energy density (equation 2.7) in terms of the exchange stiffness (A) (equation 2.8). The exchange stiffness is a material parameter which can be used to describe the whole of a material, rather than the local exchange parameter.

$$\boldsymbol{U}_{Exchange} = A|\nabla \overline{\boldsymbol{m}}(\bar{\boldsymbol{r}})|^2 \tag{2.7}$$

$$A = \frac{JCS^2}{a} \tag{2.8}$$

where S is the electron spin, C describes the number of sites per unit cell, and a is defined as the distance between nearest neighbouring sites. Due to the formation of domains and defects in real ferromagnets, a sufficiently large external magnetic field must be applied in order to saturate the magnetisation in the field direction. However, the simplified picture holds up well under these conditions.

Each ferromagnetic material has a critical temperature limit known as the Curie Temperature (T_c) [18,19]. In the Ising model, T_c is directly related to the exchange parameter by equation 2.9 [23].

$$T_c = \frac{Jz}{4K_B} \tag{2.9}$$

where z is the number of nearest neighbouring atoms, and K_B is the Boltzmann constant. Above T_c the magnetic ordering is destroyed as the spin states orient randomly, leaving only paramagnetic effects within the sample. A high T_c is essential to the application of ferromagnetic devices in order to preserve spin moment alignment during device operation. All of the materials examined in this thesis have a T_c >>300K.

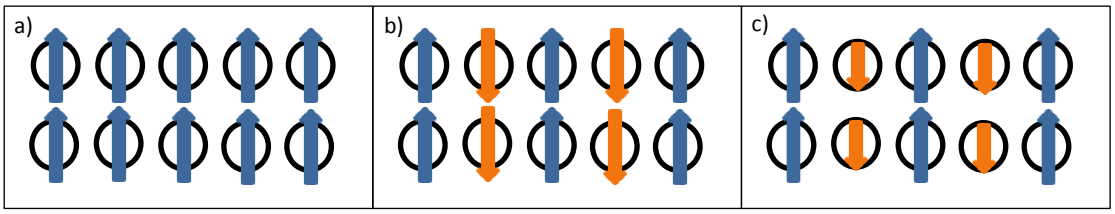

Figure 2.1 *A schematic diagram of electron spin moments aligned in a) ferromagnetic, b) anti-ferromagnetic and c) ferrimagnetic order. In each case, the magnitude of the spin moment is proportional to the size of the arrow.*

2.2.2 Anti-Ferromagnetism and Ferrimagnetism

A variant of ferromagnetism can occur when the exchange constant J is negative. In this case, the preferential alignment of the two spin moments is antiparallel and therefore one of the spin moments acts directly against the other, reducing the total magnetisation. For a two site system, this antiparallel arrangement can have one of two outcomes: either the opposing spin moments on sites A and B are equal in magnitude, thus cancelling each other out (figure 2.1b) or sites A and B are inequivalent and the opposing spins are unequal. In the case where the moments are equal, no net magnetic moment is observed over the system. This is known as *anti-ferromagnetism* (figure 2.1.b) [18,24,25]. In the second case, where the moment on one site is larger in magnitude than the other, there is still an observable magnetisation at zero applied field like a ferromagnet,

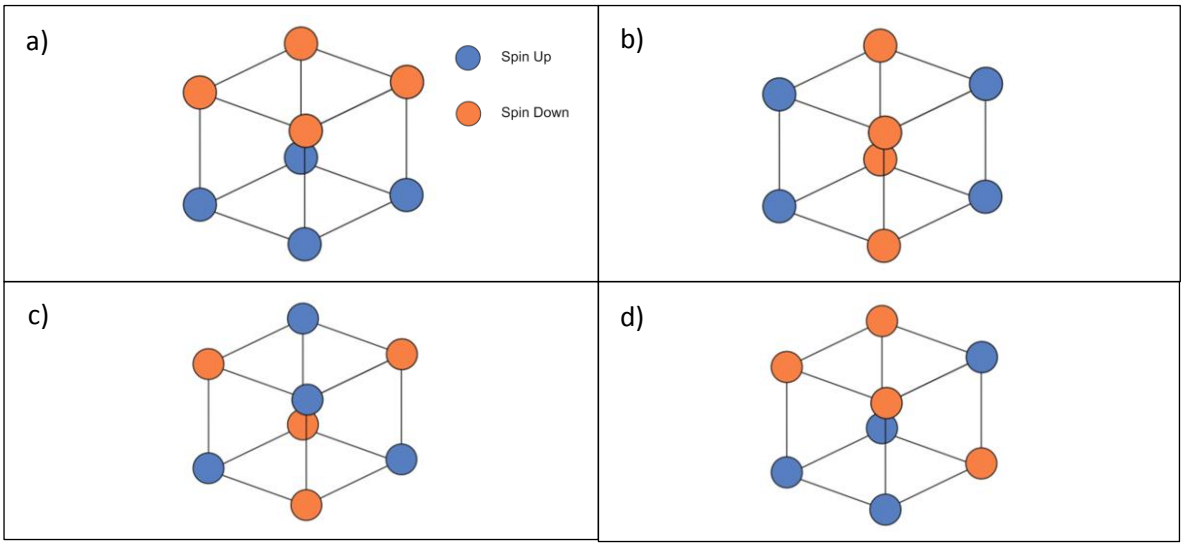

Figure 2.2 *A schematic diagram of the different arrangements of simple cubic antiferromagnetic lattice, including the a) A-Type, b) C-type, c) G-type and d) E-type order*

though it is smaller than the total moment when both spins align in parallel. This is known as *ferrimagnetism* (figure 2.1.c).

For the purposes of macroscopic analysis, the ferrimagnetic system can be approximated as a ferromagnet of small net magnetisation. The *Neel temperature* in antiferromagnets is analogous to the Curie temperature in ferromagnets: above this temperature the spin alignment is overcome by thermal effects and the magnetic ordering is destroyed.

Depending on the ordering of magnetic ions within a lattice, antiferromagnetic materials can be categorised into different types of antiferromagnet. Four different arrangements, known as types A, C, E and G are observed in simple cubic structures [18,26]. The simplest of these types are the A, C and G type ordering (figure 2.2a, b and c respectively), which have antiferromagnetic coupling between the ions arranged in adjacent (100), (110) and (111) planes respectively. The E-type order is similar to the A-type, but with the ions in one corner of each unit cell reversed (figure 2.2.d).

Three types of antiferromagnetic ordering are possible in body centred cubic crystals. In the first case, the central ion in each cubic structure is antiferromagnetically aligned with the surrounding ions at the cubic vertices (figure 2.2.a). The second has antiferromagnetic alignment between adjacent (101) planes (figure 2.2.b). The third and final type follows a similar pattern to the simple cubic type G, with antiferromagnetic coupling between each adjacent atom in the cubic lattice sites, with the sublattice of body-centred sites also antiferromagnetically aligned between adjacent sites (figure 2.2.c).

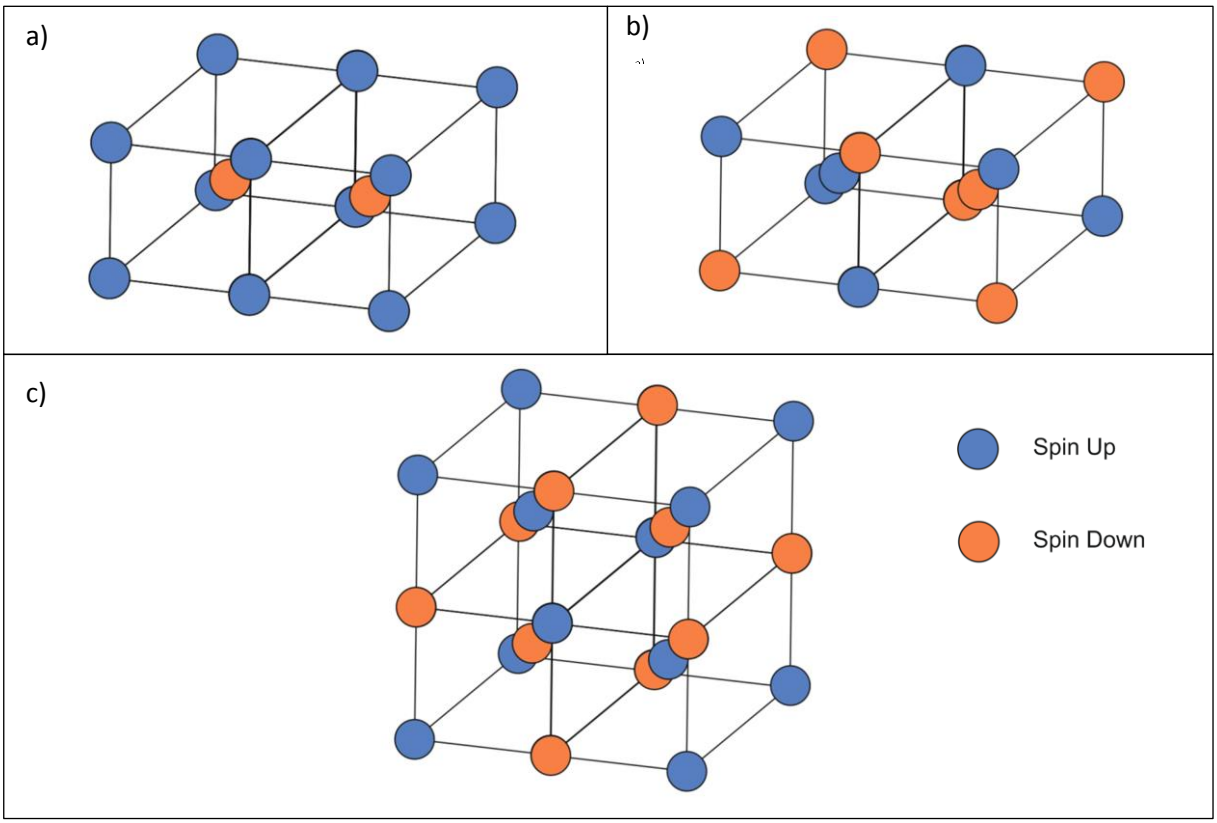

Figure 2.3 *A schematic diagram of the body-centred cubic antiferromagnetic lattices*

2.2.3 Superexchange

In structures where a non-magnetic atom separates two magnetic atoms, the overlap of local wavefunctions (electron orbitals) can give rise to interactions between the magnetic atoms which are mediated by the shared interstitial atom [18,27,28,29]. This is known as *superexchange* (or *indirect exchange*) and occurs often in ionic crystal structures such as magnetic oxides. Along with the double exchange process, discussed in section 2.2.4, superexchange is particularly relevant when considering the behaviour of magnetite [30], where the exchange interaction occurs between magnetic iron sites through the interstitial oxygen atoms. Superexchange also occurs across the non-magnetic Al and Si ions which separate some of the Co and Fe sites in the ordered phases of the CFAS structure. Both of these crystal structures are discussed in more detail in section 2.6.

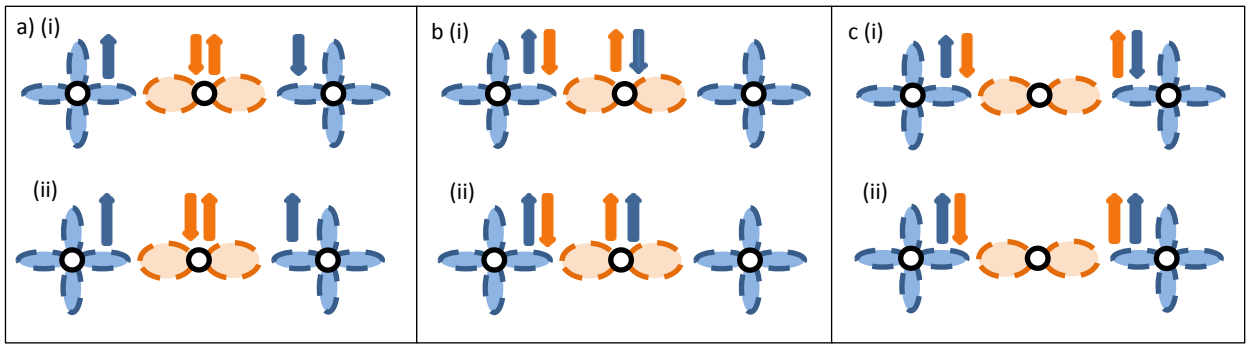

Figure 2.4 *A schematic representation of the electron state combination in a metal-interstitial-metal ion system in (i) the antiferromagnetic and (ii) the ferromagnetic electron arrangement. The arrows represent the spin states (up or down) of the electrons contributed by the metal (blue) and interstitial (orange) ions.*

The unpaired d-electrons in the transition metal ions interact with each other through the valence shell of the interstitial ion. The valence electrons in the interstitial ion form covalent pairs with the unpaired electrons from the metal ions. As in the case of direct exchange, the resulting alignment between the metal electrons determines the magnetic behaviour of the compound. In the initial state of a linear system, the d-electrons of the metal ions are isolated on the metal ions (figure.2.4.a) and could occupy either an antiferromagnetic (i) or ferromagnetic (iii) alignment.

However, the energy of the system can be reduced by delocalising and sharing the electrons between the metal ions and the interstitial. In the antiferromagnetic case (figure 2.4.b(i), fig 2.4.c(i)) these shared states are allowed. The electrons can therefore delocalise across the

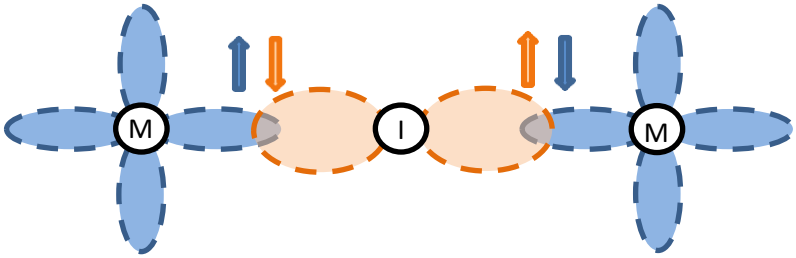

Figure 2.5 *A Schematic diagram of the superexchange effect between the unpaired 3-d electrons in two transition metal ions (M) and the p-orbitals of a non-magnetic interstitial ion (I)*

interstitial ion and reduce the total kinetic energy of the system. If the electrons are ferromagnetically aligned (figures 2.4.b(ii), 2.4.c(ii)) the shared states are prohibited by the Pauli exclusion principle. Since the ferromagnetic combination does not allow the sharing of these electrons, the higher energy state would need to be maintained in this arrangement. The antiferromagnetic alignment is therefore energetically favourable. The resulting shared electron state is shown in figure 2.5. Since the metal ions still carry a net spin moment, the magnetic behaviour is not suppressed. A different form of the exchange interaction must be used to describe this process, since the exchange interaction is now modified by the charge transfer between the ions. A new effective exchange constant (J_E) is defined, such that

$$J_E = 2\lambda^2(J + W) \tag{2.10}$$

where λ is an arbitrary constant, J is the exchange constant from the direct coupling and W is a second exchange constant which arises from the charge transfer. The resulting exchange interaction has the form

$$\boldsymbol{U}_{Super} = -2J_E\overline{\boldsymbol{S}}_a \cdot \overline{\boldsymbol{S}}_b \tag{2.11}$$

It should be noted that different outcomes may arise based on different initial electron arrangements in the metal ions: so far they have been assumed to be identical. If, for example, one of the metal ions has a filled valence shell, and the other an empty valence shell, the electrons from the filled metal ion can make use of the delocalisation to migrate to an empty orbital on the other metal ion. This occurs as a result of Hund's rules [18,31], as the electrons attempt to maximise the total spin. The net result of this behaviour is a ferromagnetic compound, albeit with a weaker superexchange coupling than the anti-ferromagnetic case explored initially. The effect also becomes more complicated when multiple overlapping orbitals are present. Care must therefore be taken when characterising this behaviour in complex crystal lattices.

2.2.3.1 Goodenough-Kanamori-Anderson Rules

While the simple case shown in section 2.2.3 leads to antiferromagnetic alignment, there are other ways in which superexchange might occur. Since the overlap of the orbitals is key in facilitating the superexchange process, the length of and angle between the metal-interstitial-metal bonds are critical in determining how the interaction behaves. The number of available valence electrons is also known to impact the superexchange effect, since it relies on the minimisation of the system energy by forming effective electron pairs: the number of occupied and empty states in each ion's valence shell is therefore of great importance.

The combination of these effects leads to either a ferromagnetic or antiferromagnetic coupling, depending on how the electrons behave. These interactions are described by the Goodenough-Kanamori-Anderson (GKA) rules [18,20,32]. These rules concern the sign of the exchange coupling constant and can therefore be used to determine whether a given structure results in a positive (ferromagnetic) or negative (anti-ferromagnetic) value of J_E. The first of the GKA rules state that for a bond angle of 180 degrees(two half-filled d-orbitals coupled by the same p-orbital) the superexchange coupling is strong and antiferromagnetic. This is the simple case outlined in the previous section. The second rule states that for a bond angle of 180 degrees, one half-filled orbital will interact with an orbital which is either empty or full in the same p-orbital, and that the resulting superexchange coupling will be weak and ferromagnetic. This corresponds to the imbalanced case touched on at the end of the previous section. The third rule states that for a 90 degree bond angle, two half-filled d-orbitals must couple using different p-orbitals, and that this results in a weak ferromagnetic coupling. Each of these three cases is shown in figure 2.6.

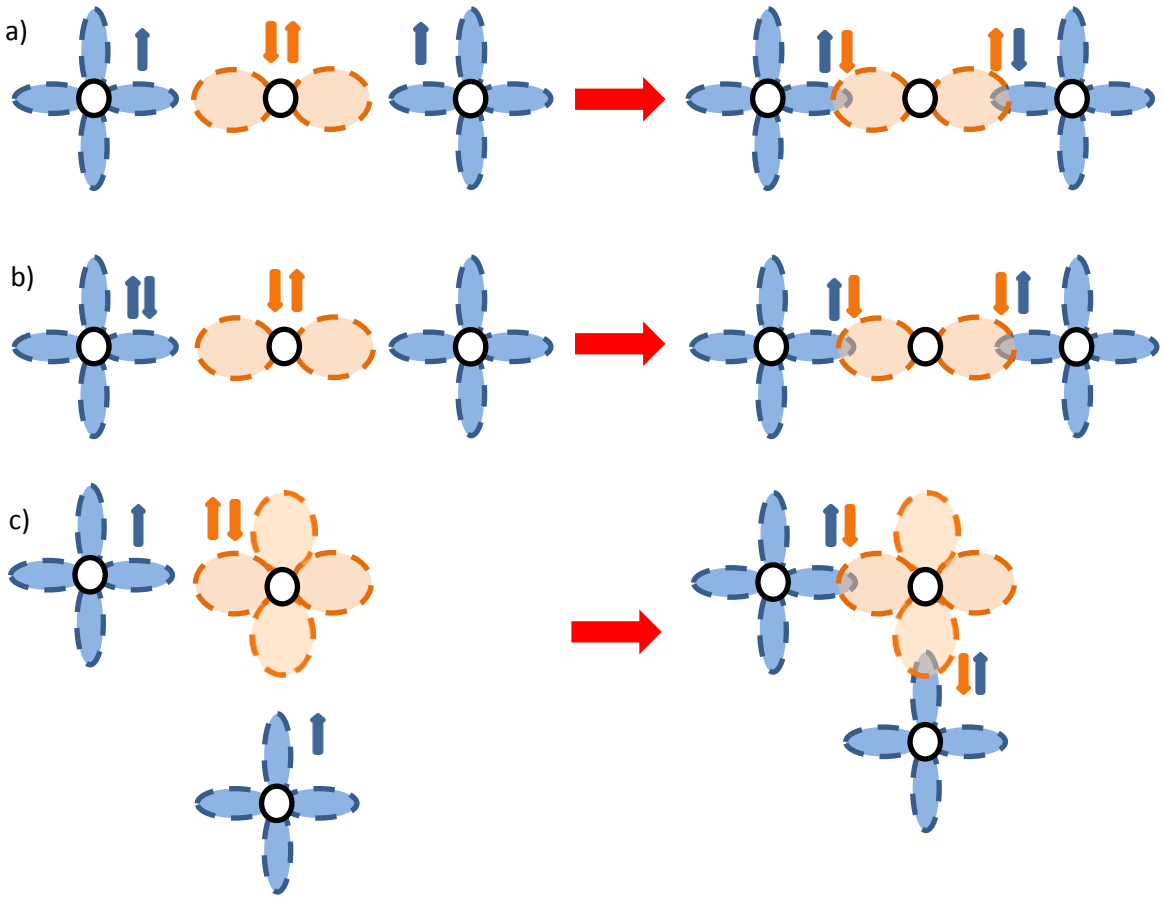

Figure 2.6 *A schematic diagram of the Goodenough-Kanamori-Anderson rules, showing a) the first, b) the second and c) the third of the GKA rules governing Superexchange coupling in ionic solids*

2.2.4 Double Exchange

In magnetic materials like magnetite, the mixed valency of the different iron sites gives rise to a secondary exchange effect known as *double exchange* [18,33]. Double exchange occurs when the magnetic ions within a metal are of the same element, but have different valence: for example, between the Fe^{2+} and Fe^{3+} sites in Fe_3O_4. Neighbouring sites can share electrons by hopping, as

long as an empty site is available with the corresponding spin: since spin-flip cannot occur during this process, the neighbouring sites must be ferromagnetically aligned in order for this to occur. Since it is energetically favourable to share electrons by this hopping process, and unfavourable to align the sites antiferromagnetically, the parallel configuration is preferred. The sharing of electrons between these sites also enables hopping conduction between the magnetic ions.

2.3 Contributions to the Magnetic Free Energy

The exchange energy is useful for describing interactions between isolated pairs of electrons, although it does not define the preferred orientations of the magnetisation along certain crystallographic directions. Additional interactions, particularly with the structural lattice, give rise to magnetic anisotropies which are discussed below.

2.3.1 The Magnetic Free Energy Equation

The Helmholtz magnetic free energy of a crystal lattice is made up of a number of parameters, such that [20,34,35,36,37,38,39]

$$\boldsymbol{U} = \boldsymbol{U}_{Zeeman} + \boldsymbol{U}_{Exchange} + \boldsymbol{U}_{Magnetocrystalline} + \boldsymbol{U}_{Magnetostatic} + \boldsymbol{U}_{Magnetoelastic} \quad (2.12)$$

where **U** is the total magnetic free energy and each of the constituent terms represents a different contribution to the total: these are the Zeeman, exchange, magnetocrystalline, magnetostatic and magnetoelastic energies respectively. As the materials studied in this thesis have reasonably small magnetostriction constants and isotropic strain in the sample plane, the corresponding energy term is treated as a small isotropic effect and therefore has a negligible impact on the shape of the free energy surface. The magnetostriction constants are given by λ, where at room temperature λ_{Fe3O4} = -1.67x10^{-5} in the (100) plane and +9.06x10^{-5} in the (111) [40].While a value for λ_{CFAS} is difficult to find in the literature, values for the similar full-Heusler alloy CFA are of comparable magnitude to that observed in Fe_3O_4 (λ_{CFA} = 1.38x10^{-5})[41].

The energy density terms are typically defined in spherical polar co-ordinates and plotted as a function of the angles θ and ϕ (polar angle and the azimuthal angle in the x-y plane respectively) to define the magnetic free energy surface, as described in figure 2.7. The definitions provided in the figure will be used throughout this thesis for consistency. For the purposes of defining the magnetic free energy surface, the spin moments will be treated as acting uniformly under magnetic saturation and as such a macrospin model will be assumed.

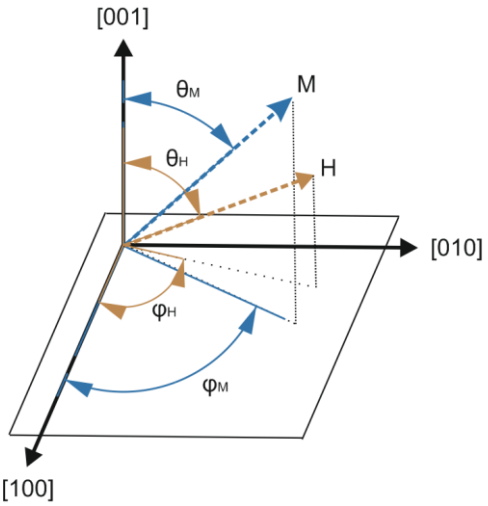

Figure 2.7 *A schematic of the geometry relating* ***M****,* θ_M*,* ϕ_M*,* θ_H *and* ϕ_H *in a general model of magnetisation dynamics*

2.3.1.1 Zeeman Energy

It is well known that spin moments in a magnetic field are driven to align in parallel with the applied magnetic field (sometimes known as the *Zeeman* or *bias* field) [19,21]. This is a result of the Zeeman energy term, described as

$$\boldsymbol{U}_{Zeeman} = -\mu_0 \boldsymbol{M}_s \bar{\boldsymbol{m}} \cdot \bar{\boldsymbol{H}}_{applied} \tag{2.13}$$

where μ_0 is the permeability of free space, $\mathbf{M}_s$ is the saturation magnetisation, $\bar{\mathbf{m}}$ is the unit vector in the direction of the magnetisation and $\mathbf{H}_{applied}$ is the applied magnetic field. This energy is minimised when the reduced magnetisation and the applied field are in parallel, leading to a natural alignment between the two vectors. At saturation, the magnetisation of a ferromagnetic material will therefore try to align in parallel with an applied bias field if no other energy terms are considered. As the magnitude of the applied field increases, the Zeeman term dominates the magnetic free energy surface. This results in the deformation of the free energy surface, forcing a free energy minimum to be induced along the direction of the bias field.

2.3.1.2 Crystal Field Effects

Variations in the local electron environments can distort the electronic structure. Coulomb repulsion between electrons in non-spherically symmetric orbitals acts to minimise the energy of the local environment. This results in an additional electric field known as the *crystal field* [18,19]. This additional field removes the degeneracy of the orbitals by introducing an energy gap between orbitals of different character – E_g and $t2_g$. Distortions in the lattice also give rise to shifts in the crystal field lifting the degeneracy further. For the purposes of defining the magnetic free energy surface, the crystal field term is accounted for within the magnetocrystalline anisotropy energy term.

Crystal field effects eliminate the orbital degeneracy in transition metal ions, which quenches the orbital angular momentum [18]. A non-degenerate ground state ($|0\rangle$) must be determined by a real wavefunction. The total angular momentum operator **L** is Hermitian so $\langle 0|\mathbf{L}|0\rangle$ must be purely real. However, the operator **L** is purely imaginary. The only value which can meet both of these requirements is **L** = 0. In a real crystal structure, a small spin-orbit coupling may occur and the orbital moment may not be entirely quenched. This can produce a g-factor where the spin

contribution of g = 2 is bolstered by an additional component which is proportional to the orbital angular momentum contribution.

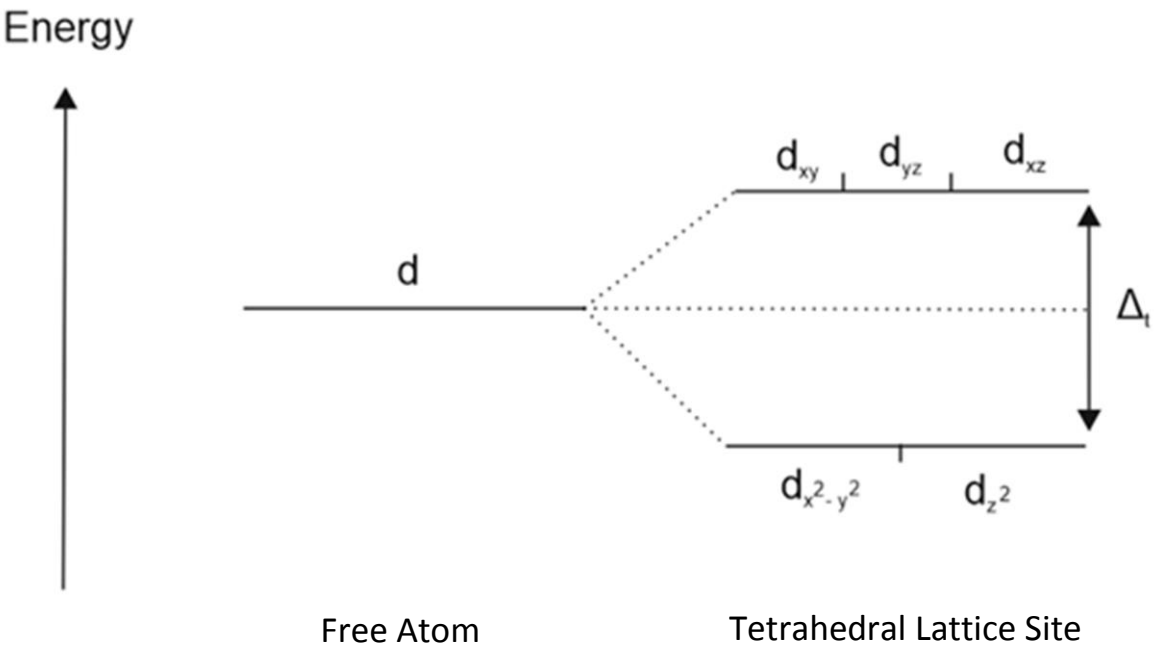

Figure 2.8 *A schematic of the energy level splitting in tetrahedral lattice sites arising from the crystal field*

2.3.1.3 Magnetocrystalline Energy

The crystal structure of a ferromagnet will also introduce an energy term to the system as a result of spin-orbit coupling. This is the result of interaction between the spin angular momentum of the electrons and their orbital angular momentum within the crystal lattice [19]. This coupling gives rise to an energy term which minimises the electrostatic repulsion between electrons. The result of this realignment is often that the free energy is no longer isotropic, and that energetically favourable directions for the magnetisation now exist. This directional dependence is known as *magnetocrystalline anisotropy* (MCA) [19,20,22]. Since all of the materials examined in this thesis have cubic crystal structures, only the cubic form of the magnetocrystalline anisotropy needs to be considered.

The MCA has a directional dependence which is governed by the structure of the crystal lattice. The anisotropy can be described using an energy density ($\mathbf{U}_{\text{Magnetocrystalline}}$) related to the directional cosines (α_i) between the magnetisation and the principal crystallographic axes (u_n, where: u_1 = [100], u_2 = [010], u_3 = [001]). Considering a cubic crystal structure, the magnetocrystalline anisotropy energy is defined as [19,42]

$$\boldsymbol{U}_{Magnetocrystalline} = K_{c0} + K_{c1}(\alpha_1^2\alpha_2^2+\alpha_2^2\alpha_3^2+\alpha_3^2\alpha_1^2) + K_{c2}(\alpha_1^2\alpha_2^2\alpha_3^2) \ldots \qquad (2.14)$$

where K_{ci} is the i^{th} order cubic anisotropy constant, an energy density parameter which varies depending on the material. The terms in α correspond to the directional cosines [42,43], defined as $\alpha_1 = \cos(\varphi_M)\sin(\theta_M)$, $\alpha_2 = \sin(\varphi_M)\sin(\theta_M)$ and $\alpha_3 = \cos(\theta_M)$. Given that the 0^{th} order

term has no directional dependence, it does not contribute to the overall anisotropy. Second order terms and higher are usually of small magnitude, and therefore have minimal impact on the anisotropy. The magnetocrystalline energy term in a cubic crystal is therefore usually simplified to

$$\boldsymbol{U}_{Magnetocrystalline} = K_c(\propto_1{}^2\propto_2{}^2+\propto_2{}^2\propto_3{}^2+\propto_3{}^2\propto_1{}^2) \tag{2.15}$$

when the cosines are inserted, the expression simplifies to

$$\boldsymbol{U}_{Magnetocrystalline} = K_C\left(\frac{1}{4}sin^2(2\varphi)sin^2(\theta) + cos^2(\theta)\right)sin^2(\theta) \tag{2.16}$$

The sign of the cubic anisotropy constant also determines the shape of the anisotropy. When the sum of the free energy terms shows non-zero anisotropy, **M** moves to minimise the energy and therefore points along the free energy surface minima, which are designated as *easy axes* [19]. The maxima, known as *hard axes*, require extra energy for **M** to align along the direction in a stable state, which requires the application of a bias field of sufficient magnitude. When the anisotropy constant is positive the easy axes are aligned along the cubic axes and the hard axes along the [111] directions. For negative values of K_c the axes invert, moving the easy axes to the [111] directions and the hard axes to the cubic directions.

In thin film samples which are subject to strain as a result of lattice mismatch, tetragonal distortions can lift the cubic anisotropy and give rise to an out of plane uniaxial anisotropy in addition to an in-plane cubic magnetocrystalline anisotropy.

The measurement of this anisotropy using magnetic spectroscopy techniques can therefore be used to examine the magnetic free energy surface and provide insight into the crystal structure under examination.

2.3.1.4 Magnetostatic Energy

Since the magnetic dipoles associated with each individual lattice site also induce a corresponding magnetic field, an energy term must therefore arise as a result of these moments interacting with the magnetisation. This interaction always acts in opposition to the magnetisation, and therefore the field responsible is known as the *demagnetising field* [19,21]. Each magnetic site in the crystal lattice has a corresponding magnetic moment (μ) which induces a magnetic field at a distance (r) given by

$$\boldsymbol{h}_j = \frac{1}{4\pi}\left[-\frac{\mu_i}{|\boldsymbol{r}+\boldsymbol{r}_i|^3} + \frac{3}{|\boldsymbol{r}+\boldsymbol{r}_i|^5}\left(\mu_i\cdot(\boldsymbol{r}-\boldsymbol{r}_i)\right)(\boldsymbol{r}-\boldsymbol{r}_i)\right] \tag{2.17}$$

at the i^{th} lattice point, where $\mathbf{r}_i$ is the position of the site in the lattice. This magnetic field gives rise to a corresponding energy (E_i) as described in equation 2.18. Since this expression only accounts for one lattice site, it is useful to treat this energy as a summation over the whole system, which is given in equation 2.19.

$$\boldsymbol{E}_i = -\mu_i\cdot\sum_{j\neq i}\mu_0\boldsymbol{h}_j \tag{2.18}$$

$$\boldsymbol{E}_{Magnetostatic} = -\sum_i\mu_i\sum_{j\neq i}\mu_0\boldsymbol{h}_j \tag{2.19}$$

It is useful here to introduce the demagnetising field term here, described in equation 2.20, as it simplifies the treatment of the magnetostatic energy term. It can now be expressed in terms of a single convenient sum over the moments in the lattice structure, as seen in equation 2.21.

$$\boldsymbol{H}_d = \sum_i \boldsymbol{h}_i \tag{2.20}$$

$$\boldsymbol{E}_{Magnetostatic} = -\frac{\mu_0}{2}\sum_i \mu_i \boldsymbol{H}_d \tag{2.21}$$

This expression is still dependent in part on a treatment of individual lattice sites. In many cases, it is easier to treat the demagnetising field as a continuous field term: it is then no longer necessary to treat each lattice site individually and the expression can be applied in the general case. $\mathbf{H}_d$ may therefore be re-written as in equation 2.22.

$$\boldsymbol{H}_d = \frac{1}{4\pi}\left[\int_V \frac{\rho_V(\boldsymbol{r}')(\boldsymbol{r}-\boldsymbol{r}')}{|\boldsymbol{r}-\boldsymbol{r}'|^3}\, dV + \int_S \frac{\rho_S(\boldsymbol{r}')(\boldsymbol{r}-\boldsymbol{r}')}{|\boldsymbol{r}-\boldsymbol{r}'|^3} dS\right] \tag{2.22}$$

where ρ_s and ρ_V represent the surface and volume magnetic charge densities respectively. This treatment also has the advantage of simplifying the system in the case where the magnetisation is uniform across the whole sample, since the volume integral goes to zero, leaving

$$\boldsymbol{H}_d = \frac{1}{4\pi}\left[\int_S \frac{\rho_S(\boldsymbol{r}')(\boldsymbol{r}-\boldsymbol{r}')}{|\boldsymbol{r}-\boldsymbol{r}'|^3} dS\right] \tag{2.23}$$

and the corresponding energy density may be written as

$$\boldsymbol{U}_{Magnetostatic} = -\frac{\mu_0 \boldsymbol{M}_S}{2}\bar{\boldsymbol{m}} \cdot \boldsymbol{H}_d \tag{2.24}$$

The remaining integral term in equation 2.23 has the form of a uniaxial anisotropy, and depends only on the magnetisation direction and the shape of the sample. As a result it is commonly known as the *shape anisotropy* [18]. In the case of magnetic thin films, the shape anisotropy tends to align the magnetisation in the film plane in order to minimise the energy. All of the samples examined in this thesis are thin films and are therefore expected to show this property. The combination of the resulting uniaxial anisotropy with the magnetocrystalline anisotropy may be observed when measuring the total anisotropy in the plane of the film.

The magnetic field induced by these dipole moments extends beyond the boundaries of the sample, but under these circumstances no longer has a significant effect on the magnetisation of the sample. It is therefore useful to define a separation between the two components of the dipole field: inside the sample it is still referred to as the demagnetising field, whereas the external component is called the *stray field*.

In thin film geometries, the demagnetising field can be approached more simply. The discontinuity in the magnetic field at the sample faces can be written as

$$\nabla.\boldsymbol{H} = -\nabla.\boldsymbol{M} \tag{2.25}$$

Given that the opposite charge is induced at opposing surfaces, this can be treated as an effective magnetic dipole. The demagnetising field arises in response to the magnetic dipole which forms across a sample. If the magnetisation is aligned out of the plane of the sample, the magnetic dipole forms between the upper and lower faces of the sample, and follows the form [44,45]

$$\boldsymbol{U}_{Magnetostatic} = \frac{1}{2}\mu_0 \boldsymbol{M}^2 cos^2\theta \quad (2.26)$$

If the magnetisation is aligned in the plane of the sample, however, the dipole which induces the demagnetisation field forms at opposite sides of the sample. In the case where the sample width >> the sample thickness, this can be treated as an infinite separation and therefore the demagnetising field induced tends to zero [18].

2.3.2 The Magnetic Free Energy of a Cubic Crystal Structure

All of the free energy terms in section 2.3.1 collectively define the total shape of the magnetic free energy surface. It is useful to calculate this free energy surface in order to determine the anisotropy of the system. In this thesis, two different materials with cubic structures will be considered: it is therefore prudent to calculate the free energy surface for a cubic crystal in order to set some expectations for the anisotropy. In accordance with equation 2.12, all of the free energy terms for a cubic crystal structure are collected to describe the surface. However, for the purposes of determining the shape of the anisotropy, this can be simplified by considering only those terms which have a directional dependence. Since the other terms only affect the magnitude of the free energy surface, only the magnetocrystalline (equation 2.16) and the demagnetising (equation 2.26) will be used. Isotropic terms only affect the magnitude, not the shape, and are therefore all effectively described by a constant. For ease of description, the Zeeman term is set to zero. In this case, the shape of the free energy surface can therefore be modelled using a simplified expression, given in equation 2.27.

$$\boldsymbol{U} = Constant + \frac{1}{2}\mu_0 \boldsymbol{M}^2 cos^2(\theta) + K_C\left(\frac{1}{4}sin^2(2\varphi)sin^2(\theta) + cos^2(\theta)\right)sin^2(\theta) \quad (2.27)$$

Since the crystals investigated in this thesis are aligned with the [111] crystal direction, it is useful to rotate this expression from the [100] into the [111]. Under the correct transformation, equation 2.27 becomes

$$\boldsymbol{U} = Constant + \frac{1}{3}K_C cos^4(\theta) - 0.4\dot{6}K_C \cos(\theta)\, cos(3\varphi) sin^3(\theta) + \frac{1}{4}K_C sin^4(\theta) + \frac{1}{2}\boldsymbol{M}[\boldsymbol{M} cos^2(\theta) - 2\boldsymbol{H}\cos(\theta)\cos(\theta_H) - 2\boldsymbol{H} cos(\varphi - \varphi_H)\sin(\theta)\sin(\theta_H)] \quad (2.28)$$

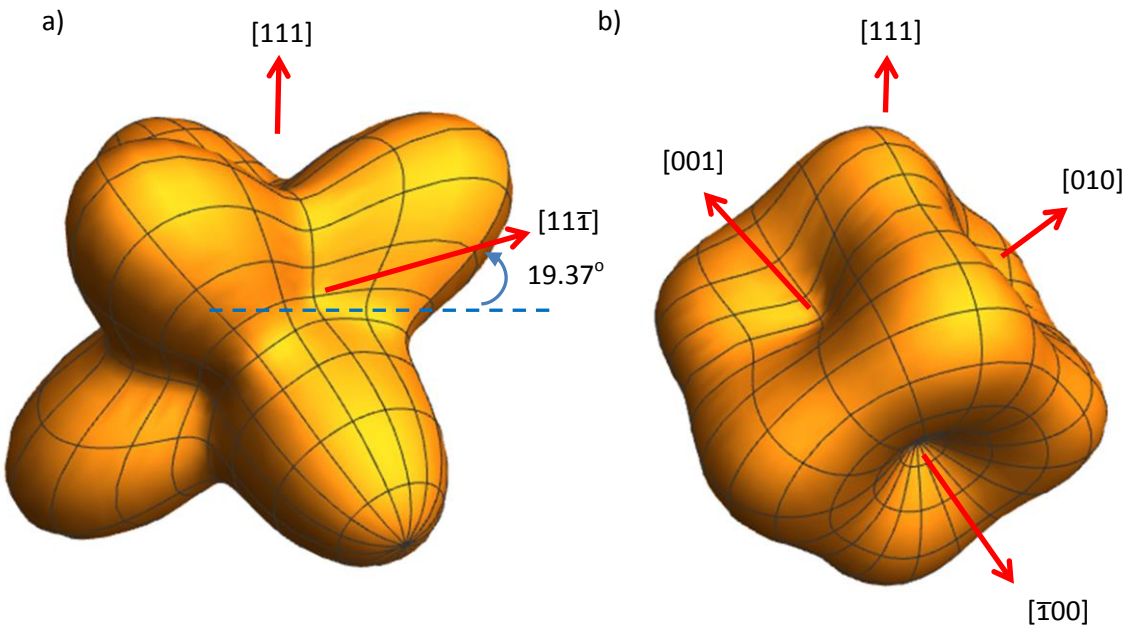

Figure 2.9 *A model of the magnetic free energy surface for a cubic crystal with a) a negative K_c and b) a positive K_c*

With the system sufficiently simplified, the shape of the magnetic free energy surface can be calculated for a cubic crystal. The magnetic free energy surface of a 111-aligned cubic crystal with a negative K_c is plotted in figure 2.9.a, and a positive K_c in 2.9.b. A significant difference is observed in the energy surface depending on the sign of the cubic anisotropy constant K_c. If $\mathbf{M}_{eff}$ is aligned perfectly with the plane, the anisotropy exactly in the plane is isotropic. However, the easy axis along [11$\bar{1}$] is not exactly in the plane of the thin film. It can be observed in figure 2.9.a that the easy axis is not perfectly aligned in the sample plane: since the [111] and [11$\bar{1}$] are separated by 70.63°,an offset of 19.37° is observed from the plane (shown in figure 2.9.a). This leads to a slight out-of-plane alignment in the free energy minima. In the case where the magnetisation or the shape anisotropy is greater the magnetocrystalline anisotropy, the

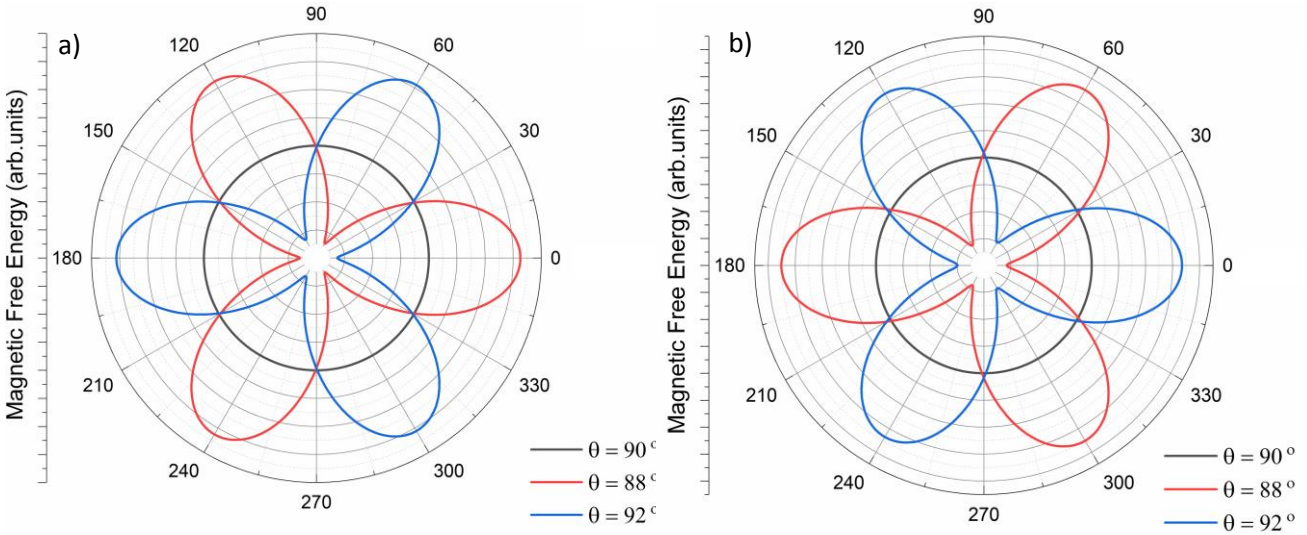

Figure 2.10 *A comparison of the magnetic free energy surfaces at various polar angles for a 111-aligned cubic crystal with a) a negative K_c and b) a positive K_c*

magnetisation is pulled into the plane of the film by the demagnetising field. However, in a structure such as magnetite, with a relatively small magnetisation, a competition arises between the demagnetising effects, pulling the magnetisation towards the film plane, and the magnetocrystalline energy, pulling $\mathbf{M}_{eff}$ towards the <111> directions. This results in an effective magnetisation slightly out of the plane of the thin film. As the $\mathbf{M}_{eff}$ is rotated, the free energy surface moves and the easy axes switch from above the plane to below the plane, dragging $\mathbf{M}_{eff}$ in an oscillating path around the free energy surface. This slight deviation away from the plane results in the isotropic behaviour being superseded by a cubic anisotropy. The free-energy surface has a six-fold anisotropy in the (111) plane. As K_c changes sign, the easy and hard axes in the free energy surface invert and the corresponding peaks trade positions, as observed in figure 2.10. Given that each of the samples presented in this thesis have been grown aligned with the (111), it is therefore expected that the easy axes will align with the <111> directions when $K_c<0$ and with the <100> directions when $K_c>0$, if the shape anisotropy term is small.

2.4 Magnetisation Dynamics

Measurement of magnetic behaviour under static conditions is useful for structural applications, but recently devices have begun to emerge based on dynamic magnetic behaviour.

The magnetic moment of an electron (μ) is related to the total angular momentum (J) by the expression

$$\boldsymbol{\mu} = \gamma \boldsymbol{J} \tag{2.29}$$

where *γ* is a constant known as the *gyromagnetic ratio* [18,46]. This ratio is an important component of many of the magnetic properties of magnetic systems, and is a useful value to extract from magnetic spectroscopy.

Another key term to be considered is the Landé g-factor (g) [47], which is a proportionality constant which relates the spin and orbital magnetic moments of the electron to the magnetic dipole moment. The free electron value of g ≈ 2 is observed in in most materials, but varies in magnetically ordered materials depending on the ratio between the spin and orbital magnetic moments. The g-factor is directly related to the ratio of spin and orbital magnetic moments in a magnetic material by equation 2.29 [48]. Gamma may also be extracted from g, and vice versa, since they are related by equation 2.30.

$$g = 2\left(\frac{\mu_l}{\mu_s} + 1\right) \tag{2.30}$$

$$\gamma = \left|\frac{g\mu_B}{\hbar}\right| \tag{2.31}$$

The g-factor is also important in the Zeeman effect since it determines the magnitude of the energy separation between spin-up and spin-down states (equation 2.32). In the transition metals, L-S coupling occurs [18,49] and the total angular momentum (J) is defined by the sum of the spin angular momentum (S) and the orbital angular momentum (L) if the valence shell is less than half filled, or by L – S if the shell is more than half filled. However, in transition metal systems, the orbital component is generally quenched, so L ≈ 0. In these cases, the approximation J ≈ S can be made. It is therefore useful to extract g using magnetic spectroscopy techniques, in order to describe the magnetic behaviour of different materials.

$$\boldsymbol{E} = g\mu_B \boldsymbol{B} \tag{2.32}$$

Zeeman splitting of spin states in a magnetic field provides two discrete energy levels which are occupied by the spin-down and spin-up electrons. Excitation of the electrons at the frequency corresponding to this energy difference can therefore be used to drive magnetic dipole transitions, as long as an empty spin state is available to accommodate the transition. Driving the electrons between these spin states induces motion in the magnetisation which has well-understood dynamic behaviour governed by the magnetic parameters of the system.

2.4.1 The Landau-Lifshitz-Gilbert Equation

Measurements of the dynamic behaviour can therefore be used to extract useful magnetic parameters in order to classify and compare the properties of magnetic materials. Using a macrospin model, the magnetisation dynamics can be described by the Landau-Lifshitz Gilbert equation. It is well-known that the precession of spin magnetic moments in ferromagnetic samples can be described using the Landau-Lifshitz-Gilbert equation (equation 2.33) [48,50,51].

$$\frac{d\boldsymbol{M}}{dt} = -\gamma\left(\boldsymbol{M} \times \boldsymbol{H}_{eff} - \frac{\alpha}{\boldsymbol{M}_s}\boldsymbol{M} \times \frac{\partial \boldsymbol{M}}{\partial t}\right) \tag{2.33}$$

where **M** is the magnetisation, $\mathbf{M}_s$ is the saturation magnetisation, γ is the gyromagnetic ratio, and $\mathbf{H}_{eff}$ is the effective field, which arises as a combination of several contributions including the bias field, the demagnetisation field, the magnetocrystalline anisotropy and the magnetoelastic effects within the crystal structure. This model of the precessing magnetisation provides a useful method with which to quantify the magnetic damping behaviour (equation 2.34).

$$\boldsymbol{H}_{eff} = \boldsymbol{H}_{Zeeman} + \boldsymbol{H}_{Exchange} + \boldsymbol{H}_{Magnetocrystalline} + \boldsymbol{H}_{Magnetoelastic} + \boldsymbol{H}_{Shape} \tag{2.34}$$

The $\mathbf{M}\times\mathbf{H}_{eff}$ term describes the torque exerted on $\mathbf{H}_{eff}$ by **M** and the second term describes the damping of the precessional motion. This term includes the Gilbert damping parameter, α, which is a scalar quantity which describes the amount of intrinsic damping that affects a dynamic magnetisation. This parameter and the magnetic damping phenomena are covered in more detail in section 2.5.4.

2.5 Ferromagnetic Resonance

If a magnetic field is applied to a series of magnetic moments, they will tend to line up parallel to the field, because this minimizes their magnetostatic energy. In this configuration, the magnetic moments can be considered as a single macrospin. If the macrospin is taken away from

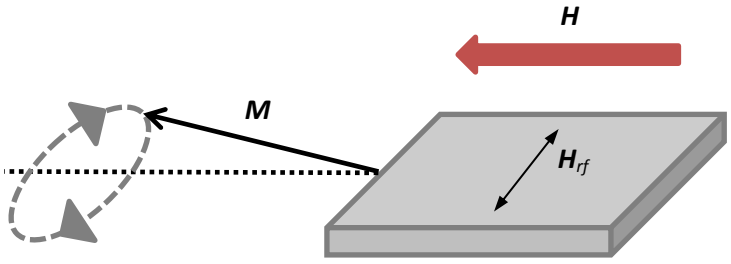

Figure 2.11 *A schematic representation of the FMR effect in a sample subject to a magnetic field* $\boldsymbol{H}_{eff}$ *and a transverse RF excitation* $\boldsymbol{H}_{rf}$*. The precession is driven by* $\boldsymbol{M} \times \boldsymbol{H}_{eff}$ *at the frequency ω*

equilibrium, by a small perturbing field pulse perpendicular to the bias field, it will try to return to equilibrium through the torque exerted by the magnetic field. If the perturbing field ($\mathbf{H}_{rf}$) is applied at a specific frequency such that it matches the Larmor frequency of the magnetic moment, the macrospin can precess resonantly about the equilibrium direction [52,53]. Resonant precession of the magnetisation about an applied field is known as Ferromagnetic Resonance (FMR). The LLG equation describes the time-evolution of the magnetisation in a ferromagnet in an external magnetic field [51]. The precession varies with the frequency of the applied RF wave and resonates at a critical (resonance) frequency. In a magnetically ordered system this occurs in all of the electrons simultaneously, so the magnetisation is seen to precess about the axis of the external magnetic field. (figure 2.11).

2.5.1 The Classical Picture

The original treatment of the FMR effect was a classical picture developed by Kittel in 1948 [52]. In this model, the magnetisation is treated as a macroscopic vector aligned with the bias field, in which a small precession about the bias field can be induced by an RF excitation. A Larmor-like precession is then observed when the resonance condition is met, as the RF drives the magnetisation to precess about the bias field. This behaviour is described as a magnetic torque ($-\boldsymbol{M}x\boldsymbol{H}_{eff}$).

An additional term describing the magnetic damping is needed in order for the magnetization to align with the bias field when there is no RF present. This is provided by the damping term in the in the LLG equation.

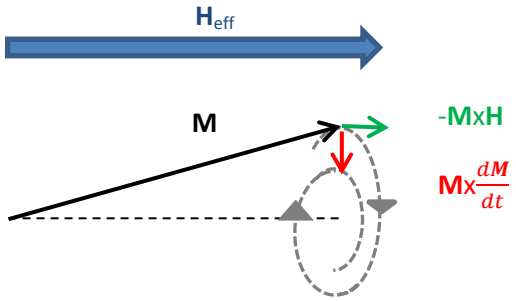

Figure 2.12 *A schematic representation of the Larmor precession in the classical picture of FMR*

2.5.2 The Quantum Picture

The FMR effect may also be considered using a quantum mechanical picture [54]. When the photon energy ($\hbar\omega$) is equal to the Zeeman splitting energy (equation 2.32), an excitation from the low to high energy spin states is driven by the absorption of RF photons. The subsequent re-emission of the photon allows the electron to decay back to its original state. This switching between states results in the precession of the magnetisation vector about the bias field.

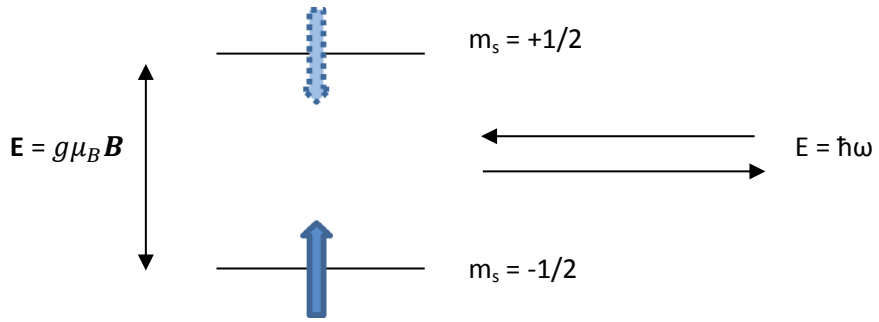

Figure 2.13 *A schematic diagram of the FMR excitation in the quantum mechanical model, where m_s is the spin magnetic moment of the electron*

2.5.3 The Kittel Equation

The Kittel equation describes the field dependence of the FMR frequency: a typical FMR curve in frequency – field space, commonly known as a Kittel Curve, is shown in figure 2.14. At low bias fields, the curve displays a $\sqrt{H}$ behaviour transitioning to a linear dependence at higher bias fields. This equation is derived from a combination of the formula derived by Kittel, which states that the resonance condition is met when [52]

$$\omega_0 = \gamma\sqrt{\boldsymbol{H}_{eff}\boldsymbol{B}_{eff}} \tag{2.35}$$

Using the well-known results for cubic crystal structures [55]

$$\boldsymbol{H}_{eff} = \frac{2}{\boldsymbol{M}}K_{c(par)}\cos(4\varphi) + \mu_0\boldsymbol{H}cos(\varphi-\varphi_M) - \frac{2}{\boldsymbol{M}}K_{u(par)}\cos(2\varphi-2\varphi_u) \tag{2.36}$$

where $K_{c(par)}$ is the cubic anisotropy constant parallel with the sample plane, $K_{u(par)}$is the uniaxial anisotropy constant parallel with the plane, φ_M is the relative angle of M in φ and φ_u is the relative angle of the uniaxial direction in φ.

$$\boldsymbol{B}_{eff} = \frac{1}{2\boldsymbol{M}}K_{c(par)}\,(3+\cos(4\varphi)) + \mu_0\boldsymbol{H}cos(\varphi-\varphi_M) + \mu_0\boldsymbol{M} - \frac{2}{\boldsymbol{M}}K_{u(per)} + \frac{2}{\boldsymbol{M}}K_{u(par)}\sin^2(\varphi-\varphi_u) \tag{2.37}$$

where $K_{u(per)}$is the uniaxial anisotropy constant perpendicular to the sample plane. The resonance condition can therefore be written as

$$\left(\frac{\omega_0}{\gamma}\right)^2 = \left(\frac{2}{\boldsymbol{M}}K_{c(par)}\cos(4\varphi) + \mu_0\boldsymbol{H}cos(\varphi-\varphi_M) - \frac{2}{\boldsymbol{M}}K_{u(par)}\cos(2\varphi-2\varphi_u)\right)*$$
$$\left(\frac{1}{2\boldsymbol{M}}K_{c(par)}\,(3+\cos(4\varphi)) + \mu_0\boldsymbol{H}cos(\varphi-\varphi_M) + \mu_0\boldsymbol{M} - \frac{2}{\boldsymbol{M}}K_{u(per)} + \frac{2}{\boldsymbol{M}}K_{u(par)}\sin^2(\varphi-\varphi_u)\right) \tag{2.38}$$

Depending on the sample geometry, these expressions can be considerably simplified: in the case of a cubic structure with the magnetisation aligned along the easy axis in the sample plane, $\phi = 0$ and $\phi_u = 0$. This reduces the expression to

$$\left(\frac{\omega_0}{\gamma}\right)^2 = \left(\frac{2}{\boldsymbol{M}}K_{c(par)} + \mu_0\boldsymbol{H} - \frac{2}{\boldsymbol{M}}K_{u(par)}\right)\left(\frac{2}{\boldsymbol{M}}K_{c(par)} + \mu_0\boldsymbol{H} + \mu_0\boldsymbol{M} - \frac{2}{\boldsymbol{M}}K_{u(per)}\right) \tag{2.39}$$

Given that the term $\mu_0 \boldsymbol{M} - \frac{2}{\boldsymbol{M}} K_{u(per)}$ can be condensed to $\mu_0 \boldsymbol{M}_{eff}$ using equation 1.2, (which is multiplied by 4π when converting from Si to cgs units) a term in $4\pi \boldsymbol{M}_{eff}$ is recovered. The term in $\frac{2}{\boldsymbol{M}} K_{c(par)}$ describes the anisotropy field ($\mathbf{H}_a$) and the $-\frac{2}{\boldsymbol{M}} K_{u(par)}$ term is combined with this to become the anisotropy field $\mu_0 H_a$. In the simplified case where the uniaxial and cubic anisotropy components are parallel, they can be treated as a single combined anisotropy term. This simplifies equation 2.39 to the in-plane Kittel equation (equation 2.40).

$$\omega_0 = \gamma \sqrt{(\boldsymbol{H} + \boldsymbol{H}_a)(\boldsymbol{H} + \boldsymbol{H}_a + 4\pi \boldsymbol{M}_{eff})} \tag{2.40}$$

Varying the relative angle between the crystal structure of the sample and the bias field also allows the anisotropy of the sample to be investigated, since the position of the Kittel curve will shift depending on the field direction relative to easy and hard axes in the crystal structure. As the relative orientation approaches the easy axis, the resonance field is minimised at a fixed RF excitation frequency. Conversely, along the hard axis of a crystal structure the resonance shifts to higher field values at a given frequency. This results from the additional anisotropy field contribution to the total field acting on the free energy density and therefore the magnetisation.

Fitting ω(**H**) using FMR spectroscopy data can therefore be used to probe a number of useful magnetic properties, such as the saturation magnetisation, magnetic anisotropy field and the gyromagnetic ratio. Other parameters may be extracted from FMR spectroscopy data; for example, measuring FMR can be used to probe the Gilbert damping parameter α.

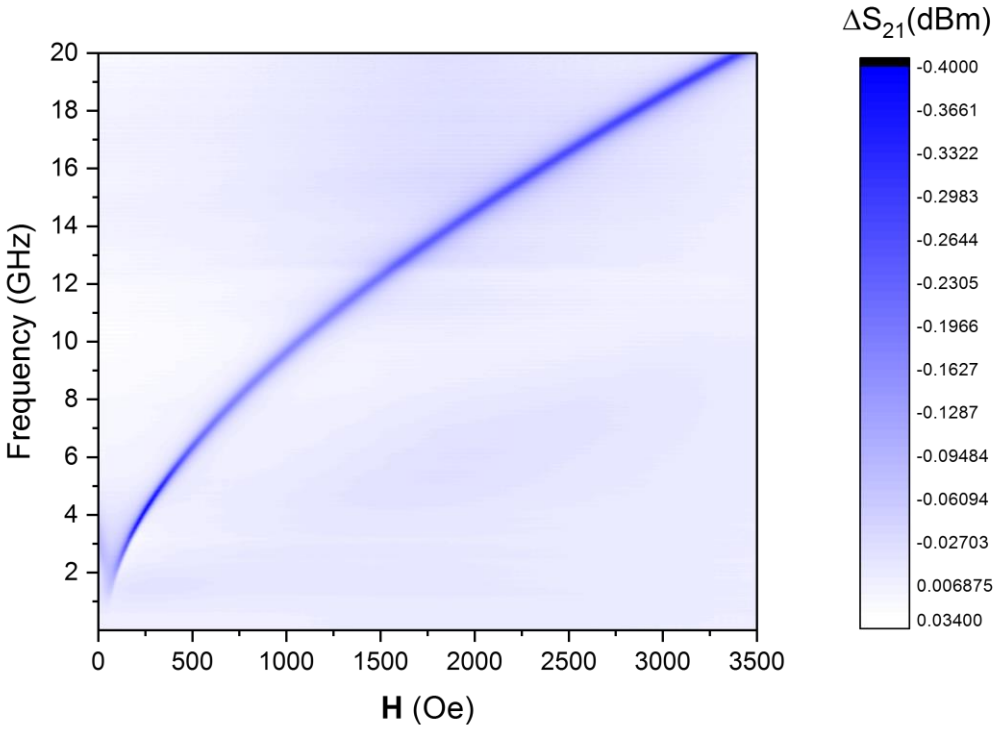

Figure 2.14 *An example of a typical Kittel Curve in frequency as a function of applied magnetic field, measured from an FeGa test sample using VNA-FMR*

2.5.4 FMR Damping

As the magnetisation precesses, it encounters resistance to the precessional motion known as magnetic damping [50,56]. The damping is strongly dependent on the structure of the magnetic material, and plays an important role in determining how the dynamic behaviour occurs. In materials with high damping, large excitations must be used to drive resonant precession, and therefore the manipulation of these highly damped spins is impractical. Conversely, a weakly damped system may be driven to precession and flip the direction of **M**, only to continue flipping and return to its initial state. The control of the spin direction therefore necessitates a critically damped system. Measuring the damping within a material is crucial to understanding the magnetisation dynamics within materials and assessing their practicality for spintronic device systems.

Magnetic damping effects in metallic ferromagnets can be divided into two categories based on their source. These are intrinsic (Gilbert) damping effects [50,57], which arise from interactions within the crystal lattice, and extrinsic damping effects, which are a product of interactions between precessional behaviour and growth defects within the structure [56,58]. Three major mechanisms have been identified which give rise to intrinsic damping effects. These are magnon-phonon coupling [59], eddy currents [60,61], and itinerant electron relaxation [62,63]. In the case of magnetite, the relative immobility of the Fermi electrons and poor electrical conductivity render the itinerant electron relaxation and eddy current effects much smaller than the magnon-phonon coupling. Although the Gilbert damping in CFAS has been well-explored, the dominant damping mechanism is less well defined in the literature. Generally, it is accepted that itinerant electron behaviour is the dominant cause of intrinsic damping, while eddy currents are proportional to the square of the film thickness [64,65] and in ultrathin films contribute a negligible amount to the total damping [66], or those with a low electrical conductivity like magnetite. Since all of the materials measured in this thesis are either very thin (¬20nm) or poorly conducting, the eddy current effect is neglected.

2.5.4.1 Intrinsic Damping Mechanisms

It is accepted that the itinerant electron behaviour is responsible for the majority of intrinsic damping effects in ferromagnetic materials, although the mechanism by which this damping arises is still a matter of some debate. A number of different theories have been put forward [67,68,69,70], although no single theory currently describes the behaviour completely. A recent review by Kamberský [69] provides further details, and attempts to link existing theories, although a complete theory is still missing.

Perhaps the most widely accepted current model of the intrinsic damping effects is achieved using Kamberský's breathing Fermi surface model [71,72]. In simple terms, the breathing Fermi surface model describes the transfer of angular momentum from Fermi level electrons to the crystal lattice as a result of spin-orbit coupling effects. The Bloch state of Fermi electrons is dependent on the magnetic moment (**μ**), and changing the direction of **M** changes the energy of the Bloch states (as a result of spin-orbit coupling) and therefore the energy of Fermi electrons, shifting the Fermi surface [73,74]. The Fermi surface is seen to shift over time as **M** changes direction, and these distortions are referred to as 'breathing'. The Fermi electrons relax into the new lowest available energy states over a non-zero time (the momentum relaxation time τ_m) and lag behind the

instantaneous magnetisation. The spins relax towards **M** and transfer angular momentum to the d-electrons, leading to damping of the spin moments. The phase lag, and therefore the damping, is proportional to the angular frequency ω, and therefore to the frequency of the applied RF signal. The mathematical description of this model is given in equation 2.41

$$\alpha_{tens} = -\frac{\gamma}{\boldsymbol{m}}\sum_{\boldsymbol{ki}} \tau_{\boldsymbol{ki}} \frac{\partial f_{\boldsymbol{ki}}}{\partial \epsilon_{\boldsymbol{ki}}} \frac{\partial \epsilon_{\boldsymbol{ki}}}{\partial e_l} \frac{\partial \epsilon_{\boldsymbol{ki}}}{\partial e_m} \tag{2.41}$$

where $\epsilon_{\boldsymbol{ki}}$ is the energy of the i[th] Bloch state with wavevector **k**, $\tau_{\boldsymbol{ki}}$ is the relaxation time of the i[th] magnetic moment, *γ* is the gyromagnetic ratio, $e_{\boldsymbol{ki}}$ is the unit vector of the i[th] magnetic moment and $f_{\boldsymbol{ki}}$ is the Fermi-Dirac occupation number.

Modifications have been shown to improve the accuracy of this model, particularly to improve on issues accounting for transitions between electron bands, which are corrected for by the inclusion of the torque-correlation model [69]. This addition quantifies the inter-band transitions which result from spin-orbit torque and represents both inter- and intra-band behaviours [73]. Combining the breathing Fermi surface and torque-correlation models produces equation 2.42, which defines the elements of the Gilbert damping tensor α_{lm}.

$$\alpha_{lm} = \frac{\gamma}{m}\sum_{\boldsymbol{kij}} \boldsymbol{T}^{l}{}_{\boldsymbol{kij}}\, \boldsymbol{T}^{m}{}_{\boldsymbol{kij}} W_{\boldsymbol{kij}} \tag{2.42}$$

where $T^{l}{}_{\boldsymbol{kij}}$ is the transverse torque operator between the spins i and j in the l direction, and W is a scaling (weighting) factor determined by

$$W_{\boldsymbol{kij}} = -\int \frac{\partial f_{\boldsymbol{ki}}}{\partial e} A_{\boldsymbol{ki}} A_{\boldsymbol{kj}}\, d\epsilon \tag{2.43}$$

where $A_{\boldsymbol{ki}}$ is a Lorentzian spectral function determined by the scattering effects experienced by the i[th] magnetic moment.

This additional effect can also be thought of classically as accounting for the damping in the precession of itinerant (d) electrons which are coupled with their non-itinerant (s) neighbours. These interactions are determined by the s-d exchange field [66] and as such show coupled precession. However, the finite mean free path of the spin in the s electrons leads to a phase lag between the two moments as they attempt to align with the effective magnetic field. As in the breathing Fermi surface model, this phase lag leads to a transfer of angular momentum and therefore damping of the spin moments proportional to the angular frequency ω. A more complete treatment of these models of itinerant electron behaviour is given in an in-depth review by Eriksson [73].

The magnon-phonon coupling effect was recently described using the relaxation of the electrons by phonon drag [61,75]. Assuming that the magnetisation and the lattice strain are homogeneous, the Gilbert damping arising from phonon interactions can be described in small geometries by equation 2.44, as a result of the LLG equation and lattice strain equations.

$$\alpha_{\text{phonon}} = \frac{2\eta\gamma}{\boldsymbol{M}\boldsymbol{s}} \left(\frac{\mathrm{K}(1+\nu)}{E}\right)^2 \tag{2.44}$$

where, η is the phonon viscosity, *Y* is the gyromagnetic ratio, K is the magneto-elastic shear constant, ν is the Poisson ratio and E is the Young's modulus. While η is historically difficult to

obtain, it can be found empirically in the microwave frequency range using transmission experiments [76]. The remaining parameters can be easily obtained by other methods. Since α_{phonon} is linear in ω, the total damping (and therefore the FMR linewidth) will also show a linear trend if the Intrinsic effects are dominant.

In a perfect crystal structure, the general form of the damping is described by the resonance linewidth (ΔH) as a function of angular frequency according to equation 2.45.

$$\Delta \boldsymbol{H}(\omega) = \Delta \boldsymbol{H}(0) + \alpha \frac{\omega}{\gamma} \tag{2.45}$$

where **H** is the magnetic field strength, α is the Gilbert damping parameter and γ is the gyromagnetic ratio. The gradient, given by α describes the intrinsic damping behaviour of the crystal structure, while the intercept Δ**H**(0) describes the extrinsic damping effects arising from structural defects. This is a combination of effects arising from two sources. The first is the mosaicity within the sample, which broadens the linewidth by introducing a range of spin alignments which subtly shift the resonance. The second cause are differences in local effective field caused by magnetic inhomogeneity, which give rise to de-phasing between local spins and therefore a de-coherence within the precession [56]. Since these terms are usually small, no further consideration will be given here.

2.5.4.2 Two-Magnon Scattering

Non-linearity in the damping primarily arises from extrinsic damping effects, chiefly due to two-magnon scattering in the sample. This adds a third term to the linewidth expression, as described by equation 2.46 [56,58,76]. The scattering of spin waves (magnons) in ferrites is a key source of extrinsic damping effects in these materials. A uniformly precessing magnon (wavevector k ~ 0, called the FMR mode) scatters into two or more spin waves which must have the same frequency (ω(0) = ω(k)) as a result of energy conservation. The magnon-dispersion relation governs the value of q. The two-magnon scattering increases with increasing density of defects in the sample structure: the magnitude of the scattering effect is directly proportional to the Fourier transform of the magnetic inhomogeneities in the structure.

$$\Delta \boldsymbol{H}_{2m} = \Gamma sin^{-1} \sqrt{\frac{\sqrt{\omega^2+(\omega_0/2)^2}-\omega_0/2}{\sqrt{\omega^2+(\omega_0/2)^2}+\omega_0/2}} \tag{2.46}$$

where Γ is a dimensionless parameter describing the magnitude of the 2-magnon scattering, ω is the angular frequency and ω_0 is described by

$$\omega_0 = 4\pi\gamma \boldsymbol{M}_{eff} \tag{2.47}$$

This 2-magnon scattering behaviour gives rise to non-linearity in the linewidth [56]. If this term dominates the damping instead of the intrinsic terms, the linear trend in Δ**H**(ω) will instead be replaced with a characteristic two-magnon dependence. The total damping in a 2-magnon dominated scattering term is therefore better described using equation 2.48.

$$\Delta \boldsymbol{H}(\omega) = \Delta \boldsymbol{H}(0) + \alpha \frac{\omega}{\gamma} + \Delta \boldsymbol{H}_{2m} \tag{2.48}$$

2.6 Materials

Two different metals with high predicted spin-polarisation will be the focus of this thesis: magnetite and CFAS. High spin polarisation is desirable for device applications such as spin filters. The structure and magnetic properties of these samples has been well-documented.

2.6.1 Magnetite

The spinel group are cubic crystals with Fd3m space group and a chemical composition of AB_2O_4. Each unit cell has 8 formula units and two sites of different coordination known as A and B sites. Each site is defined by the configuration of the ions and the surrounding oxygen ions. The 'A' site has a tetrahedral arrangement while the 'B' site forms in an octahedral structure. The sites are present in the structure in a ratio of 1:2, where 8 A sites are occupied and 16 B sites per formula unit [20,77]. A-site ions in normal spinels have a valency of $^{2+}$ while the B-site ions are $^{3+}$. A second class of spinels, known as inverse spinels which share the same structure but the site occupation is rearranged. In an inverse spinel, the A-sites are occupied by 3+ ions and the B-site is a mixed-valence of equal parts B^{2+} and B^{3+}. The mixed valence of the B sites can give rise to competing interactions between the sites and therefore considerably alter the ground state of the crystal compared with the normal spinel structure. Magnetite is an oxide ferrimagnet which crystallises in the inverse spinel configuration. It has a high Curie temperature (T_c) of ~860K [78,80,81], and a predicted 100% spin polarisation at the Fermi level, which makes it a good candidate for room

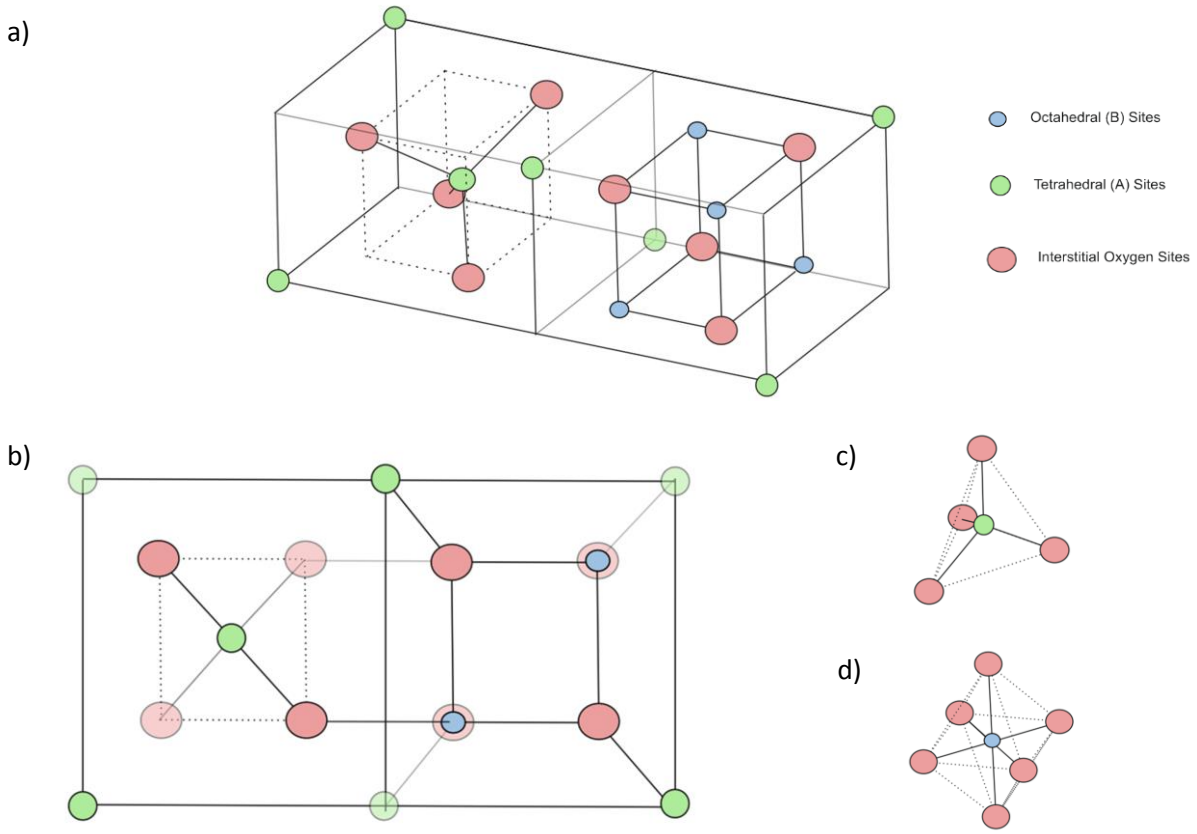

Figure 2.15. *A simplified schematic diagram of one quarter of the structure of magnetite viewed from a) a 3D perspective and b) in the 2D elevation only. The structure of the individual sites are shown in c) the tetrahedral and d) the octahedral arrangements. The unit cell structure is achieved by stacking four such units in a cubic arrangement, mirroring each adjacent unit [85]*

temperature spintronic applications. The chemical formula of magnetite is $[Fe^{3+}]A[Fe^{3+}Fe^{2+}]BO4]$ where A and B denote two different sites within the crystal lattice. The A sites in magnetite are occupied by Fe^{3+} ions with a $3d^5$ electron configuration and a spin (S) = 5/2, L = 0, J = 5/2. The B sites, in contrast, are occupied by two types of ion in a 1:1 ratio. These are the Fe^{2+} ion (electron configuration = $3d^6$, S = 2, L =3, J = 5 and the Fe^{3+} ion as in the A sites.

The density of t2g spin-down electrons dictates the density of itinerant charge carriers at the B-sites in the crystal lattice of magnetite [81,82,83]. These charge carriers can move between sites on the B sublattice by hopping conduction [84]. Since the density of these charge carriers is low in magnetite, however, this itinerant electron behaviour is quite limited. An electrical conductivity of 200-250 $ohms^{-1}cm^{-1}$ [86,87] is commonly found in magnetite at room temperature, making it a poor electrical conductor relative to other metals.

Double exchange arises between the Fe^{2+} and Fe^{3+} ions in the octahedral sites as a result of the neighbouring sites of different valence, as discussed in section 2.2.4. This promotes ferromagnetic alignment between these ions within the structure. The tetrahedral Fe^{3+} ions are not subject to this interaction as a result of their place in the magnetite structure, instead undergoing superexchange with the octahedral Fe^{3+} ions. This results in antiferromagnetic superexchange, as discussed in section 2.2.3. This results in the parallel alignment of the octahedral sites, with the tetrahedral sites in antiparallel. The equal numbers of Fe^{3+} ions in each site results in their corresponding magnetic moments cancelling out. Only the tetrahedral Fe^{2+} ions have a non-zero contribution to the magnetic moment, resulting in a total moment of 4μB per formula unit. It is well-known that the spin polarisation of Fe_3O_4 at the Fermi level is predicted to be 100%, [88,89,90] but whether this is real half-metallicity is still a matter of some debate [91].

At temperatures below 120K, a structural transition occurs in stoichiometric bulk magnetite, changing from the cubic phase to a monoclinic structure. This is known as the Verwey transition [92,93], and the critical temperature is denoted as T_V. Despite a number of studies, it is still uncertain whether this process also initiates a charge ordering of the Fe^{2+} and Fe^{3+} ions in the B-site sublattice in a process similar to Wigner crystallisation [84,94]. This structural transition has also been shown to induce a discontinuity in both the magnetisation [92,95] and the resistivity (ρ) of magnetite, showing a $\Delta\rho \approx$ two orders of magnitude as a result of the so-called 'freezing out' of the hopping conduction effect. This change is only observed in highly stoichiometric $Fe_{3-\delta}O_4$, however. It has been shown that if δ>0.0117, this transition, and the corresponding changes in **M** and ρ, is suppressed [96,97,98]. Further reports on the changing structure of Fe_3O_4 suggest that it also exhibits ferroelectric properties at T<38K [99], and a switchable polarization of 11μC cm^{-2} is reported at T< 20K.

The Verwey transition alters the structure of the magnetite crystal and therefore the bond angle between adjacent ions. This changes the superexchange interaction in Fe_3O_4 and by extension changes the magnetic ground state of the system, from the electrically conducting metallic phase to an insulating one. It may be possible to take advantage of this strong magnetic dependence on superexchange: if small perturbations can be used to induce switching between magnetic ground states, this may be a practical effect in applied spintronics. Combined with the high T_c, natural abundance and high spin polarisation, magnetite is an ideal candidate for applied spintronics.

Despite these qualities, however, the application of magnetite is still impractical as a result of defects which arise during the growth process.

As a well-known, widely available magnetic material, the structure and properties of magnetite have been the subject of many studies. Many experiments on the magnetic properties of magnetite have been performed in the literature, with Fe_3O_4 having been grown on a number of different industrially relevant substrates: MgO and III-V semiconductors like GaAs are common choices, for example. Improvements to the structure by thermal annealing has been pursued to reduce the defect density. Different post-growth annealing conditions have been explored, including annealing under air, under vacuum and using a gas mixtures in order to promote improved stoichiometry[16,100,101,102]. In each case, the annealing of the films is observed to improve their structural order. This should, therefore, show a measurable effect on their corresponding magnetic parameters as well. However, care must be taken to prevent diffusion of the substrate material into the thin film at higher annealing temperatures [103].

Experiments on the damping behaviour in Fe_3O_4 have also been presented by a number of groups. For example, Serrano-Guisan et. al. [104] measured a value of $\alpha = 0.037$ for the Gilbert damping parameter in epitaxial thin films of Fe_3O_4/MgO in 2011. This compares well with the values of $\alpha = 0.07$ and 0.03 observed by Zou et.al. [105] in Fe_3O_4/GaN films (of 6nm and 3nm in thickness respectively) observed in the same year. Later experiments by Nagata et. al.[106], in 2013 yielded a value of $\alpha = 0.02$ in rf-sputtered epitaxial magnetite films. More recent experiments on spin-orbit coupling in epitaxial Fe_3O_4 thin films grown on GaAs by Huang et. al. [100] have yielded a value of $\alpha = 0.013$ and $\mu_l/\mu_s = 0.05$ in 6mm films, which increases to $\alpha = 0.022$ and $\mu_l/\mu_s = 0.09$ in 4nm films.

The reduction of the total Gilbert damping with the improvement of the Fe_3O_4 structure is therefore well documented, and as growth techniques improve and the defect density in Fe_3O_4 thin films is reduced, further improvement in α is predicted.

2.6.1.1 Antiphase Boundaries

It has been shown that antiphase boundaries (APBs) formed by growth defects contribute strongly to the spin damping in magnetite thin films [11,16,79,107,108] and that these defects contribute to the notorious tendency of magnetite to require high magnetic fields to reach saturation. APBs are regions in the crystal structure where a mismatch between grain boundaries leads to either a displacement in planar lattice site spacing or a 90 degree rotation between grains. APBs commonly arise at the intersection of grains which are not perfectly structurally aligned, for example if they nucleate separated by a distance $r \neq na$ (an integer multiple of the lattice constant).

APBs distort the magnetic ordering and increase the electrical resistivity of the system [108,109] and large magnetic fields are required to overcome the effects of these boundaries. The distribution of APB's has been observed to be denser in thinner structures and thus they have an increased impact on thin film structures. These defects reduce the spin polarisation and therefore must be reduced if the critical current density is to be minimised, as discussed in chapter 1. If these APBs are the primary source of structural defects in Fe_3O_4, then reducing the local APB

density may provide a pathway to not only minimising j_c, but also to aid in solving the problem of the notoriously high saturation fields of thin film Fe_3O_4.

2.6.2 $Co_2FeAl_{0.5}Si_{0.5}$ (CFAS)

$Co_2FeAl_{0.5}Si_{0.5}$ (CFAS) is a well-studied quaternary Heusler Alloy with a predicted 100% spin polarisation at the Fermi level. CFAS is a ferromagnet with the X_2YZ full Heusler alloy structure, where X and Y are transition metal species and Z is one or more main group elements. CFAS has a bulk lattice constant of 0.568nm [110] and a high T_C, (1150°C.) [111] The saturation magnetisation of CFAS is observed to be ~1100 emu cc^{-1} [36,112,113,114]. Combined with a small lattice mismatch with technologically relevant substrates ($\sim 0.4\%$ on Ge(111) [115], increasing to ~4% on Si(111)) [116], these properties make CFAS an excellent candidate for applied spintronics. Depending on the growth conditions, CFAS forms either an L_{21} or B_2 ordered structure.

The L_{21} structure is a body-centred cubic structure in the $Fm\bar{3}m$ space group. It consists of 8 lattices stacked in a cubic arrangement [114,117]. The outer vertices of each cube are made up of the X species while the body-centred ions form a cubic sublattice with the Y and Z ions occupying alternating (111) planes.

The B_2 structure is similar to the L_{21}, although the YZ sublattice is disordered in the B_2 structure. The magnetic structure of Heusler Alloys is strongly dependent on the atomic arrangement [117,118]. The half-metallicity which gives rise to the high spin-polarisation is a feature of the L_{21} ordering. This effect is significantly reduced in the B_2 ordered state. If instead no order exists between the X and YZ sublattices, the structure is A_2 ordered. It has been shown that the difference in structure arises as a result of different growth and annealing conditions. Typically the structure grows in the B_2 phase, and transitions to the L_{21} phase with thermal annealing between 500-700°C [119,120]. Direct exchange between the Co-Co and Fe-Co pairs result in a parallel alignment of the spin moments [120]. Discussions of the superexchange effects in CFAS are not common in the literature. At first glance, it would appear that strong AFM coupling occurs in the L_{21} phase across the Fe-Al/Si-Fe bond due to 180° superexchange, but this is not the case. The Fe sites in L_{21} would be expected to align antiparallel and have their spin moments cancel out,

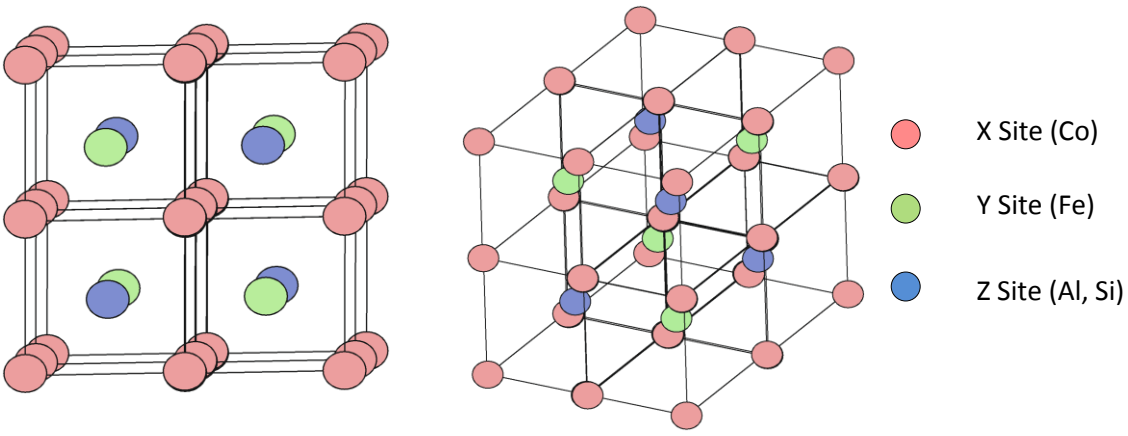

Figure 2.16 *The Full Heusler X_2YZ Structure, with the X (red), Y (green) and Z (blue) sites highlighting the L_{21} Order. In B2 order, the Y and Z sites are disordered and the green and blue sites become interchangeable*

except the direct exchange between the Co and Fe sublattices is sufficiently strong to keep the moments aligned in parallel.

It has been calculated using spin dependent DFT that, in the L_{21} phase, a finite density of states are present in the majority sub-band of CFAS at the Fermi level, with no states in the corresponding minority sub-band [13,121]. This is not the case in the B_2 phase, however, where both spin sub-bands have a non-zero density of states. Indeed, in this configuration the minority spin sub-band has a larger occupancy, reversing the direction of the spin polarisation relative to the L_{21} phase. In mixed phase CFAS, which sometimes occurs as a result of intermixing at interface regions, these effects compete with each other, lowering the total spin polarisation of the film and increasing the magnetic damping. Eliminating this competition between phases using thermal annealing is therefore a research field of considerable interest for CFAS.

The difference between the L_{21} and B_2 structure can be observed using X-Ray Diffraction (XRD). The different lattices give rise to unique diffraction peaks based on their structure. This arises as a result of the selection rules which are applied to the different structures. The structural (444) and (400) reflections arise from the fundamental cubic structure and are therefore observed in all of the phases of CFAS (A_2, L_{21} and B_2). The structural peak arises from the fundamental reflections from the cubic structure and the selection rules h+k+l=4n and h, k and l are all even. Different lattice arrangements give rise to additional diffraction conditions: in the L_{21} structure, reflections are allowed if h, k and l are all odd (known as the 'odd' diffraction condition), and in both the L_{21} and B_2 structures the reflections are allowed if h+k+l=4n+2 [110,120] (known as the 'even' diffraction condition). As a result, both the L_{21} and B_2 ordered films show (222) and (200) reflections [113], which are absent from A_2 ordered films. A (111) peak is observed if the L_{21} structure is present, but is absent from the B_2 and A_2 ordering types. A similar effect is observed in the [100] plane: the (400) structure peak should appear in all CFAS structures, while the (200) peak is observed in both L_{21} and B_2 ordered films, and the (100) only appears if the crystal has L_{21} order. Depending on the crystal structure, different reflections can therefore be identified in XRD measurements. An angle of χ_r = 54.7 degrees separates the (111) and (100) planes in the CFAS crystal structure [113].

The current state of research progress on damping in CFAS is limited due to the relatively recent emergence of the quaternary Heusler Alloy as a prospect for spintronic device applications. However, some prior investigations into $Co_2FeAl_{0.5}Si_{0.5}$, and its precursor materials Co_2FeAl (CFA) and Co_2FeSi (CFS) show promising results.

Tezuka [119] et. al. produced L_{21} ordered CFAS using thermal annealing techniques in 2006, though no damping measurements were performed at this time. Nakatani et. al. [110] then predicted an increase in spin polarization between the B_2 and L_{21} states in 2007. Experiments by Bai et. al. [36] in 2012 yielded a value for the Gilbert damping of $\alpha = 2.5 \times 10^{-3}$ in B_2 ordered CFAS grown on MgO(001), which is in agreement with later experiments on the same structure by Ming-Loong et. al. [112] in 2014. Gabor et. al. [38] managed to further reduce alpha in L_{21} CFAS/MgO(001) to 1.9×10^{-3} in 2015. To the author's knowledge, this remains the lowest measured Gilbert damping in CFAS to date, and while work on CFAS on Ge(111) and Si(111) substrates is now beginning to emerge, this is the first study of the damping behaviour in such films.

Similar experiments performed on B_2 CFA/MgO(001) by Cui et. al. yielded $\alpha = 2x10^{-3}$ in samples grown by Ion Beam Deposition and thermally annealed (either using standard furnace annealing or rapid annealing in vacuum depending on the required temperature). A value of $\alpha = 1.1x10^{-3}$ was reported in later experiments by Belmeguenai [122] grown by rf sputtering and vacuum-annealed. Thermal annealing by Kumar [123] in 2017 was observed to yield L_{21} CFA on Si with a measured value of $\alpha = 1x10^{-3}$. This is considerably below the value observed in CFAS in 2015, suggesting that further reductions in the damping in CFAS may yet be possible under favourable circumstances.

This precedent of decreasing Gilbert damping constants correlated with structural improvement in Heusler Alloy thin films suggests that further work in this field may be useful in reducing the magnetic damping in half-metallic materials. Further reduction of damping (and therefore lower critical current density requirements) in highly spin-polarised magnetic thin films may be a crucial step in the development of low-damping spintronic materials. Based on the work of Kuerbanjiang et. al. [115,116], excellent structural improvement is observed in thermal-annealed CFAS thin films grown on 111-aligned Ge, so these films provide an excellent candidate for the possibility of further reducing α in CFAS.

Chapter 3: Experimental Methods

3.1 Introduction

The experimental techniques that have been used to characterise two series of magnetic thin films of Fe_3O_4 and $Co_2FeAl_{0.5}Si_{0.5}$ are discussed in this chapter. The characterisation techniques are discussed in two distinct categories: the techniques used to characterise the magnetic behaviour of the material, and those which have been used to investigate the structure of the samples.

3.2 Structural Characterisation Techniques

The characterisation of the sample structure is important in understanding the behaviour observed in the magnetic characterisation of the samples under investigation in this project. A series of techniques have been used to assess the microstructure of samples investigated in this project, including x-ray diffraction, and transmission electron microscopy.

3.2.1 XRD

X-rays are widely used in the structural characterisation of thin films, especially in diffraction techniques, due to their high penetration depth and short wavelength. However, they make up a broad region of the electromagnetic spectrum. It is often practical to separate the spectrum of x-rays into the high-energy x-rays, known as 'hard x-rays' and the lower energy 'soft' x-rays. While the distinction between hard and soft x-ray regions is not rigidly defined, it is a useful distinction to make, since x-rays in the different energy ranges are often used for different investigative techniques. For the purposes of this thesis, I have chosen to use the definition by which the two are separated at the Diamond Light Source facility: that is, that experiments using x-rays at higher than 2keV are defined as 'hard' x-rays and must be confined within a lead-lined safety hutch. X-rays at lower energies, between 100eV and 2keV are considered 'soft' x-rays.

X-ray diffraction is a useful technique for structural analysis [124]. Hard x-rays emitted from a fixed source are reflected as spherical waves from the sample atoms as long as the incident angle (θ) is above the critical angle for total reflection θ_c.

The critical angle (θ_c) is related to the refractive index (η) by [125]

$$\theta_c = \sqrt{2\eta} \tag{3.1}$$

The waves which are separated by a path length difference of an integer multiple of the x-ray wavelength (λ) interfere constructively: waves scattered from similar crystal planes therefore correspond to the constructive superposition of scattered x-rays and a diffraction peak is observed. Constructive superposition is observed when Bragg's law is met, such that

$$n\lambda = dsin(\theta) \tag{3.2}$$

where n is an integer, d is the spacing between adjacent lattice planes and θ is the angle of the incident x-ray. Using the Bragg equation, the spacing between planes (d) can be extracted. This spacing in a cubic crystal structure is related to the lattice constant by

$$d = \frac{a}{\sqrt{h^2+k^2+l^2}} \tag{3.3}$$

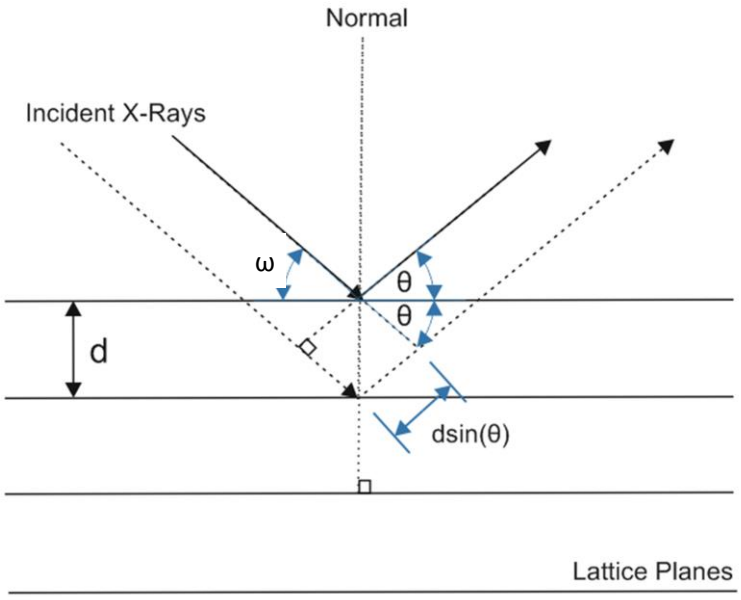

Figure 3.1. *A schematic diagram of Bragg reflected x-rays from a series of crystal lattice planes*

where a is the out-of-plane (c-axis) lattice constant and h, k and l are the miller indices of the plane. The out-of-plane lattice constant can be measured using a symmetric 2θ/ω scan, although in perfect cubic structures this gives access to the other lattice constants as well. In the case where tetragonal distortions affect the lattice structure, the out-of-plane lattice constant may be increased or decreased relative to the literature value [126]. Different scan geometries can be used to investigate different lattice constants. The grazing incidence diffraction geometry (shown in figure 3.2.a) can be used to perform in-plane XRD. This is achieved by setting a grazing angle of x-ray incidence and measuring the diffraction pattern in 2θ which arises due to structural order at the surface. Scanning over $2\theta_{Diff}$ allows the recovery of a wavevector with x- and y-components,

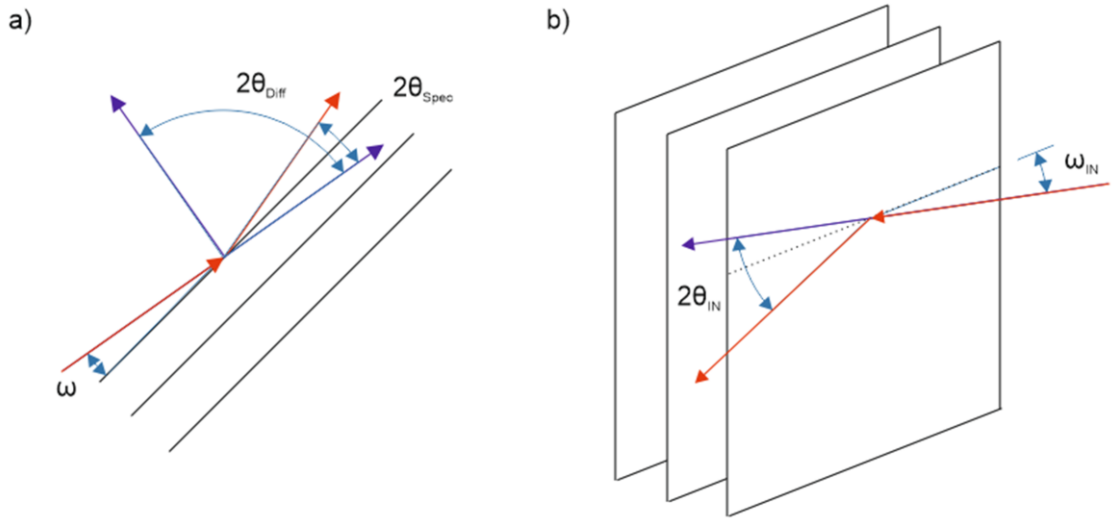

Figure 3.2. *A schematic diagram of alternate XRD geometries. A) The grazing incidence XRD geometry with the incident and specular beams shown in red and the diffracted beam in blue. B) The in-plane XRD geometry*

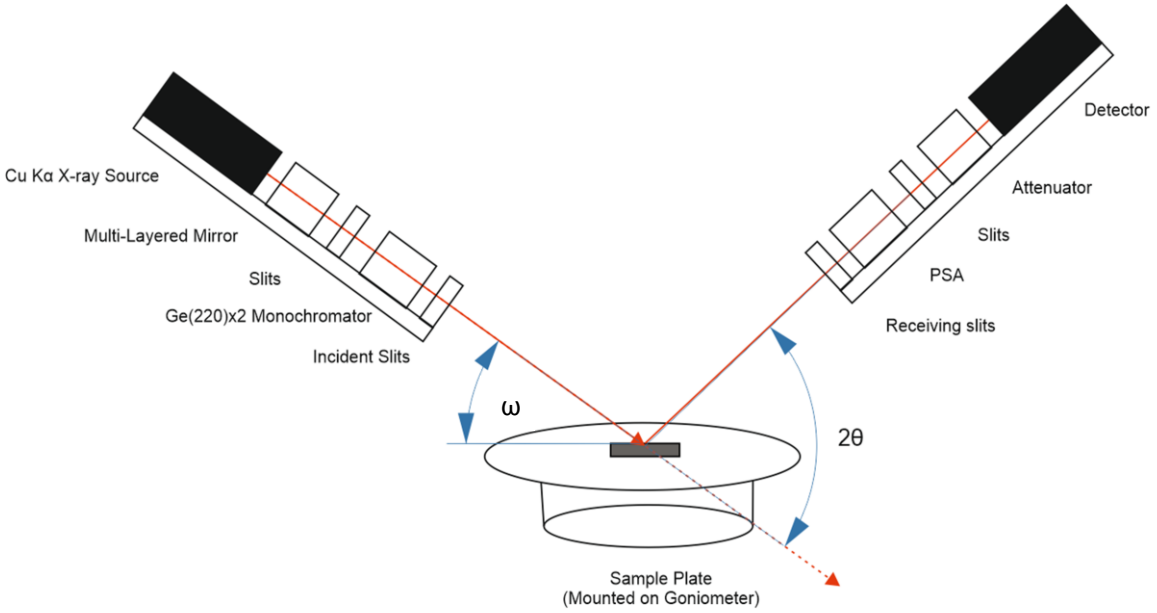

Figure 3.3 *A schematic diagram of the X-Ray diffractometer*

from which the reciprocal lattice (and therefore the real lattice) can be reconstructed [127,128,129]. In-plane ('phi-' or 'coupled' scan) diffraction can also be performed by fixing the incident x-ray angle ω_{IN} and scanning the detector over the diffraction angle $2\theta_{IN}$ (as shown in figure 3.2.b) in order to measure a diffraction pattern from the planes perpendicular to the sample face and thereby calculate the in-plane lattice constant [128,130].

All of the XRD data presented in this thesis was recorded using a Rigaku Smartlab X-ray Diffractometer with a Cu Kα X-ray source. The corresponding x-ray wavelength is therefore a constant 1.5406Å. A 2-bounce Ge(220)x2 monochromator was installed in order to eliminate additional K_β and L_α reflections which are otherwise observed in the XRD. The sample is mounted on a stage which can be rotated in five degrees of freedom, including the x, y and z axes of translation (where x and y are the dimensions in the plane of the stage and z is the vertical

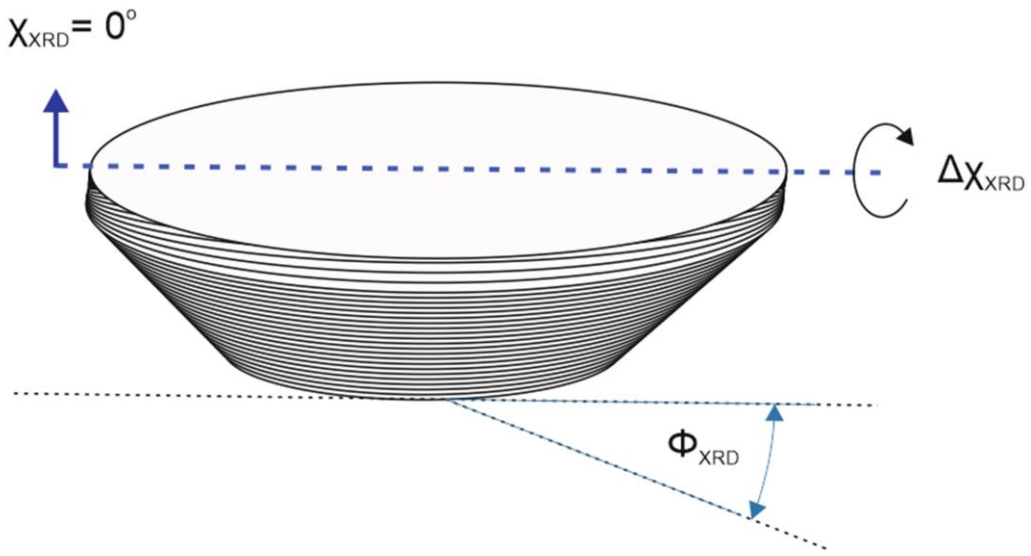

Figure 3.4 *A schematic diagram of the X-Ray Goniometer, showing the angles ϕ_{XRD} and χ_{XRD}*

elevation), the rotation of the stage in the plane (ϕ_{XRD}) and the tilt angle of the stage (χ_{XRD}). A schematic diagram of the XRD is presented in figure 3.3. The alignment of the XRD optics with the sample was performed using the automatic alignment procedure programmed into the Rigaku Smartlab control software. Manual adjustments were then made as required to account for tilt in the sample plane by fixing the θ angle and rocking in ω until a maximum in the diffraction peak was achieved. This offset was then accounted for in each subsequent measurement.

3.2.1.1 2Theta/Omega Scans

The incident angle of the x-rays (ω) and the angle of reflection (2θ) define the most common measurement in XRD, known as 2θ/ω scans [124,131,132]. In this scheme, ω and 2θ angle are swept between pre-programmed limits with ω always set at half the 2θ angle. Scanning over the 2θ angle allows access to the diffraction peaks arising from the crystal planes within the sample structure. Bragg peaks arising from non-forbidden reflections appear as intense peaks in the reflected X-ray intensity (measured in counts per second). In the case of an epitaxial crystal, a single family of planes will exist to give rise to X-ray reflections. The family of planes which are observed is determined by the geometry of the scan, as shown in figures 3.1 and 3.2. In the symmetric 2θ/ω scan, the reflection arises from planes parallel with the face of the sample and the spacing between these planes (i.e. the out-of-plane lattice constant) can be extracted. In the event that other peaks are observed, it can be inferred that the crystal structure is multi-phase or polycrystalline, depending on how many different families of planes are observed.

Depending on the crystal structure under observation, certain peaks may be excluded by the selection rules. These are known as forbidden reflections, and they occur when the interference between reflected waves are destructive rather than constructive [126]. The type of structure determines which reflections are forbidden and which are allowed based on inherent selection rules. Structural information can therefore be extracted from a combination of the peaks which are observed, and which of the peaks from that family are forbidden by the structure (and therefore missing from a 2θ/ω scan).

The selection rules for each material discussed in this thesis are governed by the cubic crystal structures. In Fe_3O_4 the basic fcc structure restricts the allowed reflections to those cases where h,k and l are either all odd or all even. In CFAS, h+k+l=4n and h, k and l must all take even values as a result of the bcc structure. Further rules are imposed depending on the y-z disorder: as discussed in section 2.6.2, h, k and l are all odd if the CFAS crystallises in the L_{21} structure and h+k+l = 4n+2 if the film has B_2 order [110,113]. Peaks in the XRD were identified using predicted values calculated using the INDX software package [133] with space group and lattice constant information from the literature. Out-of-plane lattice constants of the samples under test were then calculated using equations 3.2 and 3.3 and compared to the accepted value.

3.2.1.2 Rocking Curves

Once a diffraction peak has been observed in the 2θ/ω scan, the relative structural quality of a sample can be assessed by measuring a rocking curve (RC) [134]. Rocking curves are measured by fixing the 2θ angle and scanning ω around ω = θ: an example is shown in figure 3.5. The FWHM of the rocking curve is related to the quality of the thin film, with increased defect density resulting in increased broadening of the RC. Narrower curves arise from more coherent structures of higher quality. Conversely, the curve is broadened by defects like misalignment between grains, known as *mosaicity*, and other effects such as dislocations, sample curvature and strain [135]. Some instrumental broadening is also a factor. The discrepancies between the planes give rise to small differences in planar alignments, shifting the angle of their corresponding reflections and changing the angle in ω at which the diffraction peak can be detected. As the structural quality improves, the mosaicity is reduced and the rocking curve narrows. While the exact values are not useful in isolation, comparing the FWHM of two rocking curves allows a relative comparison of their structural quality. Further applications of the RC are available, such as applying the Scherrer equation to determine the size of crystallites within a polycrystalline sample [136]. However, since the samples in this thesis are epitaxial single crystal thin films, only the direct comparison of the FWHM will be considered.

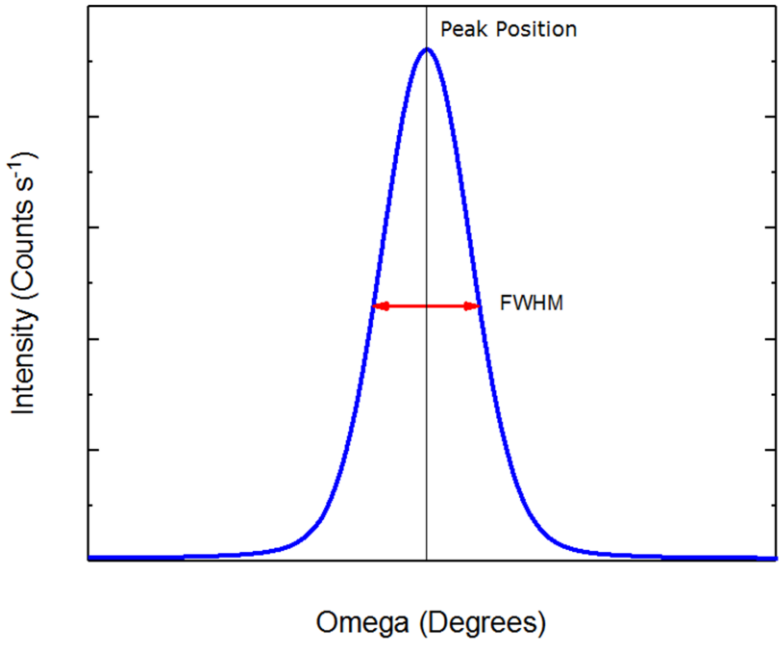

Figure 3.5. *A typical XRD Rocking Curve, with the FWHM indicated in red*

3.2.1.3 X-Ray Reflectivity

At shallow angles of incidence (below the critical angle θ_c) x-rays are specularly reflected from both the sample and substrate surfaces [125,137,138]. θ_c is typically smaller than ~1°, but the exact value is proportional to the refractive index (η, which at hard x-ray wavelengths is ~1) and sample density (ρ) and therefore θ_c changes for each layer of the sample depending on the crystal structure. Above this critical angle the reflectivity decays rapidly and the effect therefore

vanishes, giving way to the standard 2θ/ω behaviour and yielding diffraction peaks in crystalline samples. Amorphous samples still allow the specular reflection of these waves and the fitting of interference fringes, though diffraction peaks at higher angles are no longer observed. Specular reflections from the film surface and the film/substrate interface combine in an interference pattern called Kiessig fringes. The reflectivity profile observed in the shallow angle XRD can be used to extract several useful parameters from crystalline samples. In simplified terms, the gradient of the profile is proportional to the surface roughness, the amplitude of the fringes is proportional to the thin film density and the width of the fringes is proportional to the thickness of the thin film layer (figure 3.6). Samples thicker than a few hundred nanometres suppress this reflectivity as the fringes become close enough to become indistinguishable. At the same time, the increasing thickness of the film leads to the attenuation of the reflection from the film/substrate interface, impeding the interference behaviour.

The normalised intensity of the XRR can be used to determine the reflectivity profile [125]

$$R_{i,j} = \frac{I}{I_0} \tag{3.4}$$

In a single layer thin film, the reflectivity profile is defined by [135]

$$R^2 = \left| \frac{r_1 + r_2 e^{(-2ik_z t)}}{1 + r_1 r_2 e^{(-2ik_z t)}} \right|^2 \tag{3.5}$$

where t is the film thickness, k_z is the vertical component of the incident wavevector and r_1 and r_2 are the Fresnel reflectivity coefficients of the thin film structure and the substrate respectively. The reflectivity profile is therefore maximised when the exponential term = 1, which occurs when the path length difference is an integer multiple of the x-ray wavelength (λ). This can be written as

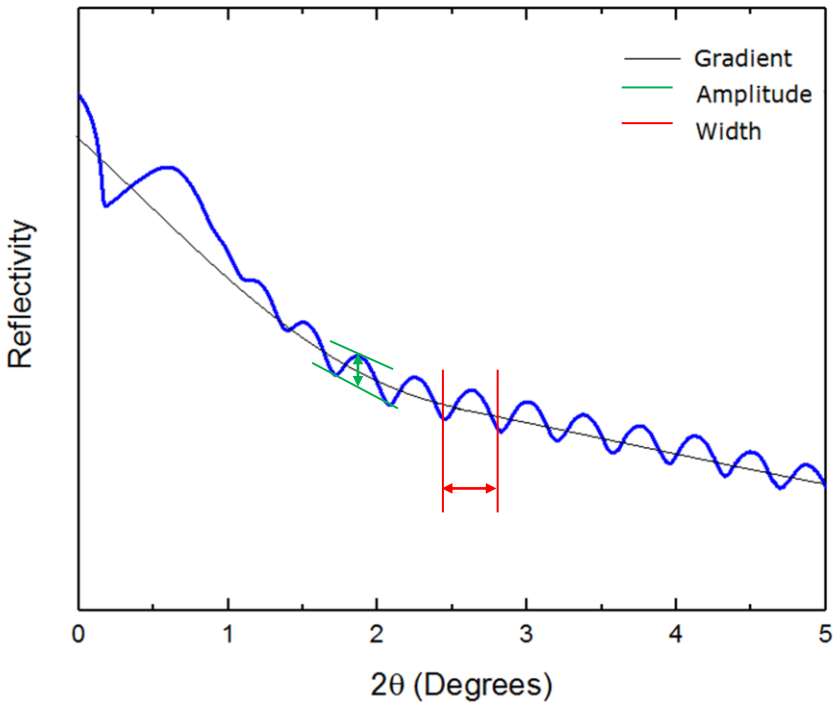

Figure 3.6. *A typical X-ray Reflectivity trace measured using an X-ray diffractometer*

$$m\lambda = 2t(sin^2(\theta) - sin^2(\theta_c))^{\frac{1}{2}} \quad (3.6)$$

where the t is the sample thickness and m is an integer. Manual fitting of these parameters can be accomplished by extracting the oscillation curve and finding the peak position of the corresponding Fourier transform [135]. However, automated fitting is more expedient. The XRR data presented in this thesis was fitted using both the GlobalFit and GenX software packages, which show agreement in the calculated values. GlobalFit uses the Parratt recursion equation in order to fit multilayer stacks (equation 3.7) [139], though for a single layer on a substrate (N=2), the single layer expression (equation 3.5) drops out of this expression. The fit also takes into account interfacial roughness by adding the exponential term in equation 3.10 [140], leading to the modified Parratt Equation (equation 3.11) [125,141]. The interface roughness reduces the reflectivity, distorting the XRR and in extreme cases eliminating the Kiessig fringes.

$$R_{i,j} = (\frac{R_{j,k} + r_{i,j}}{R_{j,k} r_{i,j} + 1}) a^4{}_i \quad (3.7)$$

where $R_{i,j}$ is the reflectivity coefficient of the i,j layer intersection, $r_{i,j}$ is the Fresnel reflectivity, the subscripts i,j,k denote the thin film layer (figure 3.7). In a simple single crystal system, for example, i corresponds to the ambient air, j to the crystal lattice and k to the substrate. The parameter a is

$$a = e^{(\frac{-i\pi g_j t_j}{\lambda})} \quad (3.8)$$

where t is the sample thickness and

$$g_j = \sqrt{n_j^2 - \cos^2(\theta)} \quad (3.9)$$

$$e^{-\frac{1}{2}\xi\xi_j\sigma^2{}_{i,j}} \quad (3.10)$$

where ξ is the scattering vector of the corresponding layer and $\sigma_{i,j}$ is the root-mean-squared roughness of the i-j interface.

$$R_{i,j} = a^4{}_i (\frac{R_{j,k} + r_{i,j}}{R_{j,k} r_{i,j} + 1}) e^{-\frac{1}{2}k_i k_j \sigma^2{}_{i,j}} \quad (3.11)$$

For the purposes of this thesis, only the film thickness will be directly extracted.

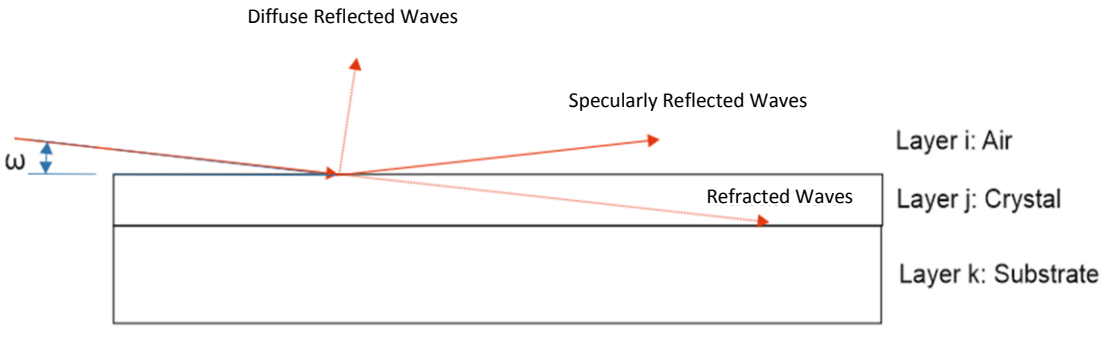

***Figure 3.7**. A schematic diagram of a single crystal sample under XRR*

3.2.1.4 Pole Figures

XRD also provides a method of mapping the texture of a sample using in-plane pole figures [142,143]. The pole figure is a 2D map acquired by fixing 2θ at a known peak and sweeping the incident x-rays in both the azimuthal rotation (φ_{XRD}) and the tilt angle (χ_{XRD}) [143] as shown in figure 3.4. Plotting the intensity of the Bragg reflected x-rays as a function of these parameters provides a 2-D projection in φ and χ averaged over a large sample area which provides textural information. In the 2D projection, the tilt angle is described by the radial distance, with the centre of the map equating to $\chi = 0^o$. The φ angle corresponds to the azimuthal angle of the pole figure plot. As in the 2θ/ω scan, reflections from planes constructively interfere, yielding diffraction peaks which appear as bright spots in the pole figure. The axes of the pole figure are denoted as the Rolling direction (RD), Transverse direction (TD) and Normal direction (ND), which correspond to the goniometer axes X (in the plane of the sample, parallel to the x-ray beam), Y (in the plane of the sample, perpendicular to the x-ray beam) and Z (out of the sample plane) respectively [143]. The axes X and Y correspond to $\varphi_{XRD} = 0^o$ and $\varphi_{XRD} = +90^o$ respectively.

This technique is useful in determining the distribution of crystallites in polycrystalline samples, but can also be applied to single crystal thin films in order to confirm the epitaxial growth. An epitaxial single crystal structure will show one primary intensity peak at the centre, corresponding to the 2θ/ω peak at which the intensity is fixed. This central peak is surrounded by the reflections from the family of similar planes which are observed at other positions in φ and χ. For example, a (111) oriented film can be measured in this way to confirm the presence of the ($\bar{1}11$) peak, and other members of the <111> family, as observed in figure 3.8. The pole figure method is primarily used to examine the distribution of the crystallographic planes in a crystal structure.

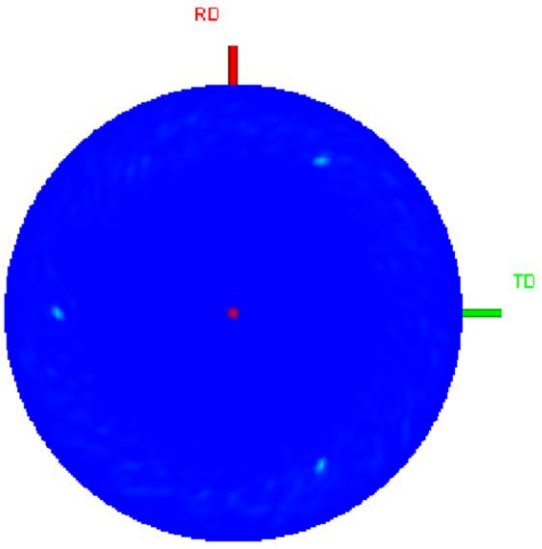

***Figure 3.8**. An example XRD Pole figure recorded from the Fe_3O_4 (111) peak in an Fe_3O_4/YSZ(111) sample. The central (111) peak is clearly observed in red, and the ($\bar{1}11$), ($1\bar{1}1$) and ($11\bar{1}$) peaks are observed in the pole figure spaced equally around the central peak*

3.2.4 HAADF-STEM

High-Angle Annular Dark-Field Scanning Transmission Electron Microscopy (HAADF-STEM) was used to image the structure of the thin film samples presented in this thesis. A schematic diagram of the STEM is presented in figure 3.9. In this technique, high-energy electrons are scattered from a sample under UHV conditions. High-angle elastic (Rutherford) scattering occurs as a result of Coulomb interaction between the incident electrons and the positive charges within the sample [144]. Inelastic thermal diffuse scattering (TDS) also contributes to the high-angle scattering of electrons as a result of phonon excitations within the sample [145].

At detector angles >50mrad, the scattered electrons are incoherent and therefore diffraction effects are not observed. Once scattered, these electrons are detected by a High Angle Annular detector. Electrons scattered at high angles have a scattering cross section proportional to Z^2, where Z is the atomic number of the scattering atom. This results in a proportional increase in the brightness of the corresponding point in the recorded TEM image which is ideal for identifying heavy (high-Z) elements including transition metals. The background of the image remains dark where no scattered electrons are observed. This *z-contrast* effect has been shown to have sub-nanometre resolution [146], allowing for the determination of individual elements in a crystal structure. The electron beam can be scanned across the sample by bending the electron trajectory using a magnetic field induced by the focusing coils.

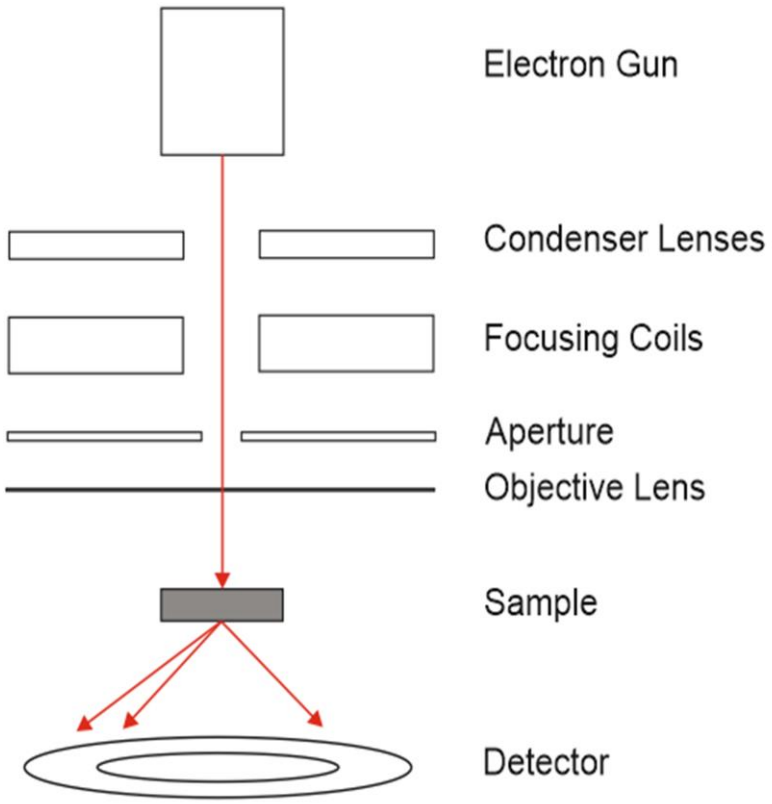

Figure 3.9. *A schematic diagram of the HAADF-STEM Technique, with the electron path shown in red*

The HAADF-STEM technique allows the high-contrast imaging of lattice structures in high resolution, which allows insight into the crystal structure. However, due to the limited penetration depth of the incident electrons in metals, samples are cleaved and polished in order to allow access to the crystal structure of the whole sample. The high resolution imaging makes HAADF-STEM an excellent technique for investigating both the sample structure and interface effects between the film crystal and substrate.

STEM images recorded using the microscope software are assigned a scale bar, which may be broken down into a length-per-pixel and used to measure the thickness of sample layers in low-magnification images.

3.2.4.1 EELS

Complementing the HAADF-STEM technique, electron energy loss spectroscopy (EELS) uses the energy loss incurred by the inelastic scattering of the incident electrons to determine the chemical composition of the sample [147,148]. As long as the sample is sufficiently thin to allow electron transmission, electrons can be passed through the sample with a finite probability of interacting with the crystal structure. Those electrons which are scattered transfer kinetic energy to the crystal. These inelastic effects induce either low-energy transitions (plasmon excitations) or high-energy transitions in the form of electron excitation in the scattering ion. It is these high-energy transitions that are of interest for the purposes of this thesis. The electrons which donate these high energies reach the detector with an energy reduction equivalent to the ionisation energy of the scattering atom. Since these transition energies are unique to each element, this 'energy deficit' can be used to identify the elemental make-up of the crystal structure.

A spectrum of detected electron energies can be built up, with the zero-loss peak (those electrons which lose no energy during the transmission) the low-loss region and the high loss region, containing the electrons which excite core-level transitions. Scanning over the sample, these ionisation energies can be used to map the elemental composition of the crystal lattice. Further information on the EELS technique is given by Egerton [149].

3.2.4.2 SAED

Selective Area Electron Diffraction (SAED) is a technique used in STEM imaging to discern the structure of the crystal lattice [150,151]. An electron gun is used to output high-energy electrons which are incident upon the sample parallel to the high-symmetry (zone) axis along which a diffraction pattern is desired. The elastic scattering of these electrons at low angles produces coherent electrons which generate a diffraction pattern according to Bragg's Law. A specialised SAED aperture is inserted into the image plane of the objective lens of the electron microscope. This aperture limits the volume of the sample which is used to produce the diffraction pattern. The high-energy (100keV) electrons have a wavelength of 4pm, which is sufficiently small to be diffracted by the atoms in the crystal structure. The resulting diffraction peaks are observed as high-intensity spots on the image, corresponding to the peak positions in the reciprocal lattice and separated by a distance proportional to the lattice spacing. For electron diffraction to occur, the incident angle (θ) must be small, so sinθ ~ θ and it follows from Bragg's law (equation 3.2) that

$$n\lambda = 2d\theta \tag{3.12}$$

so if n=1,

$$\frac{\lambda}{d} = 2\theta = \frac{r}{L} \tag{3.13}$$

where r is the spacing between the points in the SAED pattern and L is the focal length of the imaging camera. The lattice parameters, crystal structure and crystal phases can be determined from the diffraction pattern, just as with the XRD discussed in section 3.2.1.

For the purposes of this thesis, all samples were prepared for the TEM using the conventional ion-milling TEM method [152]. The SAED patterns were measured using a JEOL-2011 TEM microscope. The HAADF-STEM imaging was performed using a Nion UltraSTEM 100 microscope. This equipment was operated at an energy of 100 kV, with the convergence angle set to 30 mrad. The corresponding electron probe size was calculated at 0.9 Å. The inner detector angle for the HAADF-STEM was set to 76mrad. EELS was recorded at an angle of 31mrad with a native energy spread of 0.3eV in the electron beam. The spectrometer dispersion was set to 0.2eV per channel, resulting in an effective energy resolution of 0.6eV. Noise in the spectral images was reduced using principle component analysis in the Digital Micrograph software. The CiME plugin was used to analyse the data: a background was calculated using a power-law model and then subtracted from the signal. The data was then integrated over a 30eV window around each ionisation edge.

3.3 Magnetic Characterisation Techniques

A variety of characterisation techniques were used in this project to assess the magnetic properties of the materials under investigation. The two most important techniques used to characterise the magnetic nature of these sample were vibrating sample magnetometry and ferromagnetic resonance spectroscopy.

3.3.1 Vibrating Sample Magnetometry

Vibrating sample magnetometry (VSM) is a well-established technique which measures the magnetisation of a sample in a magnetic field [153,154]. This allows the extraction of key magnetic parameters from the sample, such as the saturation field ($\mathbf{H}_s$), coercive field ($\mathbf{H}_{coer}$), the magnetic remanence ($\mathbf{M}_r$) and the total magnetic moment ($\boldsymbol{\mu}_T$). When a sufficiently large bias field is applied, the magnetisation is saturated, achieving the maximum magnetic moment across the sample. Dividing μ_T by the sample volume gives $\mathbf{M}_s$.

Mounting the sample between two electromagnet coils allows the application of a bias field in order to saturate the magnetisation parallel to the field. The sample is mounted on a quartz rod which is suspended in the middle of the field and connected to a vibrating unit. This unit contains a piezoelectric, which is used to vibrate the sample in a steady sinusoidal waveform by the application of a sinusoidal control voltage. The vibrating sample then induces a time-varying magnetic flux (and therefore a current) across the detection (pick-up) coils mounted at the poles of the electromagnet. This current signal is measured by a lock-in amplifier, using the frequency of the oscillating piezoelectric as a reference signal. This signal is proportional to the magnetic moment of the sample. Data is collected by the control PC where it is converted back into a magnetic moment using a pre-determined calibration.

Measurement of the magnetic moment can be performed in different relative orientations between the sample and the magnetic field, two of which are practical for the purposes of data acquisition: the moment in the plane of the sample and the moment out of the plane of the sample. The magnet is mounted on a turntable to facilitate easy switching between these two orientations. Initially the field direction is in parallel with the sample mount (set at '0^{o}') corresponding to the in-plane arrangement. Rotating the magnet by 90^{o} aligns the field perpendicular to the sample mount, allowing measurements out of the plane. For the purposes of speed and continuity between datasets, it is practical to hold the sample in situ and rotate the magnet around it. Background effects and the paramagnetic component which arises as a result of the sample mounting components is removed from the data by recording a background dataset from a clean substrate mounted under the same conditions and subtracting this from the raw data. This ensures that the data analysed is purely arising from the sample.

VSM is commonly used in two ways: either the temperature is held constant and the magnetic moment of the sample is measured as a function of the applied magnetic field (referred to hereafter as **M**(**H**) measurements), or the magnetic field is held constant and the magnetic moment is measured as a function of the ambient temperature (referred to as **M**(T) measurements). Measuring **M**(**H**) allows access to the $\mathbf{H}_s$, $\mathbf{H}_{coer}$ and $\mathbf{M}_r$ parameters which are useful for characterising the sample material. In particular the saturation field will be useful for application in other techniques, since the saturation of the samples is required for complete characterisation.

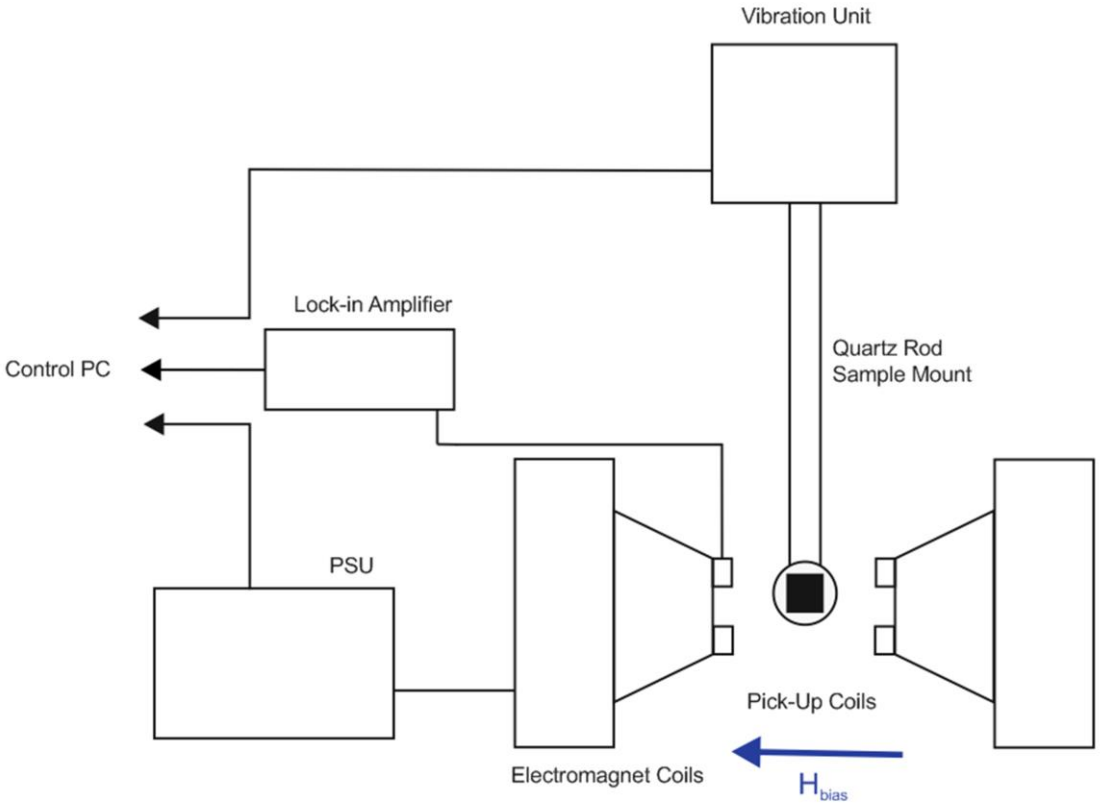

Figure 3.10. *A schematic diagram of a typical VSM system*

M(T) measurement allows useful insight into some structural behaviour of the sample, especially in the case of those materials with known structural transitions. Magnetite, for example, undergoes the well-known Verwey transition at around 120^{o}C (T_V), as described in section 2.6.1.

Measuring **M**(T) can be performed either in a field-cooled (FC) scheme, where the sample is saturated in a DC magnetic field then cooled in preparation for a temperature sweep, or a zero-field cooled (ZFC) method, where the sample is cooled in zero-field and the field is set to a non-zero level for in-field measurement [155,156]. The difference between these two methods lies in the orientation of the magnetisation: in the FC case, the magnetisation is saturated and cooled before the measurement field is applied, while the ZFC case retains any spin disorder in the sample while the temperature is lowered.

Elements of the magnetisation in the ZFC case will be less coherently oriented than those in the FC. This is maximised in polycrystalline films, where the orientation will be random in the ZFC case. When a bias field is applied in the FC case the spins are all aligned in parallel and will behave uniformly, resulting in a large magnetisation. In the ZFC case, however, the random alignment of the spins cannot be overcome by small measurement fields and therefore a reduced magnetisation will be observed as fewer spin moments align with the bias field.

The difference between the FC and ZFC VSM therefore affords some insight into the magnetic structure of the sample, as highly disordered or strongly anisotropic structures will show lower values of $\mathbf{M}_s$ in ZFC compared with FC **M**(T) if the bias field Is low enough to not overcome the energy barrier to coherent spin alignment. This can also be used to investigate phase transitions in the magnetic structure. For example, in stoichiometric Fe_3O_4 the Verwey transition is a re-structuring of the charge-order and therefore a change in the spin-state alignment. Above T_V, the spins align uniformly in ferrimagnetic order and therefore show no difference between **M**(T) in the ZFC and FC modes. Below T_V, however, the less ordered spin states induce a significantly lower value of $\mathbf{M}_s$ in the ZFC measurement.

The dynamic reversal of the spin state of magnetic domains in magnetite is prevented below a critical 'blocking' temperature T_B[157,158]. Below this temperature threshold, there is insufficient thermal energy within the crystal to allow the spin moments to move freely: they are therefore locked in the orientation which they occupied before the system was cooled. As the blocking temperature is reached, this 'freezing out' of the magnetic moments is overcome: the domains are sufficiently energetic for the spin moments to be re-aligned by interactions with the applied magnetic field. The T_B of magnetite is observed at around 210K in a 1kOe applied field [80], although the temperature at which this blocking occurs can vary strongly depending on several variables, including the sample stoichiometry and the applied field [159].

In Fe_3O_4 samples with very small domains, for example in ultrathin magnetite thin films [12, 160], and nanoparticle samples[161] the domains exhibit superparamagnetic (SPM) properties. In this state, the spin moment of each domain periodically relaxes between up and down spin states, averaging to zero over a sufficiently long measurement time. It is well known that in magnetic oxide nanoparticles, SPM behaviour arises from the single domain nature of nanoparticle systems[161]. In ultrathin films of magnetite, however, superparamagnetism arises as a result of changes to the antiferromagnetic (180^{o} Fe-O-Fe) coupling which can occur across antiphase boundaries[12,160]. SPM behaviour in ultrathin films is altered depending on the domain volume

and the relative area of the domain boundaries: as the thickness of the films increases above ~5nm, the domains become sufficiently large to suppress this effect [12]. Since all the magnetite samples considered in this thesis are much larger than this critical limit, no further consideration of this effect is required here.

For this thesis, VSM was performed using two different VSM systems. For room temperature experiments, a Microsense Model 10 VSM housed on-site at the University of York. For temperature dependent measurements, an alternate device was used: a Quantum Design SQUID magnetometer, at the Diamond Light Source Facility. All VSM experiments on the Model 10 VSM were performed at room temperature, with the magnetic field ramped to 1kOe to saturate the sample before data was collected. A background contribution from the empty sample mount was also measured and subtracted in order to remove any contribution to the data.

The SQUID-magnetometer uses highly sensitive Josephson junctions to detect very small changes in local magnetic fields, allowing for extremely high sensitivity magnetometry [162]. This increased sensitivity allows highly accurate investigation of the magnetisation behaviour of the sample under test. This is especially useful when **M**(T) experiments are performed, since even very small changes in the magnetisation resulting from phase changes in the sample structure can be observed. The SQUID-VSM also has a very low signal-to-noise ratio. ZFC **M**(T) experiments performed using the SQUID-VSM were cooled to 10K and then a bias field of 1kOe was applied. Once saturated, the magnetisation was measured as a function of temperature in 0.5K intervals, with the temperature increased at a rate of 5K min^{-1}.

When performing VSM, ideally the temperature would be raised above the Curie transition temperature where the magnetic properties change from ferromagnetic to paramagnetic behaviour, in order to eliminate any residual magnetic order in the samples. However, due to the high T_c of Fe_3O_4, this was not possible with the available equipment. Raising the temperature above T_c = 858K raised two problems in these samples. Firstly, raising the temperature above T_c would lead to further thermal annealing of the samples. Given that the purpose of this investigation is to investigate the changes brought about by the initial thermal annealing process, this secondary annealing would render any further experiments on these samples unreliable. Secondly, the SQUID-VSM must be switched between two operating modes at 400K, in the middle of the temperature range which would be required: from the low temperature mode to the high-temperature 'oven' environment. In this operational mode, the low temperatures can no longer be achieved, so a continuous measurement of **M**(T) is not possible. The best compromise in this situation was to ramp the temperature as high as possible without changing modes, in order to get as close to the transition as possible. The saturation field was then set (either to maximum output or to zero, when operating in the FC or ZFC mode respectively) and the sample cooled again to ~4K. Once the low temperature was reached, the field was set to the measurement field value. Finally, the temperature was then ramped up slowly with measurements of **M** being recorded periodically as a function of T. Raw data from the VSM is measured as magnetisation (in emu) as a function of applied magnetic field (or temperature). In order to convert from emu to emu cc^{-1}, a volume measurement of each sample is required. Approximations of the sample volumes were performed using a two-step process. Firstly, an optical microscope with a Vernier scale was used to calculate the area. By moving the edge of the sample under one side of the microscope lens, noting the value on the scale, then moving the same side of the lens to the

opposite edge of the sample, the distance moved on the Vernier scale gives the length of the measured dimension of the sample. Repeating this process for each side of a given sample allowed the calculation of an approximate area using simple geometric methods.

The second step required recording the thickness of each sample, to multiply by the area calculated in the previous step. The conversion to emu cc^{-1} was initially performed using nominal thickness values provided by the team who grew the samples, which was useful as a first approximation. The conversion was later repeated after the HAADF-STEM had been performed, using the thickness values measured from the STEM images to give a more accurate representation of the magnetisation in emu cc^{-1}. However, with the uncertainty of ±1nm on a thickness of the order of nm leaves a considerable uncertainty on the VSM measurements. This is especially true in the case of the CFAS VSM, where the ±1nm uncertainty is on the order of 10% of the sample thickness.

In order to remove the effects of background and substrate contributions to the VSM data, a second set of data has been recorded for each measurement under the same experimental conditions. In the second sweep, however, the sample is removed from the mount such that only the local background effects are measured. Any effects arising from the quartz rods and silicon grease in the sample mounts can therefore be measured without the magnetic signal from the sample. Where possible, an empty substrate was also mounted during these 'background' measurements in order to eliminate any contributions from the substrate. For the Fe_3O_4 samples presented in this thesis, a YSZ(111) substrate was available, allowing this subtraction to be performed. The Si(111) and Ge(111) substrates were not available at the time of measurement, however, so any effect of the substrate on the CFAS datasets remains within the data. In each case, the total background contribution was observed to be paramagnetic, rather than the diamagnetic effect expected from all of the substrate materials. This suggests that any contribution from the substrate material is significantly smaller than the paramagnetic effect arising from the sample mount. The subtraction of an average paramagnetic contribution was performed in order to reduce the effect of these substrates on the data, but ideally a repetition of the data analysis could be performed after the VSM has been repeated on similar substrates.

Once a complete set of data was measured, these background effects were then removed from the data by subtracting this background signal, allowing the isolation of data solely from the sample.

3.3.2 Ferromagnetic Resonance Spectroscopy

Ferromagnetic resonance spectroscopy (FMR) uses the principle of FMR discussed in section 2.5 to characterise the magnetic properties of a thin film sample. Using magnetic resonance spectroscopy the magnetic damping parameters, anisotropies, Landé g-factor and saturation magnetisation can be obtained.

Two different methods of FMR Spectroscopy have been used to collect the data presented in this thesis. These are the *Vector Network Analyser FMR* and *Modulation FMR* techniques. While both use the same principles of RF absorption exciting the magnetisation precession about an axis defined by the effective field, these two methods differ slightly in the methods of RF generation

and signal measurement. A full description of the FMR spectrometer used to perform these experiments is given in chapter 4.

FMR spectroscopy is a bulk technique and cannot therefore be used to isolate the effects of different layers in a multilayer stack, for example, or different phases of material in a given sample. Since the effect relies on RF absorption, the penetration depth of the signal must also be considered. In metallic samples, the typical penetration depth of microwave (RF) frequency photons (the RF Skin Depth) is less than a micron [163,164]. All of the samples studied in this thesis are on the order of 10-100 nm and therefore the entire sample can be driven to resonance.

3.3.2.1 Vector Network Analyser FMR

Vector Network analyser FMR (VNA-FMR) is a well-known technique for measuring ferromagnetic resonance in ferromagnetic thin films [165,166]. The technique uses a Vector Network Analyser to provide an RF signal of variable frequency which drives FMR in a ferromagnetic sample as discussed in section 2.5. The VNA works by comparing a variable frequency RF input/output signal between the two SMA ports, connected either side of the device under test. The VNA measures the scattering parameters (S-parameters) as a ratio between the signal at the input and output ports (identified as ports 1 and 2 respectively). The forward transmission coefficient (commonly known as 'S_{21}') is then defined by the ratio:

$$S_{21} = \frac{b_2}{a_1}\Big|_{a_2=0} \tag{3.14}$$

Where a_x describes the incident wave at port x and b_x is the corresponding reflected wave, and

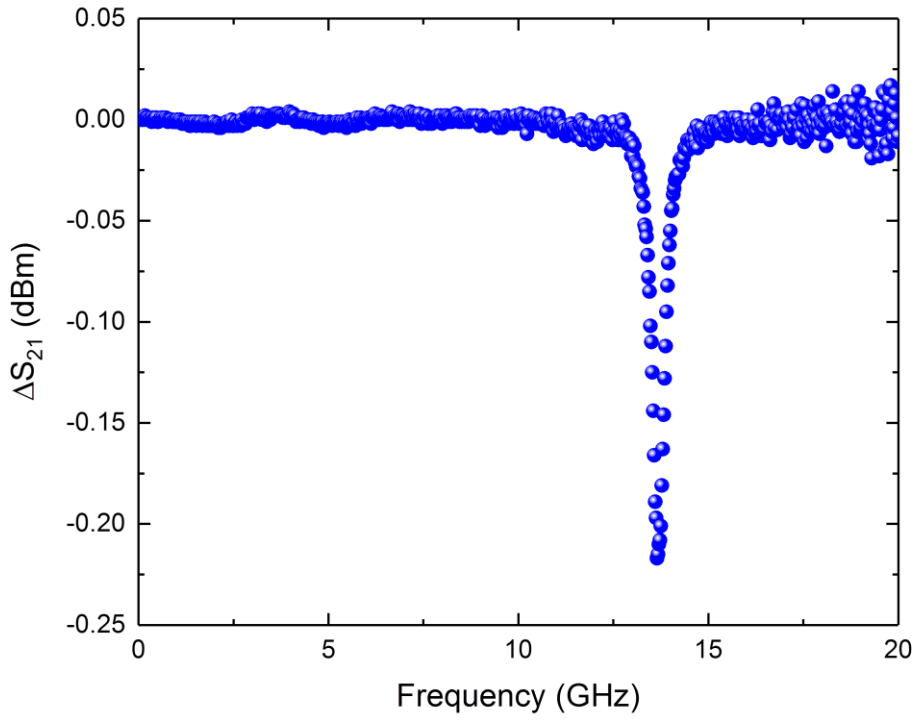

Figure 3.11. *A typical VNA-FMR linescan from a CFAS/Si sample, showing S_{21} as a function of the applied RF frequency at a fixed field of 1500 Oe*

the incident wave at port two is zero [167].

The signal is passed across the sample under test and the frequency is swept by the VNA according to user-defined input parameters. When the resonance condition is met some of the RF signal is absorbed to induce the precessional motion of the spins, which can be observed directly as a loss of signal intensity at port 2 and a corresponding reduction in the S_{21} ratio. Sweeping the frequency across the resonance frequency in a fixed magnetic field gives rise to a characteristic lorentzian absorption peak as observed in figure 3.11. Some additional structure is expected, however, since in a real device the CPW itself will have some losses as a function of frequency. The baseline will therefore not be flat. This is compensated for by forcing the resonance to high frequencies (beyond the VNA measurement range) and recording a background or reference signal from the scan data. This is then subtracted from the data in order to flatten the baseline. Since the Kittel curve is 2-dimensional and varies with both the applied frequency and the magnetic field, a lorentzian peak can also be extracted by fixing the frequency and sweeping the bias field, as shown in figure 3.12

In order to extract damping data, the linewidth of this resonance peak must be extracted. This is achieved by extracting linescans from the 2D data array at a fixed field (frequency), plotting the intensity data as a function of frequency (field) and fitting the resulting absorption peak using an asymmetric Lorentzian function [66,168], given by

$$\chi''\cos(\alpha) + \chi'\sin(\alpha) = A\frac{\Delta_H\cos(\alpha)+(H-H_r)\sin(\alpha)}{{\Delta_H}^2+(H-H_r)^2} + B \tag{3.15}$$

where A and B are constants, χ’ and χ’’ are the real and imaginary components of the AC susceptibility respectively, α is the mixing angle between the absorptive and dispersive

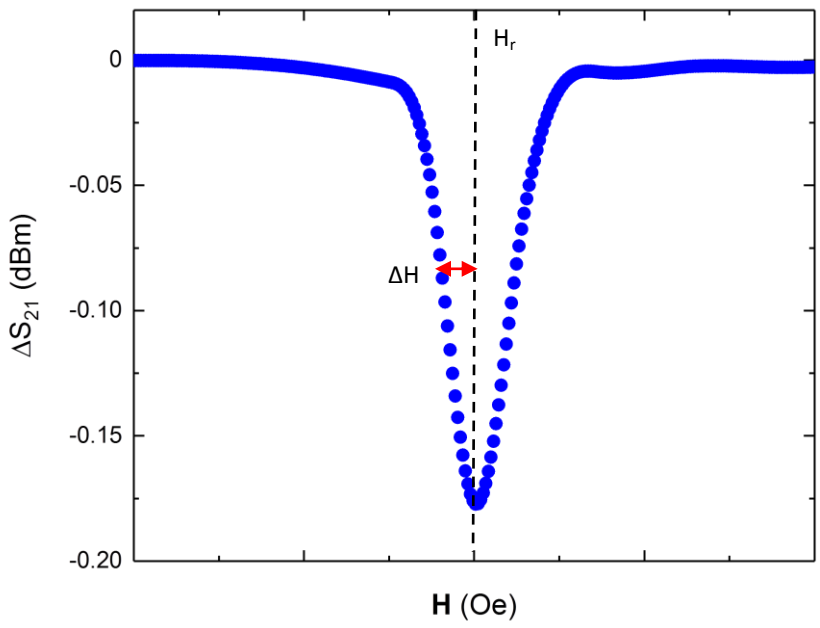

Figure 3.12. *A typical VNA-FMR linescan of S_{21} as a function of the applied magnetic field at a fixed frequency*

components of the FMR, Δ**H** is the half-width-half-maximum (HWHM) of the absorption lineshape, $\mathbf{H}_r$ is the resonance field and **H** is the applied magnetic field. A symmetric Lorentzian fit would be appropriate in a perfect system, but it is well known that asymmetry can arise as a result of coupling between the sample and the transmission line or cavity, which gives rise to mixing between the real and imaginary susceptibility components [66,166,169].

By fitting the lineshape using equation 3.15, important magnetic parameters of the material under test can be extracted at a particular angular frequency (ω). The two key parameters are the linewidth (Δ**H**) and the resonance field ($\mathbf{H}_r$). The linewidth of the resonance is linked to the damping in the sample, as discussed in section 2.5.4. By extracting Δ**H** from field linescans as a function of the RF frequency, the damping within the system can be quantified. Assuming the relation is linear, fitting this data using equation 2.45 yields the Gilbert damping parameter and a quantitative representation of both the intrinsic and extrinsic damping factors. If the trend is curved, on the other hand, the two-magnon scattering parameter (equation 2.47) can be applied as well. In this way, the dominant damping mechanism can be observed and quantified.

Extracting $\mathbf{H}_r$ as a function of ω at a fixed angle also provides a useful method of measuring several other magnetic parameters. The change in $\mathbf{H}_r$ as a function of the angular frequency yields the Kittel curve which can be fitted using the Kittel equation, as discussed in section 2.5.3. If the magnetisation is aligned in the plane of the thin film, and parallel with the easy axis, fitting the Kittel curve using equation 2.40 yields useful magnetic parameters: specifically the saturation magnetisation ($\mathbf{M}_s$), the gyromagnetic ratio (γ) and the anisotropy field ($\mathbf{H}_a$). As described in section 2.4, the g-factor can be extracted from the gyromagnetic ratio.

The extraction of H_r as a function of the azimuthal angle (Φ) facilitates examination of the in-plane anisotropy. As discussed in chapter 2, the in-plane anisotropy is dictated by the magnetic free energy surface, and the resonance field at a given angle shows the position of the energy surface. Measuring the resonance field as a function of the azimuthal angle provides a trace of the free energy surface in the plane of the sample: the easy axes in the sample plane will correspond to minima in H_r, and the hard axes to maxima.

3.3.2.2 Modulation FMR

Modulation FMR operates on the same principles as VNA-FMR, although the method of signal detection is different. In this approach, an AC magnetic field, known as the modulation field, is applied in parallel with the bias field. While this field is non-zero, the time varying total field induces a similar change in the AC susceptibility of the combined sample and waveguide. The total susceptibility can be described by [170]

$$\chi(\boldsymbol{H} + \boldsymbol{H}_m e^{i\omega t}) \tag{3.16}$$

which, when considered as a function of time can be expressed as the first two terms of a Taylor expansion, assuming that higher order terms are sufficiently small to be neglected, as

$$\chi(\boldsymbol{H}) + i\omega \boldsymbol{H}_m e^{i\omega t} \frac{d\chi}{d\boldsymbol{H}} \tag{3.17}$$

In the above expressions, χ represents the AC susceptibility, **H** is the bias field, $\mathbf{H}_m$ is the modulation field and ω is the driving frequency of the modulation coils. The lock-in signal is

proportional to the derivative of the imaginary component of the AC susceptibility with respect to field [66]. However, coupling between real and imaginary components can arise as a result of coupling between the sample and the waveguide. This can introduce asymmetry into the resonance, and must be accounted for in the fitting equations.

The modulation technique measures a change proportional to the first derivative of the absorption with respect to the magnetic field. Extracting magnetic parameters from modulation FMR data is therefore performed using the first derivative with respect to **H** of the asymmetric Lorentzian function [66]. This is given by

$$\frac{d(\chi''\cos(\alpha)+\chi'\sin(\alpha))}{d\boldsymbol{H}} = A\left[-\frac{2(\boldsymbol{H}-\boldsymbol{H_r})\Delta_H\cos(\alpha)}{[\Delta_{\boldsymbol{H}}{}^2+(\boldsymbol{H}-\boldsymbol{H_r})^2]^2} - \frac{[\Delta_{\boldsymbol{H}}{}^2-(\boldsymbol{H}-\boldsymbol{H_r})^2]\sin(\alpha)}{[\Delta_{\boldsymbol{H}}{}^2+(\boldsymbol{H}-\boldsymbol{H_r})^2]^2}\right] + B \qquad (3.18)$$

where the fitting parameters are the same as in equation 3.15.

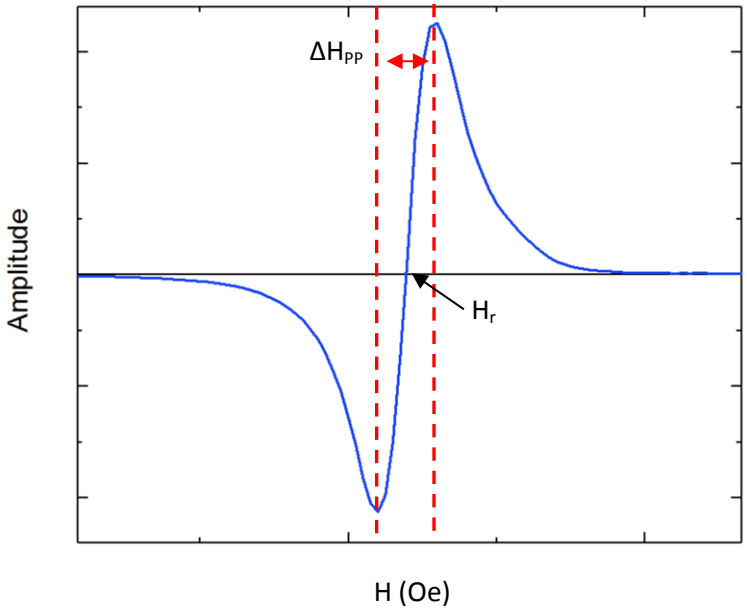

Figure 3.13. *A typical modulation FMR trace from a single crystal ferromagnet with the peak-to-peak linewidth ($\Delta\boldsymbol{H}_{PP}$) and resonance field ($H_r$) parameters indicated*

As in the VNA-FMR technique, the important parameters to be extracted from the fits to this equation are the HWHM (linewidth) Δ**H** and the resonance field $\mathbf{H}_r$. These fit parameters are the same as those extracted from the asymmetric lorentzian function in the VNA-FMR technique. However, the peak-to-peak linewidth of the modulation FMR signal is not exactly the HWHM of a lorentzian but is reduced by a factor of $\sqrt{3}/2$. Therefore

$$\Delta\boldsymbol{H}_{VNA} = (\tfrac{\sqrt{3}}{2})\Delta\boldsymbol{H}_{mod} \qquad (3.19)$$

where $\Delta\mathbf{H}_{VNA}$ is the linewidth observed in the VNA-FMR data and $\Delta\mathbf{H}_{mod}$ is the corresponding linewidth in the modulation FMR. Similarly, fits of $\mathbf{H}_r(\omega)$ at fixed angle allow the extraction of $\mathbf{H}_a$, $\mathbf{M}_s$ and γ (and therefore g), and fitting $\mathbf{H}_r(\varphi)$ can be used to examine the in-plane anisotropy of the sample. This scaling factor must therefore be accounted for in the extraction of the linewidth.

Since the relative position of $\mathbf{H}_r$ and the linewidth $\Delta\mathbf{H}$ are the important features of these datasets, the exact heights of the peaks are not of practical interest. The y-axis scale of data collected using the modulation FMR technique is therefore arbitrary as long as clear peaks are observed.

As long as the modulation FMR and VNA-FMR techniques return values for $\mathbf{H}_r$ and $\Delta\mathbf{H}$ which are consistent (within error) for the same sample, data extracted using these two different methods can be compared directly. For the purposes of this thesis, all FMR spectrometry was performed using the custom-built FMR spectrometer developed for this project. Further information is presented in chapter 4.

3.4 X-Ray Absorption Spectroscopy

Soft x-rays provide a useful method for investigating magnetic samples, since X-ray absorption spectra (XAS) can be used to perform chemical and co-ordination analysis [171,172]. The absorption of photons of the correct frequency ($E_{ph} = \hbar\omega$) excites electron energy level transitions in the atoms of the sample. The photon energies can be tuned to transitions in specific metals for element specific analysis.

Upon the absorption of a photon, both the energy and the angular momentum must be conserved. The energy gap between electron states must be met, such that the difference (δE) between initial and final energy states (E_i and E_f respectively) is equal to the incident photon energy E_{ph}, (i.e. $E_f = E_i + E_{ph}$). An electron must be available in the E_i state in order to be excited into the E_f state. Spin-flip is forbidden in these dipolar transitions, so the electrons must also have the correct spin alignment. The density of occupied electron states at the Fermi level therefore affects the absorption probability.

Angular momentum is transferred from the photon to the electrons by coupling angular momentum of the photon with the orbital angular momentum of the electron. The combination of these two effects results in excitation of the electrons to a higher energy level. However, in materials with spin-split core states, the momentum transferred from the photon couples to both the spin and orbital angular momenta as a result of spin-orbit coupling.

The absorption probability (σ) of each photon is governed by Fermi's golden rule equation 3.20, which is composed of two parts: the dipole matrix element, which governs the angular momentum, and the density of available spin states, which governs the conservation of energy.

$$\sigma = \left(\frac{2\pi}{h}\right) |< \varphi_f | \boldsymbol{T} | \varphi_i >|^2 \, \rho_f(E_f - E_i) \tag{3.20}$$

where $<\varphi_f|\mathbf{T}|\varphi_i>$ is the dipole matrix element, ρ is the density of available electron states at the Fermi level and $<\varphi_f|$ and $|\varphi_i>$ are the final (valence) and initial (core) states of the system respectively. Dipole selection rules also apply to the transition, allowing only those transitions which have $\Delta L = \pm 1$ and $\Delta S = 0$ [173].

The second part of the process is the absorption of the electrons from the lower state to the higher: an empty state must therefore be available for the excitation to occur, and the excitation is thus defined by the density of available electron states at the Fermi level. Sweeping the energy of the incident x-rays allows the measurement of the absorption as a function of energy, resulting

in an X-ray absorption spectrum (XAS). When the energy of the x-rays matches the energy of the electron transition, the photon is absorbed and a peak is observed in the XAS.

The XAS is usually measured using either a total electron yield (TEY) or fluorescence yield (FY) method. TEY is measured using a drain current, by connecting an electron source to the sample and measuring the drain current caused by secondary electron emission that occurs during the X-ray absorption. The absorption of x-ray photons produces a series of Auger, secondary and photo-electrons within the sample. Auger electrons arise from valence electrons being emitted due to changes in the electron distribution as a result of the x-ray absorption, while photoelectrons are emitted as a result of the absorption of high-energy photons within the sample. As these electrons travel through the sample structure, they interact with other electrons in the crystal structure, causing the emission of secondary electrons. This gives rise to electron emission which is directly proportional to the number of core holes created by the incident x-rays.

The drain current is directly proportional to the total electron emission which arises from the x-ray absorption as long as the electron escape depth (L) << (Λ) the absorption depth [174]. At a fixed photon frequency, the TEY is governed by the equation

$$I_{TEY} = K\frac{\mu L}{\mu L + \cos(\theta)} \tag{3.21}$$

where K is a constant, μ is the absorption co-efficient and θ is the angle of incidence of the x-rays.. It should be noted that the TEY method is a surface sensitive technique, since in the soft-x-ray spectrum L is limited to 3-5nm. This method therefore relies on the surface of the sample being representative of the whole.

Fluorescence yield (FY) detection is an alternative method of XAS detection which uses the photons re-emitted during XAS to observe the absorption effect [174]. The absorption of X-ray photons produces fluorescent photons which can be detected using a photodiode tuned to detect photons over a broad range of energies. The number of these photons which can be detected is proportional to the absorption cross-section multiplied by the emission matrix elements [175,176]. The FY is more bulk sensitive technique than TEY due to deeper penetration of the x-rays compared to the electron mean free path, but in practice returns fewer photons than are generated by the absorption behaviour. This reduction in signal is a result of the larger probability of Auger electron emission compared to the probability of photon emission at the L edges in soft x-ray spectroscopy. At the K-edges, or in hard X-ray spectroscopy, these transition probabilities are reversed, and FY detection is more commonly used.

The absorption spectrum can be used to identify individual elements based on their unique absorption energies. Local crystal field effects in different sites (discussed in section 2.3.1.2) also influence the absorption energy in the ions, resulting in shifts in the absorption energy based on the co-ordination of a given ion species and the environment which it occupies. This therefore allows for site specificity as well as element specificity. Paired with the non-intrusive nature of the technique, this makes XAS an excellent tool for structural analysis.

3.5 XMCD

In magnetic samples, a difference in the x-ray absorption probability arises when XAS is performed using left- and right-hand circularly polarised x-rays (referred to as LCP and RCP x-rays respectively). LCP and RCP can be subtracted from each other (by convention, the negative (right) – positive (left)) to reveal the difference, which is known as the x-ray magnetic circular dichroism (XMCD).

Using an appropriate applied magnetic field, the sample is saturated, aligning the spin moments and therefore increasing the density of available electron states with antiparallel spin states. The absorption is therefore made sensitive to the magnetic polarisation. The dichroism is maximised when the magnetisation is (anti-)parallel with the x-ray angular momentum. Preferential angular momentum alignment at the Fermi level changes the transition probability depending on whether the photon and spin angular momenta are aligned in parallel or anti-parallel. If, for example, RCP photons have positive (parallel) helicity, at the L_3 edge, photons RCP have a 62.5% chance to excite spin-up electrons and 37.5% to excite spin-down electrons. At the L_2 edge, RCP light preferentially couples to spin down electrons, exciting 75% spin-down electrons and 25% spin-up. For LCP photons, the opposite values are observed. This results in a difference in the LCP and RCP XAS profiles proportional to the photon helicity [174,177]. The sign of the dichroism at the L_3 edge is opposite that of the L_2 edge as a result of the opposing majority spin alignment.

The XMCD process can be best described as a two-step process. Firstly the angular momentum of

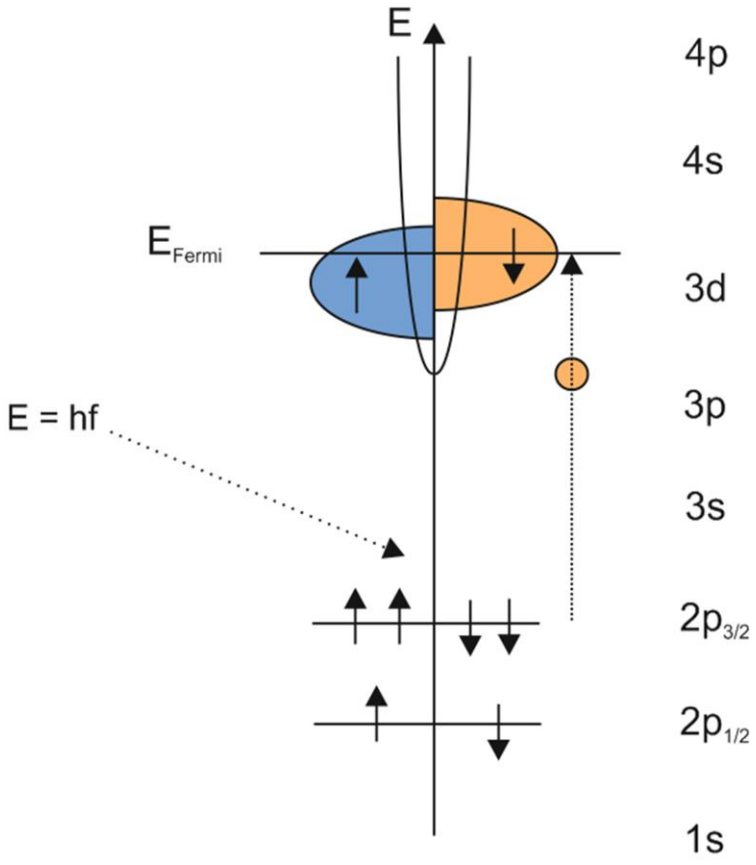

Figure 3.14. *A schematic diagram of X-ray absorption in a material with spin-split density of states*

the photon must couple with that of the atoms in the sample. When the helicity vector of the incident x-ray photon is parallel (antiparallel) to the 2p orbital moment, electrons are preferentially excited in the spin up (down) configuration. The second step of the process requires the excited electron to occupy an empty state in the 3d valence band, and the number of these states dictates the direction of the peaks in the XMCD spectrum: If the dominant species of hole is spin-down, the L_3 peak will be negative and the L_2 peak positive. If the spin-up holes are more prevalent, the XMCD peaks take the opposite orientations [174,178,179].

The XMCD allows elemental specificity by tuning the energy of the x-ray photons to specific transitions in magnetic metals. The L-edge transitions (originating from the 2p core level split into the j=3/2 'L_3' and j = 1/2 'L_2' edge) are used as they occupy distinct energies in the soft x-ray range, and the transition of electrons from occupied core states to the empty 3d levels is useful for transition metal species as the magnetism in these materials is primarily due to the 3d electrons. Since the binding energies of valence electrons in different oxidation states are shifted, the technique also allows valence specificity.

Since the measurement of XMCD requires the focusing of a narrow beam of x-rays on the sample, the area investigated using this technique is localised to the area under the x-ray beam. The local nature of the technique also means that if the sample is inhomogeneous, it may not be representative of the whole sample. This may be accounted for by measuring over a number of different areas of the sample. The geometry of the system can also be used to minimise this localisation: the insertion of the incident x-ray beam at a grazing angle of incidence can be used to gain an increased beam footprint (proportional to $\frac{1}{sin\theta}$ where θ is the incident beam angle) [180]. This increases the area which the beam interacts with, allowing a larger sample area to be measured. The grazing incidence also has the advantage of measuring effects in the sample plane, as opposed to the normal incidence which measures out-of-plane effects. All of the XMCD presented in this thesis was measured at a grazing angle of 65^{o} away from the normal in order to access the in-plane magnetisation as XMCD is proportional to the projection of **M** along the direction of the X-rays, given by $\boldsymbol{M}.\sigma$ ($\boldsymbol{M}\sigma\cos(\theta)$) where σ is the helicity vector of the incident photons.

Operating at grazing incidence also goes some way towards mitigating the self-absorption effect and is therefore preferable for FY experiments. At normal incidence, the substrate absorbs some of the elastically scattered photons and they therefore do not reach the detector. In the grazing incidence, however, fewer of the elastically scattered photons are absorbed in this way, leading to increased detection of these unwanted photons (known as 'saturation') [174,181]. The closer the photon penetration depth becomes to the electron escape depth, the greater this saturation effect becomes [182]. As a consequence of the self-absorption and saturation effects, however, the FY technique is of limited effectiveness when using the sum rules to extract useful parameters from XMCD data, although research into how to account for this is being pursued [175]. This makes the FY detection an unsuitable technique for the purposes of this thesis.

All of the XMCD experiments discussed in this thesis were performed on the I06 beamline at Diamond Light Source, with the sample held under UHV conditions at room temperature. A superconducting vector magnet was used to apply a 6T magnetic bias field across the samples. Averaging over many datasets was also performed to improve the measurement accuracy as well

as improving the signal to noise ratio of the XMCD. Comparison with the FMR data will be used to show if the extracted values are consistent with those observed in the bulk.

3.5.1 Synchrotron X-ray Generation

In the synchrotron, low energy electrons are generated using a pulsed output from an electron gun and then accelerated using a linear accelerator (LINAC) and a synchrotron 'booster': an RF cavity which is used to further energise the electrons. Once sufficiently high energies are achieved, these energetic particles are then transferred into a storage ring, where they continue to circulate under Ultra-High Vacuum (UHV) conditions in a continuous beam of electrons. As they pass around the ring, the path of these electrons are bent by large magnetic fields. This bending produces x-ray photons which propagate away from the path and can be tapped off from the storage ring for use in x-ray experiments.

The x-ray photons generated using this method have a broad energy spectrum and are not collinear. It is practical to introduce another piece of equipment in order to increase the photon flux, as well as to produce a collimated x-ray beam of narrow bandwidth. In the current third generation synchrotron facilities, this is achieved using a device called an undulator.

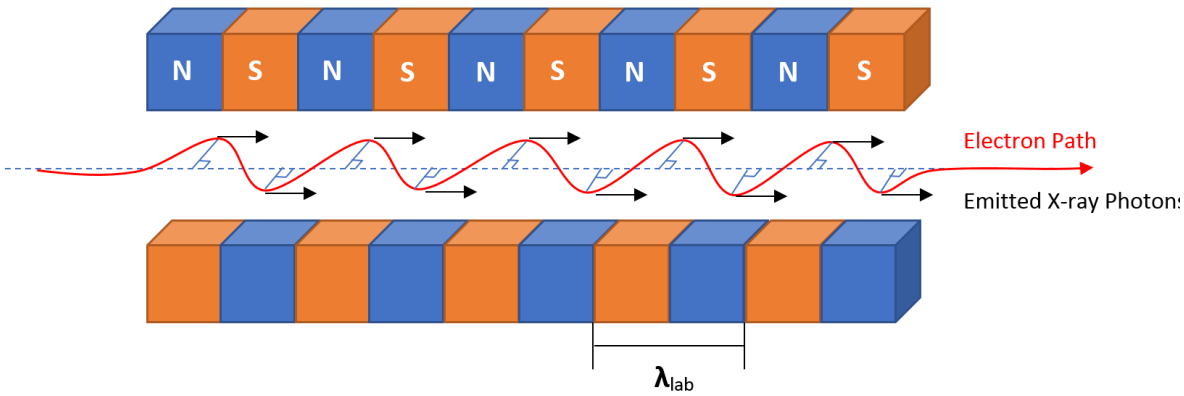

Figure 3.15. *A schematic diagram of the x-ray photon generation process in an undulator. The photon wavelength is dictated in the laboratory reference frame by* λ_{lab}

An undulator consists of a series of alternating magnetic fields which are used to bend the path of electrons repeatedly in order to produce a high intensity x-ray beam (figure 3.15) [183,184]. The repeated bending of the electron trajectory produces coherent beams of x-ray photons with a narrow bandwidth and a narrow emission cone. Since the emitted photons are generated at intervals corresponding to integer multiples of the photon wavelength, they interfere constructively, increasing the total photon flux. This produces a collimated beam of coherent electrons with a narrow energy bandwidth. The period of the magnetic fields determines the wavelength of the photons. Given that the electrons are travelling at relativistic speeds, some relativistic effects must be accounted for. At these speeds, Lorentz contraction is experienced in the electron's reference frame, reducing the effective period of the magnetic fields relative to the laboratory reference frame. A Lorentz factor of $\frac{1}{\gamma}$ is experienced by the electron as a result. The

electrons are also affected by Doppler shift, which further reduces the effective period of the magnetic fields experienced in the electron's rest frame by a factor of $\frac{2}{\gamma}$. The result of these combined effects is a reduction of the magnetic field period proportional to $\frac{1}{\gamma^2}$. A periodic arrangement of magnet poles with λ_{lab} ~60mm in the laboratory frame can therefore be used to produce photons which experience x-ray wavelengths in their own rest frame. By changing the position of the magnets, or the magnitude of the magnetic field, the photons generated in the undulator may be tuned to discrete energies. The magnets in the undulator may also be rotated or re-arranged in order to tune the polarisation of the x-ray photons.

For the XAS and XMCD experiments discussed in this thesis, 'soft' x-rays (with energies between 100eV and 2keV, as discussed in section 3.2.1.) were chosen, to coincide with the L_2 and L_3 absorption edges of the iron species in magnetite. After the electrons pass through the bending magnets, the energy loss from the emitted photons is counteracted by an RF cavity, containing magnetic fields oscillating at microwave frequencies. These oscillations restore the energy of the electrons, which can then be used to repeat the bending process and thereby produce additional x-ray photons on multiple rotations around the storage ring.

3.5.2 The XMCD Sum Rules

The well-known XMCD sum rules can be used to extract important magnetic parameters, such as the ratio between orbital and spin magnetic moments, allowing access to the g-factor in the magnetic materials. Since the incident photon only interacts with the orbital component of the electron wavefunction [177], the spin and orbital moments of the electrons can be examined independently. These rules define the relationship between the magnetic properties. The parameters used to define the sum rules are shown in figure 3.16. The sum rules are [174,185,186]

$$n_h \propto r \tag{3.22}$$

$$\frac{< l \,.\, s >}{n_h} = 2 - \frac{3s}{r} \tag{3.23}$$

$$< L > = \frac{-4qn_h}{3r} \tag{3.24}$$

$$< \mathrm{S} > + \frac{7<T>}{2} = \frac{-(3p-2q)}{n_h} \tag{3.25}$$

$$\frac{<L>}{\left(<S> + \frac{7<T>}{2}\right)} = \frac{4q}{(9p-6q)} \tag{3.26}$$

where n_h is the number of d-electron holes in the material, r is the integral over the total XAS (RCP+LCP) at the L_2 edge, s is the integral over the total XAS at the L_3 edge, $<l.s>/n_h$ is the branching ratio (the ratio of intensities at the L_2 and L_3 edges), q is the integrated XMCD at the L_2 edge, p is the integrated XMCD at the L_3 edge, <L> is the expectation value of the orbital angular momentum, <S> is the expectation value of the spin angular momentum and <T> is the expectation value of the magnetic dipole term. <T> is small compared to <S> in 3d transition metals [174,186], allowing the simplification of the last two sum rules to

$$< \mathrm{S} > \cong \frac{-(3p-2q)}{n_h} \tag{3.27}$$

$$\frac{<L>}{<S>} \cong \frac{4q}{(9p-6q)} \tag{3.28}$$

Chen *et al*. [174,187] further refined the sum rules using a modified notation in order to simplify these rules. The underlying assumption used is only valid in the case where the spin-orbit splitting in the core electrons is larger than the transition between the core and valence states. This can be reliably applied to the Fe, Co and Ni L_2 and L_3 edges (and can therefore be applied to the XMCD presented in this thesis) although in the case of other materials, further modification is required [174,188,189]. This representation allows the sum rules to be written in terms of the orbital magnetic moment (μ_L) and the effective spin magnetic moment (μ_{Seff}), such that

$$\mu_L = -\frac{4q}{3r} n_h \tag{3.29}$$

$$\mu_{Seff} = -\frac{(6p-4q)}{r} n_h \tag{3.30}$$

$$\frac{\mu_L}{\mu_{Seff}} = \frac{1}{(\frac{9p}{2q}-3)} \tag{3.31}$$

These expressions allow easy extraction of the ratio between the orbital- and spin-magnetic moments. By comparing the ratio of μ_l/μ_s observed in different samples, the difference in the orbital angular momentum contribution can be assessed. This ratio can be used to calculate the g-

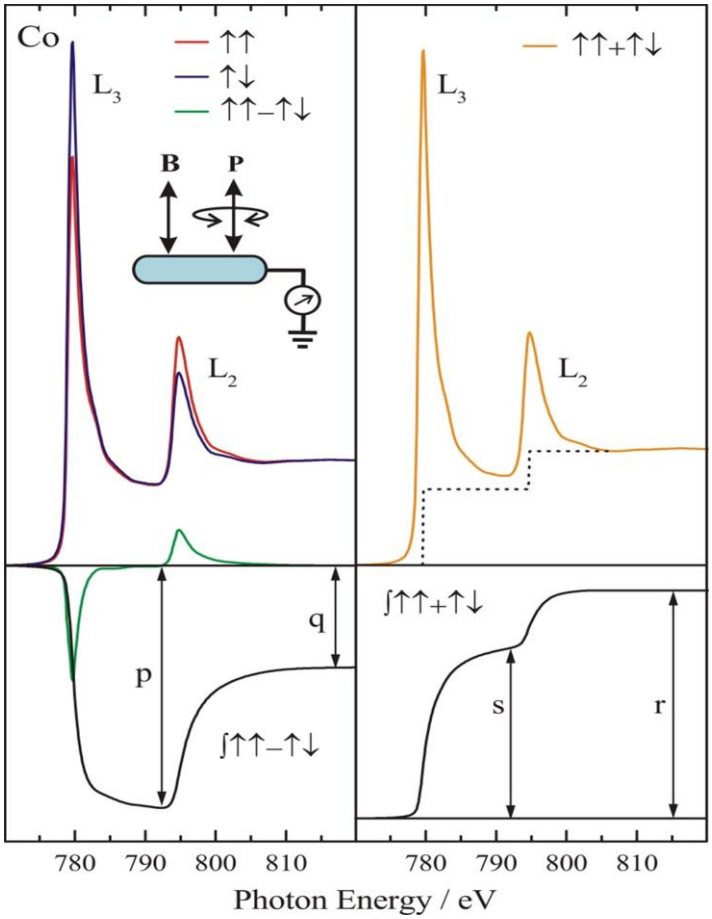

Figure 3.16. *A typical XMCD measured at the iron L-Edges including a schematic displaying the sum rules parameters*

factor of the sample using equation 2.26, and therefore provides useful information about the g-factor and the gyromagnetic ratio of the sample.

3.5.3 Atomic Multiplet Calculations

Atomic multiplet calculations can be performed on the XMCD in order to determine the relative occupation of each site in the structure. Cowan's ab-initio Hartree-Fock method with a relativistic correction [174,190,191] can be used to calculate a theoretical XMCD spectrum for each atomic species. The linear combination of one or more of these spectra is then used to calculate the relative occupation between sites. Cowan's code has long been available to the community, although further alterations have been made over the years, such as to account for crystal field effects, for example. Both the atomic multiplet theory and crystal field theory are combined in the CTM4XAS software which can be used to calculate the atomic spectra for transition metal ions of the appropriate element and valence [192]. The calculated spectra can then be linearly combined in order to achieve best fit with experimental data. Broadening effects are accounted for by a Gaussian term and a Lorentzian term in the CTM4XAS code. Without these broadening effects, the spectrum would appear as a delta function, representing electron transitions at exact energies. When the combined calculated datasets closely fit the experimental data, the relative amplitude of the spectra correspond directly to the relative occupation of each site.

This method may be used to assess the stoichiometry of the sample, since the site occupation is determined by the chemical formula. For example, stoichiometric magnetite has a 1:1:1 ratio of $Fe^{2+}(O_h)$: $Fe^{3+}(T_d)$: $Fe^{3+}(O_h)$ as discussed in section 2.6.1. Using atomic multiplet calculations to calculate the spectrum of each of the iron species, the combined spectra can be fitted to the data, with the amplitude of each corresponding to the relative site occupation. For the purposes of the XMCD in this thesis, spectra for the Fe sites in magnetite were simulated in the commercially available software CTM4XAS. These calculated spectra were then combined in Origin and compared with the data from the XMCD experiments to assess the occupation of the sites in each sample.

Using the techniques discussed in this chapter, it is possible to characterise the structural and magnetic properties of the magnetic thin films under investigation in this thesis. Data acquired from these techniques will be presented in chapters 5 and 6 of this thesis. Before the data could be acquired, however, it was necessary to construct and test an FMR spectrometer in order to conduct the experiments described in section 3.3.2. The design and testing of this equipment will be discussed in depth in the next chapter.

Chapter 4: The FMR Spectrometer

4.1 Introduction

A versatile technique for probing the magnetic damping in ferromagnetic materials is Ferromagnetic Resonance Spectroscopy (FMR). This technique allows the extraction of several useful magnetic parameters, such as the magnitude of the Gilbert damping parameter, as well as allowing access to the anisotropy of the crystal structure. In order to perform accurate, high resolution spectroscopy, a custom-designed high-resolution FMR Spectrometer was designed and constructed. This chapter contains details of the design and construction of a Ferromagnetic Resonance Spectrometer including test data recorded from well-known magnetic materials, in particular a thin film of permalloy ($Ni_{81}Fe_{19}$).

This chapter will examine the design, construction and testing of the FMR spectrometer including a detailed discussion of the spectrometer and the different modes in which it can operate. Since the spectrometer can be operated in two different modes, each corresponding to a variation on the well-known FMR spectroscopy technique, the equipment used in both of these techniques is presented. The merits and drawbacks of each technique are included with reference to how the operation of the spectrometer is affected. A comparison of the two techniques will also be presented, showing that both operating modes measure the same values for magnetic parameters in a permalloy test sample. These values are found to be in agreement with literature, establishing the accuracy of the spectrometer. Finally, further development of the spectrometer is discussed and a plan for improvements to the existing equipment will be presented.

4.2 Spectrometer Design

Over the course of the project, a Ferromagnetic Resonance Spectrometer was designed and constructed by the author based on plans similar to designs discussed in the literature, particularly those described by Kalarickal *et.al*. [166] and Montoya *et. al.* [193].

A schematic diagram of the spectrometer is given in figure 4.1 which outlines the basic design of the spectrometer operating with a vector network analyser as RF source and detector. Modifications to this scheme were made when the RF source was switched over to a variable output signal generator in the modulation FMR mode. These changes are outlined in chapter 4.4.2.

The spectrometer consists of two large (700mm diameter) Helmholtz coils with iron pole pieces which can be used to induce a magnetic field of up to 2T. The field induced between these coils is used as a bias (Zeeman) field in FMR experiments, in order to saturate the magnetisation in ferromagnetic samples parallel to the applied field. A soft iron pole piece is connected to each coil, focusing the field between the centre of the coils. These poles serve to focus the magnetic field as a result of the increase in magnetic permeability in the iron cores [194]. An air gap of 86mm between the poles was left to allow the positioning of a sample mount within the centre of the magnetic field.

The electromagnet was connected to a Bruker MN-100/100Si power supply unit in order to supply a variable DC current and therefore a variable bias field between the coils. Control of the power supply was provided by a Bruker BMN-100/100 control unit, which is governed by a scaled +/- 5V voltage input provided by a computer using a 16-bit NI MyDAQ card. The 16-bit output allows high field resolution since the scaled 0-5V output from the DAQ can take one of 65536 values, corresponding to a nominal minimum step size of 0.76Oe. Since the Power supply unit is unipolar, it can only output positive voltages. The reversal of the field must therefore be performed by either rotating the magnetic field orientation or the sample orientation, rather than inverting the

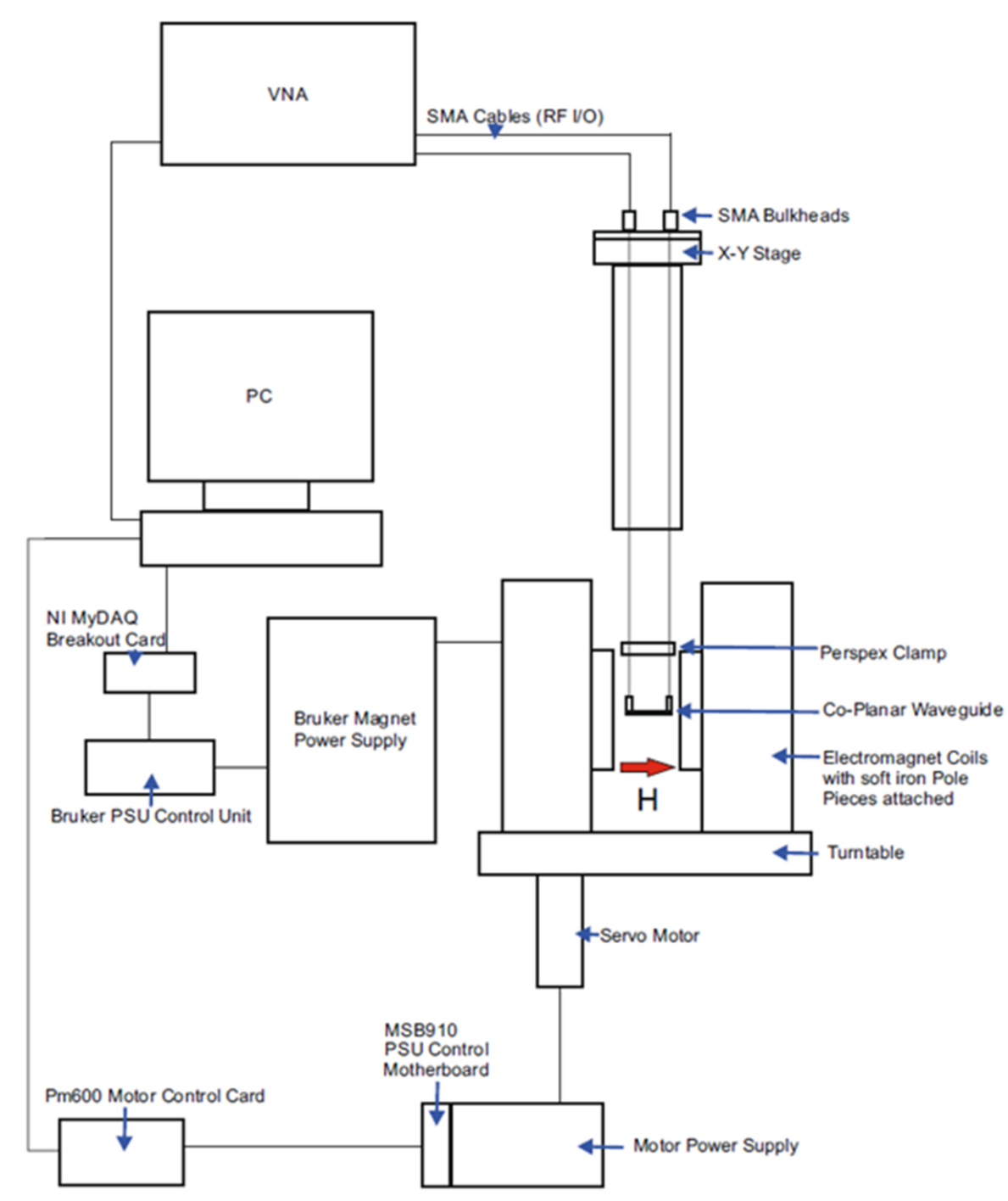

Figure 4.1. *A schematic diagram of the FMR Spectrometer operating in VNA-FMR mode*

polarity of the field. The magnetic field can be rotated in the azimuthal plane, since the electromagnet was mounted on a turntable driven by a Matador Control Systems DCM3D DC servo motor. This rotation also allows the bias field to be rotated relative to the sample mount, and therefore due to the sample mount orientation the in-plane anisotropy of a sample can be measured. The motor is driven using a scaled voltage output from a McLennan Motors PM600 Motor control unit, which is controlled using a local PC and connected to a power supply unit by a Mclennan Motors MSB910 motherboard. A single channel Baumer Electric BDB series rotary encoder connected to the motor unit by a drive belt provides feedback from the motor rotation to the control unit. The control unit reads this feedback as movement in the motor system and moves the motor accordingly based on the initial input parameters. The encoder used in this system provides high angular resolution, feeding back four steps per degree rotated. The magnet frame is grounded in order to prevent accumulation of static electricity. An external aluminium frame surrounds the magnet in order to prevent contact with the turntable assembly during rotation, serving as both a safety mechanism for the operator and as a stable base for attaching the sample mounting system, which is discussed later in this chapter.

Stray field tests were performed on the magnet coils to assess local safety concerns and positioning of the electrical equipment. Using a Hall probe, it was found that the field is well contained between the coils and the field intensity decays to the local background level over a distance of a few cm outside of the air gap between the coils. The magnetic remanence ($\mathbf{H}_{remanence}$) between the poles of the electromagnet was measured to be 50Oe. In order to prevent the introduction of additional inductance in the circuit, cables in the spectrometer were prevented

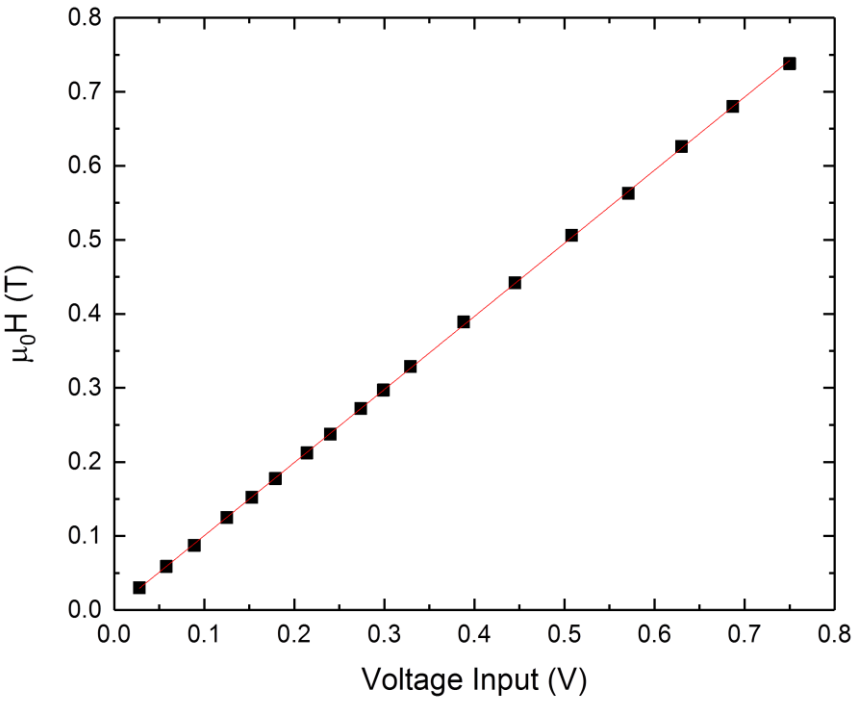

Figure 4.2. *Calibration data from the Bruker PSU showing the magnetic field induced as a function of the voltage applied by the DAQ unit output*

from forming coils. Both the Bruker power supply unit and the electromagnet are cooled using an internal water cooling system.

After the construction of the spectrometer, it was necessary to test the system for stability in order to yield reliable data from experiments. Firstly the magnetic field was calibrated as a function of the input current through the electromagnet coils. A steady DC current was passed through the coils using the Bruker power supply unit and the resulting magnetic field was measured at the centre of the coils using a calibrated Hirst GM-07 Gaussmeter. Time was allowed for the field to stabilise since the current was required to ramp and then settle to an equilibrium value. It was found that 30 seconds wait time was sufficient to ramp the field to 0.5T. Using the Gaussmeter to measure the field output in the centre of the coils as a function of input current, it was possible to calibrate between the output from the DAQ card and the magnitude of the bias field. The gradient of the calibration graph (figure 4.2) is observed to at 0.996 ± 0.001 VT^{-1} resulting in a conversion factor of 1.004.

The spatial variation in the field was also measured in order to establish the uniformity of the bias field, and to locate any local maxima for the purposes of applying bias fields to the sample mount. With the sample mount removed from the system, the current though the coils was set to output a nominal 5kOe field (based on the previous calibration) and the field was measured in x, y and z

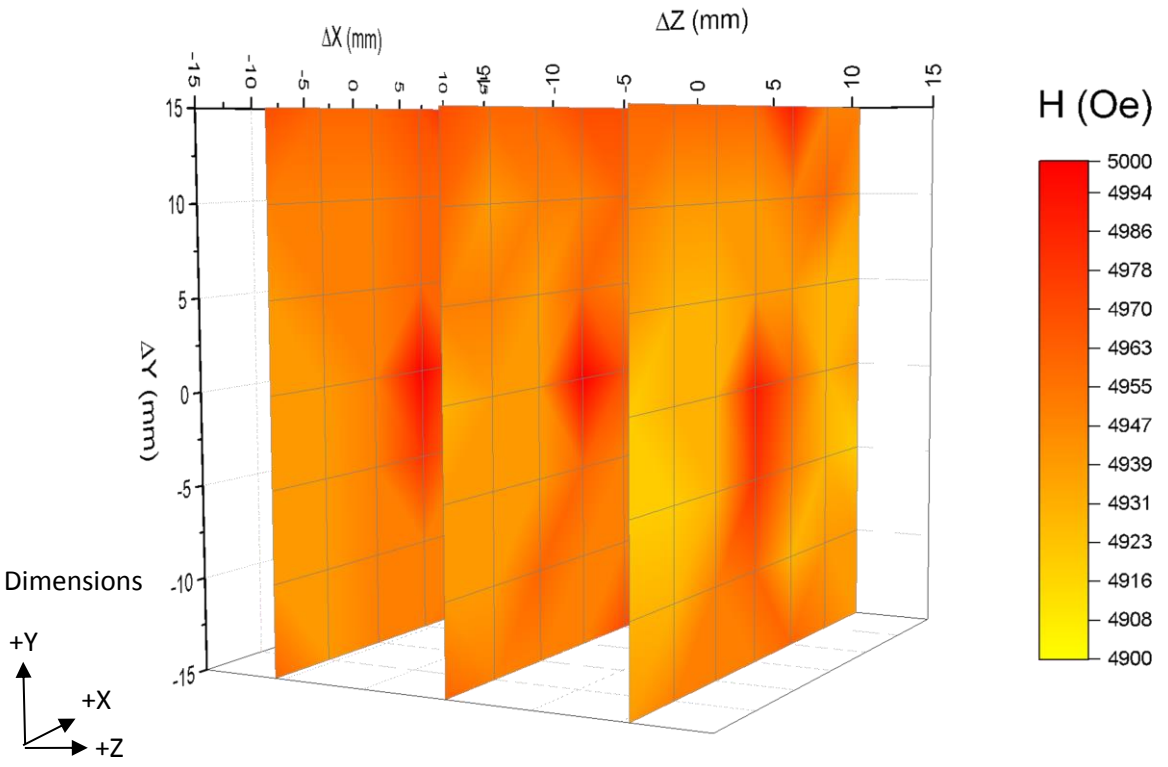

Figure 4.3 *A spatial map of the bias field output by the electromagnet coils. Little deviation from the 5kOe maximum is observed around the centre, but the field is observed to decay quickly as the distance from the origin increases. Every second dataset (+/-5mm, +/-15mm) is removed for clarity*

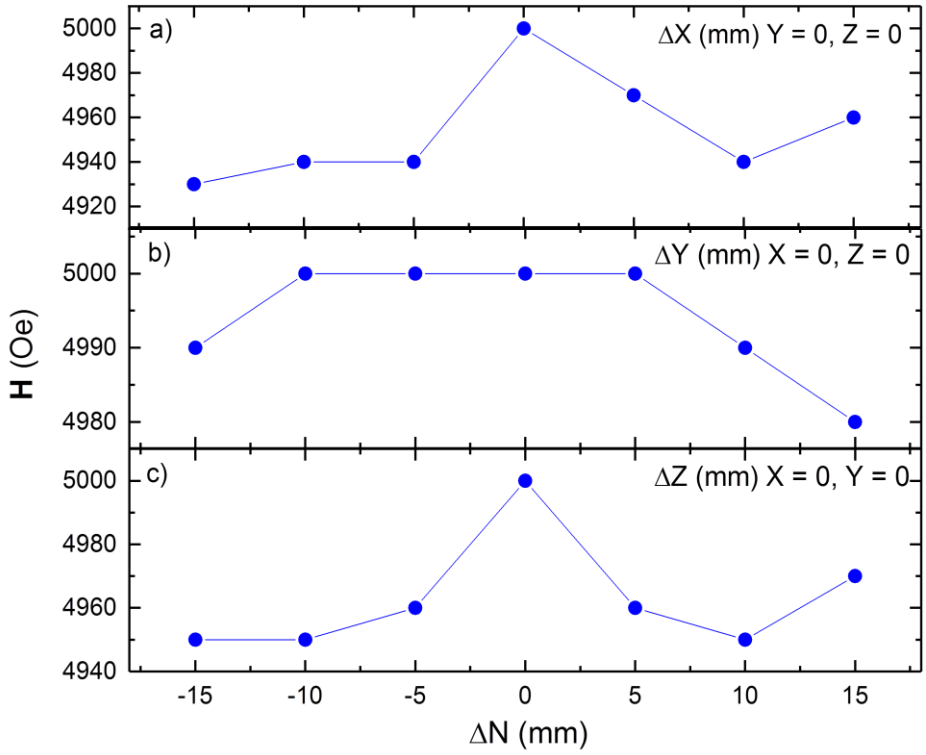

Figure 4.4 *A comparison of the magnetic field over 30mm around the centre of the Helmholtz coils in the FMR spectrometer in the a) x- b) y- and c) z-axes, where ΔN denotes the distance from the centre of the coils in the relevant axis*

planes in 5mm intervals over a 20x15x15mm area around the centre of the air gap between the coils (figures 4.3 and 4.4). The highest field strength (equal to the field set point) was recorded at the centre of the air gap. A small variation of 10 Oe was observed within ±10mm around the centre point in the y-axis, although a more significant change of up to 50 Oe within ±10mm is observed in the z-axis and up to 60 Oe within ±10mm in x. It was therefore important to keep the sample mount correctly centred at all times in order to avoid these local fluctuations in the bias field. Away from the centre, the field is observed to decrease by as much as 100 Oe at r = 20mm. Over a 5mmx5mm thin film sample the field is uniform, but the rapid decay of field over larger distances requires careful alignment of the centre of the CPW with the centre of the air gap, such that any sample is exposed to the appropriate nominal bias field for a given calibrated current input.

The power supply is operated in constant current mode in order to ensure that the magnetic field is steady, although the ambient conditions were kept as uniform as possible in order to ensure consistency between experiments. The local temperature of the spectrometer was regulated as well as possible under laboratory conditions. A room temperature of 21^{o}C (+/- 1 degree) has been maintained for the duration of the experiments discussed in this thesis. A plot of the temperature measured in the laboratory over one day is presented in figure 4.5. A measurement was made every 20 seconds over the course of one day using a Lascar EL-USB-1 temperature logger.

A pair of modulation coils were mounted inside the electromagnet to allow the application of a small intensity, low-frequency modulation field in addition to the main bias field. The modulation coils used in this experiment consist of two identical 40-turn coils of copper wire mounted on 300mm aluminium spools which were designed and built in-house. The total impedance of the modulation coil circuit was recorded at 3 ohms using an LC meter. The coils are driven by an amplifier which requires a 4 ohm load. A 1 ohm resistor was therefore added to the circuit in series with the coils to raise the total impedance to 4 ohms. The resistor was mounted inside an aluminium box which acts both as a heat sink and as protection for the component.

Samples were mounted in the centre of the electromagnet coils using a custom-designed sample mount consisting of non-magnetic components (figure 4.6). An RF signal line was incorporated into the sample mount using two semi-flexible RF cables connected to a custom-built co-planar waveguide. A lightweight plastic pipe surrounds these cables in order to protect the cables while the spectrometer is in operation. The sample mount is connected to a Newport M-406 2-axis translation stage for fine control of the sample position in the magnetic field. This stage allows two-axis adjustment of the waveguide position over a range of 13mm in both horizontal axes with micrometer sensitivity.

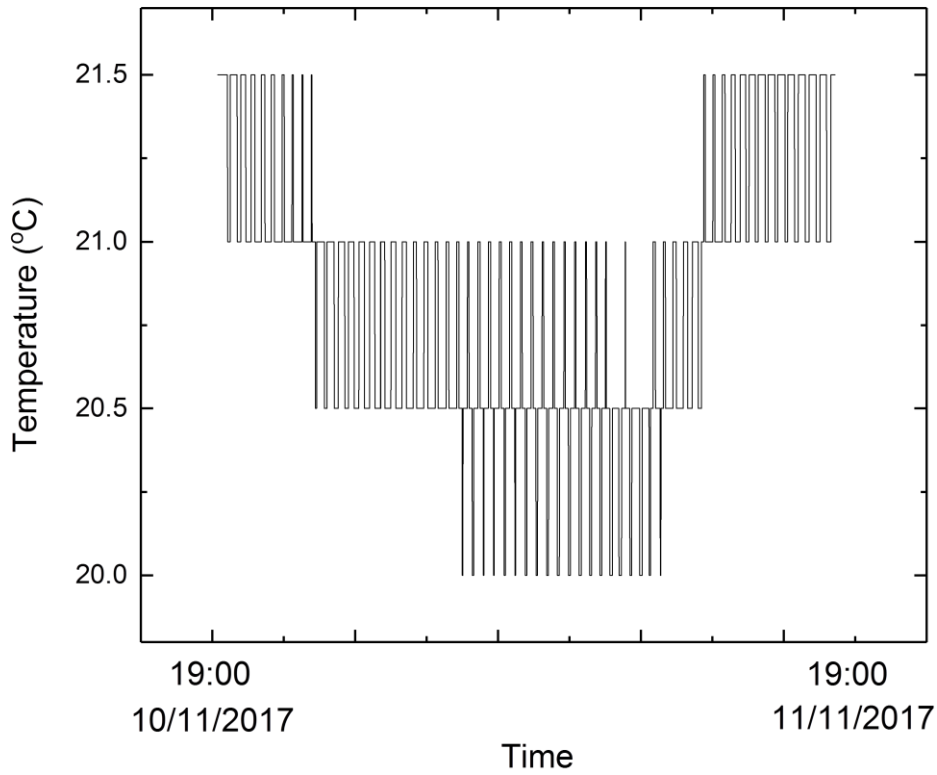

Figure 4.5. *Temperature data logged over one day in the spectrometer laboratory*

A custom-built co-planar waveguide is used to mount samples on the FMR spectrometer. The waveguide is supported by the SMA connectors on a pair of custom-sized (645mm) EZ-Form semi-flexible male-to-male non-magnetic SMA cables. These cables connect directly to the female-to-female SMA bulkheads on the top plate of the sample mount construction. An externally

generated RF signal can then be passed along these cables and through the waveguide in order to provide the RF excitation signal required to generate the FMR modes. Since the bulkheads are easily accessible, the device used to generate the RF signal can be changed at will, requiring only that a male SMA connector be attached to the input and output ports. This gives the advantage of flexibility in the system design and easy replacement of the RF generator in the event that specific frequency ranges are required, or repairs become necessary.

The cables support the waveguide alone due to the lightweight construction of the waveguide. A pair of right-angled SMA connectors either side of the stripline allow the RF passage through the waveguide. Care must be taken not to exert pressure on the waveguide when mounting samples, since this risks damage to the connectors. The cables are supported 50mm above the waveguide by a perspex clamp which prevents rotation of the semi-flexible cables. The stability of the waveguide is key for measuring the anisotropy in azimuthal sweeps in order to make direct comparison of different samples at the same orientation. It must therefore be kept as motionless as possible in order to ensure that the sample is not moved in the bias field between datasets.

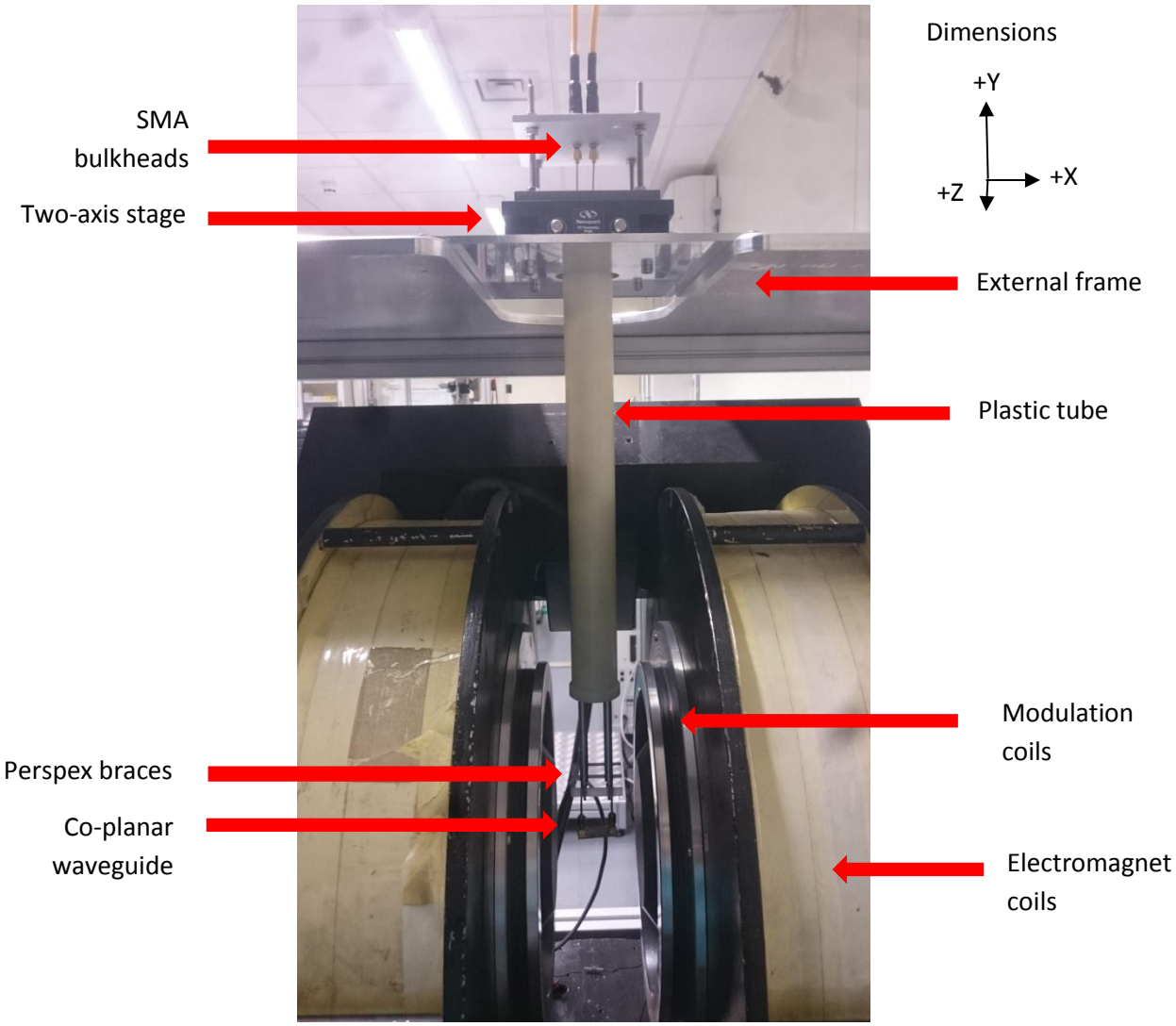

Figure 4.6. *A photograph of the custom-built sample mount system in the FMR spectrometer, including the two-axis stage, SMA bulkheads and mounting cradle, including the CPW, between the coils of the electromagnet*

All the components of the RF through-line, including the SMA connectors are impedance matched to 50 Ohms to prevent damage and reduce reflections of the RF within the system. All of the RF components used in this system are rated for use at frequencies up to or above 20GHz with the exception of the SMA bulkheads at the top of the sample mount system, which are rated to 18GHz. The use of a co-planar waveguide allows FMR measurements to be made using a broad range of RF frequencies. This broad band approach allows the operator to observe the change in the linewidth as a function of RF frequency and therefore extract information about the magnetisation damping behaviour.

4.3 The Co-Planar Waveguide

The co-planar waveguide (CPW) is a surface strip transmission line device designed to operate over a broad frequency range [195]. A central conducting stripline is laid between two ground planes situated atop a dielectric layer. This transmission line carries an electrical current and thereby induces a magnetic field perpendicular to the direction of the current propagation. The CPW is designed for low loss, wide-band operation, although the properties can be varied depending on the dimensions of the waveguide.

The waveguide used in this work is a 40mm x 20mm x 1.6mm grounded coplanar waveguide with a 1.4mm wide central transmission line flanked by a series of 0.9mm diameter circular vias in two linear fences (one either side of the transmission line). A schematic cross section is shown in figure 4.7. This waveguide is impedance matched to 50 Ohms to reduce the effect of reflections within the RF components [163,196]. The waveguide used for these experiments has ground vias connecting the ground plane on the top of the CPW with the ground plane on the bottom. The use of vias is a well-documented technique used in previous work [197] which increases the bandwidth of the CPW and suppresses higher order modes of oscillation in the CPW including the parallel plate modes [198]. Since the operation of the FMR spectrometer is only required between 100kHz and 20GHz, a standard single via fence design [197] provides suitable grounding between the top and bottom planes of the CPW. The waveguide therefore acts as a ground-backed co-planar waveguide (GBCPW). It is desirable to have a high Q-factor in resonant cavities in order to improve the sensitivity of resonators [199]. However, due to the broad-band nature of the CPW, it is common for these devices to have a very low Q relative to traditional cavity resonators. The flexibility allowed by the broad-band CPW device makes it more practical in a spectrometer which is designed to be used over a wide range of frequencies.

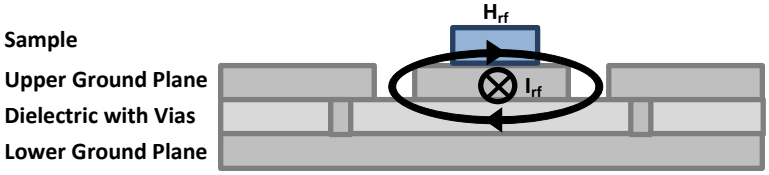

Figure 4.7. *A schematic representation of the planar field* $\boldsymbol{H_{rf}}$ *induced by a current* $\boldsymbol{I_{rf}}$ *through a Coplanar Waveguide*

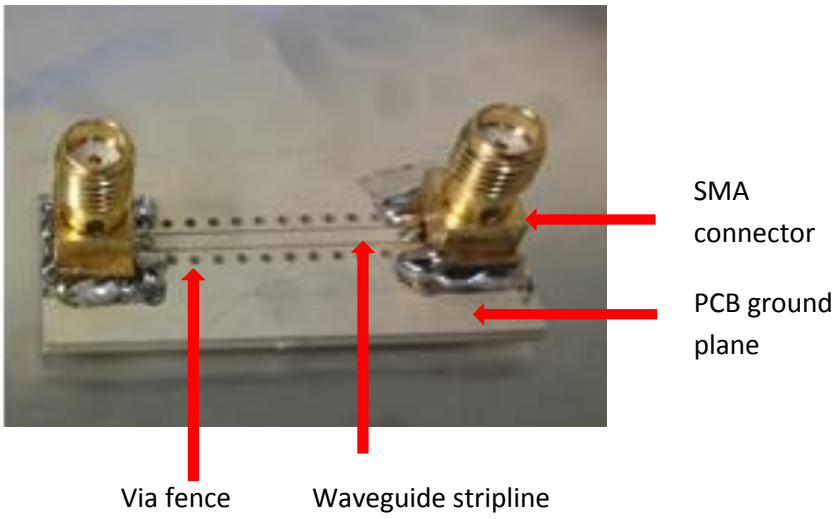

Figure 4.8. *A photograph of the co-planar waveguide used in the FMR spectrometer*

The CPW allows the mounting of thin film samples and measurement of the FMR effect in the in-plane geometry. A silver-coated copper stripline on the waveguide conveys the RF signal current which induces a local magnetic field parallel to the plane of the sample. The coupling of this RF field with the Zeeman split spin states of the electron spin moments in the sample drives resonant precession about the axis of the bias (Zeeman) field when the resonance condition is met, as discussed in chapter 2.

The co-planar waveguide serves as a sample mount within the FMR spectrometer, as well as transmitting the RF signal. The CPW used in this thesis is shown in figure 4.8. Samples under test are mounted directly onto the centre of the waveguide with the sample face in direct contact with the stripline, in order to maximise the coupling between the sample magnetisation and the RF field induced by the current flow through the stripline. This is known as the 'flip-chip' geometry [200]. Since the RF magnetic field used to excite the FMR decays with the square of the distance from the stripline, the closer the sample can be mounted to the stripline, the greater the field magnitude felt by the magnetisation, and therefore the magnitude of the RF excitation is increased. This in turn leads to a larger observable absorption of the RF, which induces the characteristic FMR curves discussed in chapter 2. These curves can then be fitted to extract important magnetic parameters, as previously discussed.

It should be noted that the alignment of the sample on the CPW is performed by eye: a small deviation is therefore be expected between the exact angular position of each sample that is mounted. However, since the turntable can be rotated with a 0.25 degree resolution, this offset can be compensated for in repeated measurements. The horizontal alignment of the CPW was confirmed using a hand spirit level after each modification to the sample mount, to ensure the CPW remained level and parallel to the axis of the applied magnetic field. In the event of misalignment, a tilted CPW would lead to the sample being tilted and the resulting magnetisation being tilted out of the plane of the sample (and therefore not a true representation of the in-plane anisotropy of the magnetic free energy surface). In the event of a misalignment between the sample plane and the bias field (of angle ψ), the field component acting to drag the field out of the sample plane is $\boldsymbol{H}\sin(\psi)$, which for a 1 degree misalignment in a field of 0.5T = $0.5 * Sin(1) = 87\ Oe$. At the maximum measurement field used in these experiments, **H** = 0.3T and

this out-of-plane component is reduced to 52 Oe. The out of plane component is significantly smaller than the shape anisotropy term ($4\pi\mathbf{M}_s$, where $\mathbf{M}_s$ in these samples alone is 450emu cc^{-1} or greater) which acts to keep the field in the sample plane. It is therefore reasonable to assume that, even in the event of a small misalignment, **M** remains parallel with the sample plane. This method relies on the sample face being electrically insulating for best results, since conduction of the RF signal away to the ground plane of the CPW will cause losses. In extreme cases, the signal can be shorted across the ground plane of the waveguide. These losses are typically observed as a strong dispersive component in the FMR measurement. This can be prevented by separating the sample face from the waveguide but any barrier must be very thin. Typically the separation of these layers is achieved by introducing a layer of insulating PTFE tape between the sample and the CPW. A single layer is used in order to maximise the FMR response and to eliminate the conduction. All of the data presented in this thesis was measured using either a single layer of PTFE or no barrier layer due to minimal surface conductivity.

4.4 RF Generation Methods

An RF signal generator is required in order to provide the RF field which drives the precessional behaviour. Two different methods are commonly used for this, depending on the FMR measurement technique being employed. One option is the use of a Vector Network Analyser (VNA) connected across the waveguide, providing rapid access to broad-band spectra over a wide range of frequencies that are measured by comparing the input and output signals known as S-parameters [167]. The other option is to generate a fixed frequency output using a standard RF signal generator and apply a modulation field in order to measure the FMR response using a lock-in technique [169,201]. Since the input and output connectors of the RF line in this sample mount are freely accessible SMA ports, either method can be used. Both a Rohde and Schwarz ZNB20 Vector Network Analyser and a Rohde and Schwarz SMB100 variable output Signal Generator are available for use with this FMR spectrometer, allowing operation in either VNA-FMR or Modulation-FMR mode. In both modes of operation, any SMA connectors that are not part of the transmission line are capped with a 50-Ohm blank to prevent both reflections from and interference with the RF signal.

Both measurements show agreement in fitted data recorded from permalloy test samples and can therefore be considered equivalent. Data acquired using both of these methods will be presented in the following chapters of this thesis.

4.4.1 The VNA-FMR Technique

A Vector Network Analyser can be used to induce FMR in magnetic samples as discussed in section 3.2.2.1. By passing the output signal from the VNA through the stripline on the CPW, this signal can be used to induce an AC RF field which propagates parallel to the direction of the waveguide and oscillates perpendicular to the direction of propagation. This field can be used to drive FMR oscillation in a ferromagnetic sample by coupling with the magnetisation and inducing resonant precession of the magnetisation when the RF signal oscillates at the frequency matching the Larmor frequency, as discussed in chapter 3. This resonant behaviour is dependent on the absorption of the RF, which causes attenuation of the RF current passing through the CPW: this attenuation is observed in the VNA trace as a minimum in the difference signal between the input

and output ports at a given frequency. This leads to a characteristic absorption peak (trough) in the VNA output which is proportional to the magnitude of the FMR oscillation.

The VNA can be used to sweep over a range of RF frequencies and record the S_{21} signal (as discussed in section 3.3.2.1) as a function of RF frequency. Changing the applied field and repeating the frequency sweep allows a series of these traces to be displayed side-by-side to construct a map of the attenuation intensity as a function of both the applied RF frequency and the bias field. In a ferromagnetic material, this frequency-field map will display a distinctive Kittel curve, as discussed in section 2.5.3. In single crystal ferromagnetic structures, a single ferromagnetic resonance and its higher order modes are expected to occur [202]. It is therefore possible to observe a single Kittel curve at a sufficiently low bias field range. However, higher order modes of the oscillation should also emerge in the field frequency map if the field and frequency ranges are sufficiently increased. In multilayer structures, the field-frequency map can become more complex as the acoustic and optical modes of multilayers can be observed. For the purposes of this thesis, only single crystal samples have been investigated, and it is therefore expected that only single Kittel curves will be observed for each sample.

When the system is operated in the VNA-FMR mode, a pair of Atlantec ACW-CA18 semi-flexible cables connect the SMA bulkheads atop the spectrometer system to a Rohde and Schwarz ZNB20 Vector Network Analyser. The VNA acts as an RF source for the VNA-FMR operation mode. This model provides access to a frequency range between 100kHz and 20GHz in a customisable range of frequency steps. The data presented in the following chapters of this thesis uses either 801 or 1001 steps in frequency to provide high resolution frequency datasets. Typically each VNA sweep takes several seconds to scan over the whole frequency range. In order to improve the signal-to-noise ratio in the data, a series of 8 to 10 averages of each VNA sweep were taken at each field step. For a full series of sweeps over a 3.5kOe range in 20Oe steps, with a single reference at a fixed angle, around 20 minutes is required. This makes general measurement using this technique very fast. Higher resolution datasets can be recorded by increasing the number of frequency steps or decreasing the field increment, though this increases the time required to record a complete dataset. The increased time requirement also increases the risk of drifting from the original reference due to local environmental fluctuations such as temperature. Since each VNA scan can be completed quickly, it is practical to take a series of successive datasets at each angle and average them in order to reduce the effect of these fluctuations. For the data presented in this thesis, each VNA dataset was averaged over seven to ten scans. As discussed in chapter 3, the extraction of useful magnetic parameters including the resonance field ($\mathbf{H}_r$) and the linewidth ($\Delta\mathbf{H}$) from the VNA-FMR data is achieved by fitting the absorption curve using an asymmetric Lorentzian function as discussed in section 3.3.2.1.

In order to maximise the intensity of the FMR effect in this operation mode, the RF output from the VNA was set to the maximum possible output over the complete frequency range: all of the VNA-FMR data presented in this thesis was driven using an RF power of +8dBm. While the VNA-FMR technique is practical in terms of speed, it is limited by the sensitivity of the VNA. In the case of samples with low-intensity FMR responses, for example thin-film metal oxides or deposited nanoparticle systems, the VNA technique often lacks the sensitivity for reliable extraction of useful magnetic parameters. In order to examine this type of system, a different technique is

required. Typically, increased sensitivity can be obtained using a modulation technique and measuring using a lock-in amplifier.

4.4.2 The Modulation FMR Technique

The most common technique used in FMR Spectroscopy is to apply a low-intensity AC modulating field oscillating parallel to the bias field and measuring the response of the magnetisation using a lock-in amplifier [169,201,203] The lock-in technique requires similar experimental equipment to the VNA-FMR, with a few minor changes.

As in the VNA-FMR technique, the FMR precession is driven using an RF signal applied along the CPW stripline and inducing a corresponding magnetic field perpendicular to the plane of the CPW. However, in this technique the RF signal is provided using an R&S SMB100A variable signal generator operating at a fixed frequency. The signal detection is also performed differently. The modulation coils are driven using a fixed output supplied by a Stanford Systems SR830 lock-in amplifier and amplified by a audio power amplifier. The lock-in is also used to measure the FMR response in this operation mode. These coils are used to drive the AC modulation field as described in section 3.2.2.2.

Since the change in susceptibility in the waveguide is constant regardless of the field, it is eliminated. The change in susceptibility ($d\chi/d\boldsymbol{H}$) is maximised when the gradient is largest, either side of the Lorentzian peak. The first derivative of the resonance absorption is therefore observed as two peaks in the data either side of $\mathbf{H}_r$. The driving signal is also used as a reference signal for the lock-in. This is used to eliminate the first term in the expansion, which is static with the field. The second term oscillates at the driving frequency of the amplifier and is therefore detected. This change is proportional to the AC susceptibility and can be fed into an Atlantic Microwave zero-bias Schottky Diode rated between 10MHz and 18GHz. The diode converts the signal into a voltage which can be measured by the lock-in amplifier.

The lock-in amplifier is capable of measuring signals at a fixed reference frequency and disregarding non-matching frequencies in a process known as *phase-sensitive detection*. This allows the lock-in to isolate signals at the specified frequency and eliminate other frequencies which might otherwise induce noise in the measured data [204]. A reference frequency provided by the built-in signal generator is passed into the lock-in amplifier to establish the measurement frequency. An input signal, measured from the FMR experiment, is then multiplied by the lock-in reference and filtered, allowing the amplifier to phase-lock the measurement to the reference signal. As long as the phase of each signal remains consistent, multiplication of the two signals returns a single signal

$$V_{PSD} = \frac{1}{2}V_{sig}V_{LIA}\left(\cos\left([\omega_{ref} - \omega_{LIA}]t + \beta_{sig} - \beta_{ref}\right) - cos\left([\omega_{ref} - \omega_{LIA}]t + \beta_{sig} + \beta_{ref}\right)\right) \quad (4.1)$$

Where V_{PSD} is the Voltage detected by the phase-sensitive detector, ω is the angular frequency, β is the phase, and *sig*, *ref* and *LIA* denote that parameter originates from the input signal, reference signal and lock-in respectively.

This produces two AC voltage outputs in the phase-sensitive detector at frequencies ($\omega_{ref} - \omega_{LIA}$) and ($\omega_{ref} + \omega_{LIA}$). A low-pass filter is then applied, removing the AC components and setting to zero

everything that doesn't meet the condition ($\omega_{ref} = \omega_{LIA}$): when this is true, a non-zero DC output, isolated in frequency, is produced with an amplitude proportional to that of the input signal.

The entire FMR response signal is directed into one of the two lock-in channels, designated 1 and 2, which are set to record datasets in X and Y. In a lock-in with 2 phase-sensitive detectors, the second detector multiplies the input signal by the reference signal with a +90^o phase shift. This results in two channels with unique phases (β_1 and β_2.) The output of each channel is given by

$$X = V_s \cos(\beta_T) \tag{4.2}$$

$$Y = V_s \sin(\beta_T) \tag{4.3}$$

where V_s is the input signal voltage and β_T is the difference between the phase of the input signal and the phase of the lock-in. By setting the lock-in phase to match the input signal phase, β_T becomes 0, maximising X and minimising Y. This therefore shifts all of the signal into the X channel (in this case, channel 1). The phase required to accomplish this is affected by modifications to the FMR spectrometer which alter the RF transmission line.

The measured signal from the FMR returns a bipolar lineshape which is the first derivative of the AC susceptibility, as discussed in section 3.2.2.2. Data recorded from the modulation-FMR technique can be fitted to extract information about the resonance field and linewidth parameters. In this technique, the fit is accomplished using the equation 3.18. The fitting of modulation FMR data can therefore be used to measure the same parameters as the VNA-FMR technique, in particular the resonance field and the linewidth. As discussed in section 3.3.2.2, the y-axis amplitude of the modulation FMR data is arbitrary since the $\mathbf{H}_r$ and $\Delta\mathbf{H}$ parameters are relative only to the magnetic field (X) axis. The sensitivity of the lock-in amplifier can therefore be tuned at will to return the maximum signal to noise ratio. For the purposes of this thesis, the sensitivity of the lock-in has been set individually for each sample to return the maximum signal amplitude at ϕ = 0^o, and then held constant, allowing easy comparison between individual datasets.

The modulation technique provides a considerable increase in sensitivity over the VNA-FMR technique. This allows the measurement of materials with less intense signals. The use of the modulation field also makes the technique less susceptible to local environmental variations. However, it should be noted that this technique can only be used at a fixed frequency and therefore extracting frequency dependence information takes a series of sweeps over a range of frequencies. This method of taking data is therefore very time consuming compared to the VNA-FMR.

4.5 Equipment Calibration

Finding a maximal output from the coils was important to ensure efficient operation of the spectrometer in the lock-in mode. The modulation frequency was kept away from harmonics of 50Hz in order to eliminate the effect of mains noise in the system. By recording the modulation field strength as a function of input frequency, it was observed that a modulation field of 0.800 ± 0.005 Oe was achievable using these coils, as observed in figure 4.9. For the operation of the modulation coils in this experiment, a frequency of 83Hz was chosen. It is observed that this is not the peak field output (which occurs at 43Hz). This frequency was chosen to be sufficiently far from

a mode of the 50Hz mains frequency as to eliminate mains noise from the equipment. It was observed that long-term operation of the coils was possible at a maximum amplification of +46db (in dual channel mode) which corresponds to a modulation field of 0.350 ± 0.005 Oe at 83Hz. This field was observed to induce sufficient oscillation in χ(t) to measure the FMR using the lock-in technique and is similar to the modulation fields used in other FMR spectrometers [201]. This frequency was therefore chosen to be standard for the data presented in this thesis. The modulation field must be applied with care: If the modulating field is too large, the resonance linewidth may be broadened, rendering the measurement inaccurate. In the case of very sharp resonances, a large modulation field could remove the resonance peak during the averaging process. If the modulation field is too small, the variation in χ(t) is minimal and the technique lacks sensitivity.

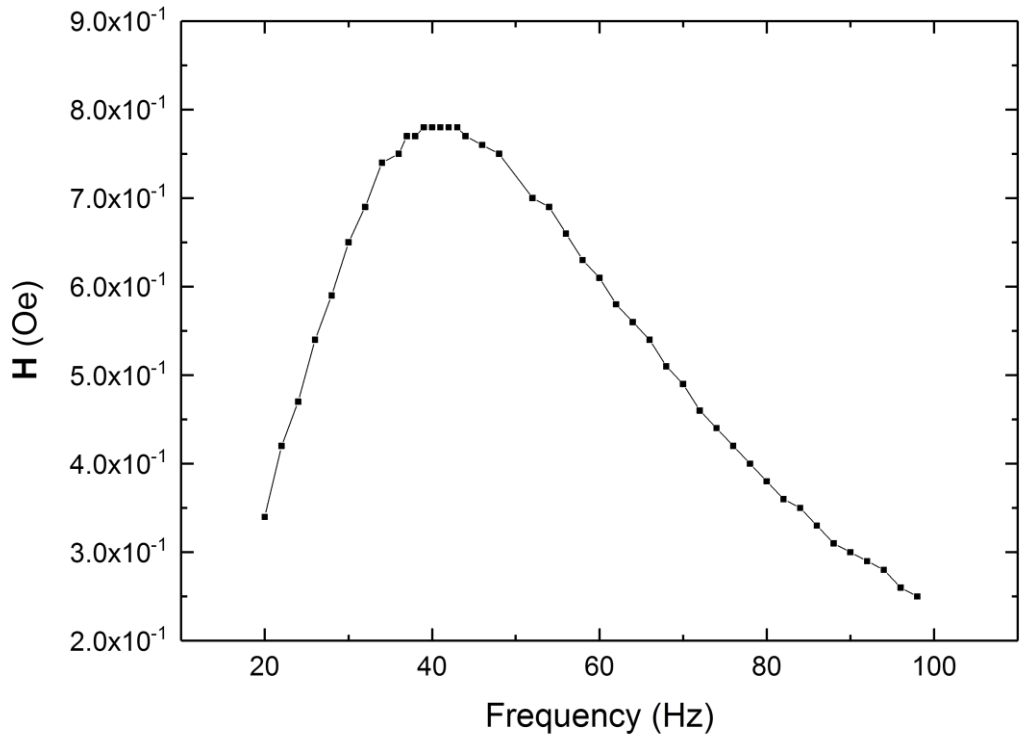

Figure 4.9. *A calibration curve showing the AC field output of the modulation coils as a function of input current at low-amplification output from the EP2000 signal amplifier*

The time constant (t_c) of the lock-in amplifier also required optimisation, since the oscillating response must be measured over a sufficient number of periods to record accurate data. t_c is directly related to the cut-off frequency of the amplifier, so it determines the bandwidth of frequencies accepted. A larger t_c helps reduce noise, but also makes the amplifier slower to respond to changes in the signal, which can manifest as the shifting or broadening of resonance peaks in the FMR. After repeated testing of the permalloy test sample using a range of different time constants (figure 4.10), it was determined that t_c = 1s was sufficient to acquire accurate data,

but short enough to allow for measurements to be completed within a reasonable time frame. The sensitivity of the amplifier was also adjusted to yield the maximum data amplitude without the signal exceeding the range of the amplifier and clipping. For the data recorded in chapters 5 and 6 of this thesis, and the corresponding background scans the appropriate sensitivity setting was found to be 50 microvolts. This setting was modified for the test samples presented in the rest of this chapter to account for the much larger signal amplitudes. Changing the sensitivity only scales the amplitude of the signal response and has no impact on the $\mathbf{H}_r$ or $\Delta\mathbf{H}$ parameters.

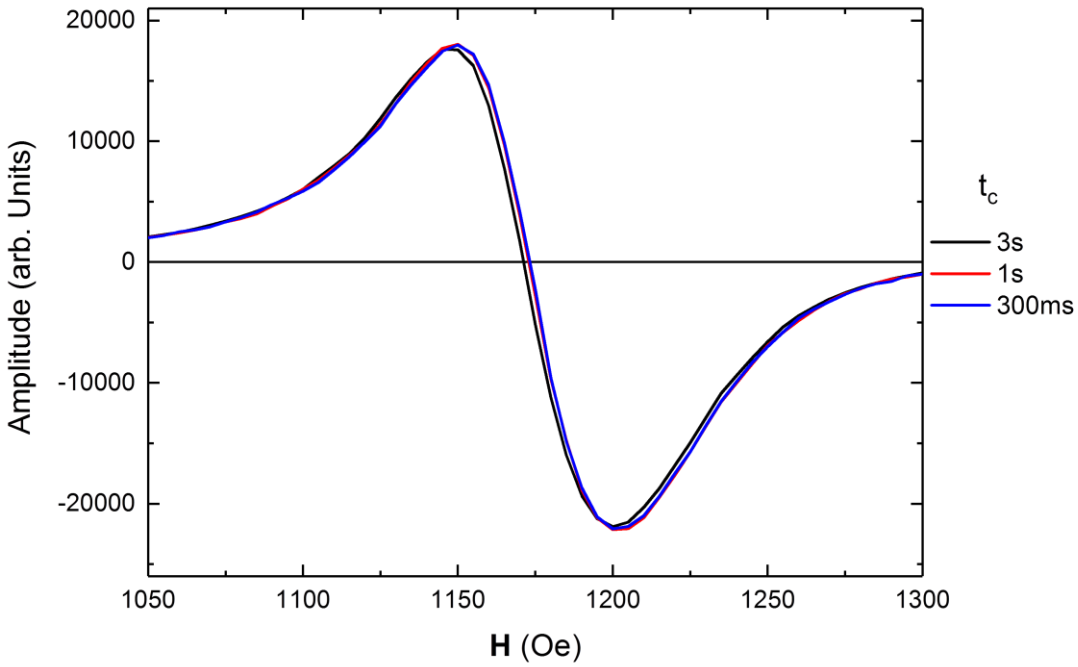

Figure 4.10 *Calibration curve showing modulation FMR resonance from a Py/MgO test sample at a fixed frequency of 10GHz as a function of varying lock-in amplifier time constant settings*

In order to increase the modulation field, the signal driving the modulation is amplified by passing through a Europower EP2000 signal amplifier. The EP2000 is operated in dual channel mode in order to increase the signal amplification. When sufficiently cooled, the amplifier can reliably operate for long periods at +24dBm in dual channel mode, effectively amplifying the signal by +46dBm. While the amplifier does offer higher amplification, the operation of the device for longer than an hour above +24dBmin dual channel mode leads to the device overheating and cutting out. While the internal safety features prevent damage to the amplifier in these circumstances, the data collection is significantly interrupted.

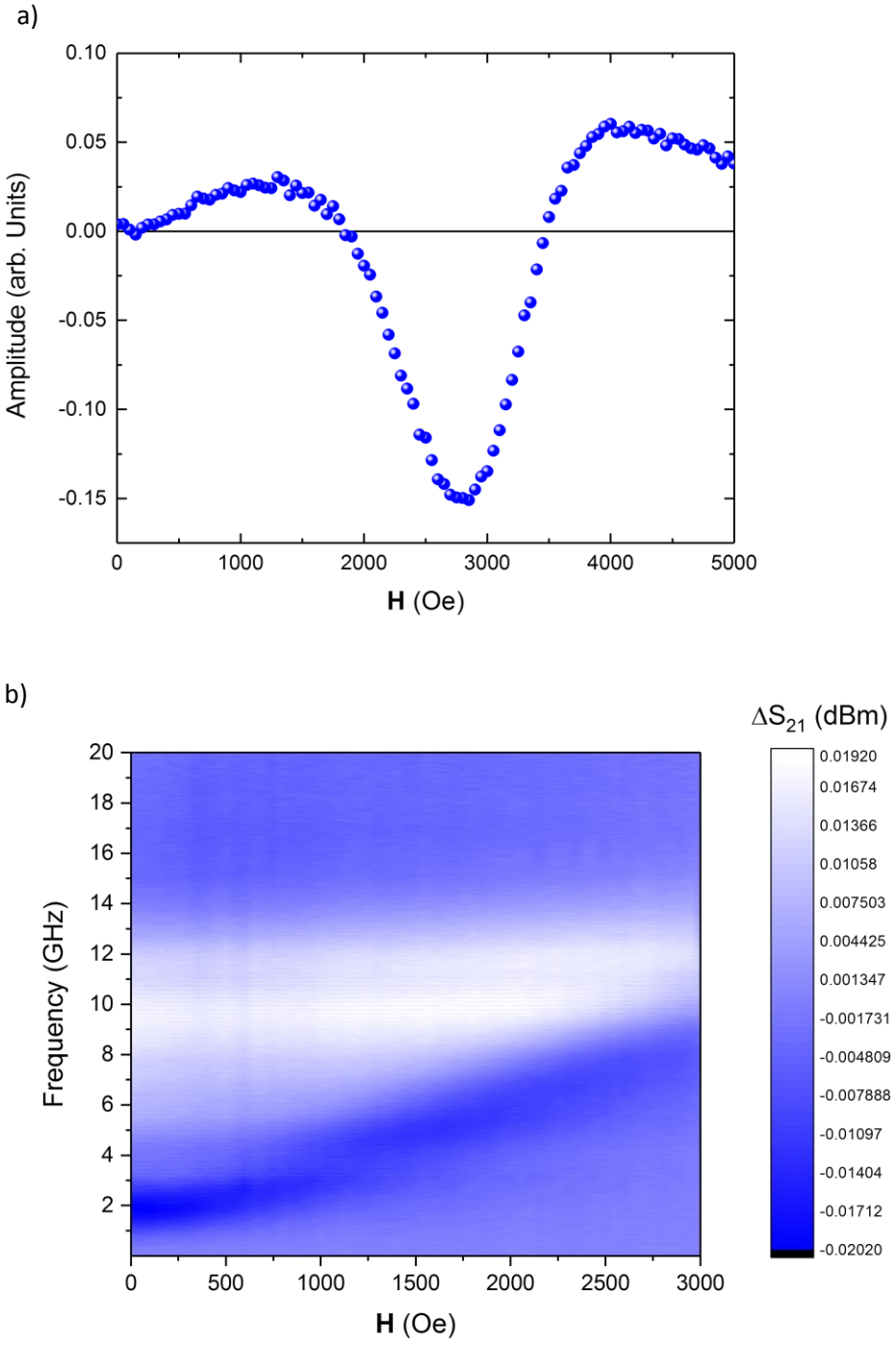

Figure 4.11. *A measurement of the background FMR signal from the empty CPW measured in a) modulation FMR mode and b) VNA-FMR mode*

Measurements of the FMR from the empty CPW were taken to provide background measurements. In an ideal case, this background would be flat since no ferromagnetic response would be present. However, in the initial background measurements it was found that a small magnetic response comes from within the CPW (figure 4.11). Further investigation revealed that the pins in the right-angled SMA connectors were magnetic: this is due to the nickel component used in binding the gold plating to the pins. Therefore, for all subsequent measurements using

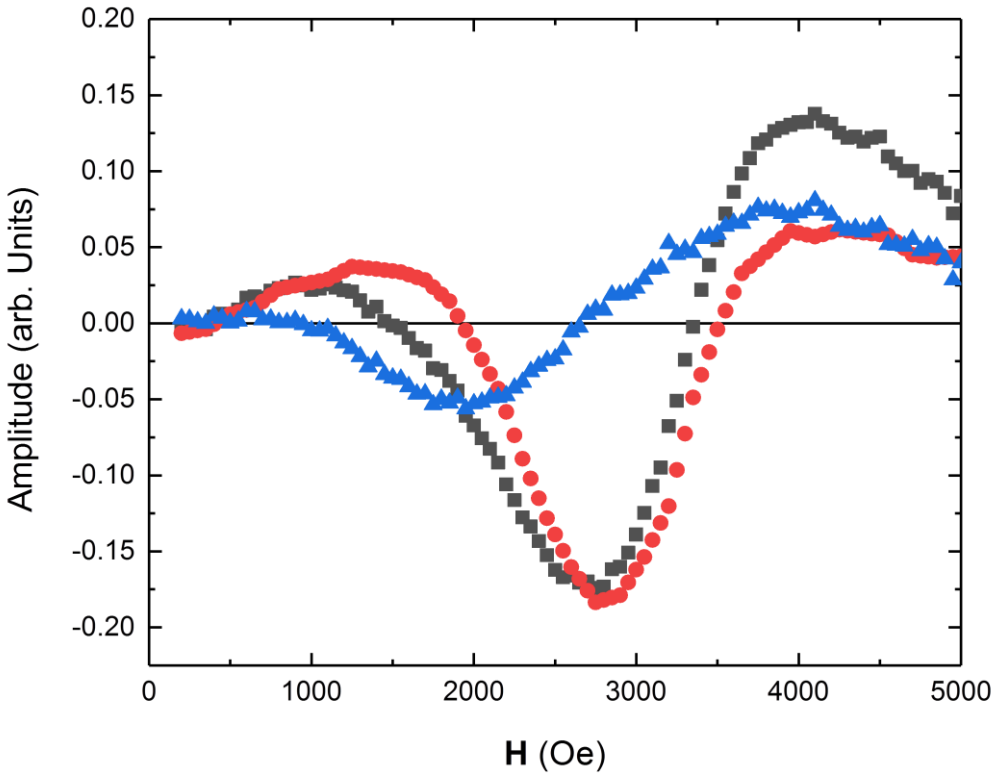

Figure 4.12. *An example of low-intensity FMR signal responses measured from Fe_3O_4 using the modulation FMR mode. The raw data (black) is similar in magnitude to the background (red) and therefore the FMR response (blue) can only be extracted for fitting by background subtraction*

this waveguide, the background response would need to be subtracted from the measured total response in order to isolate the FMR measured from the sample. While the background was found to be a small intensity signal relative to high-moment ferromagnetic thin film samples, in the case of low-moment materials such as metal oxides, the background signal could be of comparable magnitude. This is demonstrated in figure 4.12.

Over the course of taking measurements from the FMR spectrometer, it was necessary to switch between the two operating modes. It was therefore important to ensure consistency between the sets of data measured by measuring ΔS_{21} as a function of RF frequency at zero-field each time the equipment was modified. Some small variation due to environmental factors was expected, but it was possible to reconnect the equipment consistently by checking this sweep and adjusting the connectors until the trace was identical to those measured previously. Differences in the initial trace were observed to be the result of SMA connectors connected slightly differently each time. By careful modification of the connectors, the state of the system could be adjusted to match the previously observed state. Other SMA connectors in the system were also periodically checked for tight connections.

4.6 Test Sample Measurements

In order to test the accuracy of the spectrometer, a 5mm x 5mm x 20nm thin film of permalloy grown on MgO(001) was used as a test sample to record and fit FMR measurements. Initially, a single FMR sweep was measured using the lock-in technique at a fixed frequency of 10GHz. After ramping the bias field to 5kOe in order to saturate the sample, the resonance point was located using a broad scan in large field steps (50Oe). A second field sweep over the field range of interest, between 1350Oe and 900Oe was recorded in 10Oe steps and a clear bipolar lineshape effect was observed which is characteristic of FMR behaviour in the lock-in technique. The data is shown in figure 4.13. Fitting to this data using equation 3.18 returns H_r = 1177 ± 25 Oe and ΔH = 44 ± 4 Oe; this is consistent with the observations of Zhao *et. al.* [205]. Given that the observed data is consistent with previously observed values (within error), this suggests that the spectrometer is functioning as expected. A series of FMR measurements from this test sample were also recorded over a range of azimuthal angles (Φ) in order to determine the practicality of assessing in-plane anisotropies using this spectrometer. The same sweep was repeated at a fixed frequency of 10GHz over 10 degree steps between +90 and -90 degrees in order to track how the resonance field shifts as a function of the angle. The data is presented in figure 4.14. A four-fold anisotropy is clearly observed in the resonance field, reaching a minimum every 45 degrees. This is consistent with results from epitaxially grown Py/MgO observed in the literature [206], in which the normally isotropic behaviour in permalloy is overcome by the cubic ordering arising from the epitaxial growth on the MgO(100) substrate. In line with symmetry in the crystal structure, the data is repeated to complete the 360 degree plot of the anisotropy in the Py crystal structure. The amplitude of the oscillation reduces as the angle between the RF and bias fields is reduced and the corresponding torque on the magnetisation decreases.

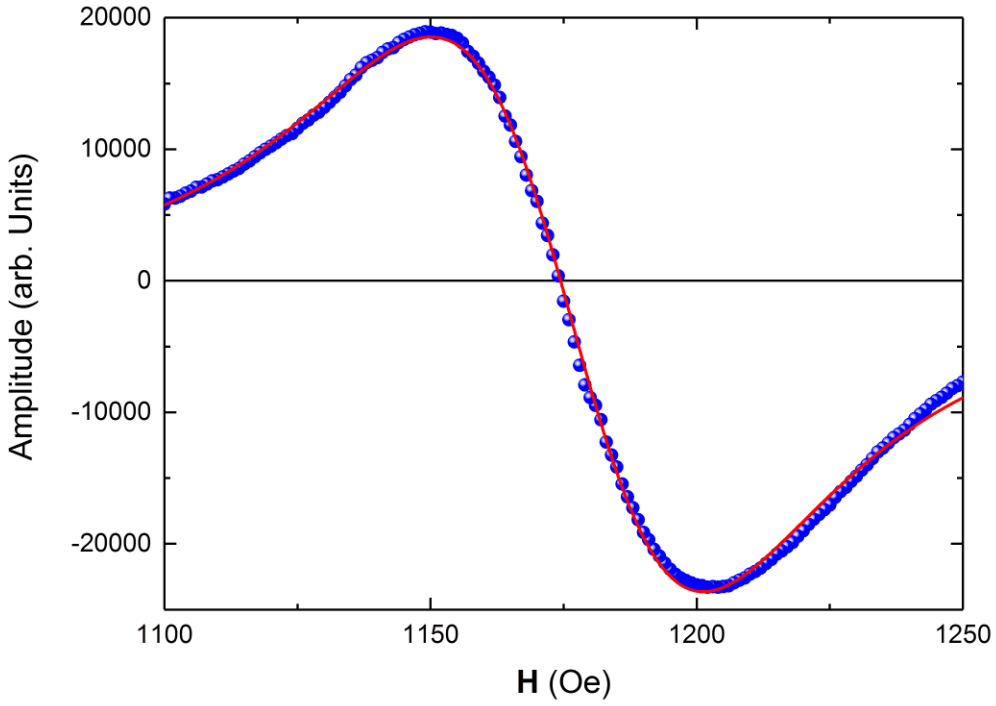

Figure 4.13. *Modulation FMR from a Py/MgO test sample at a fixed frequency of 10GHz*

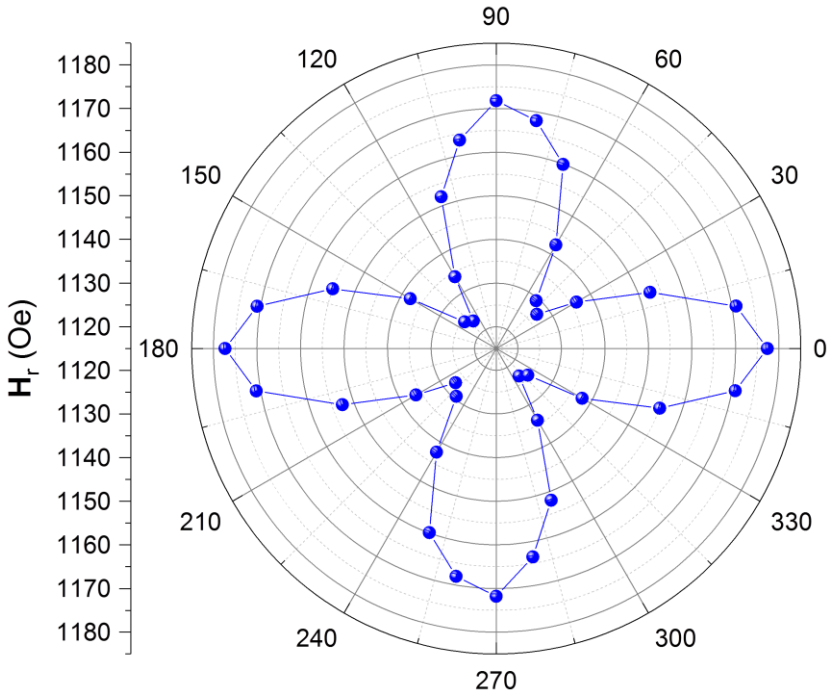

Figure 4.14. *Modulation FMR from the permalloy test sample at a fixed frequency of 10GHz over a range of azimuthal angles (ϑ) relative to a perpendicular configuration between the bias field and the applied RF field*

A second thin film sample of epitaxially grown Ni on V_2O_3 was tested, which also yielded a good FMR response in the lock-in measurement scheme at a fixed frequency of 10GHz. Fitting the data from this sample (not shown) returned values of $\mathbf{H}_r$ = 1460 ± 20 Oe and Δ**H** = 220 ± 3 Oe, which is consistent with previously measured Ni thin films in the literature [207]. As with the permalloy sample, the close matching between our linewidth measurements and those observed previously show that the spectrometer is measuring the FMR behaviour correctly.

It should be noted that the actual value is strongly dependent on the film quality and therefore will be affected by the sample growth conditions and any post-growth effects such as oxidation in ambient conditions. It was therefore important to keep samples under vacuum in a desiccator while not under measurement using the FMR spectrometer. Capping sensitive samples with thin (2-5nm) layers of non-magnetic material such as aluminium or gold can also prevent this while still allowing the FMR to be induced.

In order to ensure reliability, a series of measurements were run on a permalloy test sample under repeated conditions (f = 9GHz, 1500Oe pre-ramp, 1500 ≥ **H** ≥ 800 Oe, 50 Oe steps) and then plotted together for comparison. It was found that these repeated scans were consistent with each other and that fitting of the repeated scans returns a value for the resonance field which appears to vary on the order of 10Oe. This is much smaller than the step size and must therefore be considered within the appropriate error. Given that the step is 50Oe, it can only be considered to be accurate to within 25Oe. A series of five of these scans are shown for reference in figure 4.15. The observed deviation is attributed to a combination of the resolution of the measurement device and fluctuations in the spectrometer system resulting from variations in the local temperature.

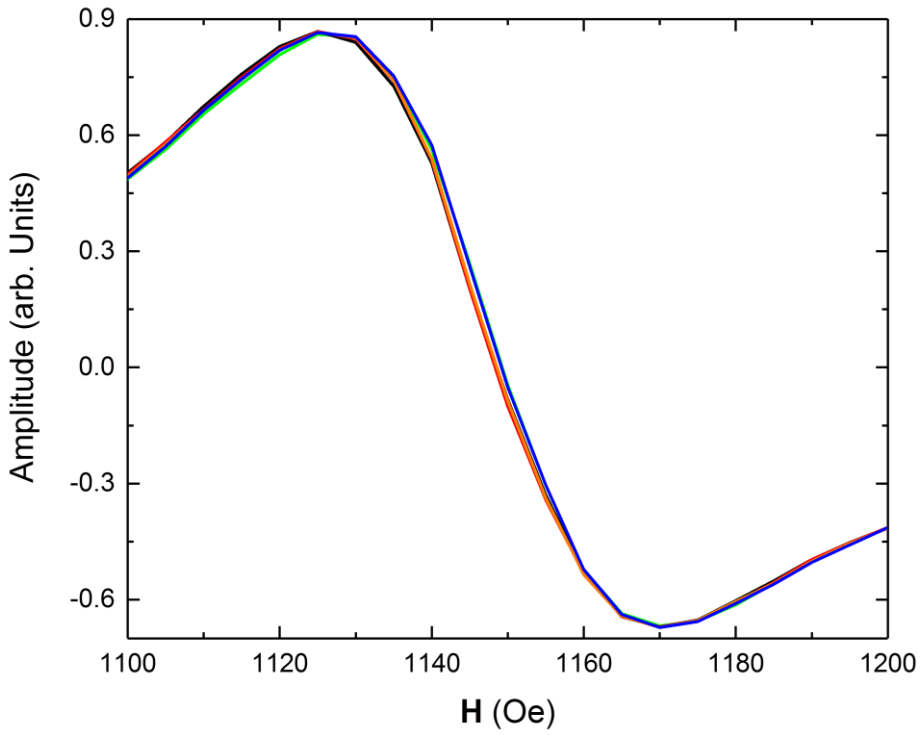

Figure 4.15. *A set of 5 subsequent modulation FMR scans from a Py test sample at 9GHz. Good overlap between subsequent scans shows that the data is repeatable*

Measurements of a CFAS test sample were then performed using both the modulation FMR and the VNA-FMR techniques in order to check for agreement between the two methods. Using identical test parameters, sweeps over the uniform resonance mode were performed. These measurements were performed at a fixed frequency of 10GHz over a range of 0 to 5kOe in steps of 20Oe (10Oe on the modulation FMR). The overlap between these two sweeps is shown in figure 4.16.

From the VNA-FMR data, fitting returns $\mathbf{H}_r$ = 788 ± 10 Oe and Δ**H** = 25 ± 10 Oe and the modulation FMR data fit shows that $\mathbf{H}_r$ = 790 ± 5 Oe and Δ**H** = 30 ± 1 Oe. Since these datasets are within error and have been observed to be repeatable, good agreement is observed between both operational

modes of the FMR spectrometer. As such, any data recorded in one mode can be relied upon in the context of the other. For example, a quick sweep in the VNA-FMR mode can be used to locate resonance behaviour quickly in a field-frequency map. In the case where the resonance has a small amplitude or broad linewidth, a more sensitive dataset can be measured in the modulation FMR scheme over the corresponding range.

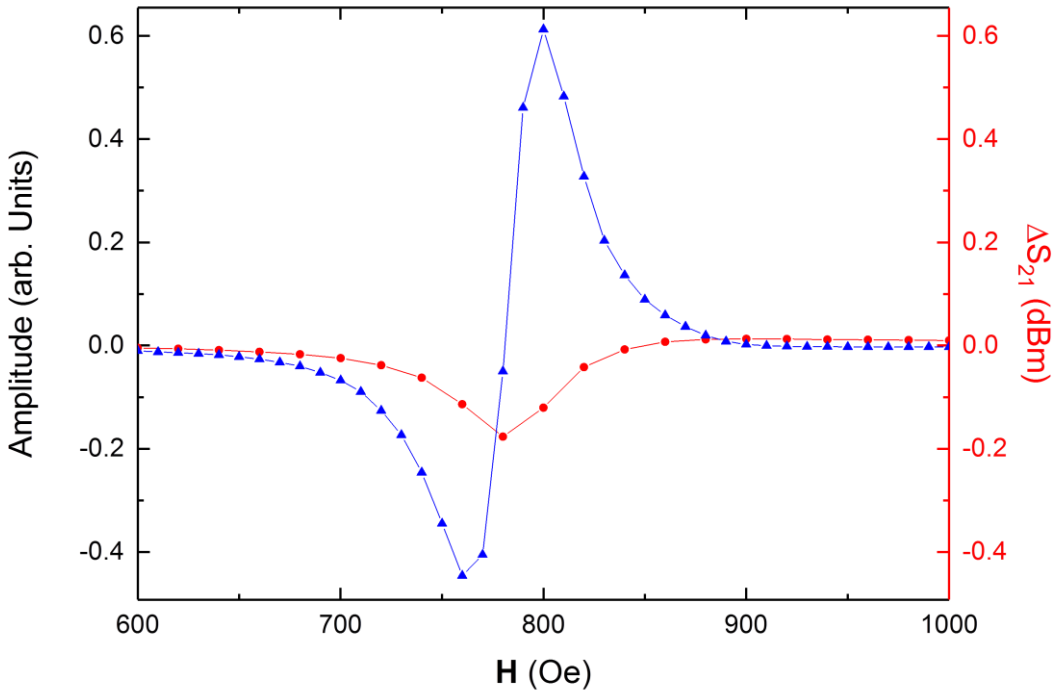

Figure 4.16. *A modulation FMR dataset (blue) at 10GHz fixed frequency compared with corresponding VNA-FMR linescan (red). These scans overlap closely at H_r, showing consistency between data collected in both operation modes*

4.7 Spectrometer Control Program

Control of the FMR Spectrometer system is made possible using frontend software developed by the author in LabVIEW (National Instruments' LabVIEW 2014 v14.0.1, Service Pack 1). Due to the differences in measurement equipment, a separate control program was developed for each of the two operational modes of the FMR Spectrometer.

A control PC was connected to the spectrometer system and used to interface with the equipment using serial VISA software communication. In both modes of operation, a National Instruments MyDAQ unit is used to control the field output using digital voltage output scaled between 0 to +10V. This voltage is fed into the power supply control unit and used to control the current output to the electromagnet coils. The PC is also connected to the PM600 control card by a USB to RS232 cable. The control programs can be used to pass data strings containing commands to the PM600 unit, which facilitates the rotation of the magnet turntable.

In the VNA-FMR mode, the VNA is connected to the PC by a LAN cable and interfaces with LabVIEW using a modified control program based on VI programs provided by Rohde and Schwarz. In the modulation FMR mode, the lock-in amplifier and signal generator are both controlled by serial communication, facilitated by RS232 outputs. An independent program was written to allow users to interface with the signal generator in isolation, setting the signal frequency and level of the RF output.

Each control program consists of a complete set of input and output operations, allowing the setting of measurement parameters and the recording of data to text file outputs for later analysis. Analysis of this data was then undertaken using a combination of manual assessment in Originlab's Origin 9.1 and using a customised code written in C, compiled using Cygwin.

External control of the spectrometer is made possible by logging into the PC via remote desktop. A webcam is also connected to the PC, overlooking the spectrometer. A check can therefore be kept on the system during long periods of operation, even from off-site. An overview of each of the LabVIEW control scripts can be found in Appendix A at the end of this thesis.

4.8 Further Development

Over the course of this project, a high-resolution FMR spectrometer has been developed for extracting magnetic damping parameters from ferromagnetic thin film samples. However, further improvements to the spectrometer are planned in order to improve functionality and increase the sensitivity when measuring very small signals. A Pasternack PE 4803 circulator has been purchased for connection in the RF through-line during operation in the lock-in mode: the circulator provides a three-way connection where RF signals can be passed one way through the circuit, but cannot be reflected back down the same path. It can therefore be introduced to the spectrometer to prevent the reflections from the circuit from affecting future measurements. This will be connected in the RF circuit after the signal generator in order to reduce the effect of RF reflections in the system which would otherwise damage the signal generator. Even broad-band circulators are still limited in their frequency range, however: the PE 4803 is limited to between 7 and 12.4GHz, so the suppression of reflections may be less effective when the RF driving frequency is set outside this range.

The replacement of the SMA connectors of the CPW with non-magnetic connectors is planned in order to reduce or remove the background signal. If entirely non-magnetic right-angled connectors can be employed, the small magnetic signal observed in background measurements should be removed. This would then eliminate the need to perform the background subtraction and therefore speed up the analysis of data recorded using the FMR spectrometer. The replacement of the waveguide would require the VNA to be recalibrated. Changes in the experimental hardware, especially in the RF path will inevitably affect the measurements from the spectrometer. Data recorded after the modifications is therefore expected to be incompatible with those recorded beforehand. Small differences within the waveguide may also shift the phase of the RF through-line, requiring the phase of the lock-in amplifier to be adjusted in order to isolate all the FMR signal on-resonance in a single channel.

Increasing the sensitivity of the spectrometer would provide both improved resolution in FMR measurements and access to samples with smaller intensity FMR responses. For example, it has

been observed that while strongly ferromagnetic thin films give excellent results in the current spectrometer, the low-intensity response observed in weakly ferromagnetic metal oxides with high damping losses gives a very small response: large damping inhibits the precessional behaviour of the magnetic moment and therefore significantly reduces the measured FMR signal. Sufficiently large damping can therefore reduce the signal intensity to levels where it becomes undetectable.

The subsequent background subtraction risks loss of resolution in an already small signal. It has been observed that any response from nanoparticle samples deposited on substrates is too small to observe, even after background subtraction. The easiest method of increasing the spectrometer sensitivity is to increase the quality factor (Q-factor) of the spectrometer: one way to achieve this is to replace the waveguide with a high-Q RF cavity resonator.

While mounting a cavity would improve the Q-factor considerably, it should be noted that this modification brings up some other changes which must be considered. A resonant cavity is specifically designed to operate at a fixed frequency (and higher harmonics of that frequency) rather than over a broad range of frequencies. This would therefore remove the ability to use the broadband technique offered by the CPW, and therefore eliminate access to the damping information offered by taking measurements over a range of frequencies. The construction of a number of cavities, optimised to a range of RF frequencies, would allow access to this information, though the replacement of the cavity after each experiment would make the experimental process very time consuming. A test cavity has been designed with a Q-factor of 6000 at a frequency of 9.8GHz. It is intended that this cavity be mounted in place of the CPW and FMR measurements made on a range of samples. A comparison with the samples discussed in this thesis would be useful for assessing the improvement of the Q-factor between the CPW and the cavity. Measurements of a series of Fe_3O_4 nanoparticles are planned if the improvement in sensitivity improves the FMR signal to a measurable intensity.

Another possible approach might be to use a CPW with a built-in half-wave resonant cavity, though this would also have the effect of narrowing the bandwidth of the CPW to the region in which the resonator is effective. This technique could improve the sensitivity considerably over the effective frequency range, though it would require careful planning, or a series of waveguides designed for operation at fixed frequencies, in order to take complete frequency-dependent datasets. It should also be noted that the need to continually replace the waveguide and perfectly realign the sample within the system is an added complication in this system, and the additional time investment in each frequency sweep would be considerable.

Despite the precautions taken to minimise the variation in temperature, it has been observed that the FMR data can still be affected by temperature variations. This is particularly evident in VNA-FMR scans of over an hour's duration, since some fluctuation of the background around the baseline is observed in the VNA trace. In order to further limit the effect of this drift, it is planned to introduce a calibrated Hall probe to the system in order to record the actual strength of the magnetic field rather than the nominal field. By connecting a Bell Gauss BH-700 Hall sensor within the magnetic field and recording data using a Keithley 2400 series sourcemeter, a voltage output can be measured which is proportional to the magnetic field. This voltage value can then be

converted, using a calibrated conversion factor, into the actual field value. This will provide greater accuracy in the field value recorded in future FMR scans.

Further modifications to the control programs are planned, although these are largely quality-of-life improvements rather than changes in functionality. For example, updates to the indicators are planned to improve the precision and timing of their output. A variable wait time is also planned in order to allow the modification of field wait times during operation, intended to make scans with multiple references more time-efficient.

Chapter 5: Fe_3O_4 on YSZ(111)

5.1 Introduction

One of the first known magnetic materials, magnetite (Fe_3O_4) is still relevant today for its potential application in next generation electronic devices. Its high Curie temperature (858K) [77,208,209] and predicted 100% spin polarisation at the Fermi level have brought a lot of attention to the potential application of magnetite in spintronic devices. The lattice constant of magnetite is 8.396Å [107,210,211], which is approximately twice that of industrially relevant substrates such as MgO (which has a lattice constant of 4.12Å) [107,211]. Despite this, Fe_3O_4 shows a good epitaxial matching to technologically relevant semiconductor substrates, such as GaAs, MgO and Al_2O_3. However, optimising Fe_3O_4 has proven to be difficult, and non-bulk effects such as non-zero magnetoresistance and high saturation fields impede the practical application of this material. Magnetite is well known to saturate at high magnetic fields, and it is well-documented that the presence of significant structural defects such as antiphase boundaries is common in magnetite structures. These defects are known to impede efficient, low-power device operation [16,108,109]. Growth conditions must therefore be optimised in order to eliminate these unwanted effects.

It is well-understood that these effects occur as a result of antiphase boundaries, as discussed in chapter 2, which generally give rise to antiferromagnetic coupling between adjacent domains. These APBs arise during the growth of magnetite on technologically relevant substrates due to the nucleation of material growth separated by 2n+1 atomic sites. If the density of these APBs can be reduced, the effects on the damping in Fe_3O_4 samples can be observed and any correlation which exists between the damping and the microstructure of the Fe_3O_4 will be revealed. In this chapter, structural and magnetic characterisation data is presented from a series of magnetite thin films which were grown and then annealed under conditions which have been recently proven to significantly reduce APB density in magnetite. It is observed that significant reduction of the damping in these samples can be gained by annealing the Fe_3O_4, which is seen to correlate directly with changes in the sample microstructure and an improvement in the stoichiometry. This annealing process is not completely effective in eliminating the defects, however, and further work is required in order to render these magnetite thin films practical for device applications.

5.2 Growth and Annealing

A series of Fe_3O_4 samples were grown by collaborators in Tokyo on a 111-aligned substrate of yttria-stabilised zirconia (YSZ(111)) using Pulsed Laser Deposition (PLD) by a KrF Excimer Laser. YSZ is a non-magnetic ceramic material with a CaF_2 cubic structure in the Fm3̄m space group, and a nominal lattice constant of 0.512nm [212,213,214,215]. Zirconia (ZrO_2) experiences three clear material phases (going from monoclinic at low temperatures, transitioning at ~1170^{o}C to a tetragonal phase and finally transitioning to the cubic phase at ~2370^{o}C). The addition of 8% per mol of yttria (Y_2O_3) to ZrO_2 in its cubic phase, however, has been observed to stabilise the structure in the cubic phase even down to room temperature and below. This results in a cubic structure which is extremely thermally stable (up to a melting point of 2780^{o}C) with diamagnetic properties (χ_{YSZ} = -1.2x10^{-7} cm^{3}g^{-1})[216]. This makes it an ideal substrate for the growth of cubic magnetic structures for potential spintronic applications.

The substrate was heated throughout to a temperature of 300°C and kept in an oxygen atmosphere at a partial pressure of $2x10^{-4}$Pa ($2x10^{-6}$mbar). After the samples were grown, four out of the five samples were annealed, with one sample kept as-grown for comparison. Each of the annealed samples was annealed at a fixed temperature of 1100°C in an atmosphere of CO/CO_2 (with the CO_2 making up 1000ppm in concentration) for one hour in order to reduce the density of antiphase boundaries. This technique has been observed to reduce the defect density in similar Fe_3O_4 thin films by Matsuzaki *et al* [16], based on the previous experiments which showed that annealing in a CO/CO_2 atmosphere is useful in improving the stoichiometry (and reducing the density of growth defects) in bulk-like Fe_3O_4 single crystals. Previous work by Harrison et. al. [217] discusses optimal growth and annealing conditions for large Fe_3O_4 crystals using this gas mixture. From further work in this field [218,219], it is well known that the stoichiometry of the post-anneal samples depends strongly on the ratio between $CO:CO_2$ in the gas mixture, and the gas pressure. This results from the change in the number of oxygen atoms available to bond with the iron oxide structure. If enough oxygen is available, then Fe_3O_4 is the energetically favourable oxidation state. As the gas pressure is reduced, the chemical equation becomes unbalanced and the Fe_3O_4 stoichiometry cannot be sustained, so different oxides such as Fe_2O_3 become more prominent instead. A useful phase diagram for the oxide structures resulting from different local conditions is provided by Shepherd et. al. [218]. Optimisation of the technique by the growth team has shown that the ratio of $CO:CO_2$ of 1:5000 will maximise the stability of the Fe_3O_4 phase [16,219].

For the purposes of this thesis, one of the annealed samples and the non-annealed sample will be characterised and compared in order to extract key magnetic parameters and investigate the effects of this annealing process on the structural and magnetic properties of magnetite.

5.3 Structural Characterisation

The characterisation of the sample structure is necessary to assess the quality of these thin films, and whether or not the data presented is representative of stoichiometric Fe_3O_4. If these samples are not epitaxial magnetite, then other defects or unexpected properties may give rise to the magnetic effects observed in this chapter. A variety of techniques have been used to assess this structure, including X-ray diffraction, TEM, XAS and XRD.

5.3.1 X- Ray Diffraction

X-ray diffraction techniques were used to assess the structure of the Fe_3O_4 thin films discussed in this chapter. A series of $2\theta/\omega$ scans were recorded from each sample to facilitate examination of the crystallographic structure. Peaks recorded from the XRD were compared with literature values for bulk Fe_3O_4.

The XRD data shows the epitaxial relation of both samples to the substrates, with the YSZ(111) || Fe_3O_4(111) and YSZ(1$\bar{1}$0)|| Fe_3O_4(1$\bar{1}$0), despite the ~40% mismatch between the lattice constants of the two materials. A shift in ω/2θ in the Fe_3O_4 peaks is clearly observed between the pre- and post-anneal samples, where the YSZ(111) peaks are the same in each scan. An out of plane lattice constant of 8.440(3)Å was calculated for the annealed sample and 8.355(2)Å in the non-annealed sample. These values were calculated by using Bragg's law (equation 3.2) and the ω/2θ angle to calculate the planar separation (d), and then using the well-known relation between the planar spacing and the lattice constant (a) in cubic structures (equation 3.3) as discussed in section 3.2.1. Given that the epitaxial Fe_3O_4 structure is cubic, a=b=c, so the in-plane lattice constant can be inferred by calculating the out-of-plane constants.

The values recovered using this method are similar to the bulk value of 8.396Å expected from magnetite [107,210,211], with the slight deviation of the annealed samples from the bulk value attributed to tetragonal distortions in the lattice as a result of tensile strain in the plane of the sample. In the non-annealed sample, the out-of-plane lattice constant is reduced compared to the expected value, suggesting a compressive strain is experienced in this axis. In order to conserve the volume of the structure, the other, in-plane, axes must be affected by a tensile strain. After

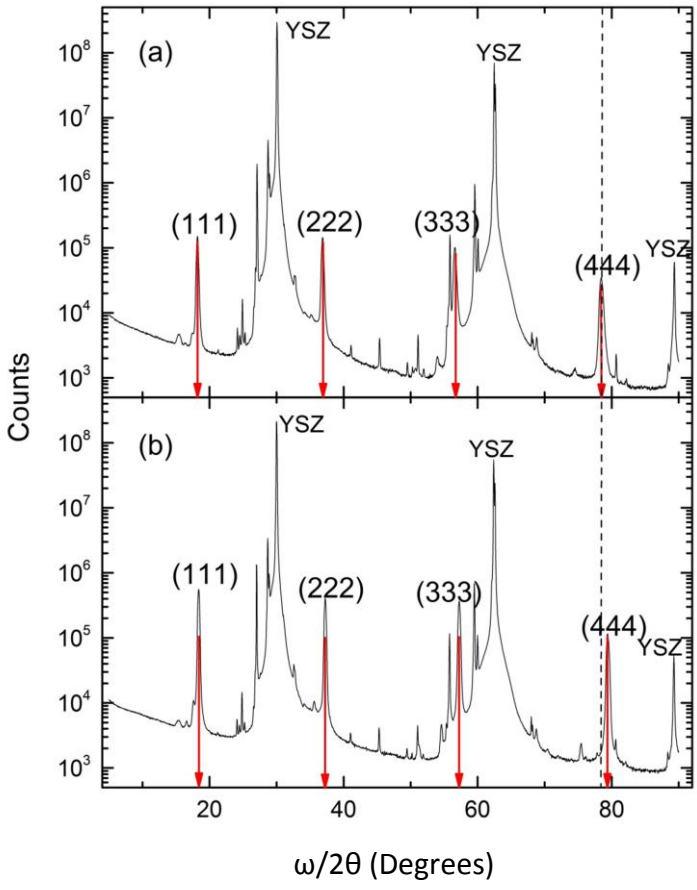

***Figure 5.1**. A comparison between the 2ϑ/ω out-of-plane XRD data from a) the as-grown and b) the annealed Fe_3O_4/YSZ(111) samples. The (111) peaks of the Fe_3O_4 material are marked with their respective h,k,l values*

the sample is annealed, the out-of-plane lattice constant is larger than the bulk, indicating that the strain directions are reversed relative to the non-annealed sample.

The 2θ/ω scans show that a single phase of Fe_3O_4 exists, since the only Fe_3O_4 peaks observed in the data are the (111) series and that the growth of the thin films is therefore epitaxial in each sample. The two large peaks correspond well to the (111)-aligned YSZ substrate peaks, with an out-of-plane lattice constant of 5.1402Å, and the remaining smaller peaks with the K_β and L_α peaks from the observed K_α peaks. Repeating the measurement with the monochromator installed more clearly shows the sample and substrate peaks (figure 5.2) isolated from their K_β and L_α components.

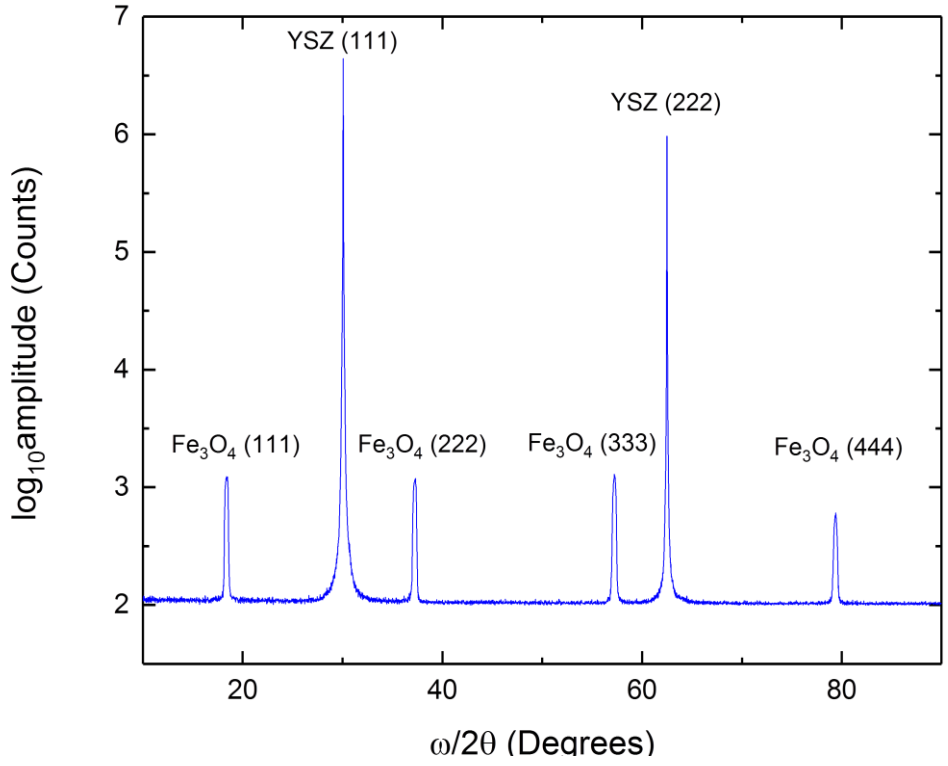

Figure 5.2. *2ϑ/ω XRD scan from the post-annealed Fe_3O_4/YSZ(111) with the additional K_β and L_α peaks removed by the monochromator. The remaining K_α peaks from the substrate and sample are clearly observed*

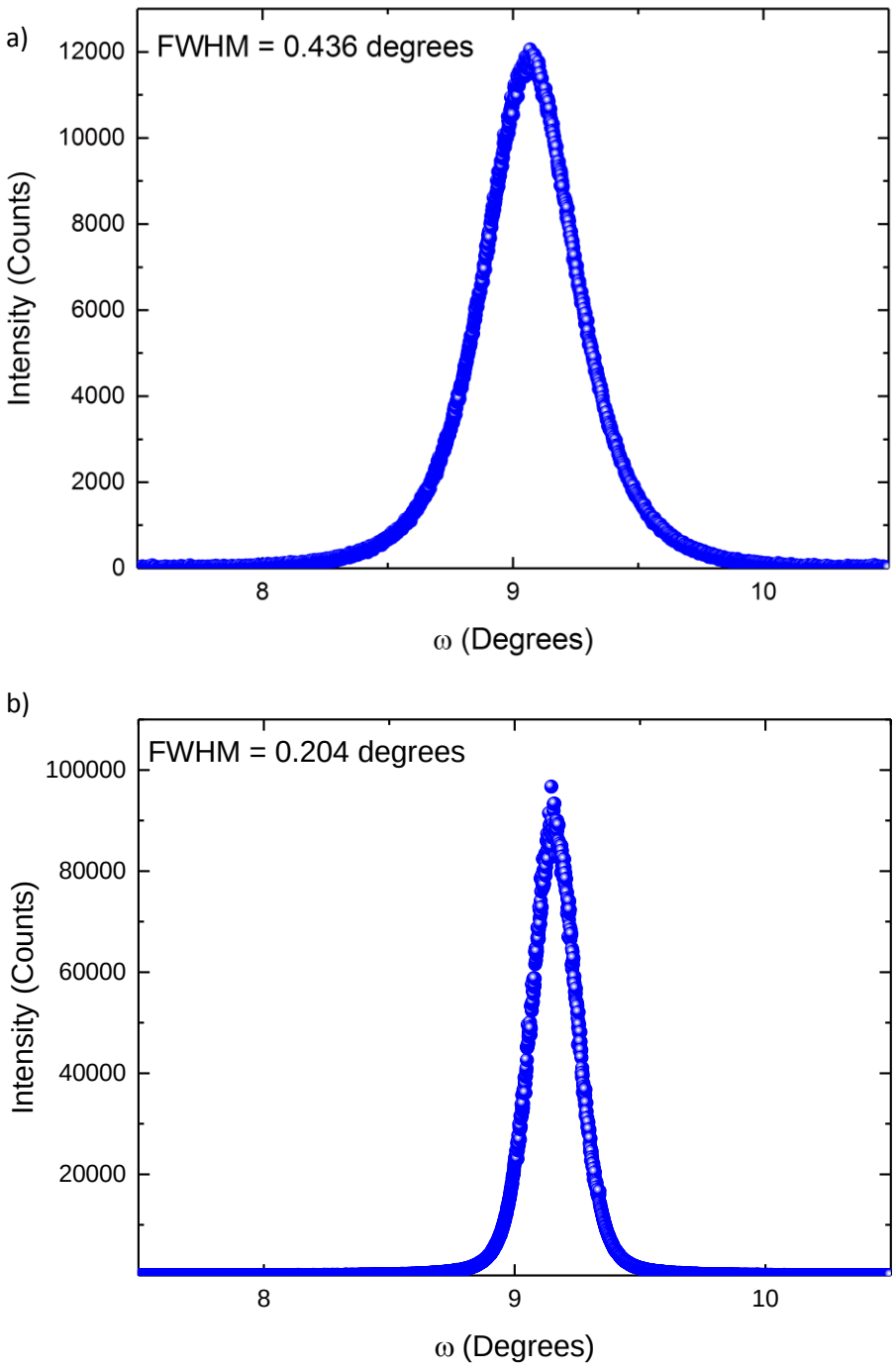

***Figure 5.3**. An XRD Rocking curve over the Fe_3O_4 (111) peak from (a) the non-annealed and (b) the annealed Fe_3O_4/YSZ(111)*

Rocking curves were recorded in ω over the Fe_3O_4(111) peaks in order to examine the film quality. It was observed that a smooth curve can be recorded in each case, which can be analysed as discussed in chapter 3. The FWHM of each curve can therefore be compared between samples to assess the relative defect density. In the annealed samples the FWHM of the rocking curve has a value of 0.2040 ± 0.0005degrees compared to the value observed in the as-grown samples, which is 0.436 ± 0.001degrees. The annealed samples therefore show a FWHM reduced by a factor of two compared with observations from the non-annealed sample, indicating significant reduction in defect density after the annealing process. This is consistent with the expected outcome of the annealing based on the literature [16].

Pole figures (figure 5.4) were also recorded from the Fe_3O_4 samples to investigate the other peaks in the <111> family. Setting the zero position to the Fe_3O_4 (111) peak, determined using the 2θ/ω data shown in figure 5.1, a map of the {111} family of peaks was made by rocking the sample mount in $0<\phi<360^{o}$ and $0<\chi<90^{o}$. A strong central (111) peak is observed in both samples, with the three surrounding points generated by the family of {11$\bar{1}$} peaks at other angles. These surrounding peaks are narrowed in the post-annealed sample (figure 5.4.b) in both ϕ and χ, supporting the improvement of the peak width observed in the rocking curves (indicating the relative improvement of the film quality engendered by annealing).

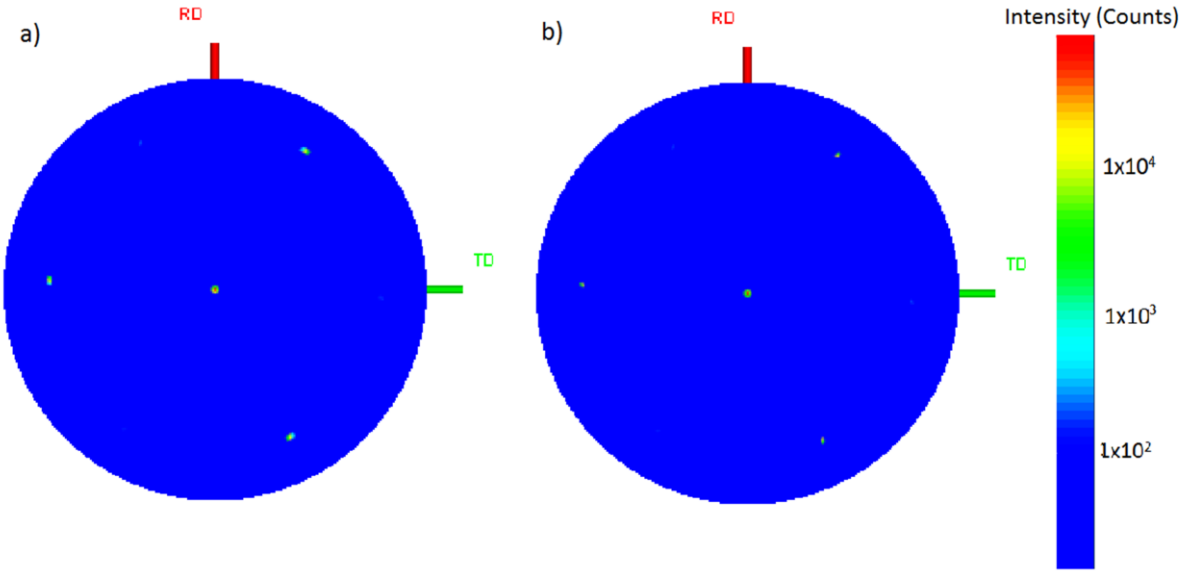

Figure 5.4. *XRD Pole figures from the Fe_3O_4 (111) peaks from a) non-annealed and b) post-annealed Fe_3O_4/YSZ(111)*

Measurements of the thickness of the Fe_3O_4 samples were attempted using XRR. Small Kiessig fringes were observed in the non-annealed sample, as observed in figure 5.5.a and fitted as discussed in chapter 3, yielding a value of 72 ± 1 nm for the sample thickness. However, the results of these measurements were inconclusive, since the annealed samples proved too thick to generate Kiessig fringes, as shown in figure 5.5.b. Despite being grown using the same method, the Fe_3O_4 samples grown for this project were not the same thickness, and the same thickness value cannot therefore be assumed for the annealed sample as well. Further data was acquired using HAADF-STEM to confirm the film thickness (section 5.3.3), where the thickness of the non-

annealed sample is observed to be considerably smaller (60nm ± 1nm). This discrepancy is likely to be a result of errors in the XRR fit: it is likely that the fitting algorithm in GlobalFit has found a local minimum in the fit function with inaccurate parameters. In particular, the interface roughness is difficult to quantify other than by fitting, which means that if the fit settles on an incorrect value for this parameter, then erroneous values will also be returned for the other dependent parameters.

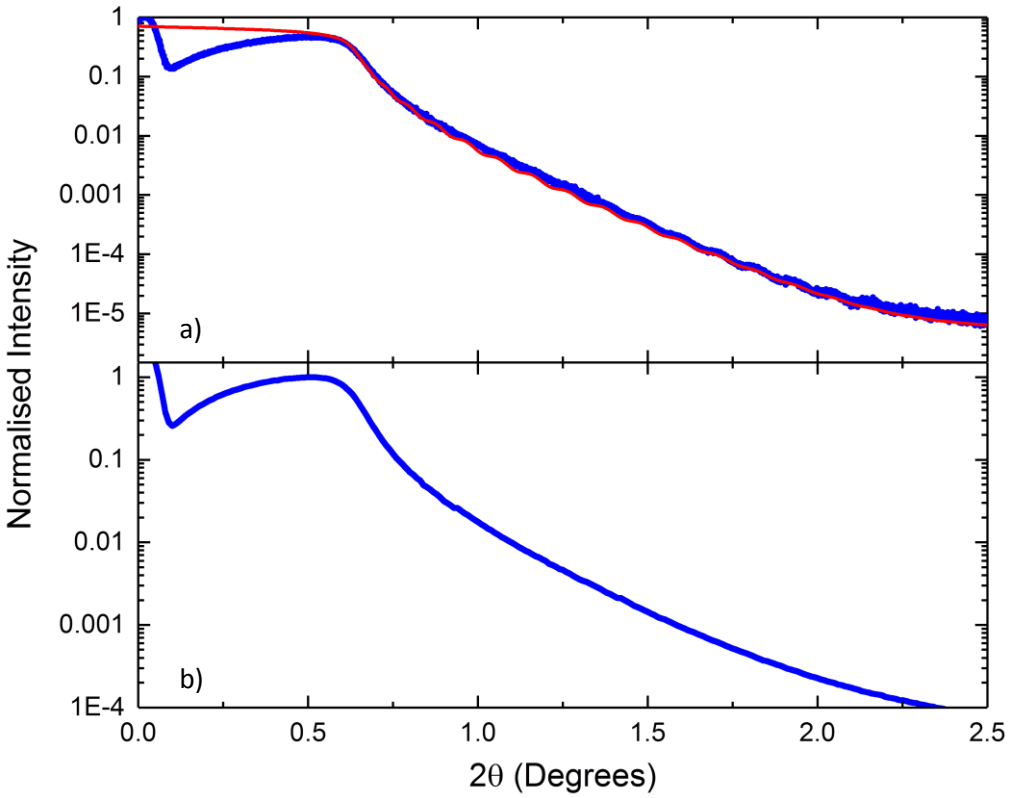

Figure 5.5. *Normalised XRR from a) non-annealed and b) annealed Fe_3O_4/YSZ(111) samples. Data is shown in blue with the fit calculated using GlobalFIt shown in red*

5.3.2 XAS and XMCD

Soft x-ray spectroscopy was performed on the samples on beamline I06 at Diamond Light Source. The absorption of soft x-rays by core electrons in ferromagnetic materials is a well understood process, as described in chapter 3, which can be used to record element specific XAS and XMCD in order to examine the structure of the thin films discussed in this chapter. Each Fe site can be examined individually due to the element specificity offered by XMCD. This allows the structure to be examined thoroughly and element, site, and valence specific data to be recovered. Measurements were recorded at 300K in a field of 6T to ensure saturation of the magnetisation within the samples. A grazing incidence of 65^{o} away from the normal was chosen to measure the

in-plane magnetisation, as discussed in section 3.5. Five sets of XMCD were averaged from each sample.

XMCD spectra have been extracted across the L_3 and L_2 edges from the as-grown sample (shown in figure 5.6) and the annealed sample (shown in figure 5.7). As expected from magnetite, three distinct peaks are observed at L_3, corresponding to the Fe^{2+} Oh, Fe^{3+} Td and Fe^{3+} Oh sites, with the central (Td) peak aligned anti-parallel to the Oh peaks due to the superexchange effects causing AFM alignment between the Td and Oh sites (as discussed in section 2.6.1). Data was recorded at 300K, well above the Verwey transition temperature for magnetite, so the structure is expected in the cubic phase.

Each of the three L_3 peaks in the XMCD occurs at a different energy, centred on the expected iron L_3 transition energy of 707eV [220]. Differences in the crystal field occur (as discussed in chapter 3) in different local crystal environments, producing three individual peaks at the L_3 edge: one for each of the three unique iron sites in the Fe_3O_4 structure. This matches well with the expected Fe_3O_4 XMCD recorded in the literature [84,174]. Chemical stoichiometry has been established using atomic multiplet calculations fitted to the data measured from the XMCD. The corresponding fit derived from the atomic multiplet calculations is shown in red overlaid on the XMCD in figures (5.6.b and 5.7.b)

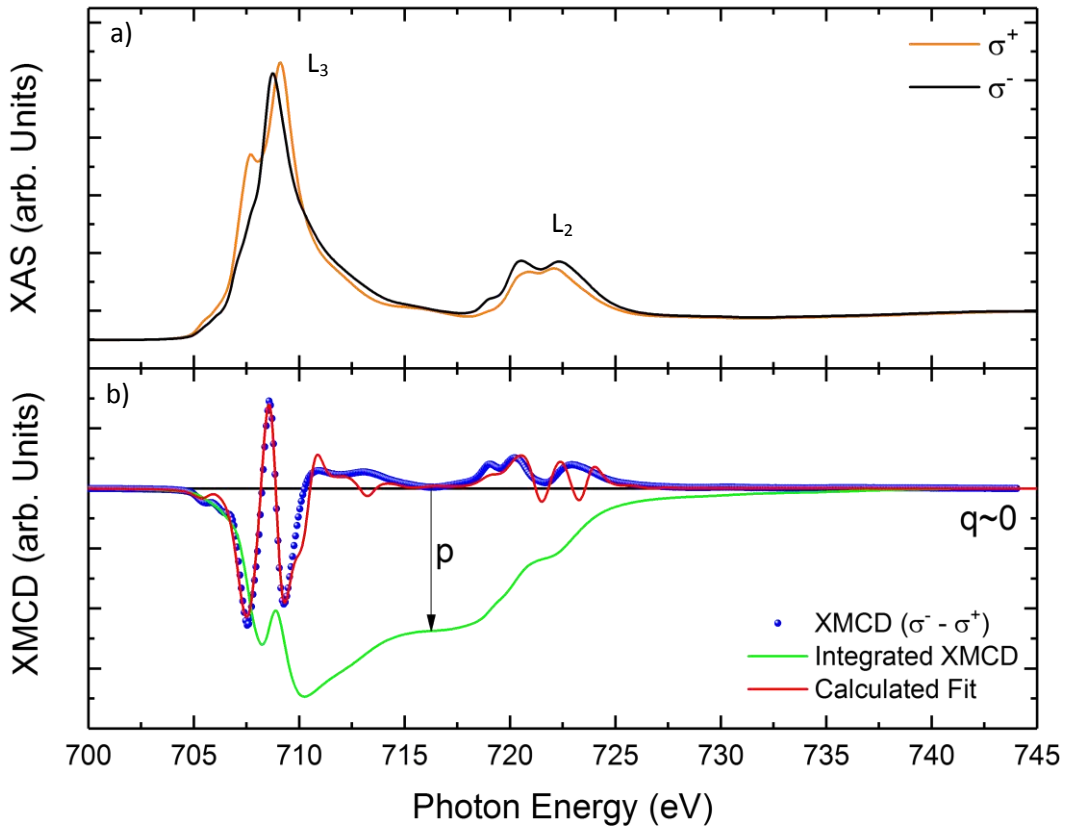

***Figure 5.6**. The a) XAS and b) XMCD from the averaged XAS of the non-annealed Fe_3O_4/YSZ(111) sample at 300K*

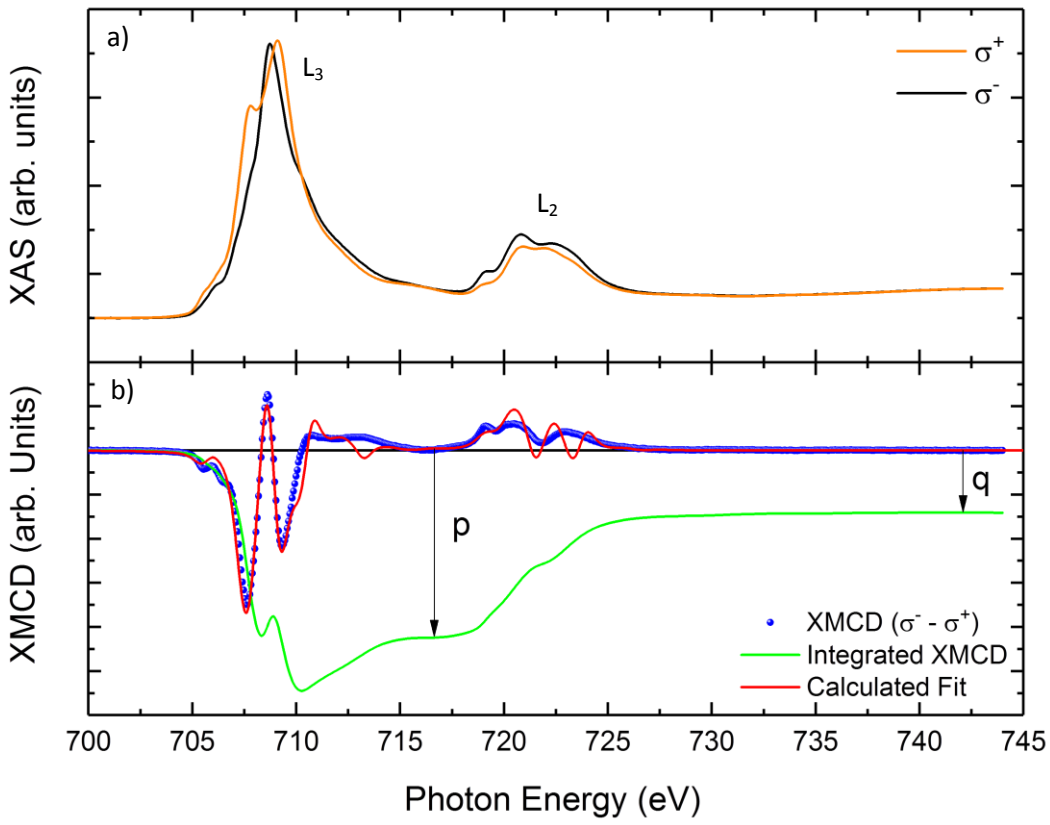

***Figure 5.7**. The a) XAS and b) XMCD from the averaged XAS of the sample of annealed Fe_3O_4/YSZ(111) at 300K*

As well as confirming that the structure is magnetite, due to the three characteristic L_3 peaks, the XMCD also shows that the stoichiometry is improved by the annealing: fitting to the data using atomic multiplet calculations shows a difference in the relative occupation of different Fe sites before and after the annealing process. The occupation of Fe^{2+} Td sites is seen to increase post-annealing. A ratio of occupied Fe sites (Fe^{2+}Oh:Fe^{3+}Td:Fe^{3+}Oh) of 0.8: 0.5: 0.3 is observed in the non-annealed sample, compared with the ratio of 1:1:1 after annealing, which is the site ratio expected from stoichiometric magnetite. Repeated fitting of each dataset using linear combinations of each site shows a maximum uncertainty of 3% in the occupation of each site.

The improvement observed in the stoichiometry after annealing is in agreement with the observations made in both the VSM and FMR data. An increased orbital moment is evident from the integrated XMCD since the q value is larger in the annealed sample, as a direct consequence of the increase in the Fe^{2+} ion density. As discussed in section 2.6.1, the Fe^{2+} ion is the major contributor to the orbital moment in stoichiometric Fe_3O_4 since the antiferromagnetic alignment of the Fe^{3+}ions in the Td and Oh sites cancel each other out.

Assessment of these spectra using the magneto-optic sum rules can also provide insight into the ratio between the spin and orbital magnetic moments μ_s and μ_l. The ratio between the integral at

the L_3 and L_2 edges (p and q on figures 5.6.b and 5.7.b respectively), provide a ratio of $\mu_l/\mu_s = 0.09$ in the annealed sample, which is consistent with previous experiments on epitaxial magnetite thin films [100]. This is consistent with the increase in the occupied Fe^{2+} Oh sites in the lattice since it is the Fe^{2+} iron atoms that primarily contribute to the orbital moment of magnetite. The measured ratio corresponds to a g factor of 2.18, which is in agreement with the value of 2.14 observed in the FMR.

In the non-annealed sample, however, $\mu_l/\mu_s = 0$ since the observed average value of q = 0, giving a value of g = 2 in agreement with the free electron value. The value of q in this integral is proportional to the orbital magnetic moment contribution, which is finite in the annealed sample but almost fully quenched in the non-annealed film. This is in agreement with the expected quenching of the orbital magnetic moment in 3d transition metals.

5.3.3 HAADF-STEM

The SAED along the [110] zone axis shows some differences between the samples, as shown in figure 5.8. A series of additional peaks are observed in the non-annealed sample which are not present post-anneal, indicating the presence of an additional material phase which is eliminated by the annealing process. Improved structural coherence is observed as the diffraction pattern becomes more ordered, with fewer, brighter peaks corresponding to more uniformly ordered, higher intensity diffracted waves.

The low-magnification HAADF-STEM shows that the non-annealed sample has a thickness of 60 ± 1 nm which is 13nm smaller than the value returned by the XRR. The annealed sample is observed to be 146 ±1 nm. In both samples, an intermixing layer is observed between the Fe_3O_4 and YSZ layers. In the non-annealed sample, this layer is generally ~10 ± 1nm, interspersed with thinner regions. The mixed layer is thinner in the post-annealed film, with a depth of 4.5 ±1 nm, which correlates with the improvement in the Fe_3O_4 structure observed in the XRD and the narrowing of the rocking curves. This is confirmed in the high-magnification HAADF-STEM data (figures 5.9 and 5.10, showing the as-grown and annealed samples respectively). While the defect density is

a) b)

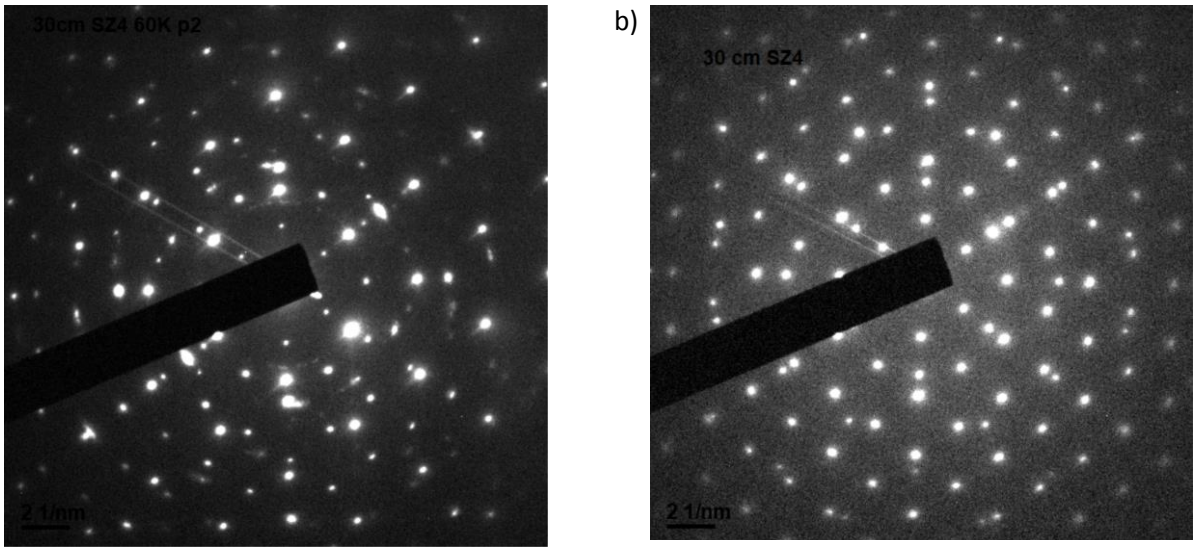

Figure 5.8*. A comparison of SAED Patterns along the [110] zone axis observed in Fe_3O_4/YSZ(111) from a) the non-annealed and b) the post-annealed samples*

difficult to observe in the high-magnification HAADF-STEM, other TEM experiments on these samples have shown a reduction in the density of APB defects in the literature [16].

a)

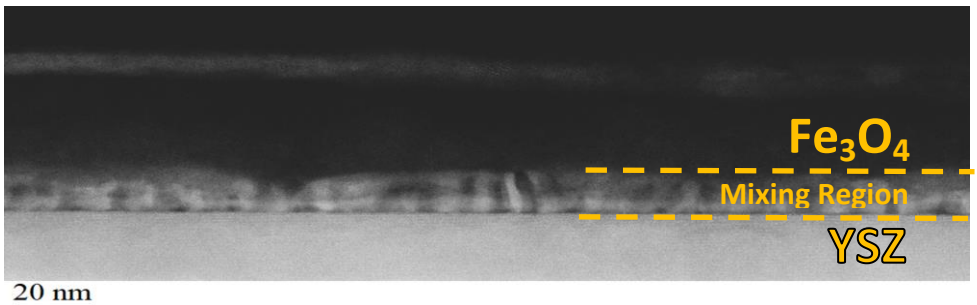

b)

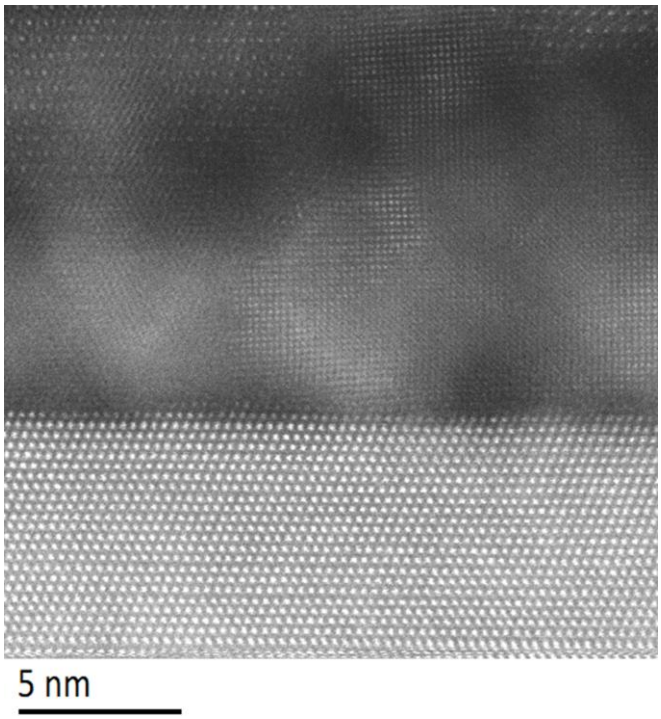

***Figure 5.9**. A comparison of a) Low-magnification and b) high-magnification HAADF-STEM images observed in Fe_3O_4/YSZ(111) from the non-annealed sample*

a)

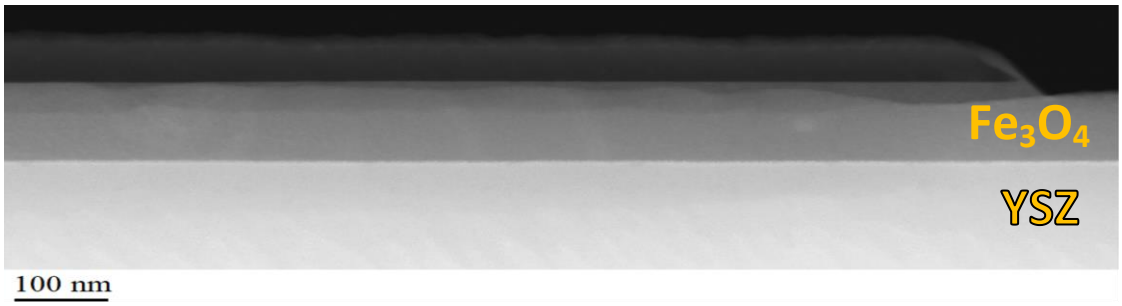

b)

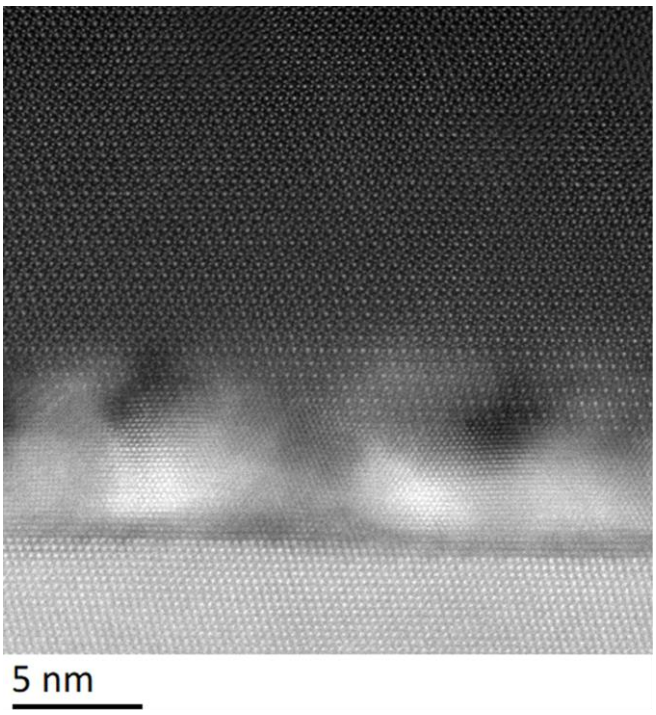

***Figure 5.10**. A comparison of a) Low-magnification and b) high-magnification HAADF-STEM images observed in Fe_3O_4/YSZ(111) from the post-annealed sample*

5.4 Magnetic Characterisation

With the structural characterisation complete, it is observed that the annealed thin films grown for this project are indeed epitaxial Fe_3O_4, although before annealing the stoichiometry is imperfect. With the microstructure of these films characterised, the magnetic properties of the samples can be analysed using a series of investigative techniques, including VSM and FMR spectroscopy.

5.4.1 VSM

Vibrating sample magnetometry (VSM) has been used to measure the magnetic properties of the samples, by measuring **M**(**H**) and **M**(T). **M**(**H**) measurements were performed using both the Microsense Model 10 VSM at the University of York, and the SQUID-VSM at DLS. A comparison of the **M**(H) data from the annealed sample recorded at 300K is shown in figure 5.11, with the Model 10 data in red and the SQUID data in blue. Good agreement is observed between both sets of data, and therefore both sets of equipment. The **M**(T) data can therefore be considered in good agreement with the **M**(**H**) data, and the **M**(**H**) sets from each set of equipment complementary. All VSM data shown was measured with the magnetic field applied in the plane of the Fe_3O_4 thin films.

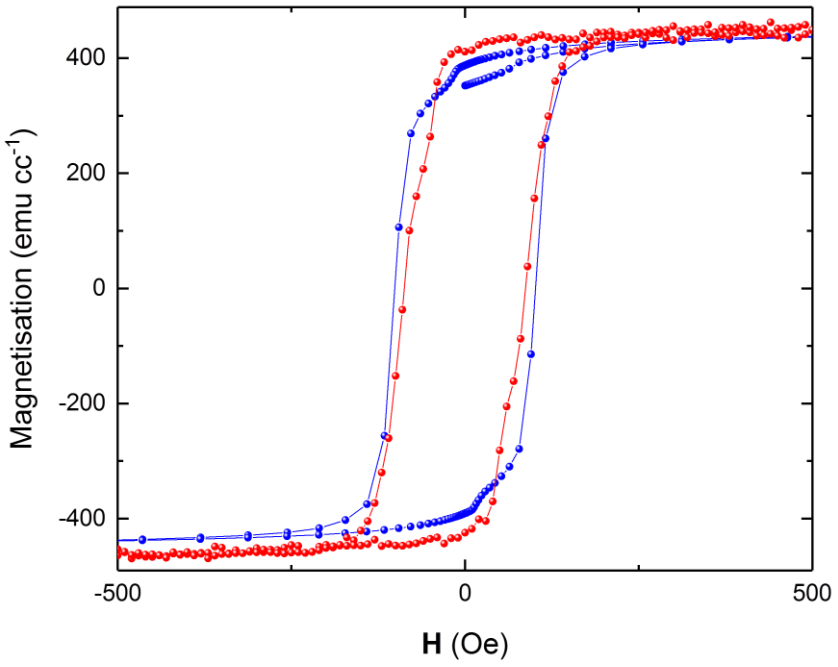

***Figure 5.11**. A comparison of **M**(H) VSM recorded using the SQUID magnetometer (blue) and the Model 10 VSM (red)*

Room temperature M(**H**) data is shown in figure 5.12, with data from the non-annnealed film shown in red and the annealed film in blue. This data was measured along the [11$\bar{2}$] axis in each sample. The effect of annealing in the CO/CO_2 environment is evident from the increase in saturation magnetization of 260 emu cc^{-1} to 480 emu $cc^{=1}$, the decrease in coercivity from 350 ±20

Oe to 50 ± 10Oe (more easily observed in the inset of figure 5.12), and the increased squareness (numerically characterised by the ratio of the remanence field to the saturation magnetisation ($\mathbf{H}_r/\mathbf{M}_s$))of the loop which all suggest an improved structure with bulk-like properties.

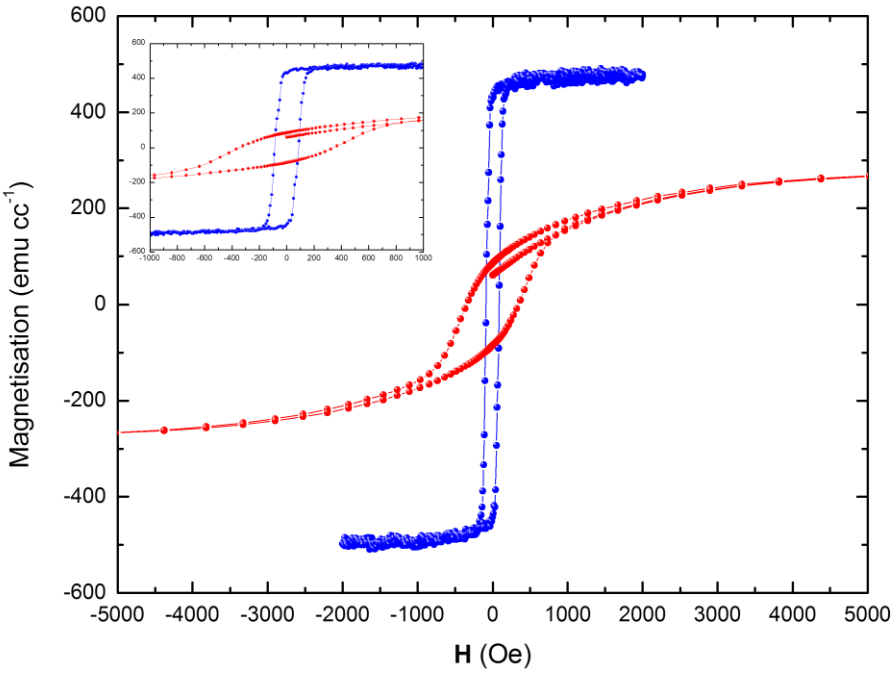

Figure 5.12. *In-plane M(H) recorded from as-grown (red) and post-anneal (blue) Fe_3O_4/(111) VSM at T = 300K*

The **M**(T) has been measured to confirm the presence of the well-known metal-insulator Verwey transition (T_V). As discussed in section 2.6.1, stoichiometric magnetite undergoes a structural shift from an insulating state to a metallic one at T_V ~120K. This charge-order transition can be observed as a sharp increase in both the resistivity and the magnetisation at around the transition temperature. Data from the annealed film is shown in figure 5.13 for reference, showing the FC VSM (saturated in a field of 30kOe)) in red and the ZFC in blue. The datasets converge at the blocking temperature T_B = 116.5 ± 0.1K. A different curve is observed in the low temperature limit, showing a smaller **M** (and therefore suggesting greater disorder between local magnetic domains) at low temperature in the ZFC data. Both datasets show that $\mathbf{M}_s$ increases with T until T_V, and then gradually declines as T is increased further. Measurements from the annealed sample therefore show a distinct Verwey transition which is consistent with the literature [92,93] indicating good stoichiometry in the magnetite: it is well-known that the Verwey transition is not observed in non-stoichiometric magnetite ($Fe_{3-\alpha}O_4$) when $\delta > 0.0117$ [96] as discussed in section 2.6.1.

M(T) data from the annealed sample is compared with the non-annealed sample in figure 5.14. In the non-annealed sample, shown in figure 5.14, the transition is suppressed, as observed by the lack of the characteristic increase in $\mathbf{M}_s$. This indicates that the annealing significantly improves the stoichiometry. In fact, the **M**(T) in the non-annealed sample is seen to reduce as T increases,

falling from $\mathbf{M}_s$ = 295 emu cc^{-1} at 5K to 173 emu cc^{-1} at 300K. This decrease begins sharply at ~115K, and slows at ~120K, however, which still coincides with T_V.

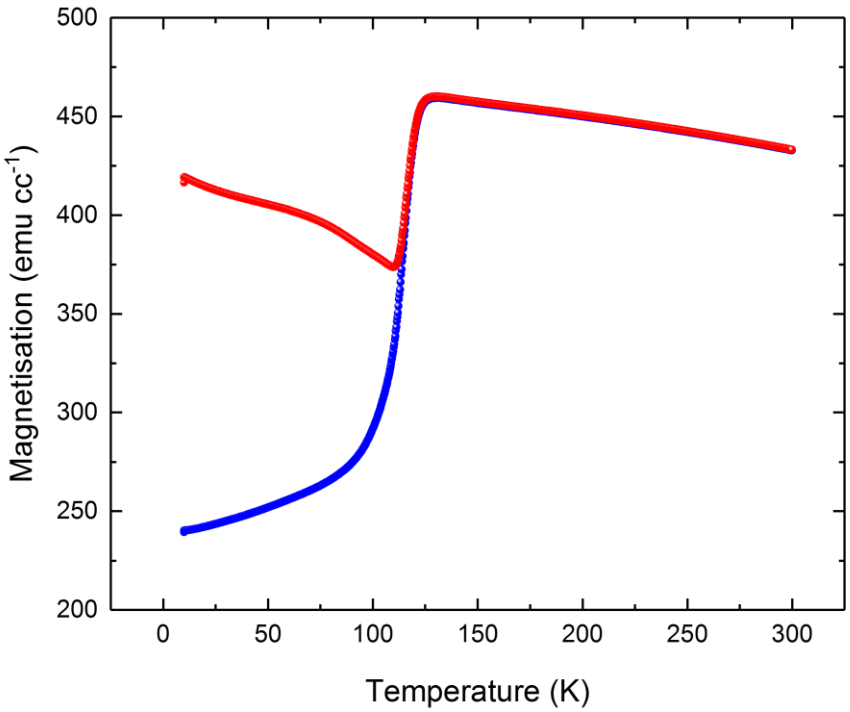

***Figure 5.13**. A comparison of M(T) VSM recorded from the annealed Fe_3O_4/YSZ(111) using the SQUID magnetometer in ZFC (blue) and FC (red) modes*

The transition behaviour can be observed more clearly in the first derivative of the **M**(T) measurements (shown in red in figure 5.14a,b). A sharp positive peak in the first derivative is observed at T_v = 120K in the annealed sample, but a negative peak is observed in the non-annealed sample.

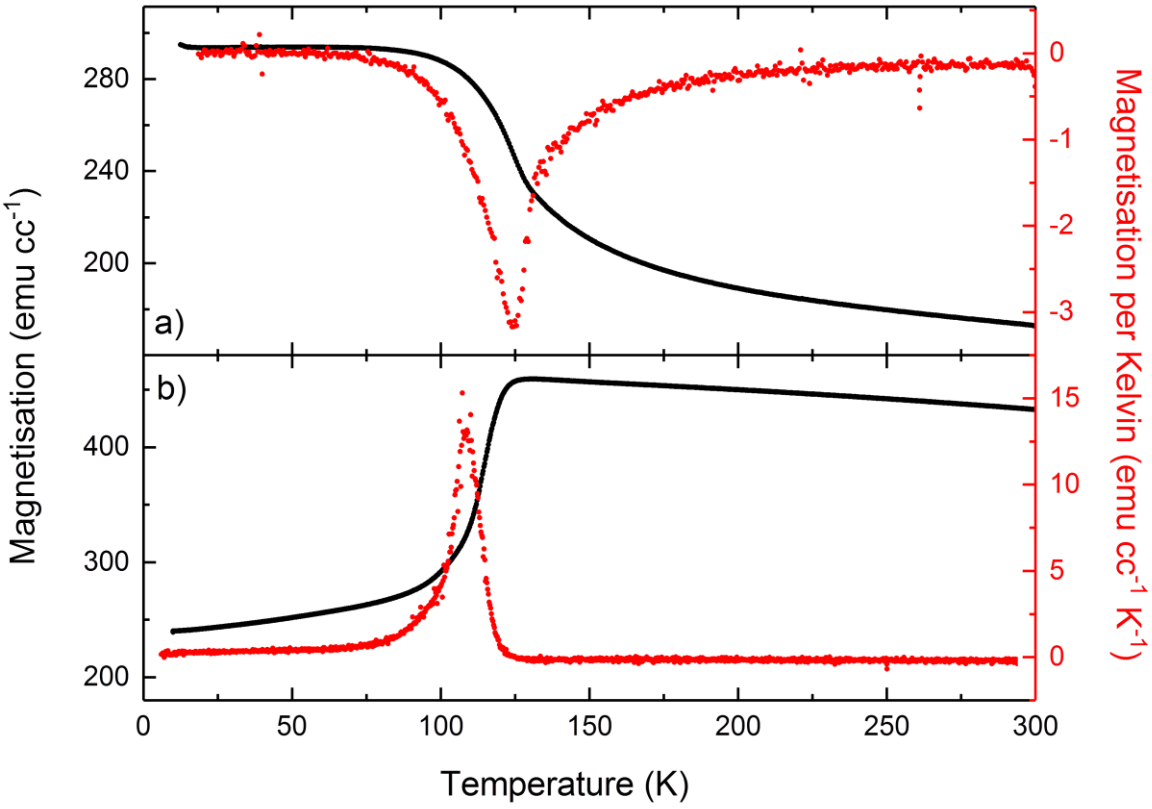

Figure 5.14. *The temperature dependent ZFC M(T) recorded at 400Oe from the a) as-grown and b) post-annealed Fe_3O_4/YSZ(111), showing the magnetisation as a function of temperature (black) and the first derivative with respect to temperature (red)*

5.4.2 Ferromagnetic Resonance Spectroscopy

Ferromagnetic resonance spectroscopy allows access to information about both the in-plane anisotropy and the damping in FM thin films. Initial measurements using the VNA-FMR showed that the annealed samples show a strong response, which can be easily fitted in order to extract damping parameters. The non-annealed sample, however, shows a very weak signal in the VNA-FMR operation mode, which is barely distinguishable from the background. As a result, the data from the non-annealed sample was measured using the modulation FMR technique. Confirmation of agreement between techniques was achieved by recording both modulation FMR and VNA-FMR and comparing the values fitted to both sets of data. This further supports the observations made in chapter 4, that the two modes of operation of the FMR spectrometer are in direct agreement with each other. Hence the values extracted by fitting the two sets of data are comparable with each other.

Measurements of the FMR linewidth as a function of frequency at the in-plane easy axis have been used to probe the magnetic properties in these samples. An example of the FMR linescan data from each sample is shown in figure 5.15. This data was recorded along the [112] axis at a fixed frequency of 10GHz. A broad resonance of $\Delta\mathbf{H}$ = 1060 ± 25Oe Oe is observed at $\mathbf{H}_r$ = 2370 ± 25Oe in the non-annealed sample. After annealing, the linewidth is much narrower, showing $\Delta\mathbf{H}$ =

230 ± 25Oe at $\mathbf{H}_r$ = 920 ± 25Oe, corresponding to a significant reduction in the total damping and an improved magnetic structure.

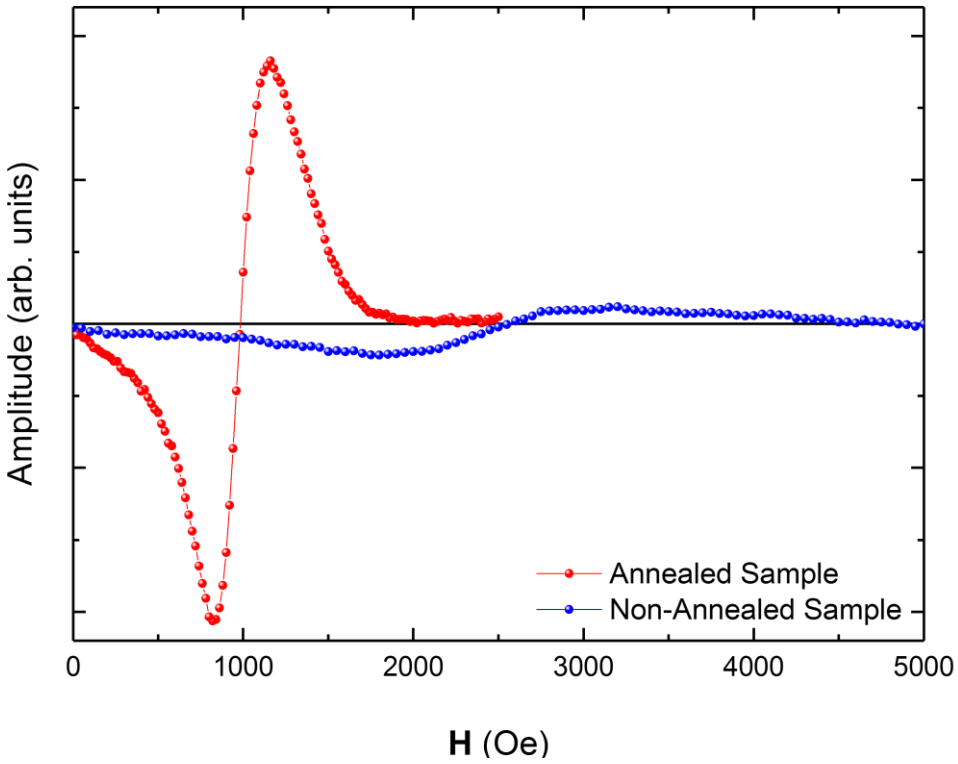

Figure 5.15. *A direct comparison of the Modulation FMR field sweep at 10GHz from the as-grown (blue) and annealed (red) Fe_3O_4/YSZ(111)*

Kittel curves from the easy axis in each sample were recorded in a field-frequency map between 0 Oe<**H**<3kOe and 100kHz<f<20GHz. The position of the extracted minimum values of ΔS_{21} are shown in 1GHz frequency intervals in figure 5.16. For the non-annealed sample, fitting $\mathbf{H}_r(f)$ using equation 2.40 gives a g-factor of 2 and an $\mathbf{M}_s$ of approximately 120 emu cc^{-1}, considerably lower than the 470 emu cc^{-1} expected from bulk magnetite. The fit also returns $\mathbf{H}_a$ = 290 ± 85Oe, which is very large for a FM thin film. The large uncertainty arises as a result of uncertainties in the fit, since the broad linewidth makes fitting the curve below 7GHz difficult. For the annealed sample (figure 5.16.b), fitting the easy axis Kittel curve returns a g-factor of 2.14 and an $\mathbf{M}_s$ of 450 emu cc^{-1}, which is consistent with the expected bulk value.

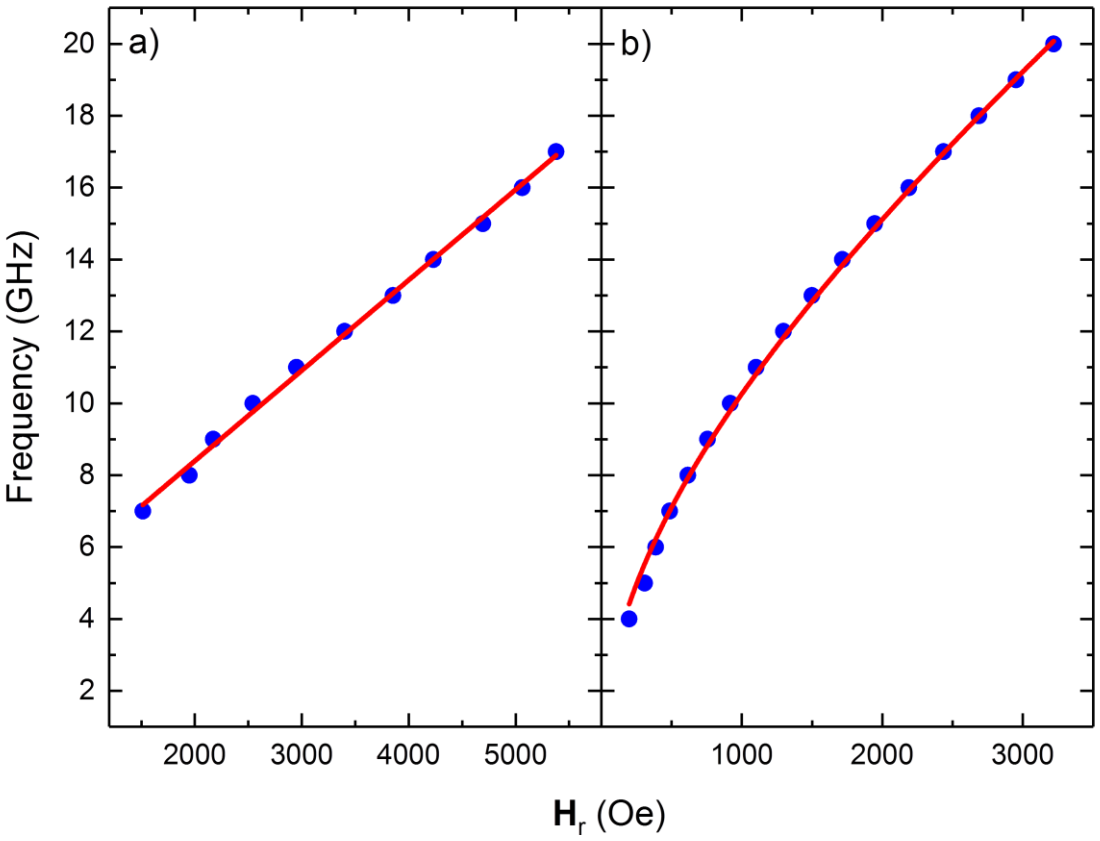

Figure 5.16. *The resonance frequency as a function of field in the a) as-grown and b) post-annealed Fe_3O_4/YSZ(111), extracted from the ferromagnetic resonance spectroscopy data. Fits to equation 2.40 are highlighted in red*

It should be noted, however, that the simplified in-plane version of the Kittel equation discussed in chapter 3 doesn't give a completely accurate fit. Modelling the free energy surface shows the magnetisation prefers to settle at an easy axis that isn't in the plane of the thin film. This is in agreement with the VSM data presented previously, where an out-of-plane component is observed in the magnetisation as expected in (111}-oriented magnetite. This explains the difference between the values observed in the FMR and the values measured using the previous methods. It can therefore be assumed that, even at saturation, the fits are not completely

accurate for $\mathbf{M}_s$: rather the fit values presented above must be treated as a first approximation. Instead of the simplified fit discussed in chapter 3, a numerical solution is required.

5.4.2.1 Anisotropy

Both the annealed and non-annealed samples of Fe_3O_4 were measured using FMR spectroscopy in order to assess the in-plane anisotropy in each of the samples. For the annealed sample, using the Modulation FMR technique at a fixed frequency of 10GHz, a linescan was extracted at each angle (in five degree steps) and the linewidth fitted using the equation described in chapter 3.The fitted data was then used to extract a value for the resonance field ($\mathbf{H}_r$) which was plotted as a function of the azimuthal angle (figure 5.17.a). A plot of the extracted $\mathbf{H}_r$ value from this data as a function of azimuthal angle can be found in figure 5.17.b.

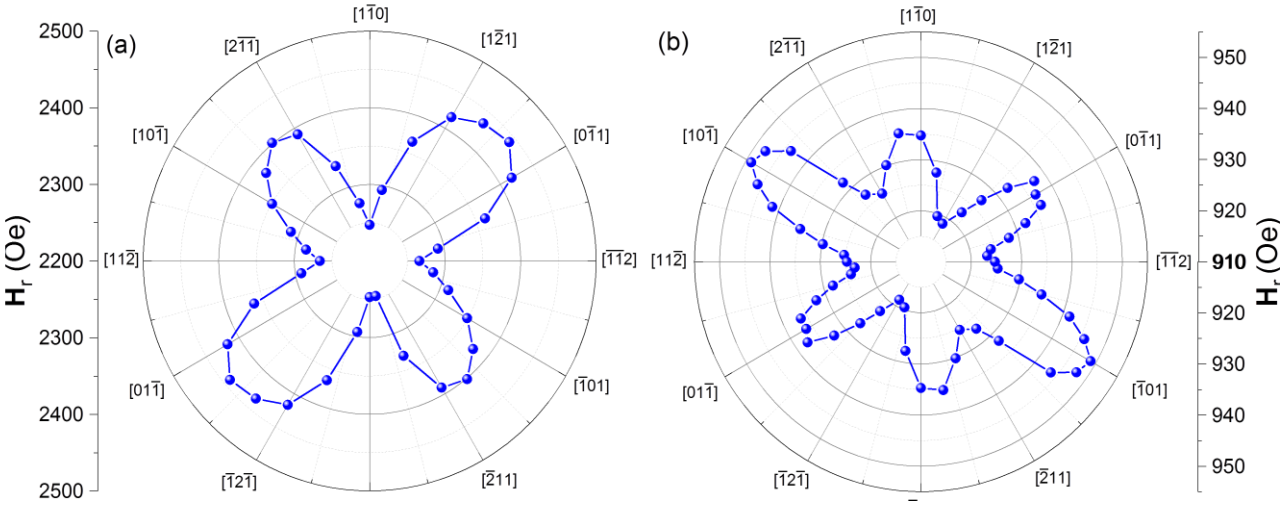

***Figure 5.17**. Polar plots of the resonance field as a function of azimuthal angle from (a) the non-annealed and (b) annealed Fe_3O_4/YSZ(111)*

In each case the samples were aligned in the plane of the film with the bias field parallel to the [11$\bar{2}$] axis. It is observed that the as-grown sample shows a four-fold anisotropy with an easy axis along [$\bar{1}$10], but this changes after annealing: the annealed sample has a six-fold anisotropy with an additional uniaxial component in the [10$\bar{1}$] direction, most likely as a result of shape effects arising from step edges on the surface of the substrate as observed in Fe/Si(111) in the literature [222].It is well documented that step-edges in vicinal substrates (defined such that the surface normal lies close to, but not parallel with, a major crystallographic axis) may give rise to changes in the magnetic anisotropy of a given crystal structure. For example, it is observed in Fe grown on [111]-aligned silicon substrates that an additional uniaxial component is added to the magnetic anisotropy when the films are grown on films with a shallow miscut angle, compared to those films grown on flat substrates [202, 223]. This additional anisotropy term is attributed to step-edges on these substrates. The component of the canted magnetisation perpendicular to the step-edges is also suggested by Liu et. al. as a contributing factor to this effect.

The same effect is observed in Fe on W(001) by Chen and Erskine [224] and in Co on Si(111) by Stupakewicz et. al. [225]. In these papers, however, step edges at the interface between sample and substrate are treated as additional periodic magnetic charges which arise from the broken symmetry of the crystal structure. These periodic charges give rise to a dipolar anisotropy in the plane of the film. This results in an additional contribution to the total magnetic anisotropy with an easy axis perpendicular to the step edge direction, similar to that observed in samples with a shallow miscut angle.

Given that the HAADF-STEM images show some uneven areas at the interface, and a slight tilt was observed when acquiring data from the XRD, either a shallow miscut angle or step-edge effects (or indeed a combination of the two) could be the reason for this additional uniaxial anisotropy. However, without further investigation of the entire sample-substrate interface under high-magnification TEM, it is difficult to make a decisive judgement.

The easy axis also rotates after annealing, and is seen to lie along the $[\bar{1}2\bar{1}]$ direction in figure 5.17.b. This recovery of the cubic anisotropy further supports the improvement of the microstructure observed in the structural analysis [221]. The distorted four-fold anisotropy in the non-annealed film is unexpected, however, and does not match the expectation of a cubic anisotropy in (111)-oriented Fe_3O_4. For a cubic system measured in the (001) plane a four-fold symmetry, similar to figure 4.14, would be expected with easy axes along the [100] and [010] directions displaying resonant field minima. However, for the as-grown film on YSZ(111), the anisotropy should be 6-fold symmetric. Non-epitaxy with the substrate may relax this condition yet the XRD data gives clear evidence that the film is (111) orientated. The reason for this anomalous behaviour is currently unknown, and further investigation is required to establish the reason for this effect. No combination of free energy surface parameters yields a biaxial cubic anisotropy in this plane and, to the author's knowledge, no precedent has been observed for overlapping non-exchange coupled layers to combine their anisotropies in this way. Whatever the reason for this effect, a change in the microstructure must occur as a result of the annealing process to recover the six-fold anisotropy observed in the annealed film. The magnitude of the total anisotropy decreases considerably during the annealing process, from 240 ± 25 Oe in the non-annealed film (corresponding well to the value extracted from the Kittel curve fit) to 30 ± 10 Oe in the post-anneal data. This shows a significant improvement in the magnetic structure.

5.4.2.2. Damping

Damping measurements were performed on the Fe_3O_4 films by extracting the linewidth of the Kittel curve at fixed frequencies and plotting $\Delta\mathbf{H}(f)$, then attempting to fit the resulting plots with equations 2.45 and 2.48. Given the increased orbital moment observed in the XMCD, the Gilbert damping may be enhanced in the annealed thin film, as observed recently in permalloy thin films [48]. However, the total damping in the Fe_3O_4 films is reduced considerably by the annealing process as evidenced by the significant reduction in the FMR linewidth: at 10GHz, the total $\Delta\mathbf{H}$ decreases from 905 ± 10 Oe to 292 ± 10 Oe as a result of the annealing process. A fit of these plots was attempted using equation 2.48 (shown in red in figure 5.18), although anomalous effects made it difficult to extract reliable values for α and ΔH_0. Further investigation into the damping in these samples is therefore required before accurate comparisons with previous experiments can be drawn.

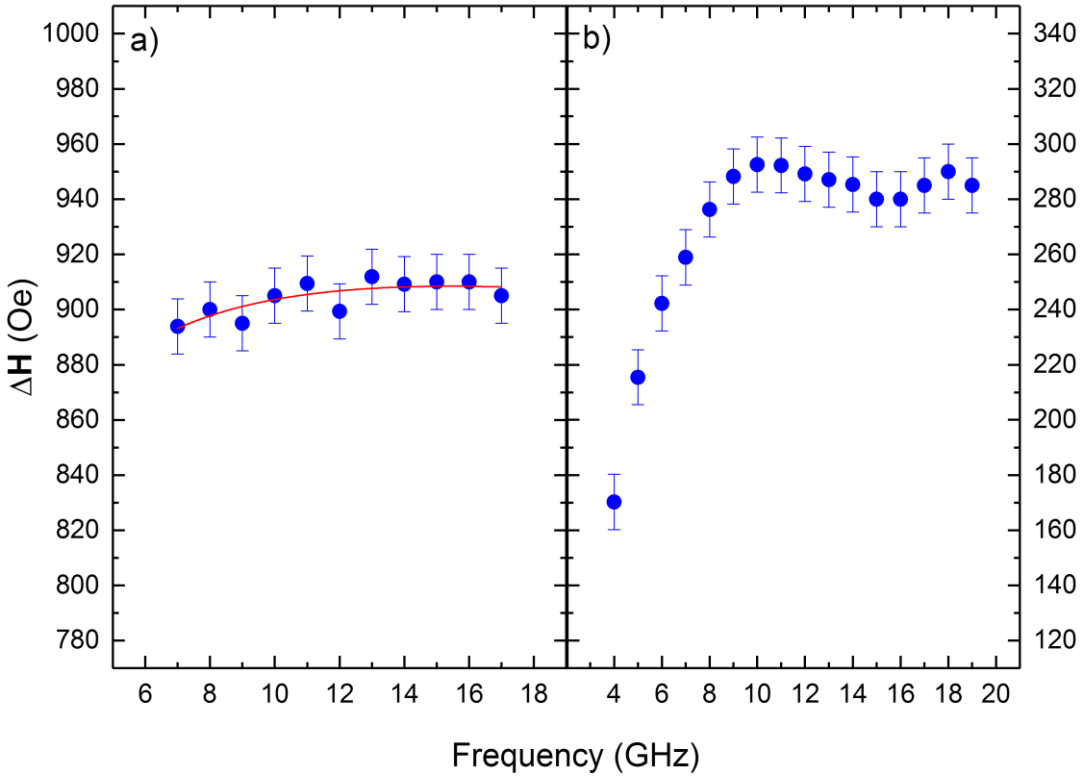

***Figure 5.18**. Graphs of the total linewidth **ΔH** as a function of frequency in a) the non-annealed and b) the post-annealed Fe_3O_4/YSZ(111)*

In the non-annealed sample, the linewidth as a function of frequency follows an approximately linear behaviour above 7GHz, which is consistent with two-magnon scattering behaviour. This shows that the dominant form of damping is the extrinsic in nature. Below 7GHz, the resonance is too broad to accurately fit both peaks of the modulation FMR response, and therefore data cannot be reliably obtained from this sample in the lower frequency region.

The damping profile is still two-magnon scattering like after annealing, indicating that the extrinsic damping is still dominant and magnetic inhomogeneities (or mixed magnetic phases) are still present within the film. This suggests that, while the defect density is reduced as observed in the HAADF-STEM, the annealed film is not defect free. More work is required before the extrinsic behaviour can be completely eliminated (and therefore the critical current density minimised).

While the data is observed to follow a 2-magnon scattering like trend, extraction of further parameters is made difficult by unknown sample parameters. Fitting the graphs in figure 5.18 using equation 2.48 should theoretically allow the extraction of the 2-magnon scattering parameter Γ, but the value extracted will vary depending on the exact shape, size, and defect density within the sample(s). Since the exact values of these parameters are unknown, the uncertainty on any given value for Γ would be too large to render the given value accurate to within reasonable error. The red line included in figure 5.18a should therefore be considered as a guide to the eye, rather than an accurate fit. Further investigation into these samples would be required in order to produce an accurate fit for this parameter.

After the steep increase in Δ**H** at low frequencies, the linewidth not only levels off but decreases before again increasing after 17GHz. The consequence of this is a broad peak in Δ**H**(f). The profile is not expected from a simplistic view of magnetic relaxation in which the linewidth should always increase with frequency. The shape is similar to that of a "Buffler" peak [226] although these effects are purely geometrical and therefore do not occur in thin films. There is, however, a phenomenon which explains this effect: Landeros *et al.*[227] show a similar feature in calculations of the FMR linewidth due to two-magnon scattering when there is a small tipping angle (≈ 5°) between the magnetization and film plane. The non-monotonic behaviour of Δ**H**(f) at these angles (shown in figure 5.19) is similar in shape to the data observed in figure 5.18.b.

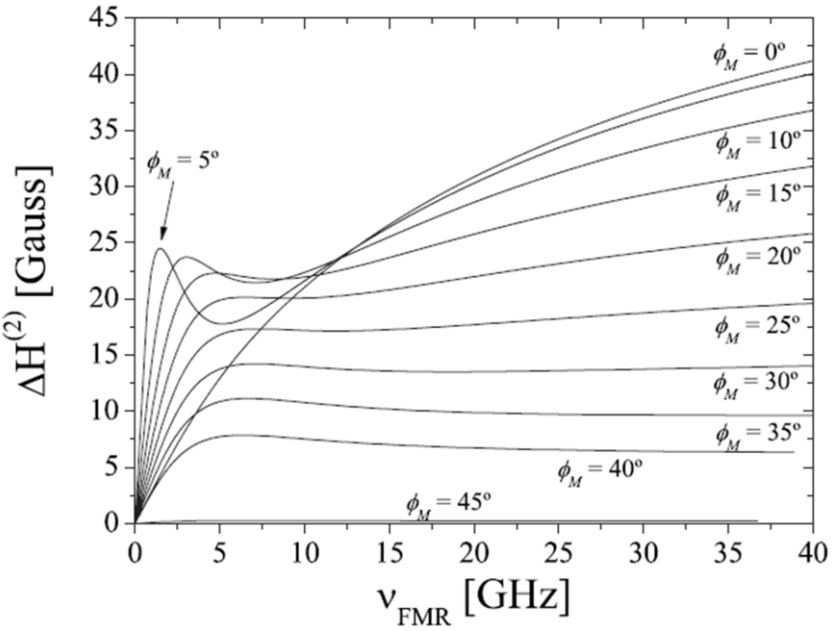

***Figure 5.19**. The calculated dependence of the 2-magnon scattering damping behaviour as a function of fixed RF frequency for different polar angles (designated ϕ_M in the figure, corresponding to θ in this thesis) reproduced from Landeros et. al. [227]*

For the calculation in [227] the angle is kept constant as a function of frequency, which is not possible experimentally due to the increasing in-plane magnetic field (**H**) with frequency. However, this would smooth out the effect for modest changes in the polar angle of the magnetization and the effect is visible over a broad range of polar angles. Only when **M** is exactly in-plane does Δ**H**(f) show monotonic behaviour. Calculating the magnetic free energy density (**U**) for the (111)-oriented Fe_3O, including the MCA, demagnetisation and Zeeman energy terms for an in-plane field of 1000 Oe (θ_H = 90°, ϕ_H= 180°), the free energy is minimized ($\partial F/\partial\theta = 0$, $\partial F/\partial\phi = 0$) when the magnetization is tilted marginally out of plane by 2.4 degrees as shown in figures 5.20 and 5.21. According to Landeros *et al.*[227], this tilting would give rise to the observed non-monotonic behaviour observed in Δ**H**(f) in the annealed Fe_3O_4. It should be noted that the literature calculations were made for a specific size, density and distribution of defects, and that the two-magnon scattering behaviour (which originates from the structural defects) is very sensitive to the structural arrangement.

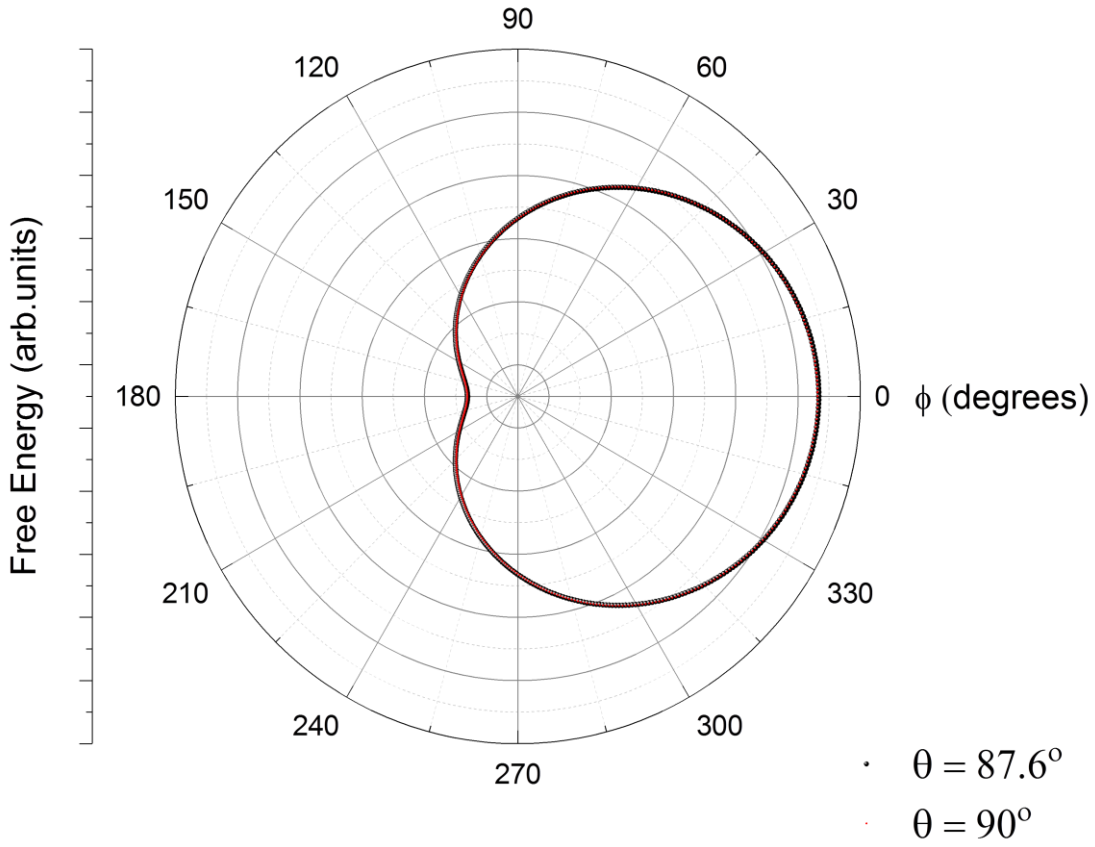

Figure 5.20 *The calculated Free energy surface in ϕ for the MCA, Zeeman and demagnetisation effects in the (111) plane of a cubic crystal in a 1kOe applied field. A comparison of the entire free energy surface between perfectly in-plane (red) and 2.4° out of plane (black) shows a minimum in the tilted data*

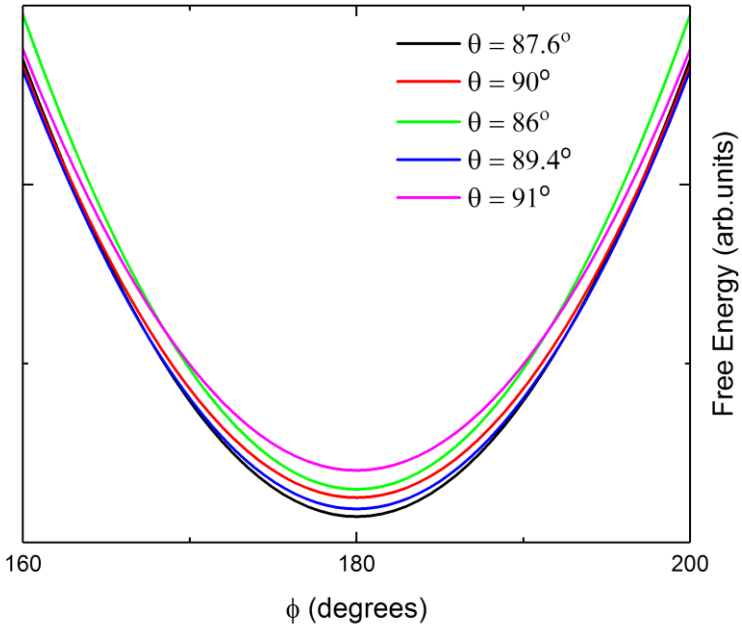

Figure 5.21 *A close-up of the free energy surface minimum over a narrow range in φ, with U calculated at a range of different angles. A minimum in U occurs at* $\theta = 2.4^{o}$

5.5 Conclusions

A significant change in the magnetic properties is observed in Fe_3O_4/YSZ(111) after annealing. An unexpected four-fold anisotropy is observed in the FMR data, but after annealing the expected six-fold anisotropy is recovered (with an additional uniaxial component which is likely induced by step-edges on the substrate). HAADF-STEM performed on the Fe_3O_4 samples confirms the presence of APB defects and a large mixing layer between the thin film and the substrate, both of which are reduced by the annealing process. The origin of the four-fold anisotropy in the non-annealed film requires further study.

The magnetic properties are also improved, as observed in the increased squareness and $\mathbf{M}_s$ observed in the VSM as well as a reduced $\mathbf{H}_{coer}$. The total damping is reduced as observed in the narrowing of the FMR linewidth. This reduction correlates strongly with the change in the microstructure of the Fe_3O_4. This improvement in the structure is seen to correspond to a reduction in the antiphase boundary density. Thermal annealing has been shown in other studies to reduce the APB density in Fe_3O_4 on YSZ(111) thin films, which decreases the extrinsic damping $\Delta\mathbf{H}(0)$.

XMCD data from these samples show a considerable change in the occupation of iron in different lattice sites before and after the annealing process, with the poor stoichiometry of the non-annealed film changing to the expected 1:1:1 ratio of occupied sites after annealing. This is especially evident in the Fe^{2+} Oh site where a considerable increase is observed in the annealed sample. Since the Fe^{2+} ion contributes the majority of the orbital angular moment contribution in magnetite, the total orbital moment contribution is increased, which is observed in the integrated

XMCD. However, the increased intrinsic damping from the greater orbital moment must be smaller than the decrease in extrinsic damping which arises from the elimination of the APBs: FMR measurements from the two samples show that the total damping is reduced in post-annealed samples.

It is also observed that the reduction of the defect density does not eliminate the two-magnon scattering behaviour, nor does it decrease the extrinsic damping significantly enough for intrinsic effects to dominate. While the annealing process is seen to significantly improve the damping behaviour of Fe_3O_4/YSZ(111), further improvement to the damping behaviour are required before Fe_3O_4 can be considered viable for spintronic devices.

Chapter 6: CFAS Heusler Alloys

6.1 Introduction

Interest in Heusler Alloys as ferromagnetic materials with low Gilbert damping has grown over the past few decades [228,229] as greater understanding of their properties has been achieved. The low damping makes highly spin-polarised Heusler alloys particularly attractive in potential spintronic device applications. The growth of $Co_2FeAl_{0.5}Si_{0.5}$ (CFAS) is of great interest, since this quaternary Heusler alloy has a high spin polarisation at the Fermi level both predicted and practically observed [9]. A high T_c, high magnetic moment and a Fermi level in the middle of a band gap also make CFAS a very promising candidate for room temperature spintronic applications, and recent experiments have shown that it can be annealed to recover atomically sharp interfaces on technologically relevant substrates such as Ge(111) [121]. Large interface regions between layers give rise to structural disorder and strain in the lattice, which decreases local spin polarisation [13] and interferes with efficient spin injection [121]. The structural disorder also creates additional scattering sites, causing increased damping. It is therefore important to obtain the sharpest interfaces possible for practical applications. As discussed in section 2.6.2, the properties of CFAS are most desirable when the structure occupies the highly-ordered L_{21} state, which is typically reached through thermal annealing at between 550-700^{o}C [119].

In this chapter, structural and magnetic analysis of two series of thin films of CFAS are presented, one grown on Ge(111) and the other on Si(111). The mismatch between CFAS and these substrates has been observed to be small in the literature ($\sim 0.4\%$ for Ge [115] and 4% for Si [116]), so it is expected that a relatively low density of growth defects should arise from this in both sample series. Thermal annealing is expected to improve the structure further, reducing any lingering defects. A series of CFAS thin films have been grown on each substrate and subsequently characterised using magnetic and structural analysis techniques. Thermal annealing has then been performed and the analysis repeated in order to assess the how growth on each of the different substrates affects the properties of CFAS thin films. The chapter concludes with a comparison between the two series and a discussion of the differences arising from the change in substrate.

6.2 Sample Growth and Annealing

Two samples of CFAS were co-deposited by room-temperature molecular beam epitaxy (MBE) using stoichiometric targets of Co, Fe, Al and Si. One sample was grown on a substrate of Ge(111) and the other on Si(111), each to a nominal thickness of 20nm. In both cases, the substrate was pre-cleaned using an aqueous solution of 1% HF, in order to remove contamination and strip away any oxide layer present on the surface. The diamagnetic properties of silicon and germanium are small compared to the ferromagnetism in CFAS and easily accounted for in magnetic measurements.

Initial characterisation experiments were performed on the samples in the as-grown state, after which the samples were cut into 3x3mm^2 sections to be annealed over a range of different temperatures between 350 and 600^{o}C. Each sample was annealed for a period of one hour. For the purposes of this thesis, data from four different samples from each series will be presented: these are the as-grown samples and CFAS annealed at 350, 450 and 500^{o}C in an ultra-high-

vacuum (UHV) chamber at a base pressure of $8x10^{-11}$ mbar. These samples were characterised using a series of techniques including VSM, XRD and TEM, as used in the previous chapter to characterise the Fe_3O_4 samples. After ascertaining the structure of these samples, FMR spectroscopy was then performed to examine the damping behaviour in each of these different samples and how each varies with the annealing temperature.

6.3 Structural Characterisation (CFAS/Ge(111))

A series of techniques were used in order to determine the structure of the CFAS thin films grown for this experiment, including X-ray Diffraction (XRD), X-ray Reflectivity (XRR) and High-Angle Annular Dark-Field Scanning Tunnelling Electron Microscopy (HAADF-STEM). The theory behind these techniques is discussed in section 3.3. For the purposes of analysis, knowledge of the structure and quality of the thin films examined in this chapter is crucial.

6.3.1 X-Ray Diffraction

X-ray diffraction was performed on each sample to determine the structural phase of the CFAS. It is well-known that the structural arrangement of Heusler alloys can be altered depending on the conditions under which they are grown [38,113]. As discussed in section 2.6.2, the L_{21} and B_2 phases of Heusler compounds are different structural arrangements which in turn affect the electronic and magnetic properties of the material. The changes in atomic arrangement are therefore expected to have an impact on the magnetic damping within the CFAS samples studied in this thesis.

As discussed in section 2.6.2, the differences between these structures are commonly observed using X-ray diffraction, since the structural changes give rise to different diffraction peaks based on which x-ray reflections are allowed [110,113]. In the case of CFAS, the structural (444) peak is observed in all of the phases of the material as a result of the fundamental diffraction condition: h+k+l = 4n for cubic crystals, where n is an integer. Reflections which match this condition appear in all phases of CFAS. However, different structural configurations give rise to other diffraction conditions. The even diffraction condition occurs in both L_{21} and B_2 structures, where h+k+l = 4n+2, and therefore the (222) peak is indicative of this behaviour. The odd diffraction condition, arising only from the L_{21} structure, requires that h, k and l are all odd. Therefore the (111) peak appears in the L_{21} structure, but not in B_2 or A_2 ordered films. It is therefore possible to observe the transition between these phases using the XRD technique by observing which reflections arise from the thin film structure. In previous studies of CFAS, the phase transition has been previously observed in epitaxial CFAS at an annealing temperature (T_{an}) ≥ 550°C [38], with the material changing phase from $B_2 < T_{an} < L_{21}$.

For the samples discussed in this thesis, 2θ/ω scans were performed along the (111) plane of the film and then repeated along the (100) plane with the sample at $\chi = 54.7^{o}$ to the original axis [113] as discussed in section 3.2.1 (figure 6.1). With the monochromator eliminating K_{β} and L_{α} peaks, only the K_{α} peaks from the substrate and the sample should appear. In practise, however, this proved to be difficult. While large peaks were observed corresponding to the Ge<111> reflections, it was difficult to observe CFAS peaks in the XRD: an example is shown in figure 6.2. Despite attempts to re-align the XRD system using both automatic and manual methods, retrieving definitive data from the CFAS peaks with reasonable errors proved to be impossible. Rocking curves were attempted over the expected position, but no appreciable response was measured. Rotating the goniometer to $\chi = 54.7^{o}$ also proved ineffective, and no (100) peaks were observed.

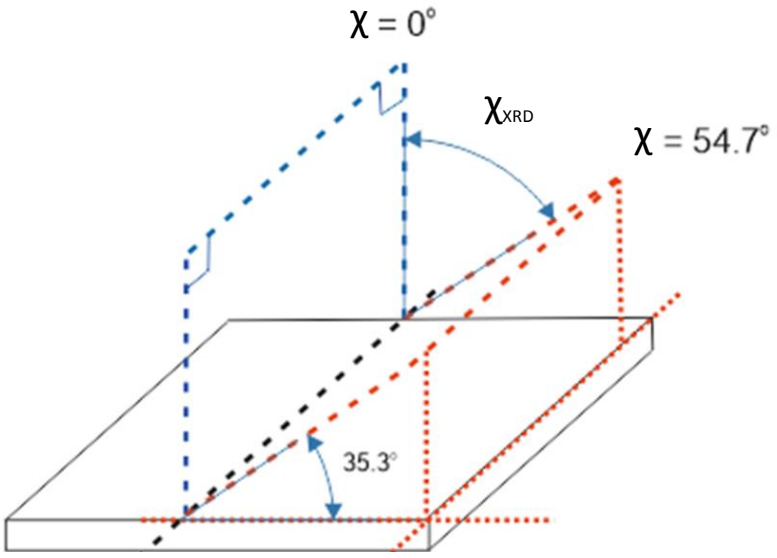

Figure 6.1. *A schematic diagram of the incident x-ray plane relative to the CFAS surface in χ, where $\chi=0^{o}$ (blue) and $\chi=54.7^{o}$ (red) are normal to the (111) and (100) plane axes respectively*

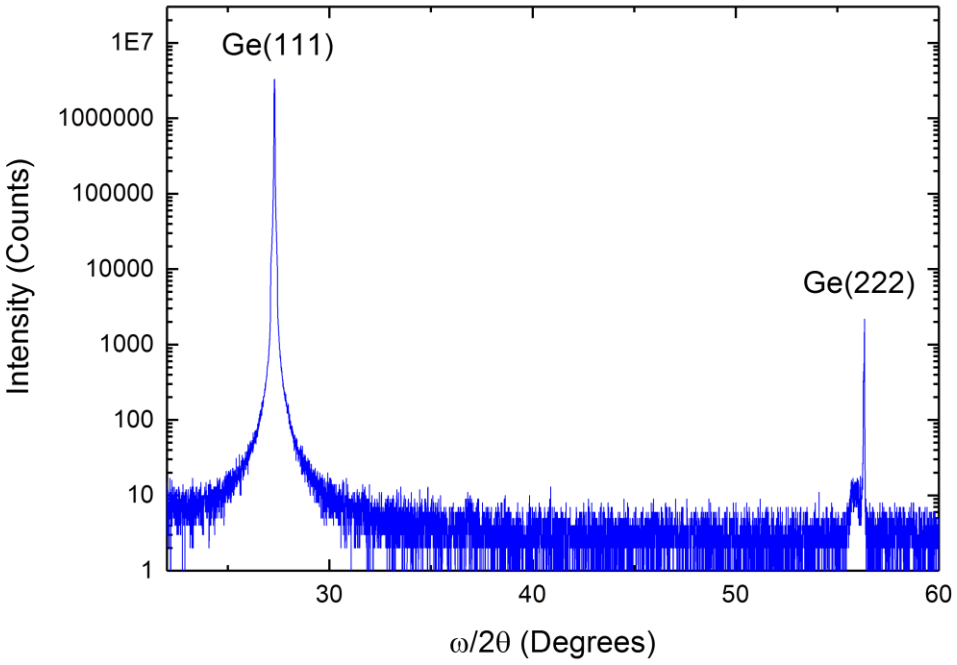

Figure 6.2. *An example XRD 2θ/ω scan from the 450°C annealed CFAS/Ge(111) with the 2-bounce monochromator installed*

For the CFAS grown on Ge substrates, the (222) peak lies almost on top of a substrate peak because of the very small lattice mismatch between CFAS and Ge. This is demonstrated in figure 6.3. Extracted parameters such as integrated intensity and diffraction angle vs anneal temperature are difficult to obtain with reasonable errors. As such the ordering as a function of

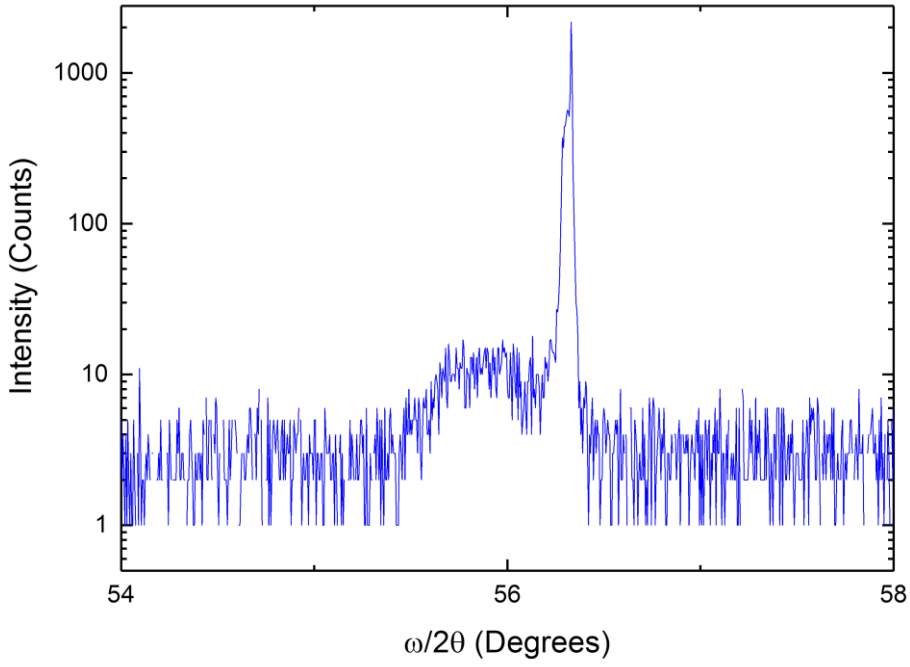

Figure 6.3. *A close-up of the 2θ/ω scan from the 450°C annealed CFAS/Ge(111) at the (222) peak position*

anneal temperature is difficult to obtain from the XRD data. The out-of-plane lattice constant can be approximated, since the peak can be extracted, but determining useful parameters within reasonable errors is difficult in this data. Due to the 0.4% mismatch between the Ge and CFAS, and the close match between the (222) peak positions in the materials, the peaks overlap closely and are difficult to separate from each other. In order to fully characterise the structure of these thin films, an alternative method was required.

6.3.2 HAADF-STEM

TEM was performed on the films after the magnetic analysis was completed, due to the destructive nature of the technique. However, this cross-sectional imaging technique provides excellent insight into the structure, far beyond what was observed in the XRD measurements.

HAADF-STEM images from the as-grown CFAS/Ge(111) are shown in figure 6.4. The cross section of the thin film is shown in figure 6.4.a. Comparing the sample relative to the scale bar yields a thickness of 18 ± 0.5nm. The observed interface between the thin film and the substrate is very well defined, but difficult to quantify in a low magnification image. Selective area diffraction was performed at the crystal/interface substrate along the [110] zone axis, both showing the single crystal structure in the CFAS and confirming that the sample growth was epitaxial with the substrate (figure 6.4.b).

Figure 6.4.c is the high-magnification HAADF-STEM image of the crystal/substrate interface aligned along the [1$\bar{1}$0] direction. This direction is chosen because it allows easy examination of the structural order: in the [1$\bar{1}$0] direction, the X and Y/Z sublattices are arranged in alternating lattice planes. It is observed from the image that the CFAS crystallises in the B_2 structure. This is

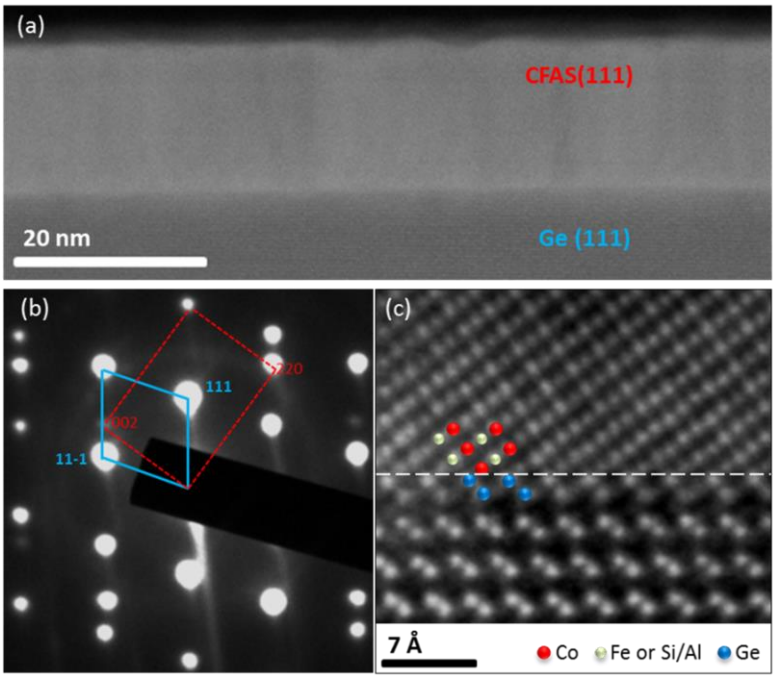

Figure 6.4. *HAADF-STEM images recorded from the as-grown CFAS/Ge(111). a) a low-magnification image used to determine the sample thickness. b) a SAED pattern from the interface between the crystal (red) and substrate (blue). c) A high magnification HAADF-STEM image along the [1$\bar{1}$0] axis at the crystal/substrate interface. The CFAS structure (red/white) is characteristic of the B_2 phase*

evident from the alternating z-contrast between adjacent layers in the structure: Y/Z sublattice disorder is observed in the crystal planes alternating between Co sublattice (in the red sites in figure 6.4.c) and Fe-Al/Si occupation (the yellow sites in figure 6.4.c). The intensity of the Fe-Al/Sisites shows disorder, indicating B_2 structure, rather than a repeating pattern alternating between lighter and darker atoms, as would be expected from the L_{21} structure. The interface with the Ge substrate (blue) is atomically sharp, with little mixing between the Ge atoms and the CFAS structure. The interface region is observed to be ~1nm in depth. It should also be noted that small diffusion of Ge along the Fe-Si planes is observed, as described in previous experiments [121].

Further experiments were carried out on the annealed film series by performing aberration-corrected electron microscopy using the HAADF-STEM. In conjunction with this, elemental mapping was performed using EELS as the contrast mechanism. The images recorded from these experiments are shown in figure 6.5. This figure consists of both the high-magnification HAADF-STEM (presented on the left of each image, in greyscale) and the EELS map of the same area (on the right, in colour) showing the $L_{2,3}$ edges in cobalt (red) and germanium (green). The as-grown sample (figure 6.4.a) and the 350^{o}C annealed sample (figure 6.5.b) show a clear interface between the two chemical species, showing that the interface is sharp and well defined. Comparing this region with the scale bar returns an interface region of 1nm, with little outdiffusion of the Ge into the CFAS thin film. In both cases, the CFAS thin film structure is consistent. The 500^{o}C annealed thin film shows that the mixing region between the crystal structure and the substrate is considerably increased. It can be observed in figure 6.4.c that the mixing region is extended to 3nm. This increase in intermixing results in a secondary material phase which accounts for ~16% of the film thickness. This phase is seen to be rich in Ge, based on the EELS imaging, and therefore is expected to reduce the total magnetisation by a similar factor. This is indeed observed in the magnetic characterisation in section 6.4.

Due to the destructive nature of the preparation process, TEM was the last experiment that was performed on each of the samples. This data was published in a recent article by Kuerbanjiang

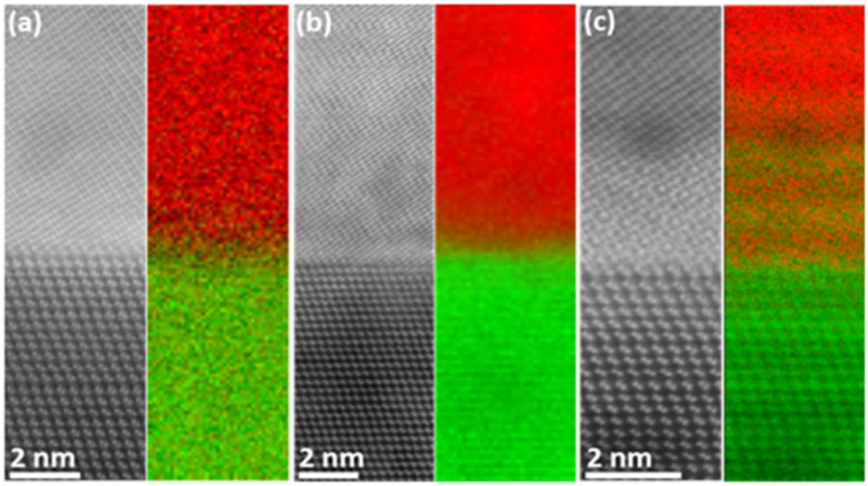

Figure 6.5. *Paired figures presenting the HAADF-STEM images (greyscale) and EELS chemical maps (coloured) from the CFAS/Ge(111) interface in the a) as-grown and annealed at b) 350^{o}C and c) 500^{o}C. In each image, the CFAS $L_{2,3}$ edges occupy the upper (red) layer and the Ge $L_{2,3}$ edges are the lower (green) layer*

[115]. This paper includes further information regarding the TEM from this sample, including a discussion of higher temperature annealing effects, and DFT calculations concerning the corresponding site occupation.

6.4 Magnetic Characterisation (CFAS/Ge(111))

Since the initial structural analysis confirmed that the samples are epitaxial CFAS, the next step is to examine the magnetic properties of the thin films. This requires analysis of each sample using some different characterisation techniques, including vibrating sample magnetometry (VSM) and Ferromagnetic Resonance Spectroscopy (FMR).

6.4.1 VSM

M(**H**) VSM was performed on the CFAS samples to investigate their magnetic properties. In-plane VSM was performed using a DMS Model 10 VSM on each sample along a series of orientations including the easy and hard axes. Each of the samples shows a characteristic easy axis with a very square hysteresis loop which becomes more rounded as the hard axis is approached. The easy and hard axes are seen to be 90° apart, suggesting a two-fold anisotropy in the plane of the samples. The in-plane VSM hysteresis loops observed for all the CFAS samples show characteristic ferromagnetic behaviour with one material phase. This data is shown in figure 6.6.

The data recorded shows square hysteresis loops with narrow openings, indicating alignment with the easy axis and small coercive fields respectively. The coercive field is more easily seen in the inset to figure 6.6, which shows the same data over a narrow field range around **H** = 0 Oe. The 350°C data has been omitted from the graph for clarity, but has a similar shape and follows the

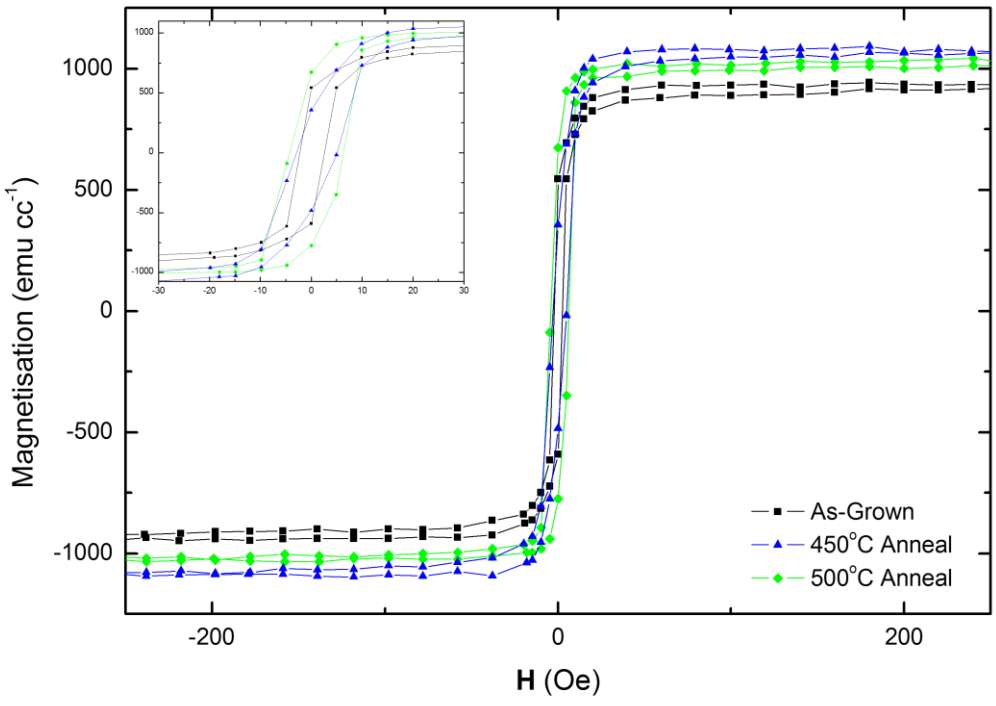

Figure 6.6. *A comparison of the **M**(**H**) hysteresis loops collected from the CFAS/Ge(111) VSM. Data from the 350°C annealed sample is omitted for clarity*

same trends in the parameters. The $\mathbf{M}_s$ value is seen to improve when the sample is annealed, suggesting improvement of the overall magnetic structure. Further improvement is observed when the annealing temperature is increased, as the 450°C anneal data shows a reduced $\mathbf{H}_c$ and an increased $\mathbf{M}_s$ compared to T_{an} = 350°C. As T_{an} increases from 450°C to 500°C, however, the magnetic properties become less bulk-like, suggesting some negative impact on the magnetic structure. $\mathbf{M}_s$ is reduced and the coercivity increases. This occurs in parallel with the reduction in structural quality as observed in the HAADF-STEM, as the outdiffusion of the substrate material into the sample occurs at 500°C, which correlates strongly with the effects observed in the VSM.

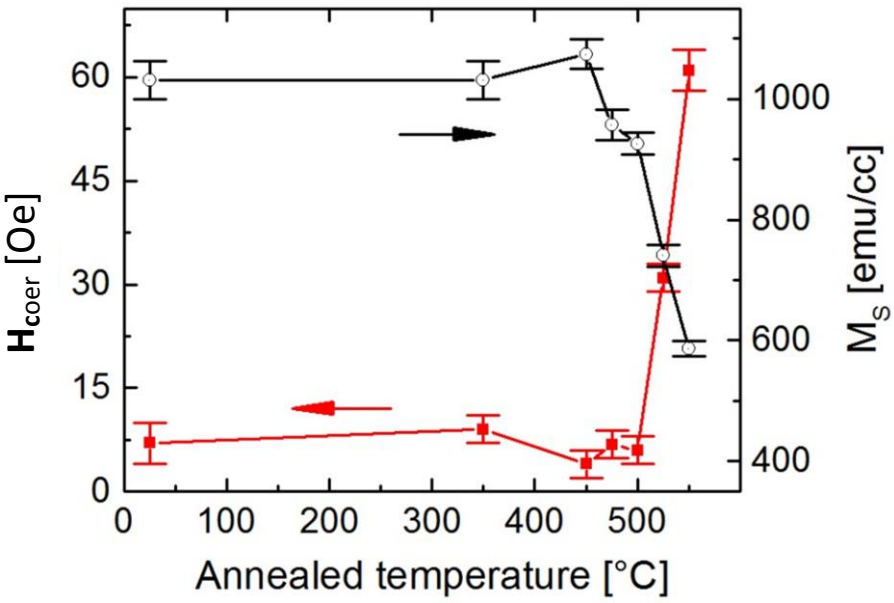

Figure 6.7. *Data derived from the VSM from CFAS/Ge(111) series [108], showing the magnetization (black) and the coercive field (red) as a function of anneal temperature*

The saturation magnetisation ($\mathbf{M}_s$) and coercive field ($\mathbf{H}_{coer}$) values have been extracted from each different sample along the magnetic easy axis. A comparison of the values extracted from each sample is shown in figure 6.7. No change in the easy axis direction is observed as T_{an} was increased. It is observed that $\mathbf{M}_s$ is constant, within error, for the as-grown, 350 and 450°C annealed samples, at values of 1050 ± 30 emu cc^{-1}, in line with the literature value of 1100 emu cc^{-1} [112]. Above this temperature, however, a significant decrease is observed with the T_{an} = 500°C showing $\mathbf{M}_s$ = 930 ±20 emu cc^{-1}. $\mathbf{H}_{coer}$ also remains approximately constant at 7 ± 3 Oe until T_{an}>500°C where a significant increase is observed (by T_{an}=550°C, $\mathbf{H}_{coer}$ has increased threefold, and the trend continues as T_{an} increases further). The combination of these effects suggests a change in the magnetic structure of the samples at this temperature. More information about this sample has been published in a recent paper [115].

6.4.2 Ferromagnetic Resonance Spectroscopy

VNA-FMR spectroscopy was performed on the CFAS samples as described in chapters 2 and 3. This allowed the in-plane anisotropy and the damping behaviour to be investigated in each CFAS/Ge sample at each annealing temperature for comparison. The easy axis Kittel curve from each sample is shown in figure 6.8, including an example of the VNA-FMR linescans for reference

shown in the inset of figure 6.8.a. The α and $\mathbf{M}_s$ parameters extracted from fitting these curves with equation 2.40 are collected in table 6.1.

As discussed in chapters 2 and 3, the magnetic torque experienced by the magnetisation is minimised as the rotation of the magnet reaches close to 90 degrees, which reduced the precession amplitude at these angles to almost zero and therefore renders the data impractical for the purposes of extracting fitted parameters. It was therefore necessary to rotate the samples and repeat the azimuthal sweep in order to obtain reliable data. A rotation of 90 degrees was chosen in order to maximise the signal observed from these regions in the second sweep. The datasets could then be directly compared and, with suitable overlap between the two sets found in each case, combined to give a complete picture of the anisotropy over this range. Given the symmetry of the crystal structure, this anisotropy behaviour must be repeated in the opposite 180^o arc, and therefore the data was mirrored to complete a 360^o polar plot of the in-plane anisotropy. Azimuthal plots of the $\mathbf{H}_r(\theta)$ at a fixed frequency of 10GHz are presented in section 6.4.2.1.

VNA-FMR was performed on all samples over a field range between 0-3kOe in steps of 10Oe, and a frequency range of 10kHz-20GHz in 801 equally spaced frequency steps. The azimuthal angle was rotated in steps of 10 degrees over a range between -90 to 90 degrees around the '0 degrees' position. All the VNA-FMR experiments discussed here were performed over a field range between $0 \leq \mathbf{H} \leq 3$kOe in steps of 5Oe, at the maximum RF power of +8dBm.

The $\mathbf{M}_s$ values quoted here are different from those recorded in the VSM in section 6.4.1. The $\mathbf{M}_s$ from the VSM was calculated by using an approximate volume measurement, with a 10% error on the thickness, which has a significant impact on the $\mathbf{M}_s$ value as a result. The data extracted from the VNA-FMR returns a value in emu cc^{-1} without the need for this volume approximation and is therefore likely to be more reliable. Other effects such as the oxidation of the samples and the outdiffusion of substrate material into the thin film could also change the thickness, which further increases the uncertainty on the VSM measurement. As well as changing the physical thickness of the thin film layer, any outdiffusion would also result in a reduced thickness of the magnetic layer: the substrate material invading the crystal structure will reduce the total magnetisation and disrupt the magnetic structure of the sample. The volume used to convert the VSM data into emu cc^{-1} assumes a perfect magnetic structure, but the HAADF-STEM in section 6.4.3 proves that this is not the case. The resulting division by a larger thickness value than is technically accurate results in an artificially reduced value for $\mathbf{M}_s$.

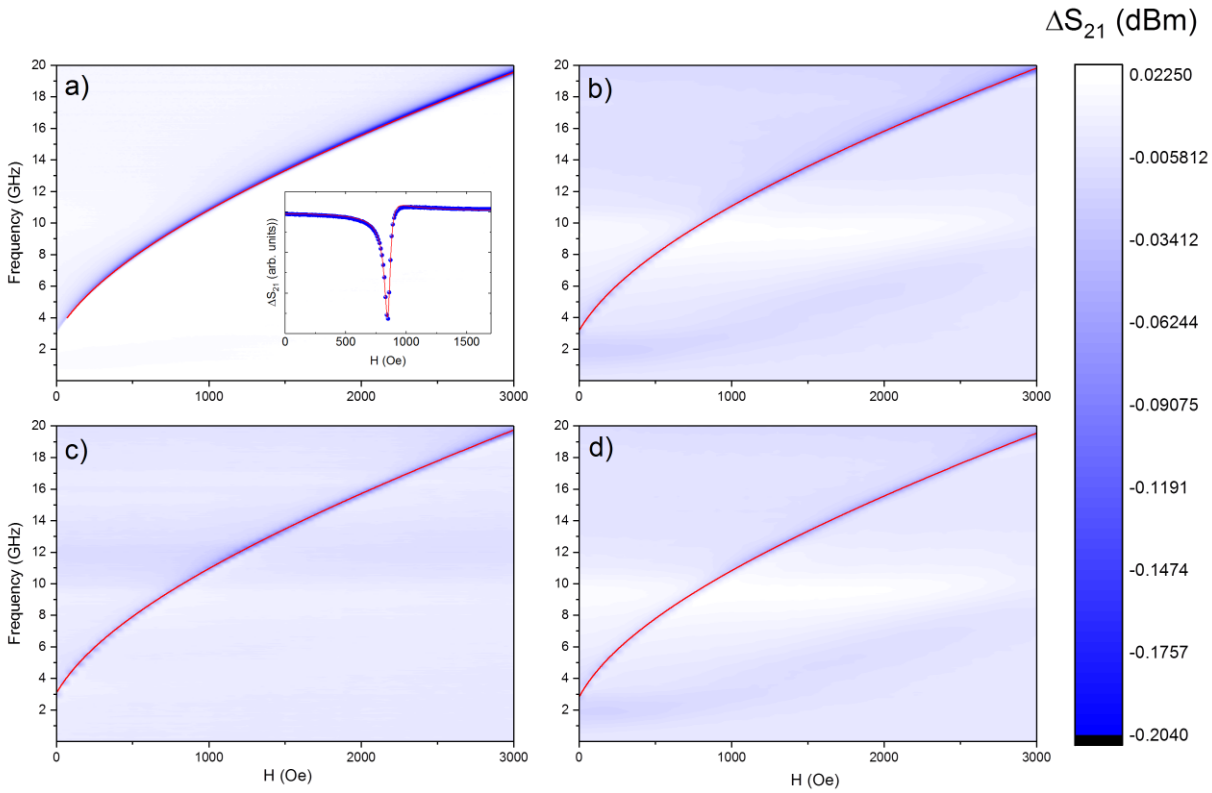

Figure 6.8. *Easy axis Kittel curves measured from the as-grown CFAS/Ge(111) at T_{an} = a) as-grown, b) 350°C, c) 450°C and d) 500°C. The red line is included as a guide to the fit. (a) Inset) The fixed-frequency linescan at 10GHz (blue) including the asymmetric lorentzian fit (red)*

Table 6.1. *Data table containing the magnetic parameters H_{cubic}, H_u, M_s and α for the CFAS/Ge(111) as a function of anneal temperature*

Substrate	Anneal temperature (°C)	H_{cubic} (Oe)	H_u (Oe)	M_s (emu / cc)	α (x10^{-3})
Ge	As-grown	2.8 ± 2	28.5 ± 2	1025 ± 0.4	5.6 ± 0.1
	350	2.4 ± 2	22.1 ± 2	1080 ± 0.5	3.8 ± 0.1
	450	2.4 ± 2	20.8 ± 2	1048 ± 0.4	2.8 ± 0.1
	500	1.6 ± 2	15 ± 2	1051 ± 0.3	--

6.4.2.1 Anisotropy Measurements

The in-plane anisotropy of each sample was investigated using the VNA-FMR technique to record azimuthal sweeps from each sample in 5 degree steps over a 180° range, centred on the initial '0 degrees' position. After the growth of each sample, a fine line was scratched into the substrate along the [11$\bar{2}$] axis using a diamond-tipped scribe. It was therefore possible to mount each sample in the same relative orientation during the VNA-FMR measurements. For consistency, each sample was measured initially with the [$\bar{1}$10] axis parallel to the waveguide transmission line at 0 degrees, as shown in figure 6.9. Linescans at a fixed frequency of 10GHz were extracted from each of the VNA-FMR datasets and then fitted using an asymmetric Lorentzian function to determine the position of the resonance field ($\mathbf{H}_r$). The variation of H_r as a function of azimuthal angle (ϕ) was then plotted in order to measure the anisotropy. Since the linescans were taken by varying the bias field at a fixed frequency, the easy axis is identified at the minimum resonance field of each polar plot.

The anisotropy data from each of the CFAS/Ge samples is presented in figure 6.10. A uniaxial anisotropy is observed in each sample with an easy axis centred on +60 degrees. This corresponds to the [$\bar{1}$01], relative to the [$\bar{1}$10] axis at 0 degrees. The total anisotropy, determined by the difference between the maxima and minima in $\mathbf{H}_r$, is seen to decrease as T_{an} increases. The anisotropy is observed at a maximum of 33.9 ± 0.5 Oe in the as-grown sample and diminishing as the annealing temperature increases to 21 ± 0.5 Oe in the 500°C sample (as shown in figure 6.10). The magnetocrystalline anisotropy in CFAS is cubic, as observed by Gabor *et.al* [38] and therefore a 6-fold anisotropy is expected in the (111) plane as discussed in section 2.3.2, instead of the observed uniaxial anisotropy. This discrepancy is attributed to a shape anisotropy arising from step-edges on the surface of the substrate, similar to that observed in Fe thin films on stepped substrates [222,230]. In order to separate out the separate contributions of the cubic and shape anisotropy fields, fits were performed to this data using the field space anisotropy fit equation B.8, as discussed in appendix B. The anisotropy plots show a deviation from the typical

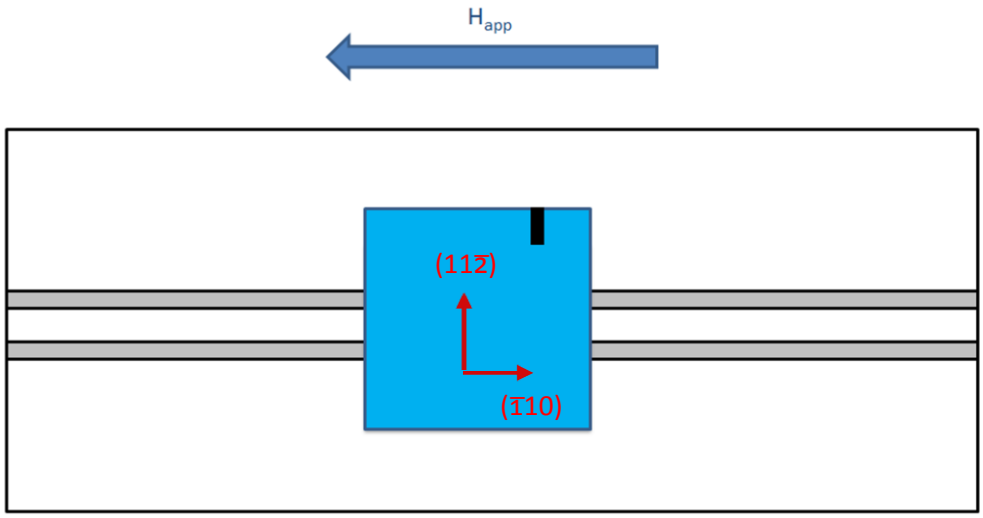

Figure 6.9. *A schematic diagram showing the relative orientation of the scratch perpendicular to the 11$\bar{2}$ axis of the sample (shown in black) and the CPW in the '0 degrees' position. The bias field direction is shown in blue*

sin^2dependence, with a dominant uniaxial term and a small cubic term. The anisotropy data has been fitted, allowing extraction of the cubic and uniaxial anisotropy field contributions. These values are presented in table 6.1, with the individual anisotropy parameters plotted as a function of annealing temperature in figure 6.11. In all the CFAS/Ge samples, the uniaxial anisotropy field is an order of magnitude larger than the cubic term, and therefore it dominated the form of the anisotropy.

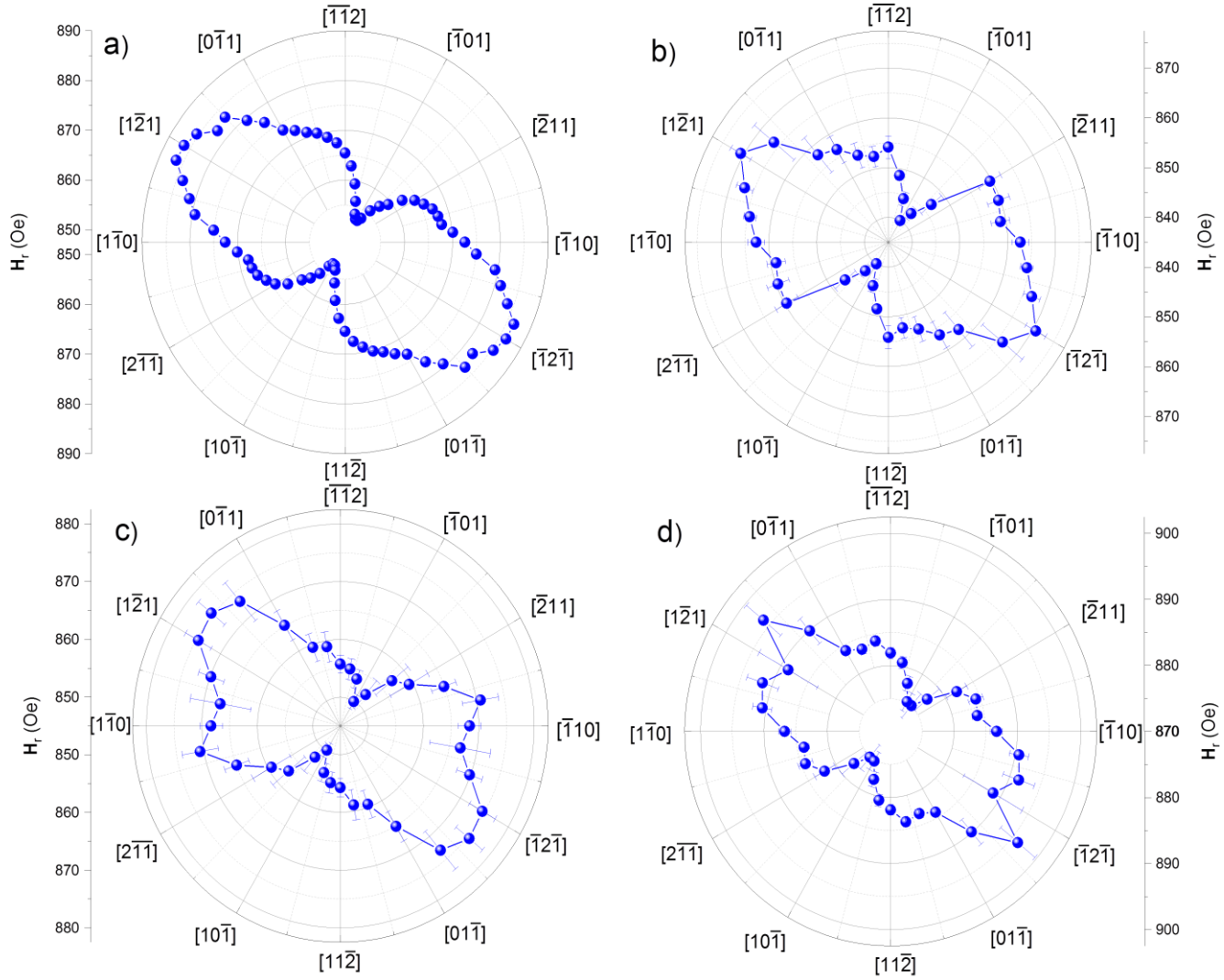

Figure 6.10 *$H_r(\phi)$ extracted from VNA-FMR data from the CFAS/Ge(111) samples at T_{an} = a) as-grown, b) 350°C, c) 450°C and d) 500°C. A uniaxial anisotropy is observed, with an easy axis at [1̄01] (+60 degrees to the [1̄10] at 0 degrees)*

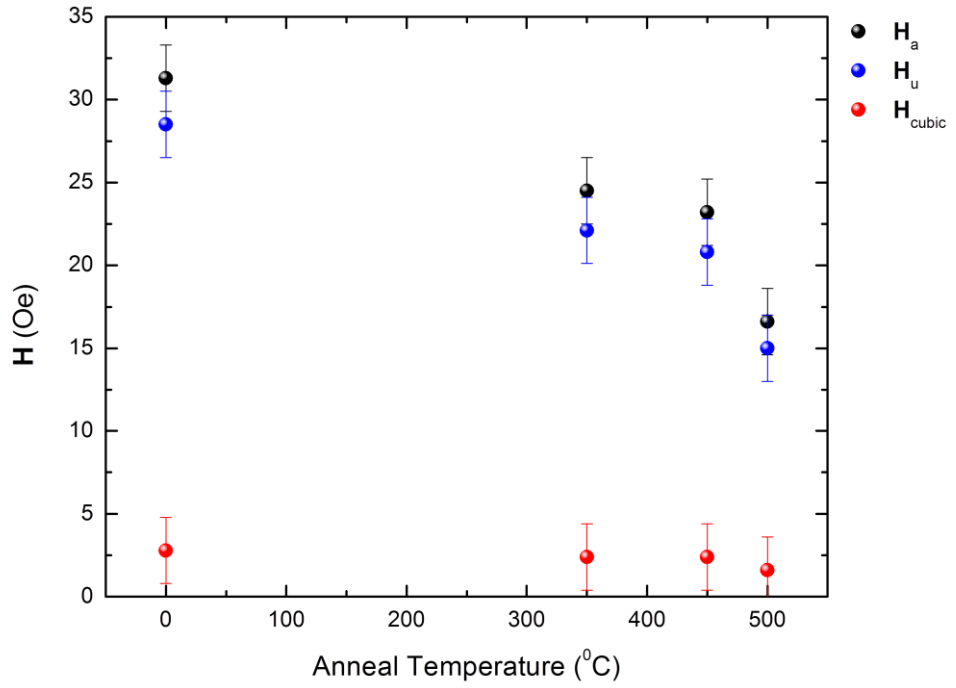

Figure 6.11. *The total (black), cubic (red) and uniaxial (blue) anisotropy field contributions extracted from the CFAS/Ge(111) VNA-FMR polar plots*

6.4.2.2 Damping Measurements

A study of the damping behaviour in these CFAS/Ge thin films was carried out. Since no out-of-plane magnetisation component was observed in the VSM, the saturated magnetisation is completely aligned in the sample plane. It can therefore be assumed that the simplified form of the Kittel equation can be applied to measurements from these samples when a Kittel curve is observed. The parameters extracted from these fits therefore reliably represent the magnetic parameters of the CFAS.

VNA-FMR spectroscopy was performed along the easy axis of each sample. Intense Kittel curves were observed in each sample, shown in figure 6.8, from which a series of linescans were extracted at fixed frequencies. The HWHM (the linewidth $\Delta\mathbf{H}$) is determined by fitting the corresponding field scan using the asymmetric lorentzian function (equation 3.15) discussed in section 3.3.2.1. This was repeated at 1GHz frequency intervals, and $\Delta\mathbf{H}$ was plotted as a function of applied RF frequency to examine the damping. Fitting $\Delta\mathbf{H}$ as a function of frequency using equation 2.45 allowed characteristic damping parameters such as $\Delta\mathbf{H}_0$ and α to be extracted. Plots of $\Delta\mathbf{H}$ as a function of frequency from each sample are shown in figure 6.12.

It is found that the Gilbert damping in the CFAS grown on Ge shows a linear relationship in the as-grown phase and when annealed up to a certain temperature. However, when $T_{an} \geq 500^{o}C$, a change in the damping behaviour is observed from the dominant Gilbert damping to damping characteristic of two-magnon scattering like behaviour. This shows that at these temperatures the extrinsic 2-magnon damping begins to dominate. This change in the magnetic properties above $T_{an} = 500^{o}C$ is attributed to magnetic inhomogeneity or the introduction of a mixed-phase into the

film. This change in the dominant damping behaviour correlates strongly with the out-diffusion of atoms from the Ge substrate into the CFAS thin film [115] as observed in the TEM.

For CFAS/Ge(111) α, decreases for both the 350 °C and 450 °C annealed samples, $\alpha = 3.8\times10^{-3}$ and 2.8×10^{-3} respectively, compared to the as-grown sample, $\alpha = 5.6\times10^{-3}$, whilst the extrinsic damping remains approximately constant. The change in α as a function of T_{an} can be seen in figure 6.13. The sample annealed at 450 °C shows a Gilbert damping parameter 2-3 times smaller than for permalloy [231] and compares well to values found in the literature for CFAS and other full Heusler films [122,232,233]. At 500 °C the shape of $\Delta\mathbf{H}$ as a function of frequency deviates significantly from a linear behaviour with $\Delta\mathbf{H}$ increasing, compared to 450°C, for each frequency. Thus T_{an} = 450 °C seems to be the optimal temperature for reducing the Gilbert damping. Above 500 °C, the frequency dependent linewidth shows a characteristic two-magnon scattering line-shape indicating magnetic inhomogeneities or mixed magnetic phases within the sample.

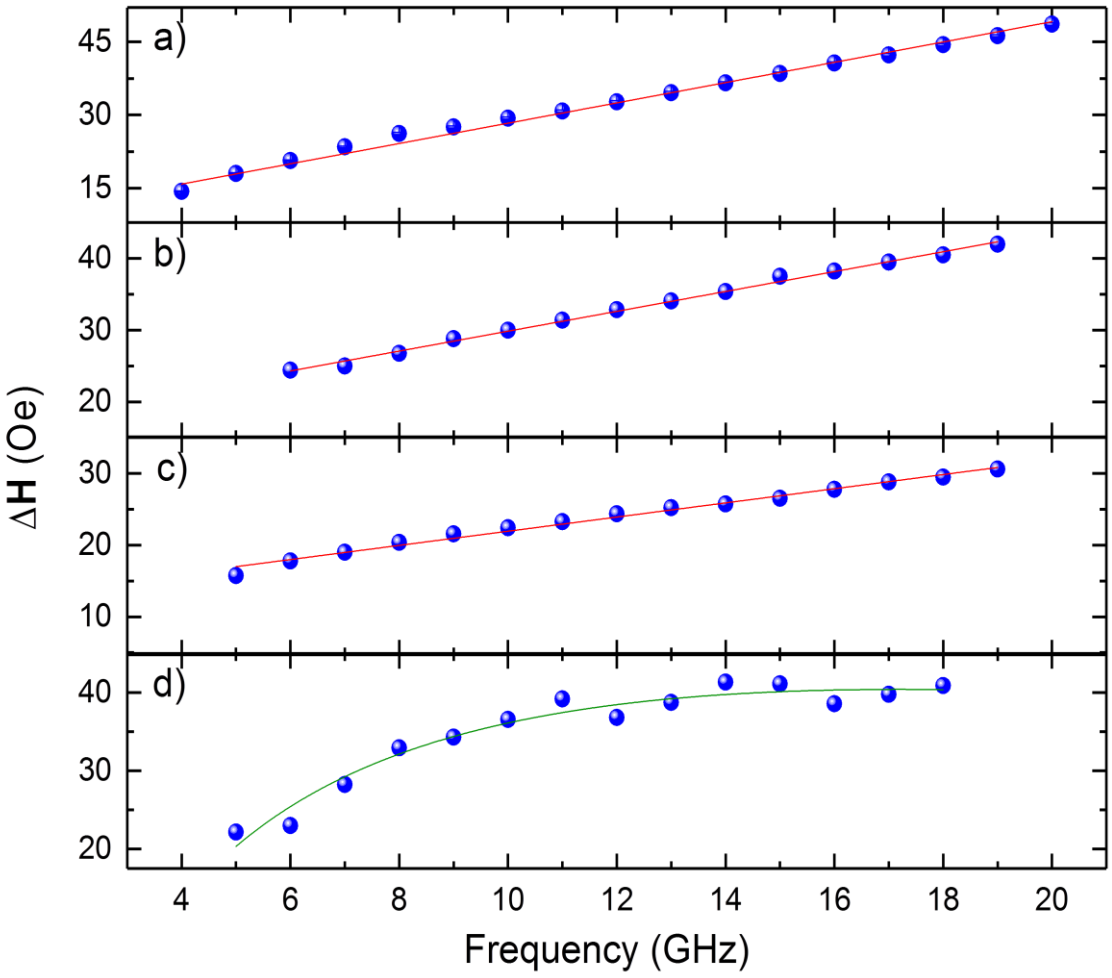

Figure 6.12. *A comparison of $\Delta\mathbf{H}(f)$ in CFAS/Ge(111) (a) as-grown and annealed at (b) 350°C, (c) 450°C and (d) 500°. The green line in (d) is included as a guide*

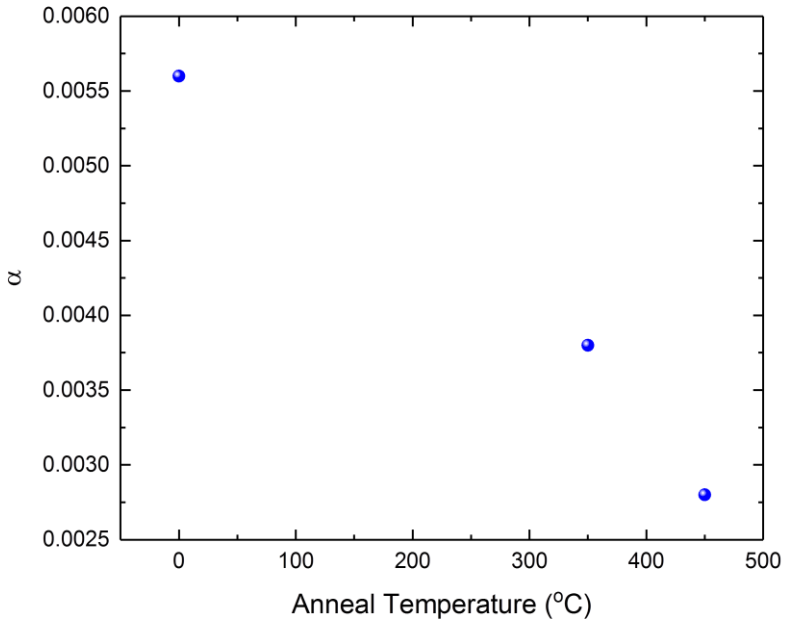

Figure 6.13. *α as a function of annealing temperature for the CFAS/Ge(111) sample series*

6.5 Structural Characterisation (CFAS/Si(111))

The CFAS/Si samples were analysed using a series of XRD and TEM to confirm the structure of the thin films after growth. Once annealed, the analysis of each sample in the series allowed the investigation of the film structure and observation of how the structure changes as a result of the annealing at different temperatures.

6.5.1 X-Ray Diffraction

As in the CFAS on Ge, the CFAS samples grown on Si(111) were examined using XRD in order to assess their structural make-up. 2θ/ω scans were performed in order to observe the {111} family of peaks. However, in the case of the CFAS on Si, the peaks returned by the XRD were weak, as shown in figure 6.14. In each set, difficulty was found observing in the (100) plane and the peaks are of very low intensity. The (222) peak indicating the B_2 phase is observed in all of the samples, while no (111) peaks appear, showing that the transition to the L_{21} phase is not achieved. However, without being able to observe the corresponding peaks in the (100) plane, this is difficult to confirm. This made the structural phase of each sample difficult to determine using this technique. As a result, a different method of structural analysis was required.

XRD measured from the CFAS/Si(111) before the introduction of the monochromator is presented in figure 6.14. Figure 6.15 shows the XRD data around the position of the (222) reflection for CFAS/Si(111). Symmetric 2θ/ω scans were used to obtain information on the {111} family of planes. The presence of the fundamental (444) reflection, corresponding to the cubic structure (not shown), and the (222) diffraction peak is indicative of B_2 ordering. The diffraction peaks were fitted with Voigt functions in order to extract the diffraction angle (2θ), integrated intensity (I) and Lorentzian linewidth (Δ_L). The Gaussian linewidth, due to instrumental broadening, was kept constant at 0.587 degrees during the fitting. A lattice parameter of 5.68 ± 0.001 Å for the as-grown film is obtained from the diffraction data, consistent with that reported previously for CFAS on Si [110,234]. Upon annealing, the integrated intensity of the (222) reflection increases with

anneal temperature up to 350°C (figure 6.14.a and d), indicating improved B_2 ordering. At higher anneal temperatures (T_{an} > 350°C) the (222) integrated peak intensity decreases implying that the B_2 ordering is progressively weakening. In addition, the diffraction angle (2θ) can be seen to move to higher angle with anneal temperature corresponding to a reduction in lattice constant. The (111) reflection associated with the full L_{21} chemical ordering is absent in all the films measured.

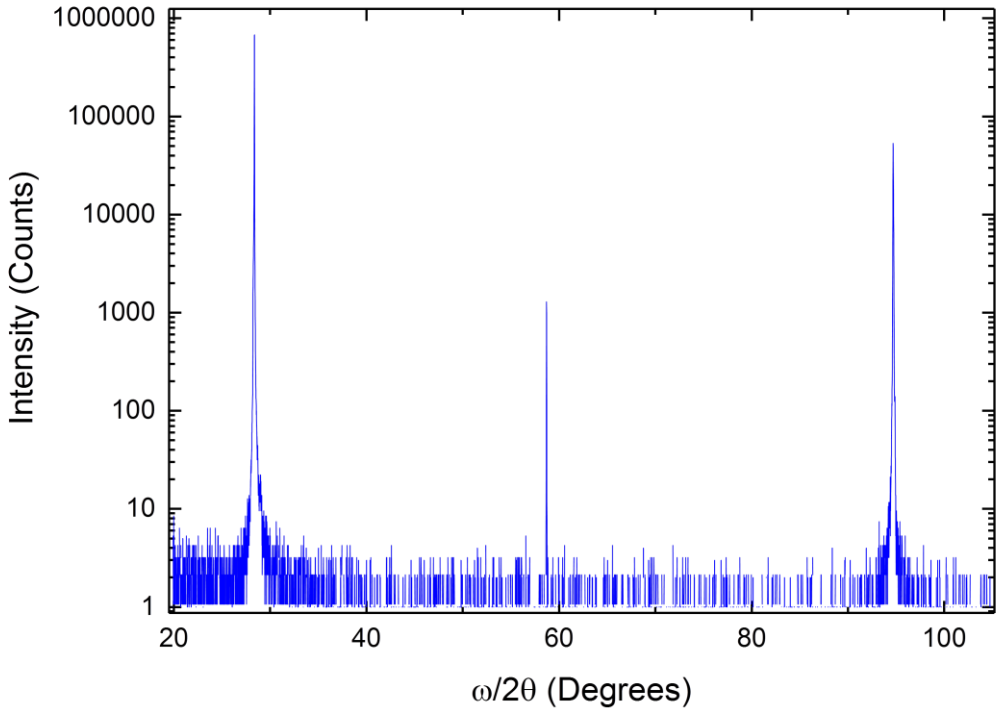

Figure 6.14. *An example 2ϑ/ω XRD scan from the 450°C annealed CFAS/Si(111) with the monochromator installed*

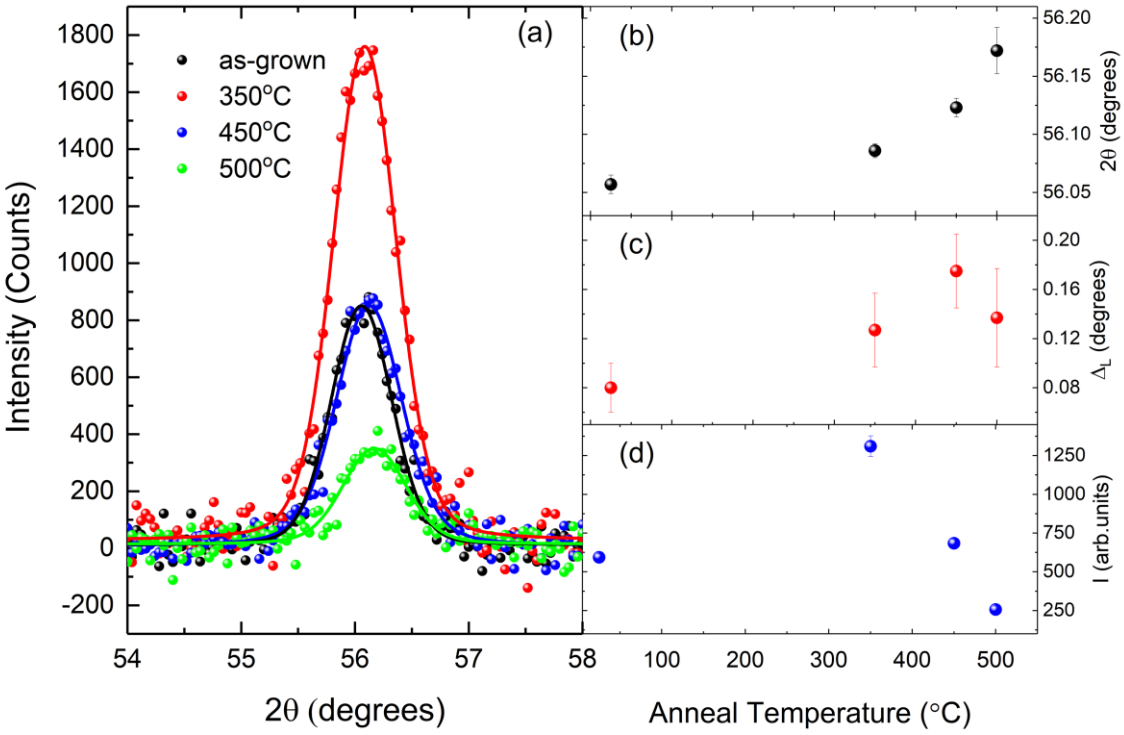

Figure 6.15. *XRD analysis over the in CFAS/Si(111) series. a) The ϑ/2ϑ scan from the CFAS (222) peak. A comparison of b) peak position, c) Lorentzian linewidth and d) integrated peak intensity as a function of anneal temperature*

After performing the 2θ/ω scans, X-ray reflectivity (XRR) measurements were performed on these samples in order to determine the sample thickness as discussed in chapter 3.3.1.3. Since all of the samples examined here were cut from one original thin film, a uniform thickness between all of the samples was expected. The results of the XRR from each sample are shown in figure 6.16. Fitting the Kiessig fringes from each sample returns a thickness value of 23 ± 1 nm from each of the samples with the exception of the 500°C anneal sample, which returns a thickness value of 27 ± 1 nm. This unexpected increase in the measured thickness of this sample is consistent over repeated measurements. Since the XRR isn't specifically sensitive to the magnetically active layer, any dead layer or significant feature atop the film would also appear in the scan. Defects in the structure caused by outdiffusion from the substrate may also give rise to this increased thickness, as observed recently in CFAS/Ge films annealed at temperatures above 500°C, which also show this effect [115]. Further examination of this is required in order to verify the cause of this discrepancy; TEM was therefore performed on the samples after the magnetic measurements were completed.

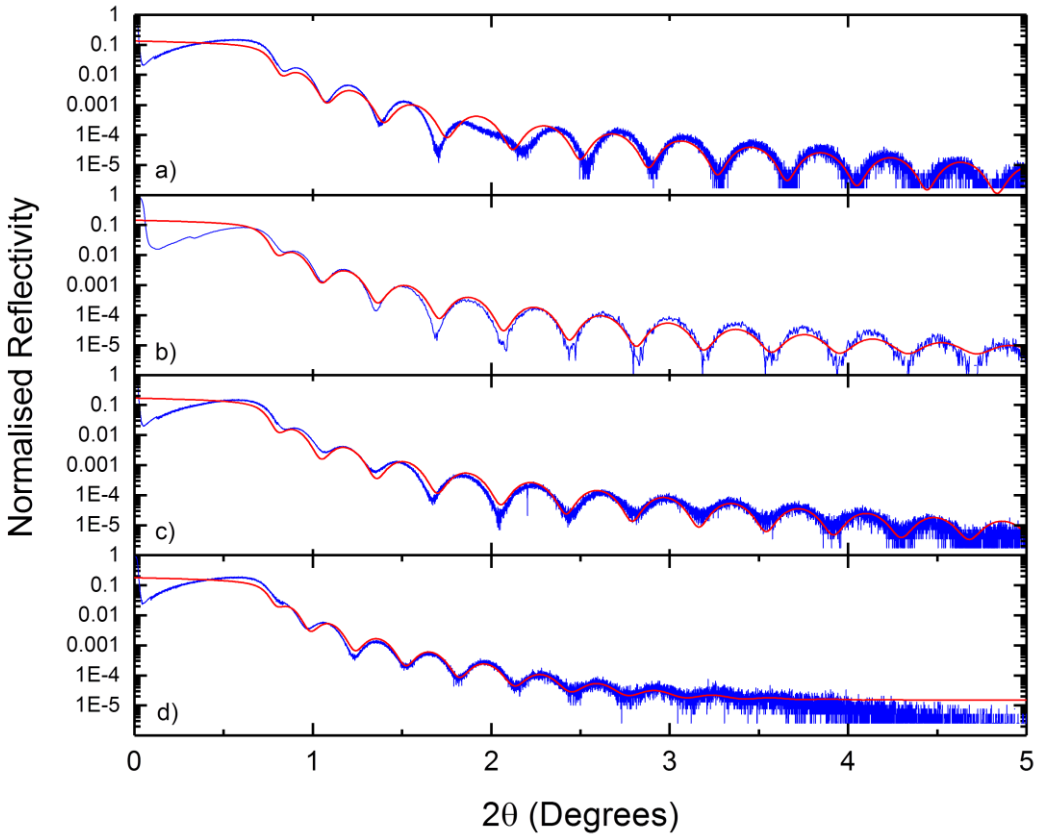

Figure 6.16. *XRR data (blue) from the CFAS/Si samples annealed at a) as-grown b) 350°C c) 450°C and d) 500°C. Fits to each dataset (red) performed using GlobatFit allow the extraction of the film thickness*

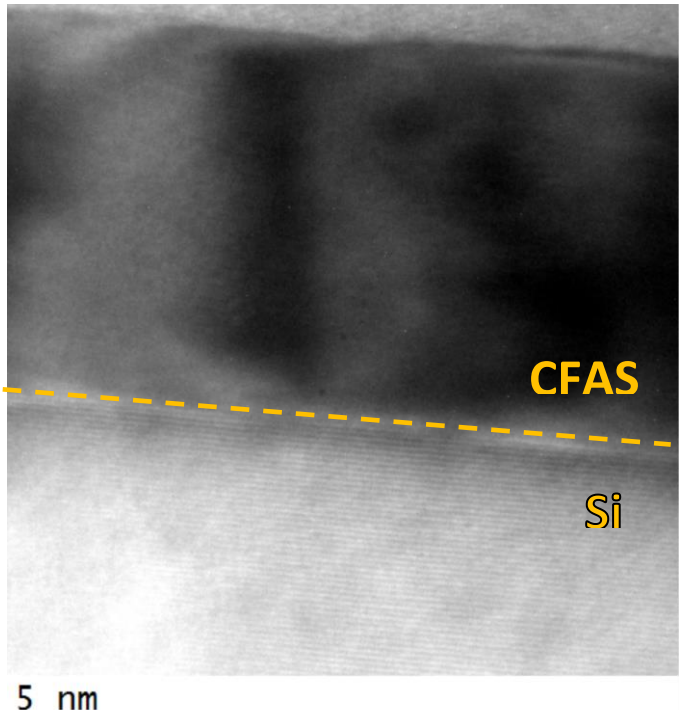

Figure 6.17. *Low-magnification TEM from the CFAS/Si(111) 350°C annealed sample. A narrow interface region (orange) is observed between the CFAS region (darker) and the substrate (lighter)*

6.5.2 HAADF-STEM

To date, two of the samples of the CFAS on Si have been prepared for the HAADF-STEM technique discussed in chapter 2. These are the 350°C and 500°C annealed samples. The TEM confirms that the thickness of the 350°C annealed sample is 21 ± 1 nm, which is consistent with the values observed in the XRR. The thickness of the 500°C sample is 27 ± 1nm, which is also consistent with the increased value observed in the XRR. This confirms that some expansion of the sample has occurred, which is consistent with previous reports of the outdiffusion of substrate material mixing with the CFAS in high-temperature annealing of CFAS/Ge and the expansion of the resulting mixed layer [115]. A step is observed in the 500°C sample, confirming that such effects are present at the sample/substrate interface.

The current series of TEM images are too low-magnification to determine the CFAS structural ordering, but based on the XRD and the similarities to the films grown on Ge, B_2 ordering is expected. Further STEM experiments are ongoing at this time, on both the two samples presented here and the other two samples in the CFAS/Si series. The same outdiffusion of the silicon into the CFAS that is observed in the films grown on Ge is expected, especially at the high temperature range. This would be consistent with the changes in the FMR as the linear Gilbert damping behaviour seen up to 450°C is replaced by the curved two-magnon scattering like behaviour in the 500°C sample. This is somewhat confirmed by the mixing region observed in the 500°C, but requires confirmation using higher magnification STEM and EELS measurements.

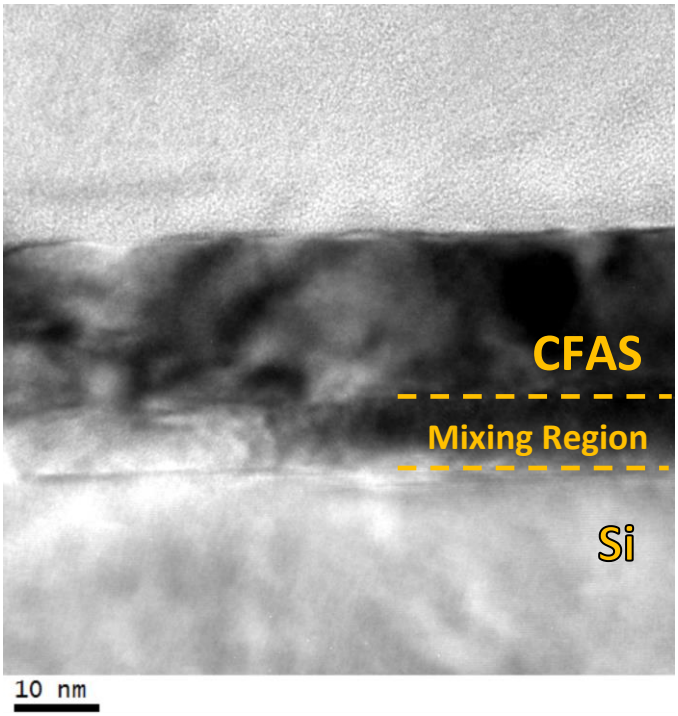

Figure 6.18. *Low-magnification TEM image of the CFAS/Si(111) 500°C annealed sample. A mixing region is observed between the substrate and CFAS layers*

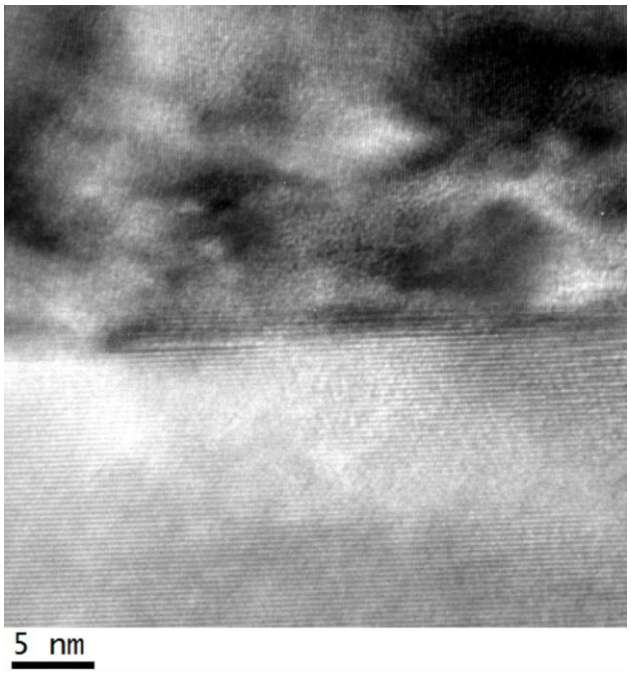

Figure 6.19. *Low magnification TEM image from the CFAS/Si(111) 500^{o}C annealed sample*

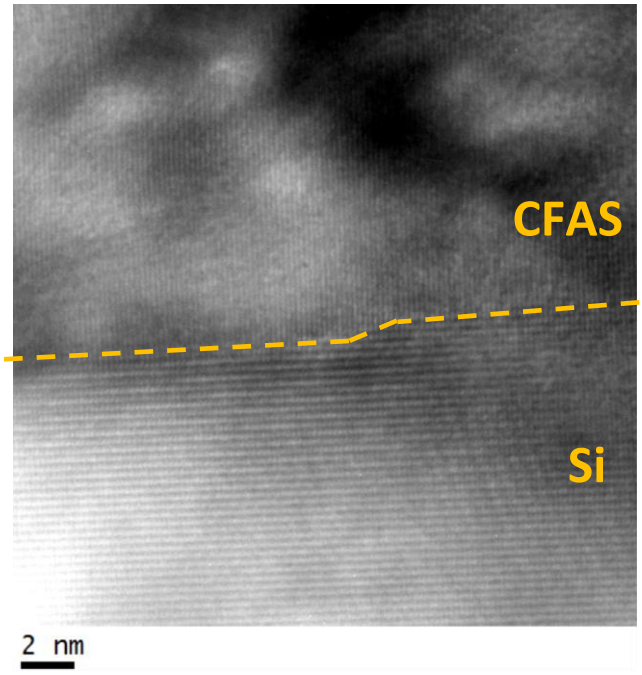

Figure 6.20. *Low-magnification TEM from the CFAS/Si 500^{o}C anneal sample, showing a step in the interface region between CFAS and Si*

6.6 Magnetic Characterisation (CFAS/Si(111))

The magnetic characterisation of these samples was performed using VSM and FMR Spectroscopy in order to allow comparison between the properties of the films grown on the different substrates.

6.6.1 VSM

Vibrating sample magnetometry was performed on the CFAS on Si(111) samples to investigate the alignment of the magnetisation. In-plane VSM was performed using the DMS Model 10 VSM in order to investigate the magnetic behaviour of these samples. A sweep of the magnetic bias field over a range between ±300 Oe was sufficient to saturate the magnetisation and reveal the hysteretic behaviour, as seen in the CFAS on Ge(111) samples. The **M**(**H**) data is shown in figure 6.21 (over a ±100 Oe range for clarity) and the corresponding $\mathbf{M}_s$ and $\mathbf{H}_r$ values extracted in figure 6.22.

Given the unexpectedly large thickness returned by the XRR, $\mathbf{M}_s$ in the 500°C annealed sample was also calculated using the standard 20nm that was observed in the other samples. In each sample, the thickness was multiplied by the sample area, which was measured using the built-in Vernier scale of an optical microscope. The corresponding volume was used to convert the moment (emu) to magnetisation (emu cc^{-1}) in **M**(**H**).

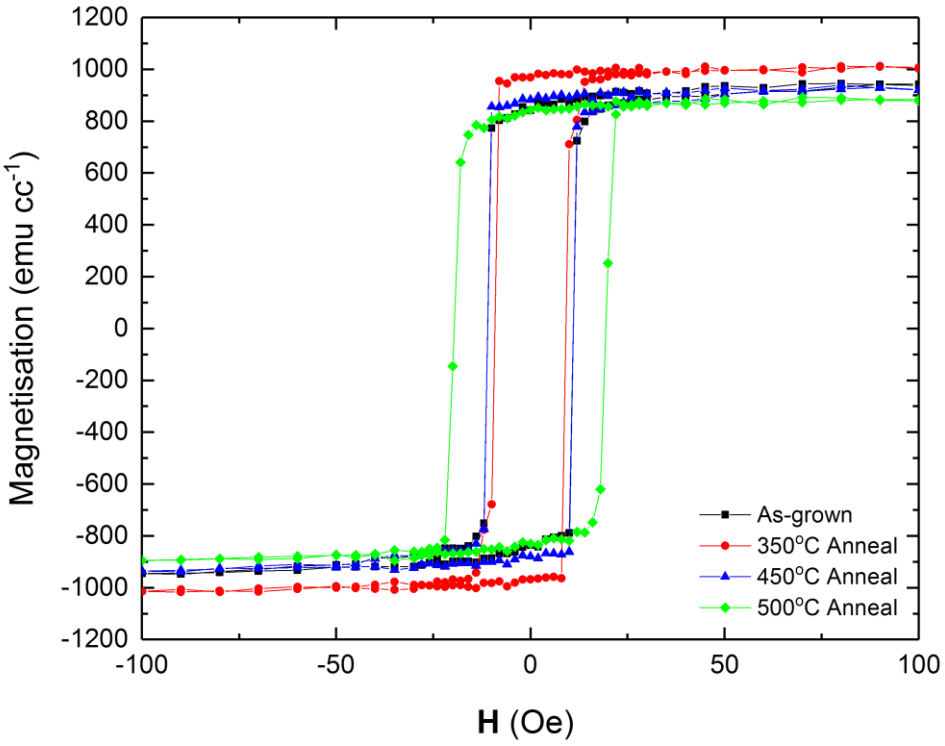

Figure 6.21. *A comparison of the hysteresis loops recorded from VSM performed on the CFAS/Si(111) samples*

In each of the CFAS samples grown on Si(111), the in-plane VSM data, measured along the easy axis, shows square hysteresis loops when the easy axis is aligned with the bias field. The observed

saturation magnetisation ($\mathbf{M_s}$) is close to the expected value of 1100 emu cc^{-1} for CFAS [112]. $\mathbf{M_s}$ in the as-grown sample is 942 $emucc^{-1}$, which is seen to improve to 1008 emu cc^{-1} at T_{an} = 350°C: this value of M_s is within 10% of the bulk value, which is within the 10% error on the thickness measurement. The reduction of $\mathbf{M_s}$ occurs at T_{an}= 450°C and 500°C is observed in CFAS/Si, similarly to the CFAS/Ge series, suggesting similar effects in the structure. The hysteresis loops are also observed to be very narrow in width, indicating a low coercivity in these samples. $\mathbf{H_{coer}}$ is seen to increase from 10 ± 2 Oe when T_{an} = as-grown, 350, 450°C, to 20 ± 2 Oe as the annealing temperature increases, which is consistent with increasing magnetic inhomogeneity. A change in the sample structure is therefore expected at T_{an} < 500°C. No out of plane component of the magnetisation is observed, confirming that the magnetisation aligns solely in the plane of the thin film. This behaviour is consistent with that observed in the CFAS/Ge in figure 6.6. The magnitudes of $\mathbf{H_{coer}}$ and $\mathbf{M_s}$ are similar in both samples, as is the trend in their behaviour as a function of the annealing temperature. This suggests a similar effect occurring between the two.

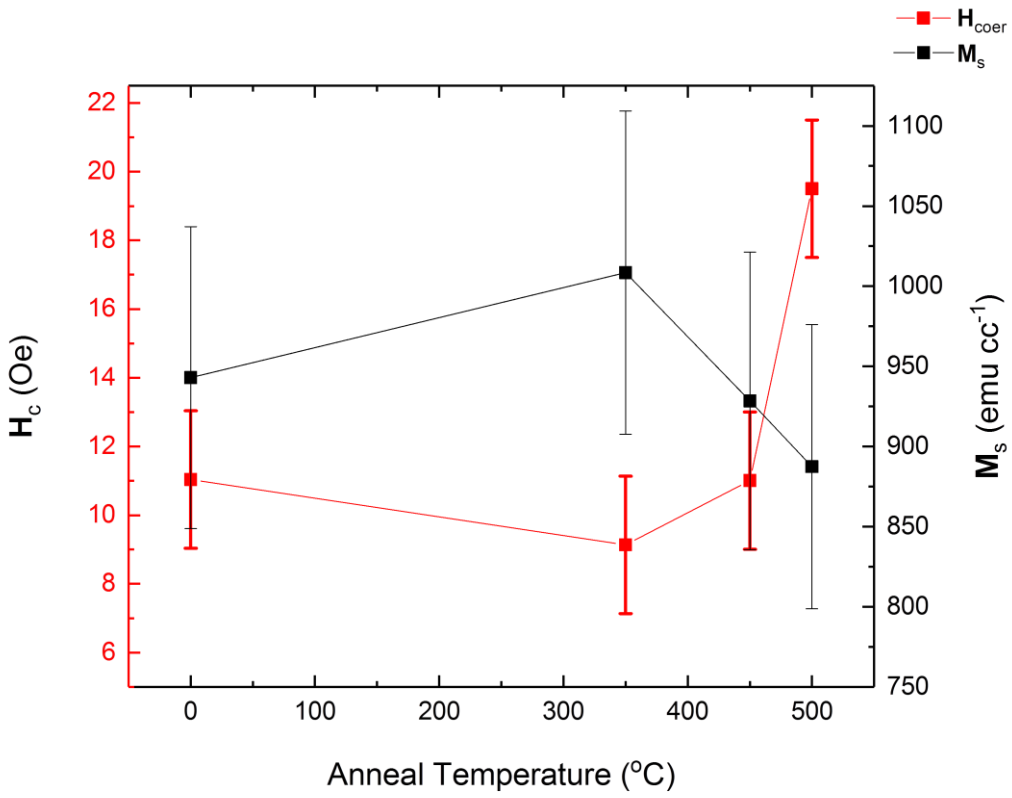

Figure 6.22. *A comparison of $\mathbf{H_{coer}}$ and $\mathbf{M_s}$ from VSM on CFAS/Si(111) as a function of anneal temperature*

6.6.2 Ferromagnetic Resonance Spectroscopy

FMR spectroscopy was performed on the CFAS/Si samples using the custom-built spectrometer discussed in chapter 4. Test measurements showed an intense resonance from each sample and that operation of the spectrometer in VNA-FMR mode was sufficient to extract accurate magnetic parameter information from these CFAS thin films. Since the VSM confirms that the magnetisation easy axis is in- plane, accurate values for the magnetic parameters can be extracted by fitting to VNA-FMR data using the equations discussed in chapter 3. The easy axis Kittel curves recorded from each of the CFAS/Si samples is shown in figure 6.23, including an example of the VNA-FMR linescan fitting show in the inset of figure 6.23.a. The α and $\mathbf{M}_s$ fit parameters extracted from these Kittel curves (fitted using equation 2.40) are collected in table 6.2.

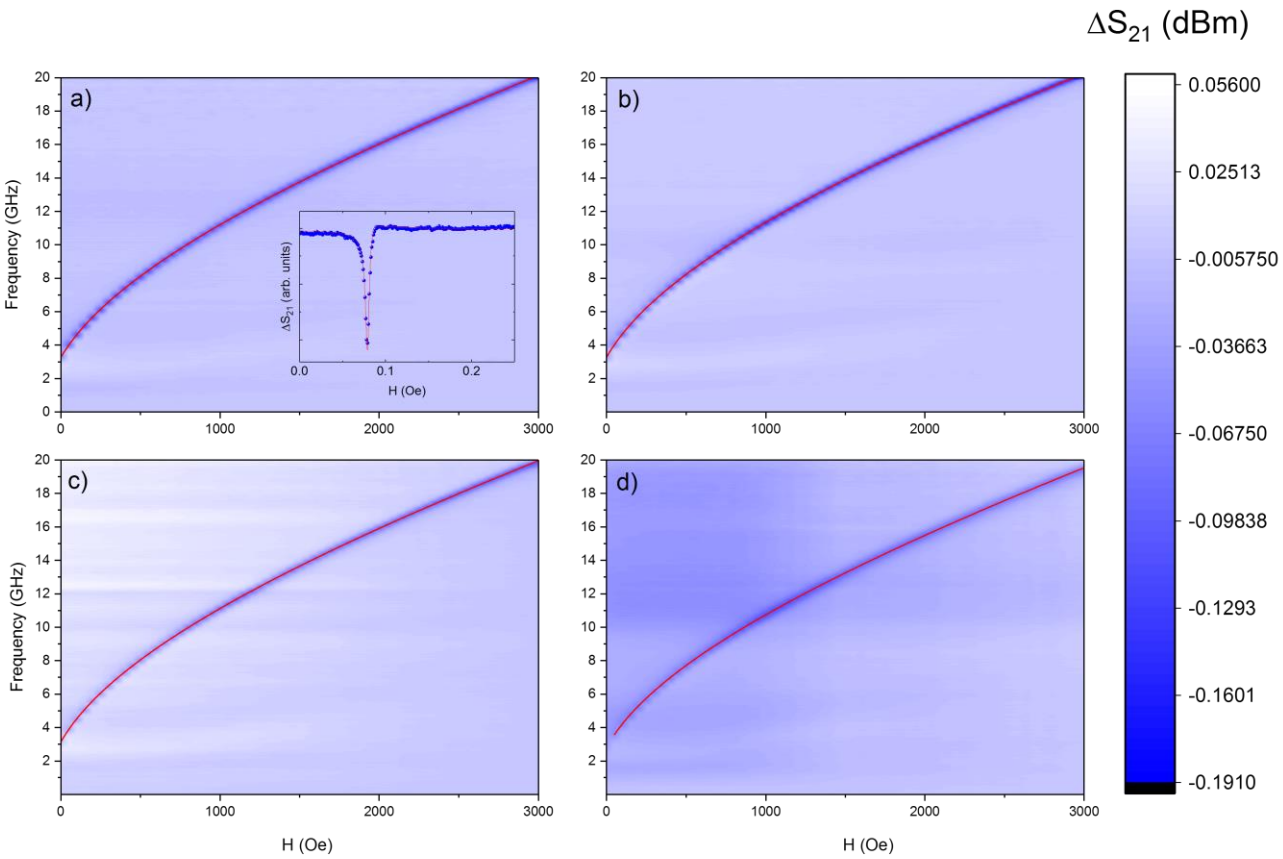

Figure 6.23. *The easy-axis VNA-FMR Kittel curves from the CFAS/Si(111) samples at T_{an} = a) as-grown, b) 350°C, c) 450°C and d) 500°C. (a Inset). Fits are included (red) as a guide*

6.6.2.1 Anisotropy Measurements

In the CFAS/Si(111) samples, anisotropy data extracted from the VNA-FMR shows a uniaxial anisotropy in the plane of the thin film. Fits were performed to this data using the field space anisotropy fit equation B.8. These datasets are shown in figure 6.24. Similar to the CFAS/Ge(111), a scratch was left on the substrate using a diamond tipped scribe. In these samples, this scratch is aligned with the [$\bar{1}$10] axis. VNA-FMR scans were taken from the samples over a range of

azimuthal angles between -90 and +90 degrees. A linescan at a fixed frequency of 10GHz was taken from each of these VNA-FMR datasets, and fitted using an asymmetric Lorentzian function to extract the resonance field ($\mathbf{H}_r$) and linewidth ($\Delta\mathbf{H}_0$) parameters. Comparing the values of $\mathbf{H}_r$ as a function of azimuthal angle (ϕ), the in-plane anisotropy of the thin films were assessed. In the case of these CFAS on Si(111) samples, a two-fold in-plane anisotropy is observed, similar to the CFAS/Ge(111) samples but with a different orientation of the easy axis. The easy axis is consistently observed at +30 degrees to the 0 degrees position, corresponding to the [01$\bar{1}$] direction in the crystal. Given the expected cubic anisotropy of CFAS thin films, this is attributed to a step-edge induced shape anisotropy [223], just as observed in the CFAS/Ge.

As in the CFAS/Ge, the magnitude of the anisotropy $\mathbf{H}_{un}$ decreases as a function of annealing temperature. $\mathbf{H}_{un}$ is observed to be a factor of two larger in the as grown than the 500°C annealed sample, as observed in figure 6.25.

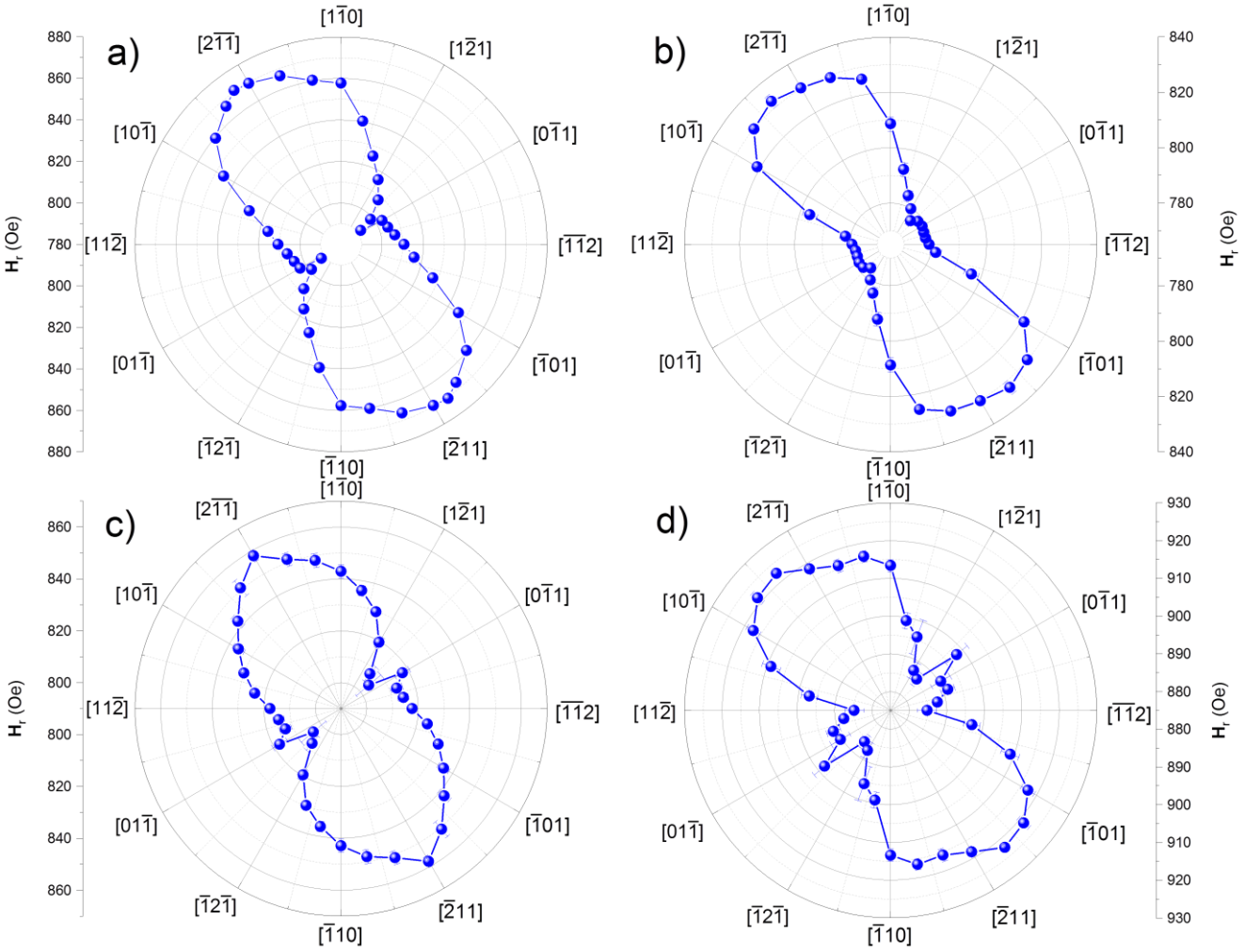

Figure 6.24. *$H_r(\phi)$ extracted from VNA-FMR data from the CFAS/Si(111) samples at T_{an} = a) as-grown b) 350°C c) 450°C and d) 500°C. A uniaxial anisotropy is observed, with an easy axis in the [01$\bar{1}$] at +30 degrees to the [11$\bar{2}$] at 0 degrees*

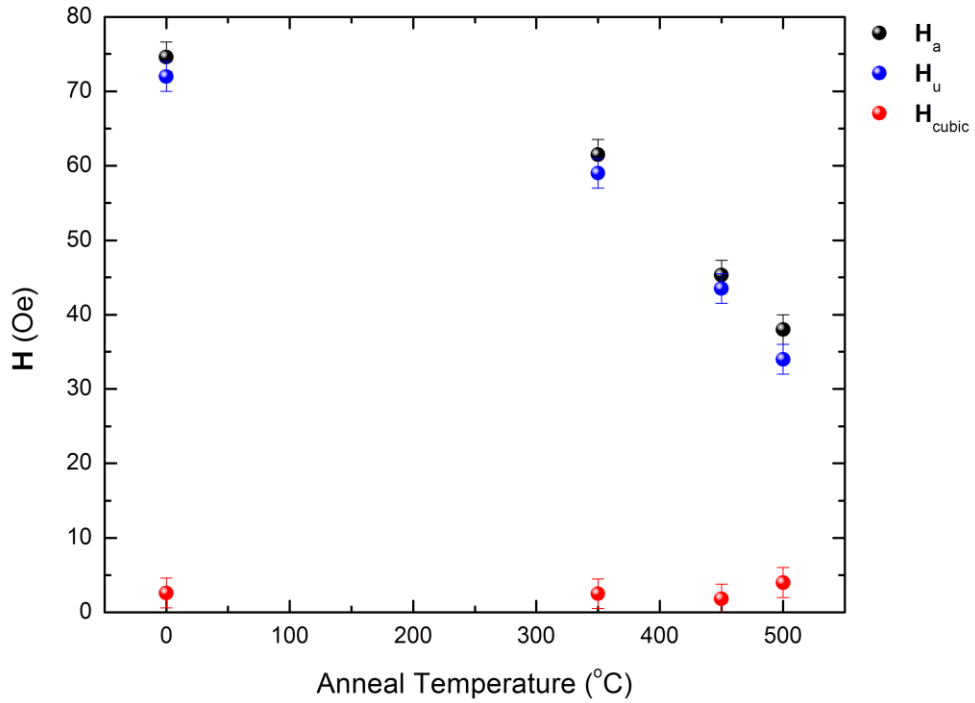

Figure 6.25. *The total (black), cubic (red) and uniaxial (blue) anisotropy field contributions as a function of anneal temperature extracted from the CFAS/Si(111) VNA-FMR polar plots*

For all the CFAS films measured in this thesis, the anisotropy of the film is predominantly uniaxial. However, the linear plots of resonant field as a function of ϕ (figure 6.26) demonstrate an additional anisotropy is present as evidenced by the deviation away from a pure $sin^2(\phi)$ dependence. For cubic magnetic thin films grown on (111) surfaces the effective out of plane demagnetizing field forces the magnetic moment of the system to lie in the (111) plane. The first order magnetocrystalline anisotropy (MCA) is along the <100> directions, for positive K_c, with the competition between the MCA and demagnetising field resulting in a small deviation of magnetization with respect to the (111) plane. As a result, the in-plane resonance field displays six-fold symmetry with the easy axis for a positive K_c. The cubic contribution to the measured anisotropy for a flat (111) film is small, with variations in the resonance field on the order of a few mT [235]. The uniaxial anisotropy should not be present in a pure cubic system. However uniaxial anisotropy on cubic (111) surfaces has also been seen on Fe grown on Si(111) substrates and attributed to step edge induced anisotropy [222,223].

Table 6.2. *Data table containing the magnetic parameters* H_c, H_u, M_s *and* α *for the CFAS/Si(111) as a function of anneal temperature*

Substrate	Anneal temperature (°C)	H_{cubic} (Oe)	H_u (Oe)	M_s (emu / cc)	α (x10^{-3})
Si	As-grown	2.6 ± 2	72 ± 2	984 ± 0.4	4.4 ± 0.1
	350	2.5 ± 2	59 ± 2	1079 ± 0.2	4.1 ± 0.1
	450	1.8 ± 2	44 ± 2	1041 ± 0.6	5.04 ± 0.1
	500	4.0 ± 2	34 ± 2	917 ± 0.2	--

An improved fit to the azimuthal dependence (the red line in the inset of figure 6.26) is obtained by adding a cubic anisotropy term to the MCA. Uniaxial (H_u) and cubic (H_{cubic}) anisotropy fields for the films are presented in table 6.2: these values were extracted from figure 6.25 using equation B.8 (as presented in appendix B). Whilst the cubic anisotropy of the film is the same for both substrates, the uniaxial anisotropy is significantly higher for CFAS on Si, evident from the deviation in resonant field with in-plane angle ϕ. The origin of this effect is unclear but it may arise due to differences in the miscut angle related step edge density. As the anneal temperature increases the uniaxial anisotropy (H_u) decreases for both CFAS on Si and Ge substrates whilst the cubic anisotropy term is roughly constant (within error) for all but the highest anneal temperature.

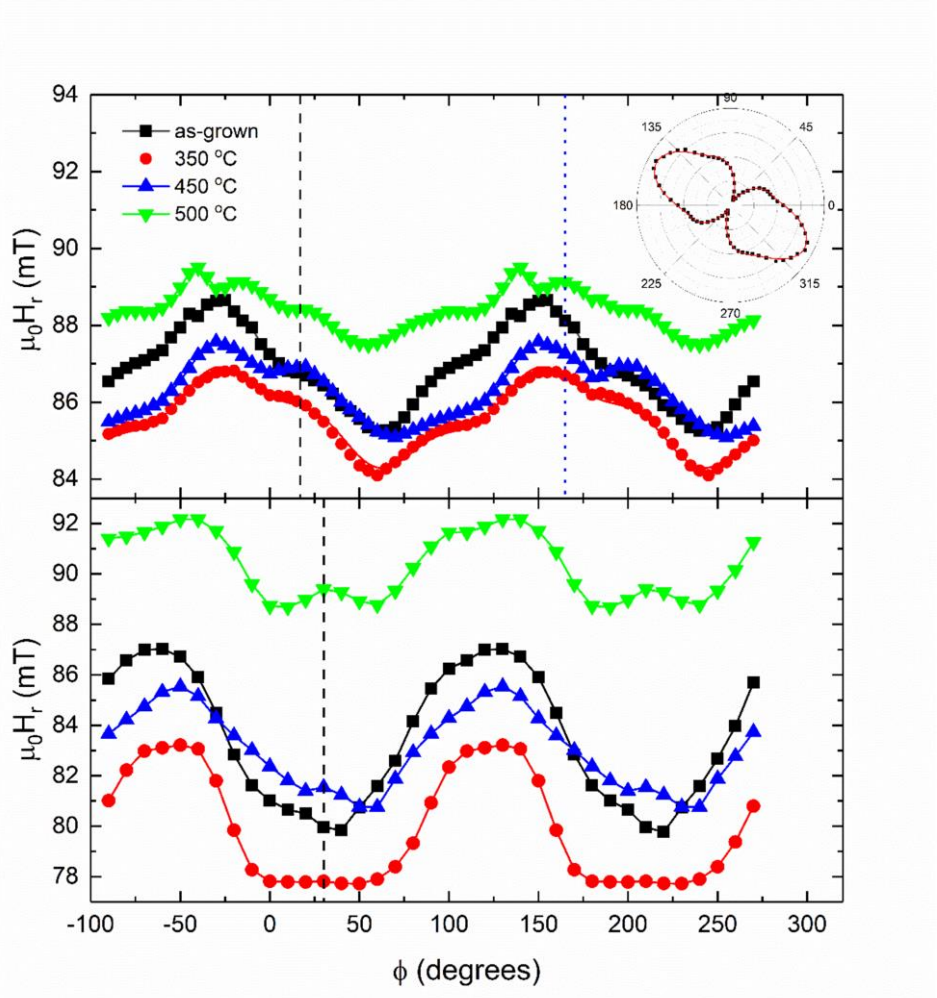

Figure 6.26. *Plots of the in-plane anisotropy of a) CFAS/Ge(111) and b) CFAS/Si(111) at a fixed frequency of 10GHz*

6.6.2.2 Damping Measurements

Damping information was extracted from each sample using the VNA-FMR measured along the easy axis, as determined by the anisotropy analysis. Field linescans at a series of frequencies were extracted from the VNA-FMR datasets and fitted to extract the linewidth parameters ($\Delta\mathbf{H}$) using an equation of asymmetric Lorentzian form, as discussed in previous chapters. Repeating this process in 1GHz frequency intervals allows the extraction of $\Delta\mathbf{H}$ as a function of frequency. Fitting this with equation 2.48 was then used to extract the damping parameters α and $\Delta\mathbf{H}_0$. Fitted data from each sample is shown in figure 6.27.

The data extracted from the VSM shows the magnetisation is fully saturated for all applied fields in the VNA-FMR measurement. For CFAS/Si(111) the as-grown α is initially lower than for the as-grown CFAS/Ge(111) (4.4×10^{-3}, as compared to 5.6×10^{-3} in the CFAS/Ge). Annealing the film at 350 °C produces only a small decrease in α (to a value of 4.1×10^{-3}), unlike CFAS/Ge(111), and further temperature increases causes a significant rise in the damping constant. At T_{an} = 500 °C the linewidth is nearly twice that of CFAS/Ge(111) and again shows a characteristic two-magnon scattering lineshape, which is correlated with the development of the intermixing layer observed in the HAADF-STEM. As in the CFAS/Ge samples, the change in structure is correlated with the change in damping behaviour. Thus for CFAS/Si(111) the optimal anneal temperature is 100K lower than for CFAS/Ge(111) and correlates to the temperature where the B_2 related diffraction peak, the (222) reflection, is maximised (as observed in figure 6.15.a.

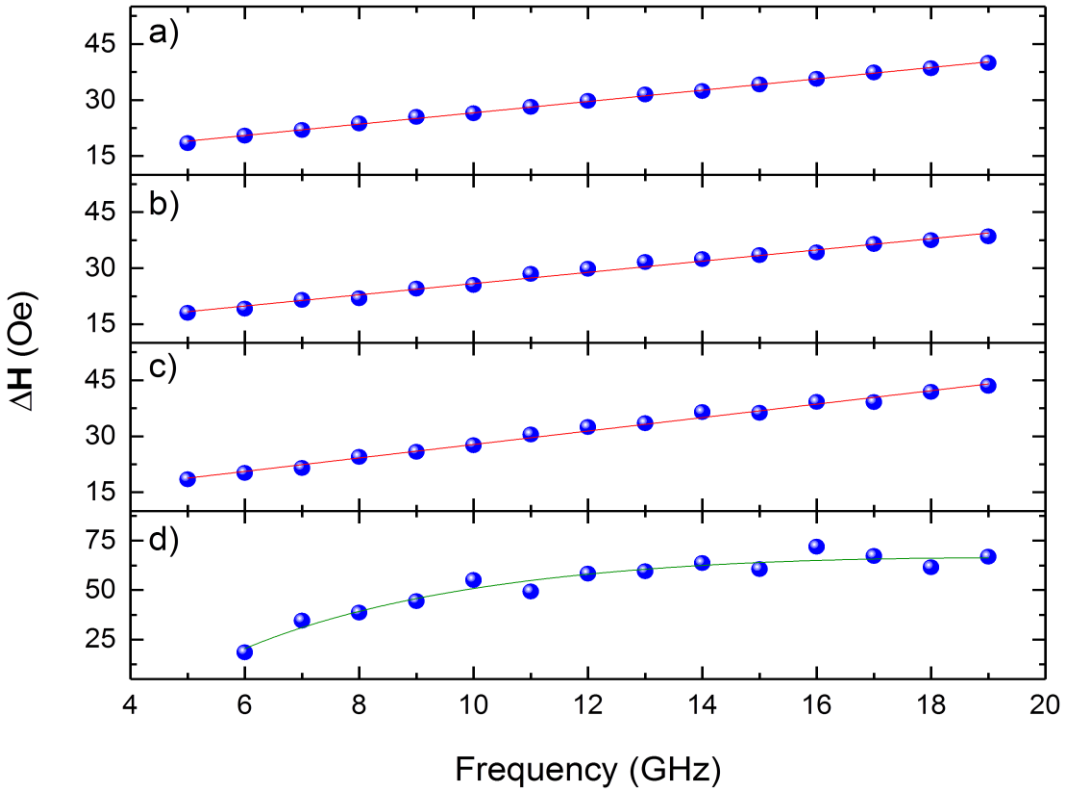

Figure 6.27. *A comparison of $\Delta\mathbf{H}(f)$ in CFAS/Si(111) (a) as-grown and annealed at (b) 350°C, (c) 450°C and (d) 500°. The green line in d) is included as a guide.*

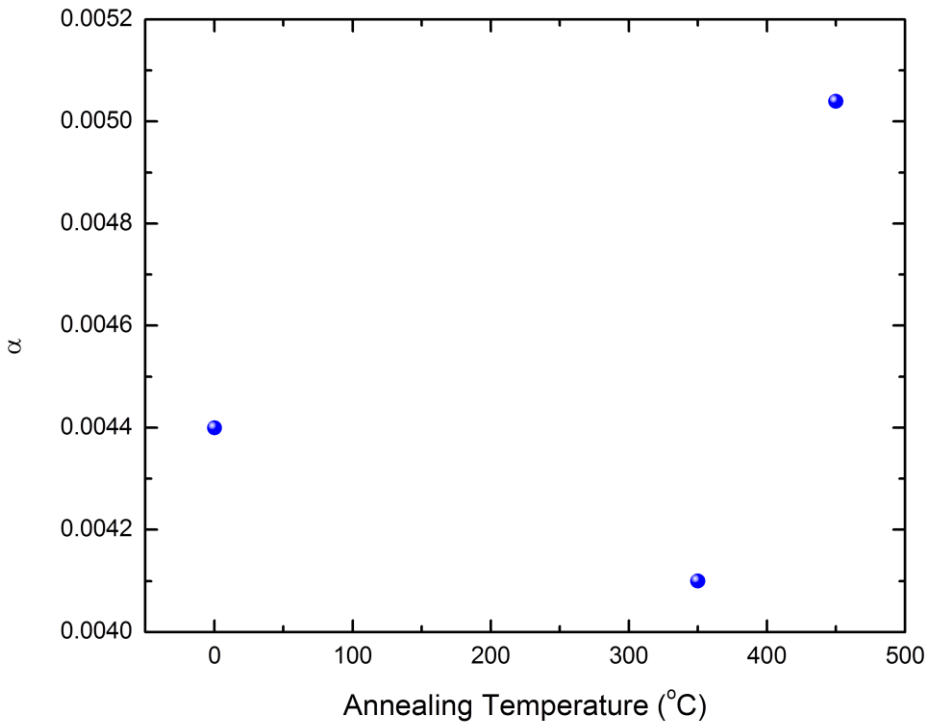

Figure 6.28. *α as a function of anneal temperature in the CFAS/Si(111) sample series*

Table 6.3. *Data table comparing the magnetic parameters from the CFAS/Ge(111) and CFAS/Si(111) samples as a function of anneal temperature*

Substrate	Anneal temperature (°C)	$\mathbf{H}_{cubic}$ (Oe)	$\mathbf{H}_{u}$ (Oe)	$\mathbf{M}_{s}$ (emu / cc)	α (x10^{-3})
Ge	As-grown	2.8 ± 2	28.5 ±2	1025 ± 0.4	5.6 ± 0.1
	350	2.4 ± 2	22.1 ±2	1080 ± 0.5	3.8 ± 0.1
	450	2.4 ± 2	20.8 ±2	1048 ± 0.4	2.8 ± 0.1
	500	1.6 ± 2	15 ±2	1051 ± 0.3	--
Si	As-grown	2.6 ± 2	72 ±2	984 ± 0.4	4.4 ± 0.1
	350	2.5 ± 2	59 ±2	1079 ± 0.2	4.1 ± 0.1
	450	1.8 ± 2	43.5 ±2	1041 ± 0.6	5.04 ± 0.1
	500	4.0 ± 2	34 ±2	917 ± 0.2	--

6.7 Conclusions

In this chapter, a series of CFAS thin films grown on Ge(111) and Si(111) substrates have been characterised in as-grown and thermally annealed states. Structural characterisation has been attempted using XRD and confirmed using HAADF-STEM, and magnetic characterisation has been achieved using a combination of broad-band FMR spectroscopy and room temperature VSM. Both CFAS/Ge and CFAS/Si series show a uniaxial anisotropy in the (111) plane which is attributed to step-edges on the surface of the substrates.

The as-grown and 350^{o}C and 450^{o}C annealed samples in both series show a linear relationship in the linewidth as a function of frequency, which is characteristic of a dominant intrinsic damping behaviour. The collected magnetic parameters extracted from the Kittel curves and the linewidth vs frequency fitting are shown in table 6.3. The change in damping with anneal temperature behaves differently depending on the substrate. The intrinsic damping is observed to be lower in the as-grown samples when grown on a silicon substrate, but the reduction in α is more significant after annealing on the germanium. A small increase in the extrinsic damping is observed in the CFAS/Ge 350^{o}C sample but annealing at 450^{o}C improves this and shows comparable $\Delta\mathbf{H}_0$ to the annealed CFAS/Si. The optimal damping parameter in the CFAS is observed on the Ge substrate at T_{an} = 450^{o}C and on the Si substrate when T_{an} = 350^{o}C.

The dominant form of damping in both CFAS series changes when the annealing temperature reaches 500^{o}C, changing from the linear intrinsic behaviour to a curve characteristic of two-magnon scattering. The extrinsic damping is observed to dominate in both series at this temperature, though it is larger on the silicon substrate relative to the germanium. This change in magnetic properties is observed in the CFAS samples correlated with the outdiffusion of the substrate material into the CFAS thin film, as seen in the HAADF-STEM and EELS imaging [115]. The reduction in magnetisation and shift in dominant damping behaviour is therefore attributed to this effect.

While the silicon substrate shows improved magnetic damping parameters in the as-grown CFAS, after annealing the Ge substrate ultimately returns more favourable damping parameters. Recovering the L_{21} phase has not been possible at these annealing temperatures, as seen in the XRD and the STEM, so the limiting factors are the annealing temperature and the Gilbert damping. At higher temperatures, it is seen that out-diffusion begins to occur from the substrate into the CFAS which limits the annealing temperature. This renders the samples annealed above this temperature impractical for application: once the outdiffusion from the substrate occurs, the change in the magnetic structure is observed to radically shift the magnetisation damping in the CFAS: extrinsic damping effects begin to dominate and the total damping within the CFAS thin films is significantly increased. This change in damping is clearly observed in the field-frequency maps measured using FMR spectroscopy.

While the smallest Gilbert damping value of $\alpha = 2.8\text{x}10^{-3}$ value recovered here is slightly larger than the 2-2.5x10^{-3}recovered previously, the experiments discussed in this thesis show reasonable agreement with previous experiments, as discussed in section 2.6.2. Further improvements to the damping are expected in the L_{21} phase. In order to recover the L_{21} phase, the temperature would need to be held above 500^{o}C which is sufficiently high for this out-diffusion to occur. An

alternative to this annealing process is therefore required to recover this phase without the large extrinsic damping effects.

Data measured using the VSM agrees with this assessment, showing that the $\mathbf{H}_{coer}$ and $\mathbf{M}_s$ values are consistent within error when T_{an} <500^{o}C, whereas $\mathbf{H}_{coer}$ dramatically increases and $\mathbf{M}_s$ decreases as T_{an} is increased to 500^{o}C. The $\mathbf{M}_s$ values recorded from the VSM are within 10% of the expected bulk value of 1100 emu cc^{-1}, although the CFAS/Ge shows less deviation from this value.

It is therefore found that the Ge provides a better substrate for the growth of CFAS (111), since the damping can be reduced lower than that in CFAS/Si, and the annealing can be performed 100^{O}C higher. However, the desired L_{21} phase is not recovered due to the outdiffusion of substrate material into the thin films in both cases.

Chapter 7: Conclusions

7.1 Conclusions

The damping behaviour and microstructure has been observed in two different species of 'half-metallic' magnetic thin films. In both magnetite and CFAS thin films, lower Gilbert damping has been shown to be correlated with improvements in the microstructure of the sample brought about by annealing under specific conditions.

Thin films of magnetite grown on YSZ(111) are shown to be improved by annealing in CO/CO_2 for 1 hour at 1100^{o}C. The stoichiometry is seen to improve in both XMCD and FMR spectroscopy and the damping is reduced significantly by the annealing procedure. This reduction in the total damping correlates with an improvement in the structural quality, observed in the narrowing and improved squareness of the in-plane VSM loops and the recovery of the expected six-fold anisotropy in the VNA-FMR data. HAADF-STEM microscopy shows that a high density of antiphase boundaries and a large mixing layer of FeO_x between the film and substrate are observed in the non-annealed thin film, and while both are still present after annealing, the density of APBs and the thickness of the mixing layer are both significantly reduced. While the improvement in the defect density and total damping is considerable, it is observed that the dominant form of damping is still extrinsic in nature. The reduction of antiphase boundaries in Fe_3O_4 is therefore a significant factor in reducing the damping of magnetite thin films, but other extrinsic effects are present which must be addressed if magnetite is to be made practical for applied spintronics. The unexpected large four-fold anisotropy observed in plane of the non-annealed sample is not clearly understood, and further work must be conducted to establish the reason for this effect.

CFAS thin films have been grown on (111) aligned substrates of both germanium and silicon, and the damping and structure have been investigated. Improvement of the damping is observed on both substrates, with an intrinsically dominated damping showing a reduction in the Gilbert damping (α) as the samples are annealed. While the as-grown samples show better damping on the silicon substrate ($\alpha = 4.4\text{x}10^{-3}$ on CFAS/Si, compared to $5.6\text{x}10^{-3}$ on CFAS/Ge), the damping parameter is improved more by annealing the sample grown on germanium: the minimum value of $\alpha = 2.8\text{x}10^{-3}$ on 450^{o}C annealed CFAS/Ge, compared to $4.1\text{x}10^{-3}$ on CFAS/Si annealed at 350^{o}C.

The observation of intrinsically dominated damping only holds true below an annealing temperature of ~500^{o}C. In both CFAS/Ge(111) and CFAS/Si(111), annealing at 500^{o}C is shown to induce outdiffusion of the substrate material into the CFAS structure. This intermixing of the two materials introduces a large extrinsic damping effect that is easily identified by the characteristic two-magnon scattering behaviour in $\Delta\mathbf{H}(\omega)$. A significant increase in the total damping is also introduced, making these high-temperature annealed films less suitable for practical application than their lower-temperature counterparts. The B_2 structure is observed in both the CFAS thin films using structural characterisation techniques. In order to achieve the more desirable L_{21} structure, the CFAS must be annealed at higher temperatures, but this is incompatible with improved damping in these particular samples due to the substrate outdiffusion observed in the EELS in CFAS/Ge (and predicted in the CFAS/Si based on its similar structural and magnetic

properties). This outdiffusion must be suppressed if L_{21} CFAS is to be grown on these substrates for practical applications, or a more thermally stable substrate must be used.

These results confirm that, depending on the annealing conditions, highly spin polarised 'half metallic' magnetic thin films are promising candidates for future applications which require low damping. However, the growth and annealing conditions play a major role in defining the damping. A correlation is observed between the improvement of the damping in both Fe_3O_4 and CFAS samples and the improvement of their stoichiometry, and the reduction of defects within the microstructure. Further work is required in order to refine these materials for the production of affordable low-α materials for spintronics.

7.2 Further Work

7.2.1 The FMR Spectrometer

A series of improvements are planned to the FMR spectrometer. The addition of a Hall probe is planned in order to consistently measure the applied field. Due to the non-uniformity observed in the bias field across the spectrometer, this requires careful consideration of both the position of the Hall probe and the method by which it is mounted. This may well require adjustments to the design of the sample mount.

Changes to the transmission line are also planned in order to increase the sensitivity of the device. Adding a resonant cavity for better sensitivity at a fixed frequency will increase the Q of the spectrometer from <1 to ~6000. This should lead the spectrometer to be practical in other magnetic oxides with low intensity FMR signals and perhaps even nanoparticle samples. However, removing the CPW also removes the broad-band capabilities of the system, and therefore a series of cavities with different resonant frequencies would be required in order to accurately assess Δ**H**(f). Converting the resonator to a modular system of different attachments would be ideal, allowing easy replacement of the resonator without affecting the rest of the RF transmission line. This will require careful planning, however, and a second sample mount/transmission line will need to be constructed for testing purposes. The system must also be easy to return to its original configuration with a minimum of changes to in the RF transmission line.

Given the versatility of the FMR spectrometer, it would be easy to branch out into measuring other materials with promising properties for spintronics. Damping behaviour in any promising highly spin-polarised material can be achieved by growing a thin film and performing FMR using this spectrometer. When considering samples, however, it must be remembered that the standard FMR technique can only make bulk measurements. This limits the effectiveness of standard FMR on multilayer stack structures since the contributions from each individual layer cannot easily be separated. Other techniques like X-ray detected FMR [236,237] can be used to assess the contribution of individual layers, though this is more easily achieved at a specialised synchrotron facility like Diamond Light Source.

7.2.2 Fe_3O_4/YSZ(111)

Further work on the Fe_3O_4 is required to completely remove the extrinsic damping effects. While the annealing process discussed in this thesis is certainly effective at reducing the total damping, and has been shown in the literature to strongly reduce the density of antiphase boundaries in

magnetite, other defects must exist within the sample structure since the total damping post-anneal is still dominated by extrinsic effects. If these additional defects can be eliminated, this should further reduce the total damping. If the extrinsic effects in Fe_3O_4 can be eliminated, the resulting damping effects are purely intrinsic, and will yield a lower total damping than the annealed Fe_3O_4 presented here. The method by which these defects might be reduced likely lies with a refinement of the annealing process, although I cannot reasonably speculate on what improvements might be best at this time. The introduction of a buffer layer between the substrate and the film might reduce the outdiffusion, although retaining the strong epitaxial relationship with the thin film and the substrate, and the close lattice match, may be difficult depending on the choice of buffer material. The replacement of the substrate with a different material might be a practical alternative, although the close lattice match would need to be retained to keep the epitaxial growth behaviour and minimise the extrinsic damping effects resulting from misaligned nucleation sites during growth. This is definitely worth pursuing, however, since if the damping can be reliably reduced further then magnetite may finally present a viable material for spintronic applications. Determination of the sign of the anisotropy constant in the annealed Fe_3O_4 thin film (expected to be negative, in line with bulk Fe_3O_4) could be performed using polar FMR, although this technique is not available using the equipment discussed in chapter 4 due to the limited axis of rotation in the electromagnet. A specialised (octopole) magnet system would be required to record data out of the plane of the thin film.

The four-fold anisotropy in the non-annealed thin film requires further investigation to determine its origin. It most likely arises as a result of the large non-stoichiometric mixing layer which is observed between the film and the substrate, although the exact origin is still unknown. Further investigation into this effect is required. Gradual annealing over a range of different temperatures interspersed with damping measured could be used to confirm how the increasing temperature reduces this large anisotropy, and perhaps link the effect to the mixing layer. The growth of additional thin films under the same conditions may also be used to establish that this effect arises consistently.

7.2.3 $Co_2FeAl_{0.5}Si_{0.5}$

The CFAS samples show promising low-damping behaviour, but the key inhibitor of further improvement lies in the outdiffusion from the Ge(111) and Si(111) substrates. Further work with these materials is therefore likely to focus on different technologically relevant substrates with small lattice mismatch with CFAS. Given how differently the α parameter has been observed to be in CFAS on two similar substrates, it is worth investigating if α can be reduced further by a different substrate. Ideally, substrates with a lattice parameter close to CFAS ought to be used, in order to minimise the strain on the thin film. If a more thermally stable substrate can be found, it may be possible to investigate the changes in the damping brought about by this structural transition. This would hopefully allow the annealing of the CFAS from the low-temperature B_2 phase into the more highly spin-polarised L_{21} phase without the outdiffusion of substrate material degrading the quality of the structure and increasing the damping.

Since Heusler alloys are a relatively young class of materials, it may be that other similar structures are discovered with similarly high predicted spin polarisation and thermal stability. A full comparison of the structural and damping behaviour in these materials would also be of great interest to the future of spintronic materials for device applications.

For both the Heusler alloys and the magnetite samples, further investigation into the substrate miscut angles and how they affect the magnetic anisotropy would be useful in adding further context to this data. Repeating the growth of similar sample series on substrates with known miscut angles would allow the further investigation of the effect of the resulting step-edge behaviour on the angular dependence of the magnetic anisotropy and damping behaviours on the polar angle θ. This would be of particular interest in the Fe_3O_4 samples for further comparison with the predictions of Landeros as discussed in section 5.4.2.

Appendix A: FMR Spectrometer Control Code

A.1 Introduction

In this appendix, the control software written to run the FMR spectrometer is presented. Constructed in National Instruments' LabVIEW 2015 by the author, three different programs are required: one to control the VNA-FMR mode and two which are used in tandem to control the modulation FMR mode. These programs were refined over the course of the project, each requiring a number of iterations. Further changes may be required for quality-of-life improvements, but for the purposes of the operating the FMR spectrometer, these programs are more than sufficient.

A.2 VNA-FMR Control Program

The control program for the VNA-FMR operation mode is shown in the primary field-frequency-phi sweep operation mode in figure A.1. This program independently controls all parts of the VNA-FMR spectrometer system, including the PM600 motor control card, the Bruker power supply for the magnet and the VNA. The software is directed to the external equipment by identifier strings in the dropdown boxes at the top of the global controls panel on the right of the screen. Once the connection to the devices is established, the main program begins, running inside a while loop which continues to operate until the stop button is pushed or the program is forced to close by the exit or killswitch functions.

The field-frequency-phi sweep mode operates in three phases. Firstly, the angle of the magnetic field is set relative to the initial 'zero' position by rotating the magnet turntable. Secondly, the magnetic field is ramped to the reference field value and after a sufficient wait for the field to ramp, a full S-parameter sweep (usually $S_{21}(f)$ for the experiments discussed in this thesis) is performed by the VNA. This data is stored as a reference sweep in a variable to be retrieved later. Thirdly, the field is then ramped to the measurement field and, after an appropriate wait time has elapsed, the S-parameter sweep is repeated, this time at the measurement field. This data is then stored in an array where the reference data is subtracted from it. The subtracted trace data is then presented to the operator and the datasets stored for saving. The third step is repeated over a series of measurement fields until the field-frequency scan is completed and the data for the scan saved. The program then steps the magnet to the next field angle and repeats the process, until a full field-frequency sweep has been measured over each specified angle.

The main program consists of a series of nested for loops which operate based on the input variables, defined by the user in the dropdown boxes on the left hand side of the program frontend. In the field-frequency-phi sweep mode, the user must define the VNA parameters, the field parameters and the field angle parameters. The VNA parameters define the frequency range of the scan (and the number of frequency steps) as well as the operational parameters of the VNA, such as the bandwidth, RF power, scan type and number of averages. Two wait times may also be defined, one to allow enough time for the initial field ramp (the 'initial wait time') and one

to allow the field to ramp between field points in the scan (the 'field wait time'). The VNA parameters may be independently redefined at any time by changing the values in these boxes and pushing the 'Update VNA' button, though these parameters are automatically read each time the field-frequency-phi scan is performed.

The field parameters require a field range and a field step size to be input, allowing the user to tailor the sweep parameters to their requirements. While a lower limit of 0.76 Oe is imposed on the scan due to the resolution of the field control, this is sufficient for high-resolution measurements in the bias field. The reference mode may also be set here using a dropdown box. Three options are available, which defines the reference field behaviour. 'No Reference' mode performs the sweep without a reference. This is mostly used for system diagnostics since without a reference sweep the data quality is reduced by background effects (specifically the attenuation of high-frequency signals observed in the CPW). 'Single Reference' mode is the most commonly used option, performing a reference sweep at the start of each field-frequency scan and subtracting all subsequent data from it. This allows the attenuation effects in the CPW to be removed from the data. This mode is generally the most practical, serving to provide a reference sweep and allow the field to be ramped down gradually over the course of a scan. The third mode runs a reference before each data sweep rather than once at the start of each dataset. This is useful when the signal is likely to drift over time, which is occasionally seen in very long scans as small shifts in the temperature affect the VNA signal. However, due to the added data sweeps, and the increased ramping time to get up to the reference field and back down to the measurement field while allowing the field to settle each time, operation in this mode greatly increases the time required to collect data. While it generally gives the highest quality data, it tends to be impractical over large field ranges or when very small field steps are used. The file path for saving the data is also provided here. The user provides a directory for the data to be saved in, and the program automatically generates a series of .txt files, one for each angle at which the field-frequency data was collected. Each data file contains a series of headers which describe the scan parameters for later reference, as well as the raw scan data. The data table contains the field value in the first row, and all of the columns contain the S-parameter value from the corresponding sweeps, including the reference dataset(s).

The angle settings require a range of angles and a step size for the rotation of the magnet. The program pre-calculates the steps based on this data and sweeps the angle from the minimum to the maximum values in steps of the given size. A wait time is included to allow the magnet to rotate before the field begins ramping in each field-frequency scan.

The data from each S-parameter scan is stored in an array and, after the reference data is subtracted, the sweep (trace) data is presented to the operator in the graphs on the right hand side of the screen. The upper plot shows the most recent trace, allowing the user to inspect the resonance behaviour at each step. The lower graph stores all the data from the current field-frequency scan so far, generating an intensity map of the data as a function of field and frequency. This allows the user to observe the Kittel curve behaviour in real-time as more data is collected.

Once the loops are complete and all the data has been saved, the system moves into idle mode (with the field zeroed to save energy and prevent wear in the magnet coils), awaiting further

instructions. This allows the program to be used repeatedly in a single session, rather than being re-booted each time a scan is performed. The progress of the scan can be assessed using the progress indicators on the panel on the right, which indicate the set point of the field and angle, as well as providing a 'sweep progress' value (either 'in progress', 'saving', 'idle' etc. depending on the progress of the current loop).

Safety features are integrated into the program, including a stop function which ends the program after the current scan data is collected. The program stays ready for further input and the field output remains at the current level. A killswitch is also included which stops the program immediately: for safety purposes, this sets the field to zero and stops all program functions, closing the VI to prevent further input. The RF can be turned on and off from the program using the RF state button on the global panel. This is useful switching off the RF during the changing of samples. The current state of the RF is displayed in the indicator alongside the button for easy reference.

The VNA-FMR program also offers two additional operating modes, depending on which tab is selected. Field-frequency mode allows the collection of field-frequency data at a single angle, which is useful for repeating datasets at known angles, or for testing the field-frequency behaviour in new samples. This mode operates in identical fashion to the field-frequency-phi sweep, except for the manual setting of the magnet angle. A manual mode is also available for performing single sweeps. This mode is generally used for diagnostics and testing new samples to see if a resonance can be observed. This mode allows single sweeps to be made, with the field value and magnet angle set manually to fixed values. Individual graphs are shown for the current trace data, the reference trace and the new data with the reference subtracted, for diagnostic purposes. The 'Data to Memory' button on the global panel is chiefly used in this mode in order to move the current sweep data into a unique array where it is used as a reference sweep for the next manual sweep.

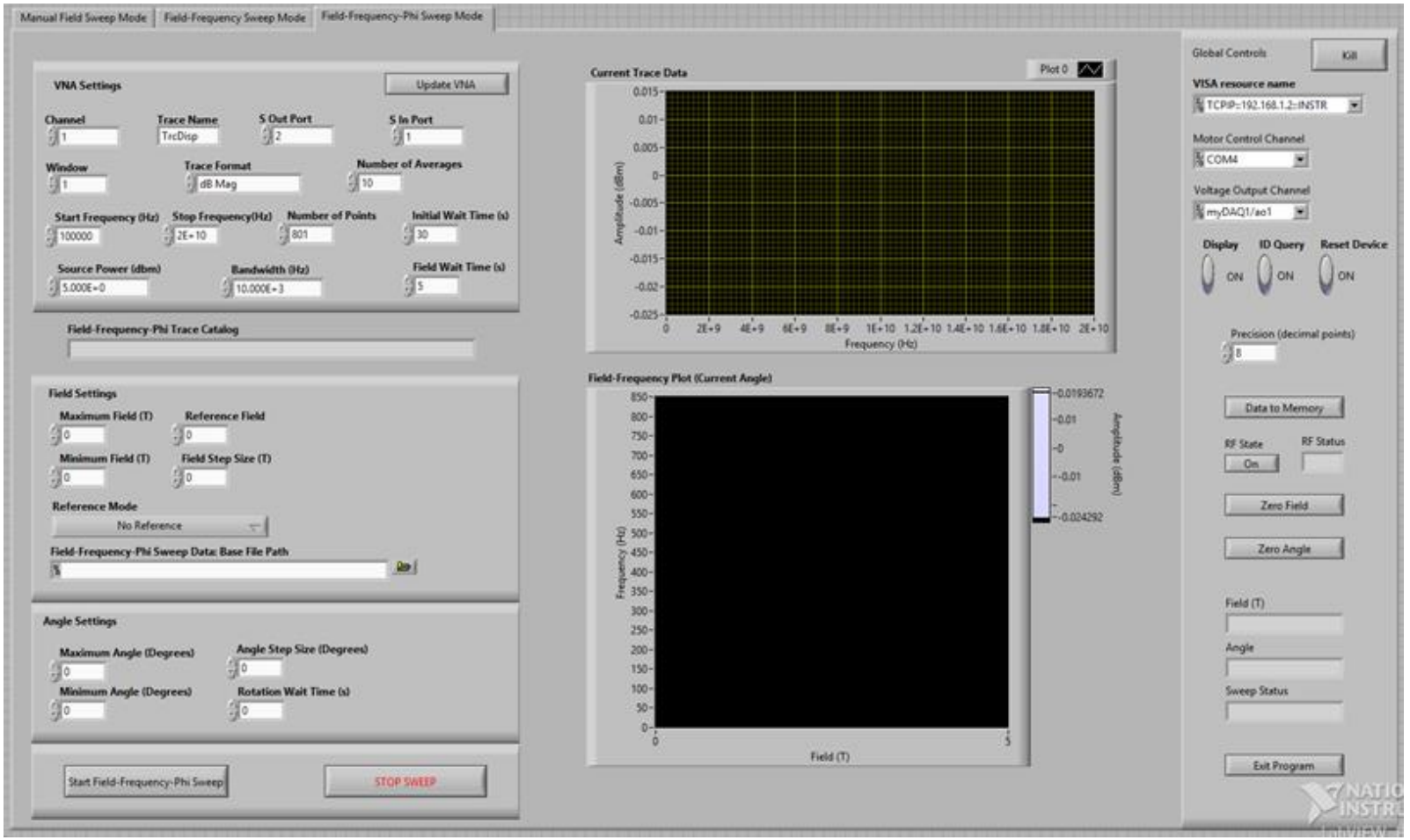

Figure A.1 *The LabVIEW frontend for the VNA-FMR Data Acquisition Program, operating in the primary Field-Frequency-Phi Sweep mode*

A.3 Modulation FMR Modifications

Similarly to the VNA-FMR control program, the modulation FMR is controlled by a LabVIEW program which sets sweep parameters based on input values and sweeps the angle and applied bias field based on the input parameters. Indeed many of the functions are performed using the same loops but with modified input sources. The key difference between modes is the RF source, which in this program is a Rohde and Schwarz SMB100A Signal generator. The RF is controlled using a separate program as a result of time constraints: while it would be relatively easy to modify the modulation FMR program to interface with the signal generator, for practical purposes the control of the RF was achieved using a separate Frequency Control program, based on a test interface developed solely for remote control of the RF unit.

A.3.1 Frequency Control Program

The RF used in the modulation FMR operation mode is provided by a different source than the VNA used in the VNA-FMR mode. Instead, LabVIEW is connected to a Rohde and Schwarz SMB100A RF signal generator. While the output is on, the signal generator outputs a continuous wave output at the set frequency and power (RF level in dBm) until the settings are changed or the output is switched off.

This program allows the user to remotely interface with the signal generator and provides simple control of three key functions: the RF frequency can be set at any value within the range of the signal generator output by typing the value into the upper box on the main panel and pushing the adjacent button. The current set figure is also displayed in the indicator on the right of the screen. The second function of this program operates the same way, setting the RF output power of the signal generator. These values can be changed at any time, depending on the requirements of the user. Since the data collection in modulation FMR mode requires fixed output frequencies, no facility for ramping or time-varying frequency settings are provided.

Finally, an on/off switch for the RF signal is provided on the right hand side of the program, allowing the user to enable the RF for experiments and disable it for sample or equipment changes.

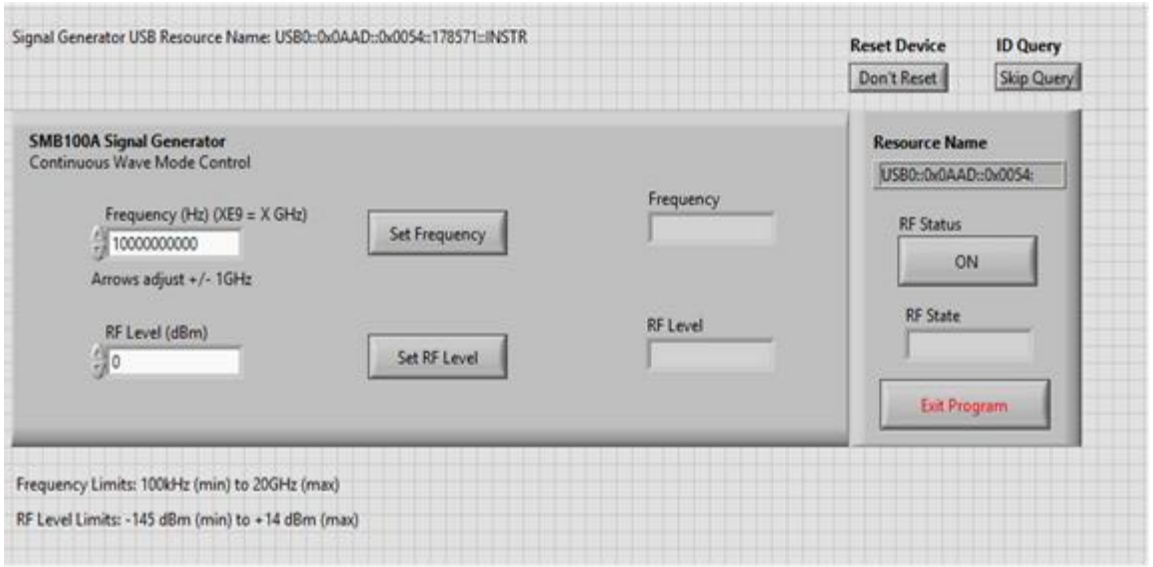

Figure A.2 *The LabVIEW frontend for the Frequency Control Program, designed for the modulation FMR experiment*

A.3.2 Data Acquisition Software

The control software for the modulation FMR operating mode functions similarly to the VNA-FMR control program, but with the frequency determined by the signal generator control program described in section A.3.1. Control of the PM600 motor control unit and the SR830 Lock-in amplifier are provided by this program, which allows control of the sweep parameters and data acquisition from the FMR spectrometer. As in the VNA-FMR control program, three sweep modes are offered. A manual sweep mode is provided for diagnostic purposes, wherein the magnet angle and magnetic field are set to single values determined by user input and single point scans can be performed. The second and third sweep modes provide most of the functionality however, allowing field-sweeps at the fixed output frequency value, either at a single user-defined angle in the 'single sweep' mode, or over a range of azimuthal angles in the 'angular sweep' mode. The frontend is shown in angular sweep mode in figure A.3.

In the sweeping modes, the frequency is set using the frequency control program. The field is then swept to the upper limit as defined by the user. After a wait time has elapsed (allowing the field to ramp to the specified value), the lock-in is queried and the data points from channels 1 and 2 returned as data. This is repeated a number of times (n) as specified in the 'number overages' field (typically ~5000) and the sum of these data values divided by n to find a mean average value. This data is then saved in an array and stored for later reference. As the averaged data points are collected, they are displayed on the graphs on the right hand side of the screen for real-time reference. The program then steps the field to the next calculated value and the measurement process is repeated until the field sweep is completed. The sweep data is then saved to a .txt file (defined by the user) along with a series of headers describing the sweep parameters (for future reference). The program then enters idle mode with the field zeroed and awaits further instructions. During the sweep, angle and field values and the current task are shown in indicators on the right hand side of the screen for quick reference.

As in the VNA-FMR control program, sweep parameters are defined by the user in the boxes on the left hand side of the program. The field range, step size and number of averages can be defined, as well as a wait time for the initial field ramp. Two inputs are also provided for the user to define the save location for the data. The data from both channels is saved independently for easy access later. Since all the data should be in one channel, the second dataset is usually not used, though the data is saved for completeness, should future reference be required.

A stop button is provided to interrupt the current sweep, in the event that this is required, for example if incorrect sweep parameters are set. A killswitch is also provided to zero the field and stop all input to the program in the event of an emergency. Buttons are also provided which zero the field and the magnet angle, for easy access to these commonly used functions.

Future iterations of this program could easily be modified to incorporate the frequency control program as well, removing the need for two control programs and further streamlining the control method.

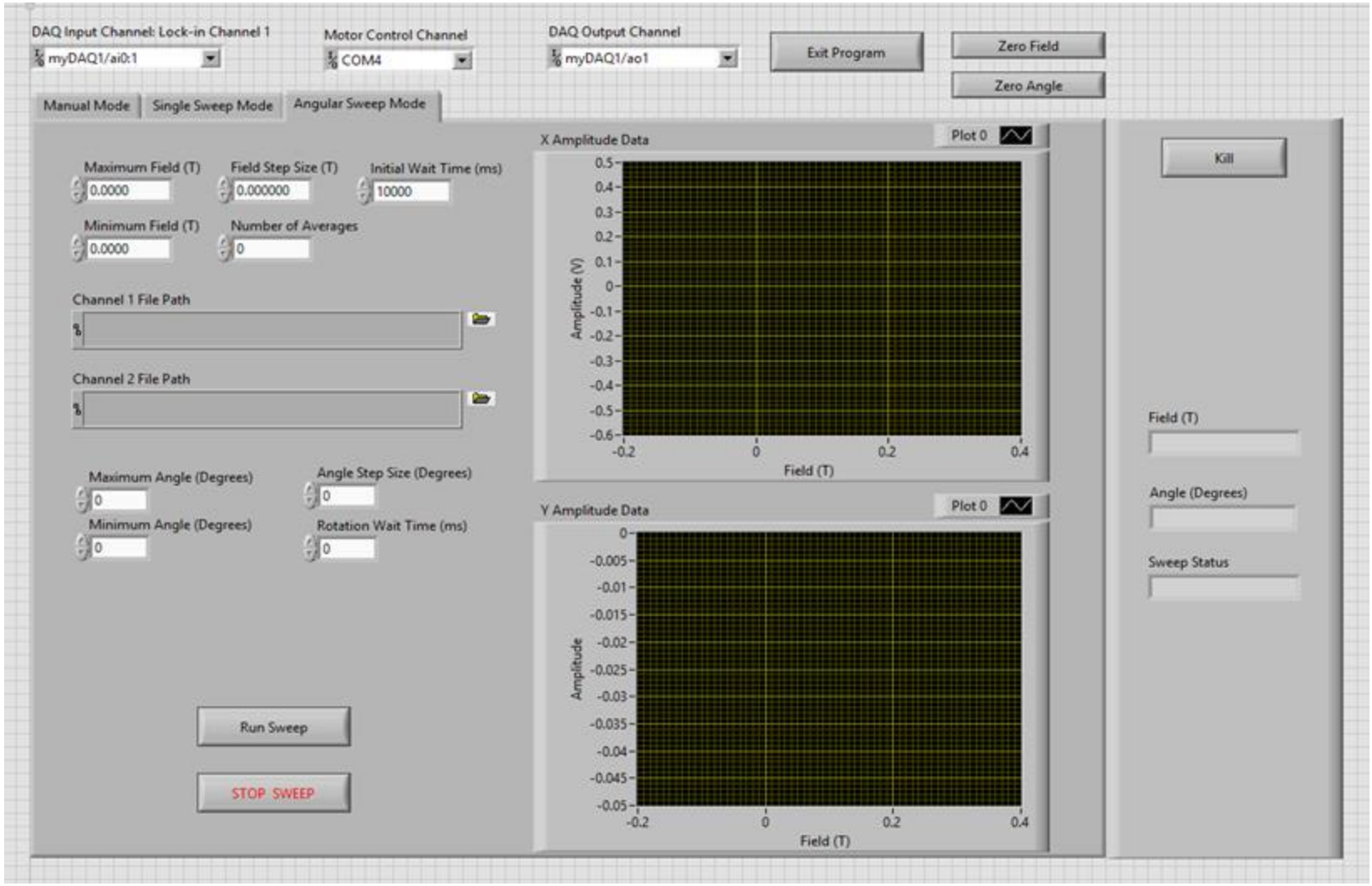

Figure A.3 *The LabVIEW frontend for the Modulation FMR Data Acquisition Program, operating in the primary azimuthal Angular (Phi) Sweep mode*

Appendix B: FMR Anisotropy Fit Equation in Field Space

In order to fit the anisotropy data in field space, the fitting equations derived in section 2.53 must be re-arranged in terms of the magnetic field component. It is useful to decompose the total anisotropy term into the cubic and uniaxial anisotropy components, in order to separate the two contributions. This appendix presents the re-derivation of equation 2.39 into field space instead of frequency space, starting from equation 2.35. The simplifications made during the original derivation were also re-assessed at this time in order to better describe the fit. The derivation presented here was reached in private communication with the project supervisor Dr. S. Cavill at the University of York.

The magnetic free energy including zeeman, demagnetisation and cubic anisotropy terms for (111) surfaces can be written as:

$$F = K_1\left[\frac{1}{3}cos^4(\theta) + \frac{1}{4}sin^4(\theta) - \frac{1.4}{3}sin^3(\theta)cos(\theta)cos(3\phi)\right] \\ +2M^2\pi cos^2(\theta) - MH\left[cos(\theta)cos(\theta_H) + cos(\phi-\phi_H)sin(\theta)sin(\theta_H)\right] \tag{B.1}$$

The Smit and Beljers formula for FMR is given by the differentials of the magnetic free energy (F) with respect to the polar θ and azimuthal ϕ angles of the magnetization such that

$$\left(\frac{\omega}{\gamma}\right)^2 = \left[F_{\theta\theta}F_{\phi\phi} - (F_{\theta\phi})^2\right]\frac{1}{M^2\sin^2\theta} \tag{B.2}$$

Substituting B.1 into B.2 gives

$$\left(\frac{\omega}{\gamma}\right)^2 = \frac{1}{M^2sin^2(\theta)}\Big[\left(4.2K_1cos(\theta)cos(3\phi)sin^3(\theta) + HMcos(\phi-\phi_H)sin(\theta)\sin(\theta_H)\right) \\ \times\Big(-4\pi M^2cos^2(\theta) - 1.33K_1cos^4(\theta) - 2.8K_1cos^3(\theta) - 2.8K_1cos^3(\theta)cos(3\phi)sin(\theta) \\ +4\pi M^2sin^2(\theta) - K_1sin^4(\theta) + cos(\theta)\left[HMcos(\theta_H) + 4.66K_1cos(3\phi)sin^3(\theta)\right] \\ +\frac{7}{4}K_1sin^2(2\theta) + HMcos(\phi-\phi_H)sin(\theta)sin(\theta_H)\Big) - \\ \Big(-1.4K_1sin^4(\theta)sin(3\phi) + 1.05K_1sin^2(\theta)sin(3\phi) + HMcos(\theta)sin(\theta_H)sin(\phi-\phi_H)\Big)^2\Big] \tag{B.3}$$

In the limit that $\theta_H \to \frac{\pi}{2}$ so that $\theta \to \frac{\pi}{2}$and $\phi \to \phi_H$ (i.e. in-plane measurements where the magnetisation is aligned with the field)

$$\left(\frac{\omega}{\gamma}\right) = \sqrt{\frac{HM(-K_1 + M(H+4\pi M)) - 1.96K_1^2sin^2(3\phi_H)}{M^2}} \tag{B.4}$$

If we assume that $H = H_r$ then

$$H_r = -\left(2\pi M - \frac{K_1}{2M}\right) + \sqrt{\left(\frac{\omega}{\gamma}\right)^2 - 2\pi K_1 + \frac{3K_1^2}{2M^2} - \frac{K_1^2}{M^2}cos(6\phi) + 4\pi^2M^2} \tag{B.5}$$

Adding in the presumably surface induced uniaxial anisotropy (K_u), such that

$$F = K_1\left[\tfrac{1}{3}cos^4(\theta) + \tfrac{1}{4}sin^4(\theta) - \tfrac{1.4}{3}sin^3(\theta)cos(\theta)cos(3\phi)\right] + 2M^2\pi cos^2(\theta) - MH\Big[cos(\theta)cos(\theta_H) + cos(\phi - \\ \phi_H)sin(\theta)sin(\theta_H) + K_usin^2(\theta)sin^2(\phi) \tag{B.6}$$

and making the same approximations for θ and ϕ gives

$$H_r = \frac{\left[2MK_1 - 4\pi M^3 + 4MK_u sin^2(\phi_H) - 2MK_u cos^2(\phi_H)\right]}{M^2} + \frac{\sqrt{\left(4\pi M^3 + 2MK_u cos^2(\phi_H) - 2MK_1 - 4MK_u sin^2(\phi_H)\right)^2 + 16\left[\frac{1}{2}K_u K_1 cos^2(\phi_H) - 2\pi M^2 K_u cos^2(\phi_H) + 2K_u^2 cos^2(\phi_H) sin^2(\phi_H) - \frac{1}{2}K_1 K_u sin^2(\phi_H) + 2\pi M^2 K_u cos^2(\phi_H) + \frac{1}{2}K_1^2 sin^2(3\phi_H) + \frac{\omega^2 M^2}{4\gamma^2}\right]}}{M^2} \quad \text{(B.7)}$$

Finally making the substitution

$$sin^2(x) = \frac{1}{2} - \frac{1}{2}cos(2x)$$

we obtain

$$H_r = \frac{\left[2MK_1 - 4\pi M^3 + 4MK_u sin^2(\phi_H) - 2MK_u cos^2(\phi_H)\right]}{M^2} + \frac{\sqrt{\left(4\pi M^3 + 2MK_u cos^2(\phi_H) - 2MK_1 - 4MK_u sin^2(\phi_H)\right)^2 + 16\left[\frac{1}{2}K_u K_1 cos^2(\phi_H) - 2\pi M^2 K_u cos^2(\phi_H) + 2K_u^2 cos^2(\phi_H) sin^2(\phi_H) - \frac{1}{2}K_1 K_u sin^2(\phi_H) + 2\pi M^2 K_u cos^2(\phi_H) + \frac{1}{4}K_1^2(1 - cos(6\phi_H)) + \frac{\omega^2 M^2}{4\gamma^2}\right]}}{M^2} \quad \text{(B.8)}$$

List of Symbols

α: The Gilbert damping parameter

d: Spacing of crystal lattice planes

ΔH: Resonance linewidth in magnetic field

ΔH_0: Extrinsic damping component of the FMR linewidth

f_r: Resonance frequency

g: Landé g-factor

γ: Gyromagnetic ratio

H_{cubic}: Cubic anisotropy field component

H_{coer}: Coercive field

H_{eff}: Effective magnetic field

H_r: Resonance field

H_u: Uniaxial anisotropy field

K_c: Cubic anisotropy constant

K_u: Uniaxial anisotropy constant

M: Magnetisation

μ_0: Magnetic permeability of free space

$\mu_0 H$: Magnetic field

μ_B: Bohr magneton

M_{eff}: Effective magnetisation

M_s: Saturation magnetisation

ρ: Electrical resistivity

ϕ: Azimuthal angle in the FMR

θ: Polar angle in the FMR

T_{an}: Thermal annealing temperature

T_B: Blocking temperature

T_C: Curie temperature

$S_{x,y}$: S-parameter measured between ports x and y of the VNA

χ: Magnetic susceptibility

χ_{XRD}: Tilt angle in the XRD

ω: Angular frequency

ω_{XRD}: Incident X-ray angle in the XRD

List of Abbreviations

AFM: Anti-ferromagnetic

APB: Antiphase boundary

CFAS: The quaternary heusler alloy $Co_2FeAl_{0.5}Si_{0.5}$

CO: Carbon monoxide

CO_2: Carbon dioxide

CPW: Co-planar waveguide

EELS: Electron energy-loss spectroscopy

Fe_3O_4: Magnetite

FM: Ferromagnetic

FMR: Ferromagnetic resonance

FWHM: Full-width at half maximum

FY: Fluorescence yield detection

Ge: Germanium

HAADF: High-angle annular dark field

HAADF-STEM: High-angle annular dark field scanning transmission electron microscopy

HWHM: Half-width at half maximum

LINAC: Linear Accelerator

LLG: Landau-Lifshitz-Gilbert (Equation)

MCA: Magnetocrystalline Anisotropy

NP: Nanoparticle

Oh: Octahedrally co-ordinated lattice site

PF: Pole figure

RC: Rocking curve

RF / rf: Radio-frequency (microwave frequency electromagnetic wave)

SAED: Selective area electron diffraction

Si: Silicon

Td: Tetrahedrally co-ordinated lattice site

TEY: Total electron yield detection

UHV: Ultra-High Vacuum

VNA: Vector network analyser

VNA-FMR: Vector network analyser ferromagnetic resonance spectroscopy

VSM: Vibrating sample magnetometer/magnetometry

XAS: X-ray absorption spectrum/spectroscopy

XMCD: X-ray magnetic circular dichroism

XRD: X-ray diffraction/X-ray diffractometer

XRR: X-ray reflectivity

YSZ(111): (111) aligned 8% per mol yttria-stabilised zirconia

Bibliography

[1] *Spin Valve Effect in Soft Ferromagnetic Sandwiches*, B. Dieny, V.S. Speriosu, B.A. Gurney, S.S.P. Parkin, D.R. Wilhoit, K.P. Roche, S. Metin, D.T. Peterson and S. Nadimi, J. Magn. Mag. Mat **93** (1991) pp.101-104

[2] *Spintronics: A Spin-Based Electronics Vision for the Future*, S.A. Wolf, D.D. Awschalom, R.A. Buhrman, J.M. Daughton, S. von Molnaŕ, M.L. Roukes, A.Y. Chtchelkanova and D.M. Treger, Science **294** (2001)

[3] *The Emergence of Spin Electronics in Data Storage*, C. Chappert, A. Fert and F.N. Van Dau, Nat. Mater. **6** *11* (2007) pp.813-823

[4] *Roadmap for Emerging Materials for Spintronic Device Applications*, A. Hirohata, H. Sukegawa, H. Yanagihara, I. Žutić, T. Seki, S. Mizukami, and R. Swaminathan, IEEE Trans. Mag. **51** *10* (2015)

[5] *Spin-Transfer Torque RAM Technology: Review and Prospect*, T. Kawahara, K. Ito, R. Takemura and H. Ohno, Microel. Rel. **52** *4* (2012) pp.613-627

[6] *Anisotropic Absorption of Pure Spin Currents*, A.A. Baker, A.I. Figueroa, C.J. Love, S.A. Cavill, T. Hesjedal and G. van der Laan, Phys. Rev. Lett. **116** 047201 (2016)

[7] *Highly Spin-Polarized Materials and Devices for Spintronics*, K. Inomata , N. Ikeda, N. Tezuka, R. Goto, S. Sugimoto, M. Wojcik and E. Jedryka, Sci. Technol. Adv. Mater. **9** (2008) 014101

[8] *Half-Metallic Ferromagnets: From Band Structure to Many-Body Effects*, M.I. Katsnelson, V.Y. Irkhin, L. Chioncel, A.I. Lichtenstein, and R.A. de Groot, Rev. Mod. Phys. **80** (2008) 315

[9] *Demonstration of Half-Metallicity in Fermi-Level-Tuned Heusler Alloy $Co_2FeAl_{0.5}Si_{0.5}$ at Room Temperature*, R. Shan, H. Sukegawa, W.H. Wang, M. Kodzuka, T. Furubayashi, T. Ohkubo, S. Mitani, K. Inomata and K. Hono, Phys. Rev. Lett. **102** (2009) 246601

[10] *Magnetite: A Search for the Half-Metallic State*, M. Fonin, Y.S. Dedkov, R. Pentcheva, U. Rüdiger and G. Güntherodt, J. Phys. Cond. Mat. **19** (2007) 315217

[11] *Atomic-Scale Structure and Properties of Highly Stable Antiphase Boundary Defects in Fe_3O_4*, K.P. McKenna, F. Hofer, D. Gilks, V.K. Lazarov, C. Chen, Z. Wang and Y. Ikuhara, Nature Comms. **5** (2014) 5740

[12] *Superparamagnetic Behaviour of Structural Domains in Epitaxial Ultrathin Magnetite Films*, F.C. Voogt, T.M. Palstra, L. Niesen, O.C. Rogojanu, M.A. James and T. Hibma, Phys. Rev. B. **57** (1998)

[13] *The Antiphase Boundary in Half-Metallic Heusler Alloy $Co_2Fe(Al,Si)$: Atomic Structure, Spin Polarization Reversal, and Domain Wall Effects*, Z. Nedelkoski, A. M. Sanchez, A. Ghasemi, K. Hamaya, R.F.L. Evans, G.R. Bell, A. Hirohata and V.K. Lazarov, Appl. Phys. Lett. **109** (2016) 222405

[14] *Spin-Torque Switching Window, Thermal Stability and Materials Parameters of MgO Tunnel Junctions*, T. Devolder, L. Bianchini, K. Miura, K. Ito, J-V. Kim, P. Crozat, V. Morin, A. Helmer, C. Chappert, S. Ikeda and H. Ono, App. Phys. Lett. **98** 162502 (2011)

[15] *Controlling and Patterning the Effective Magnetization in $Y_3Fe_5O_{12}$ Thin Films Using Ion Irradiation*, W.T. Ruanea), S.P. Whitea), J.T. Brangham, K.Y. Meng, D.V. Pelekhov, F.Y. Yang and P.C. Hammel, AIP Advances **8** (2018) 056007

[16] *Fe_3O_4(111) Thin Films with Bulk-Like Properties: Growth and Atomic Characterisation*, K, Matsuzaki, V.K. Lazarov , L. Lari, H. Hosano and T. Susaki, J. Phys. D: Appl. Phys. **46** *2* (2013)

[17] *The Quantum Theory of Ferromagnetism*, S.V. Vonsovskii, K.B. Vlasov and E.A. Turov, Soviet Physics JETP **2** *1* (1956)

[18] *Magnetism in Condensed Matter* (1st Edition), S. Blundell, Oxford University Press (2001)

[19] *Introduction to Solid State Physics* (8th Edition), C. Kittel, John Wiley and Sons (2005)

[20] *Magnetic Oxides* (1st edition), G.F. Dionne, Springer (2009)

[21] *Fundamentals and Applications of Magnetic Materials* (1st Edition), K. M. Krishnan, Oxford: Oxford University Press (2016)

[22] *Physics of Ferromagnetism* (2nd Edition), S. Chikazumi, Oxford University Press (1997)

[23] *New Correlated-Effective-Field Theory in the Ising Model*, T. Kaneyoshi, I.P. Fittipaldi, R. Honmura and T. Manabe, Phys. Rev. B **24** *1* (1981)

[24] *Antiferromagnetism and Ferrimagnetism*, L. Néel, Proc. Phys. Soc. A **65** (11) (1952) 869

[25] *Antiferromagnetism*, A.B. Lidiard, Rep. Prog. Phys. **17** (1954) 201

{26] *Electronic Structure and Magnetic Properties of Cubic and Hexagonal SrMnO3*, R. Søndenå, P. Ravindran, S. Stølen, T. Grande and M. Hanfland, Phys. Rev, B. **74** 144102 (2006)

[27] *Antiferromagnetic Superexchange Effect,* R.K. Nesbet, Phys. Rev. **119** *2* (1960) pp.658

[28] *New Approach to the Theory of Superexchange Interactions*, P. W. Anderson, Phys. Rev. **115** *2* (1959)

[29] *Orbital Physics in Transition-Metal Oxides*, Y. Tokura and N. Nagaosa, Science **288** (2000)

[30] *Origin of Reduced Magnetization and Domain Formation in Small Magnetite Nanoparticles*, Z. Nedelkoski, D. Kepaptsoglou, L. Lari, T. Wen, R.A. Booth, S.D. Oberdick, P.L. Galindo, Q.M. Ramasse, R.F.L. Evans, S. Majetich and V.K. Lazarov, Sci. Rep. **7** (2017) 45997

[31] *Hund's Rules, the Alternating Rule, and Symmetry Holes*, J. Phys. Chem. **97** (1993) pp.2425-2434

[32] *Superexchange Interaction and Symmetry Properties of Electron Orbitals*, J. Kanamori, J. Phys. Chem. Solids, **10** (1959) pp.87-98

[33] *Considerations on Double Exchange*, P.W. Anderson and H. Hasegawa, Phys. Rev. **100** *2*(1955)

[34] *Ferromagnetic Resonance Absorption in $BaFe_{12}O_{19}$, A Highly Anisotropic Crystal*, J. Smit and H.G. Beljers, Phillips. Res. Rep. **10** (1955) pp.113-130

[35] *Derivation of the Resonance Frequency From the Free Energy of Ferromagnets*, L. Baselgia, M. Warden, F. Waldner, S.L. Hutton, J.E. Drumheller, Y.Q. He, P.E. Wigen and M. Marysko, Phys. Rev. B **38** *4* (1988)

[36] *Anisotropy and Damping in $Co_2FeAl_{0.5}Si_{0.5}$ via Electrical Detection of Ferromagnetic Resonance*, L. Bai, N. Tezuka, M. Kohda and J. Nitta, Jap. J. Appl. Phys. **51** (2012) 083001

[37] *In Situ Manipulation of Magnetic Anisotropy in Magnetite Thin Films*, A. Brandlmaier, S. Geprägs, M. Weller, A. Boger, M. Opel, H. Huebl, C. Bihler, M.S. Brandt, B. Botters, G.D. Grundler, R. Gross and S.T.B. Goennenweien, Phys. Rev. B **77** (2008) 104445

[38] *Correlations Between Structural, Electronic Transport, and Magnetic Properties of $Co_2FeAl_{0.5}Si_{0.5}$ Heusler Alloy Epitaxial Thin Films*, M.S. Gabor, M. Belmeguenai, T. Petrisor, Jr., C. Ulhaq-Bouillet, S. Colis, and C. Tiusan, Phys. Rev. B **92** (2015) 054433

[39] *Anisotropic Intrinsic Damping Constant of Eptiaxial Co_2MnSi Heusler Alloy Films*, R. Yilgin, Y. Sakuraba, M. Oogane, S. Mizukami, Y. Ando and T. Miyazaki, Jap. J. Appl. Phys **46** *9* (2007) L205-L208

[40] *Magnetostriction and Permeability of Magnetite and Cobalt-Substituted Magnetite*, L.R. Bickford Jr, J. Pappis and J.L. Stull, Physical Review 99 **4** (1955)

{41] *Bending Strain-Tunable Magnetic Anisotropy in CoFeAl Thin Film on Kapton*, M. Gueye, B.M. Wague, F. Zighem, M. Belmeguenai, M.S. Gabor, T. Petrisor, Jr., C. Tiusan, S. Mercone, and D. Faurie, Appl. Phys. Lett **105** 062409 (2014)

[42] *Ferromagnetic Resonance of Ultrathin Metallic Layers*, M. Farle, Rep. Prog. Phys. **61** (1998) 755

[43] *Ferromagnetic Resonance Absorption In Magnetite Single Crystals*, L.R. Bickford Jr., Phys. Rev. **78** *4* (1950) pp.449-457

[44] *Magnetic Anisotropy in Metallic Multilayers*, M.T. Johnson, P.J.H. Bloemen, F.J.A. den Broeder and J.J. de Vries, Rep. Prog. Phys. **59** (1996) pp.1409–1458

[45] *Fundamentals of Magnetism* (1st Edition), M. Getzlaff, Springer (2008)

[46] *Magnetism: From Fundamentals to Nanoscale Dynamics* 1st Edition, J. Stohr and H.C Siegmann, Springer (2006)

[47] *Variation of Magnetisation and the Landé g Factor with Thickness in Ni-Fe Films*, J.P. Nibarger, R. Lopusnik, Z. Celinski and T.J. Silva, Appl. Phys. Lett. **83** *1* (2003)

[48] *Spin-Orbit Interaction Enhancement in Permalloy Thin Films by Pt-Doping*, A. Hrabec, F.J.T. Gonçalves, C.S. Spencer, E. Arenholtz, A.T. N'Diaye, R.L. Stamps and C.H. Marrows, Phys. Rev. B **93** *1* (2016)

[49] *Understanding Solids: The Science of Materials* (1st Edition), R.J.D. Tilley, John Wiley and Sons (2004)

[50] *A Phenomenological Theory of Damping in Ferromagnetic Materials*, T.L. Gilbert, IEEE Trans. Magn. **40** *6* (2004) pp.3443-3449

[51] *The Fascinating World of the Landau–Lifshitz–Gilbert Equation: An Overview*, M. Lakshmanan, Phil. Trans. R. Soc. A **369** (2011) pp.1280–1300

[52] *On the Theory of Ferromagnetic Resonance Absorption*, C. Kittel, Phys. Rev. 73 **2** (1948)

[53] *Spin–Orbit-Driven Ferromagnetic Resonance*, D. Fang, H. Kurebayashi, J. Wunderlich, K. Výborný, L.P. Zárbo, R.P. Campion, A. Casiraghi, B.L. Gallagher, T. Jungwirth and A.J. Ferguson, Nature Nanotech. **6** (2011)

[54] *Concerning the Theory of Ferromagnetic Resonance Absorption*, J.H. van Vleck, Phys. Rev. **78** *3*, (1950)

[55] *Magnetics, Dielectrics and Wave Propagation with MATLAB® Codes* (First Edition), C. Vittoria, CRC Press (2012)

[56] *Spin Dynamics in Ferromagnets: Gilbert Damping and Two Magnon Scattering*, Kh. Zakeri, J. Lindner, I. Barkusov, R. Meckenstock, M. Farle, U. von Horsten, H. Wende, W. Kuene, J. Rocker, S.S. Kalarickal, K. Lenz, W. Kuch, K. Baberschke and Z. Frait, Phys. Rev. B. **76** (2007) 104416

[57] *Origin of Intrinsic Gilbert Damping,* M.C. Hickey and J.S. Moodera, Phys. Rev. Lett. **102** (2009) 137601

[58] *Extrinsic Contribution to the Ferromagnetic Resonance Response of Ultrathin Films*, R. Arias and D.L. Mills, Phys. Rev. B **60** *10* (1999)

[59] *Magnon Damping by Magnon-Phonon Coupling in Manganese Perovskites,* P. Dai, H.Y. Hwang, J. Zhang, J.A. Fernandez-Baca, S-W. Cheong, C. Kloc, Y. Tomioka and Y. Tokura, Phys. Rev. B **61** (2000) 9553

[60] *Excitation of Spin Waves in Ferromagnets: Eddy Current and Boundary Condition Effects*, P. Pincus, Phys. Rev. **118** (1960) 658

[61] *Spin Dynamics and Damping in Ferromagnetic Thin Films and Nanostructures* (1st Edition), A. Barman and J. Sinha, Springer (2018)

[62] *Roles of Nonequilibrium Conduction Electrons on the Magnetization Dynamics of Ferromagnets*, S. Zhang and Z. Li, Phys. Rev. Lett. **93** (2004) 127204

[63] *Nonlocal Magnetization Dynamics in Ferromagnetic Heterostructures*, Y. Tserkovnyak, A. Brataas, G.E.W. Bauer and B.I. Halperin, Rev. Mod. Phys. **77** (2005) 1375

[64] *Magnetic Relaxation in Metallic Films: Single and Multilayer Structures,* B. Heinrich, R. Urban and G. Woltersdorf, J. Appl. Phys. **91** *10* (2002)

[65] *Radiative Damping in Waveguide-Based Ferromagnetic Resonance Measured via Analysis of Perpendicular Standing Spin Waves in Sputtered Permalloy Films*, M.A.W. Schoen, J.M. Shaw,H.T. Nembach, M. Weiler and T.J. Silva, Phys. Rev. B **92** (2015) 184417

[66] *Spin-Pumping and Two-Magnon Scattering in Magnetic Multilayers* (PhD Thesis), G. Woltesdorf, Halle, Martin-Luther-Universität (2001)

[67] *Gilbert Damping in Magnetic Multilayers*, E. Šimánek and B. Heinrich, Phys. Rev. B **67** (2003) 144418

[68] *Anomalous Damping of Spin Waves in Magnetic Metals*, V. Korenman and R. E. Prange, Phys. Rev. B **6** (1972) 2769

[69] *Spin-Orbital Gilbert Damping in Common Magnetic Metals*, V. Kamberský, Phys. Rev. B, **76** (2007) 134416

[70] *Scattering Theory of Gilbert Damping*, A. Brataas, Y. Tserkovnyak, and G. E. W. Bauer, Phys. Rev. Lett. **101** (2008) 037207

[71] *On Ferromagnetic Resonance Damping in Metals*, V. Kamberský, Czech. J. Phys. B. **26** *12* (1976) pp.1366-1383

[72] *First-Principles Investigation of the Damping of Fast Magnetization Precession in Ferromagnetic 3d Metals*, J. Kuneš and V. Kamberský, Phys. Rev. B **65** (2002) 212411

[73] *Atomistic Spin Dynamics: Foundations and Applications* (1st Edition), O. Eriksson, A. Bergman, L. Bergqvist and J. Hellsvik, Oxford University Press, (2017)

[74] *Gilbert Damping Tensor Within the Breathing Fermi Surface Model: An isotropy and Non-Locality,* D. Thonig and J. Henk, New. Jour. Phys. **16** (2014)

[75] *Phonon-Drag Thermomagnetic Effects in n-Type Germanium. I. General Survey*, C. Herring, T.H. Geballe, and J.E. Kunzler, Phys. Rev. **111** *36* (1958)

[76] *Two-Magnon Scattering and Viscous Gilbert Damping in Ultrathin Ferromagnets*, K. Lenz, H. Wende, W. Kuch, K. Baberschke, K. Nagy and A. Jánossy, Phys. Rev. B **73** (2006) 144424

[77] *Structure of Magnetite (Fe_3O_4) Above the Curie Temperature: A Cation Ordering Study*, D. Levy, R Giustetto and A. Hoser, Phys. Chem. Minerals **39** (2012) pp.169-176

[78] *Hall Effect, Magnetization, and Conductivity of Fe_3O_4 Epitaxial Thin Films*, D. Reisinger, P. Majewski, M. Opel, L. Aff and R. Gross, Appl. Phys. Lett. **35** *21* (2004) pp.4980-4982

[79] *Thickness Dependence of Anomalous Magnetic Behavior in Epitaxial Fe_3O_4(111) Thin Films: Effect of Density of Antiphase Boundaries*, J-B. Mouusy, S. Gota, A. Bataille, M-j. Guittet, M. Gautire-Soyer, F. Delille, B. Dieny, F. Ott, T.D. Doan, P. Warin, P. Bayle-Guillemand, C. Gatel and E. Snoeck, Phys. Rev. B **70** (2004) 174448

[80] *Atomic Layer Deposition of Superparamagnetic and Ferrimagnetic Magnetite Thin Films*, Y. Zhang, M. Liu, Y. Zhang, X. Chen, W. Ren, and Z-G. Ye, J. Appl. Phys. **117** (2015) 17C743

[81] *Charge-Orbital Ordering and Verwey Transition in Magnetite*, H-T. Jeng, G.Y. Guo and D.J. Huang, Phys. Rev. Lett. **93** *15* (2004)

[82] *Band Gap in Magnetite above Verwey Temperature Induced by Symmetry Breaking*, H. Liu and C. Di Valentin, J. Phys. Chem. C **121** (2017) 25736-25742

[83] *Charge Order and Three-Site Distortions in the Verwey Structure of Magnteite*, M.S. Senn, J.P. Wright and J.P. Attfield, Nature **481** (2012) pp.173-176

[84] *Stoichiometry of $Fe_{3-\delta}O_4$(111) Ultrathin Films on Pt(111)*, P. Morrall, F. Schedin, G.S. Case, M.F. Thomas, E. Dudzik, G. van der Laan and G. Thornton, Phys. Rev. B **67** (2003) 214408

[85] *Spin Wave Spectra of Magnetite*, M.L. Glasser and F.J. Milford, Phys. Rev. **130** *5* (1963)

[86] *Nanoscale Devices: Fundamentals and Applications*, R. Gross A. Sidorenko and L. Tagirov, 1st Edition Springer (2006)

[87] *Thin Films and Heterostructures for Oxide Electronics*, S.B. Ogale (1st edition), Springer (2005)

[88] *Electronic Structure in High Temperature Phase of Fe_3O_4*, A. Yanase and N. Hamada, J. Phys. Soc. Jpn. **68** (1999) pp. 1607-1613

[89] *Magnetite: a Search for the Half-Metallic State*, M. Fonin, Y.S Dedkov, R. Pentcheva, U. Rüdiger and G. Güntherodt, J. Phys. Cond. Mat. **19** *31* (2007)

[90] *Fe t_{2g} Band Dispersion and Spin Polarization in Thin Films of Fe_3O_4(0 0 1)/MgO(0 0 1): Half-Metallicity of Magnetite Revisited*, W. Wang, J-M. Mariot, M.C. Richter, O. Heckmann, W. Ndiaye, P. De Padova, A. Taleb-Ibrahimi, P. Le Fevre, F. Bertran, F. Bondino, E. Magnano, J. Krempasky, P. Blaha, C. Cacho, F. Parmigiani, and K. Hricovini, Phys. Rev. B **87** (2013) 085118

[91] *Spin Resolved Photoelectron Spectroscopy of Fe_3O_4: the Case Against Half-Metallicity,* J.G. Tobin, S.A. Morton, S.W. Yu G.D. Waddill, I.K. Schuller and S.A. Chambers, J. Phys. Cond. Mat. **19** (2007) 315218

[92] *The Verwey Transition – A Topical Review*, F. Walz, J. Phys. Cond. Mat. **14** *12* (2002)

[93] *Electronic Conductivity and Transition Point of Magnetite ("Fe_3O_4")*, E.J.W. Verwey and P.W. Haayman, Physica VIII **9** (1941)

[94] *Nature of the Verwey Transition in Magnetite (Fe_3O_4) to Pressures of 16 GPa,* G. Kh. Rozenberg, G.R. Hearne, M.P. Pasternak, P.A. Metcalf and J.M. Hong, Phys. Rev. B **53** *10* (1996)

[95] *The Verwey Transition - A New Perspective*, J. García and G. Subías, J. Phys. Cond. Mat. **16** (2004) R145-R178

[96] *Impurity Effects Upon the Verwey Transition in Magnetite*, V.A.M. Brabers, F. Walz and H. Kronmüller, Phys. Rev. B. **58** *21* (1998)

[97] *Anomalous Moment and Anisotropy Behaviour in Fe_3O_4 Thin Films*, D.T. Margulies, F.T. Parker, F.E. Spada, R.S. Goldman, J. Li, R. Sinclair and A.E. Berkowitz, Phys. Rev. B **53** *14* (1996) pp.9175-9187

[98] *Influence of Non-Stoichiometry on the Verwey Transition*, R. Aragón, D.J. Buttrey, J.P. Shepherd, and J.M. Honig, Phys Rev. B **31** *1* (1985)

[99] *Ferroelectric Switching in Multiferroic Magnetite (Fe_3O_4) Thin Films*, M. Alexe, M. Ziese, D. Hesse, P. Esquinazi, K. Yamauchi, T. Fukushima, S. Picozzi, and U. Gösele, Adv. Mater. **21** (2009) pp. 4452-4455

[100] *Enhancing the Spin-Orbit Coupling in Fe_3O_4 Epitaxial Thin Films by Interface Engineering*, Z. Huang, W. Liu, J. Yue, Q. Zhou, W. Zhang, Y. Lu, Y. Sui, Y. Zhai, Q. Chen, S. Dong, J. Wang, Y. Xu and B. Wang, ACS Appl. Mater. Interfaces, **8** (2016) pp.27353 - 27359

[101] *Enhancement of the Magnetization Saturation on Magnetite (100) Epitaxial Films by Thermo-Chemical Treatment*, Y. Zhou, X. Jin and I.V. Shvets, J. Appl. Phys. **95** *11* (2004) pp.7357-7359

[102] *Influence of the Antiphase Domain Distribution on mthe Magnetic Structure of Magnetite Thin Films*, J.D. Wei, I. Knittel, U. Hartmann, Y. Zhou, S. Murphy, I.V. Shvets and F.T. Parker, Appl. Phys. Lett. **89** (2006) 122517

[103] I*nterdiffusion Study of Magnesium in Magnetite Thin Films Grown on Magnesium Oxide (001) Substrates*, K.A. Shaw, E. Lochner and D.M. Lind, J. Appl. Phys. **87** *4* (2000) pp.1727-1733

[104] *Thickness Dependence of the Effective Damping in Epitaxial Fe_3O_4 /MgO Thin Films*, S. Serrano-Guisan, H.-C. Wu, C Boothman, M. Abid, B.S. Chun, I.V. Shvets and H.W. Schumacher, J. Appl.Phys. **109** (2011) 013907

[105] *Damping in Magnetisation Dynamics of Single Crystal Fe_3O_4/GaN Thin Films,* X. Zou, J. Wu, P.K.J. Wong, T.B. Xu, R. Zhang, Y.Zhai, C. Bunce and R.W. Chantrell, J. Appl. Phys. **109** (2011) 07D341

[106] *Ferromagnetic Resonance in Magnetite Thin Films*, M. Nagata, K. Tanabe, T. Moriyama, D. Chiba, J.-H. Ohe, M/ Myoka, T. Niizeki, H. Yanagihara, E. Kita and T. Ono, IEEE Trans. Magn. **50** *1* (2014)

[107] *Antiphase Domain Boundaries at the Fe_3O_4(001) Surface*, G.S. Parkinson, T.A. Manz, Z. Novotný, P.T. Sprunger, R.L. Kurtz, M. Schmid, D.S. Sholl and U. Diebold, Phys.Rev. B **85** (2012) 195450

[108]*Origin of the Anomalous Magnetic Behaviour in Single Crystal Fe_3O_4 Films*, D.T. Margulies, F.T. Parker, M.L. Rudee, F.E. Spada, J.N. Chapman, P.R. Aitchison and A.E. Berkowitz, **79** *25* (1997)

[109] *Origin of the Increased Resistivity in Epitaxial Fe_3O_4 Films*, W. Eerensein, T.T.M. Palstra, T. Hibma and S. Celotto, Phys. Rev. B. **66** (2002) 201101(R)

[110] *Structure, Magnetic Property and Spin Polarisation of $Co_2FeAl_xSi_{1-x}$ Heusler Alloys,* T.M. Nakatani, A. Rajanikanth, Z. Gercsi, Y.K. Takahashi, K. Inomata and K. Hono, J. appl. Phys. **102** (2007) 033916

[111] *Fabrication of Highly Spin-Polarized $Co_2FeAl_{0.5}Si_{0.5}$ Thin-Films*, M.Vahidi, J.A. Gifford, S.K. Zhang, S. Krishnamurthy, Z.G. Yu, L. Yu, M. Huang, C. Youngbull, T.Y. Chen, and N. Newman, APL Materials **2** (2014) 0461081

[112] *Investigation of the Temperature Dependence of Ferromagnetic Resonance and Spin Waves in $Co_2FeAl_{0.5}Si_{0.5}$*, L.M. Loong, J.H. Kwon, P. Deorani, C.N.T. Yu, A. Hirohata and H. Yang, Appl. Phys. Lett **104** (2014) 232409

[113] *Magnetic Damping and Spin Polarisation of Highly Ordered B_2 Co_2FeAl Thin Films*, Y. Cui, J. Lu, S. Schafer, B. Khodadadi, T. Mewes, M. Osofsky and S.A. Wolf, J. Appl. Phys **116** (2014) 073902

[114] *Quantitative Analysis of Atomic Disorders in Full-Heusler Co2FeSi Alloy Thin Films Using X-Ray Diffraction with Co Kα and Cu Kα Sources*, Y. Takamura, R. Nakane and S. Sugahara, J. Appl. Phys **107** (2010) 09B111

[115] *Effect of Annealing on the Structure and Magnetic Properties of $Co_2FeAl_{0.5}Si_{0.5}$ Thin Films on Ge(111)*, B. Kuerbanjiang, C. Love, D. Kepaptsoglou, Z. Nedelkoski, S. Yamada, A. Ghasemi, Q.M. Ramasse, K. hamaya, S.A. Cavill and V.K. Lazarov, Journal of Alloys and Compounds **748** (2018)

[116] *The Role of Chemical Structure on the Magnetic and Electronic Properties of Co2FeAl0.5Si0.5/Si(111) Interface*, B. Kuerbanjiang, Z. Nedelkoski, D. Kepaptsoglou, A. Ghasemi, S. E. Glover, S. Yamada, T. Saerbeck, Q.M. Ramasse, P.J. Hasnip, T.P.A. Hase, G.R. Bell, K. Hamaya, A. Hirohata and V.K. Lazarov, App. Phys. Lett. **108** (2016) 172412

[117] *Perpendicular Magnetic Anisotropy in Heusler Alloy Films and Their Magnetoresistive Junctions*, A. Hirohata, W. Frost , M. Samiepour and J-Y Kim, Materials **11** (2018) 105

[118] *First Principles Study of the Gilbert Damping Constants of Heusler Alloys Based on the Torque Correlation Model*, A, Sakuma, J. Phys. D: Appl. Phys. **48** (2015) 164011

[119] *175% Tunnel Magnetoresistance at Room Temperature and High Thermal Stability Using $Co_2FeAl_{0.5}Si_{0.5}$ Full-Heusler Alloy Electrodes*, N. Tezuka, N. Ikeda, S. Sugimoto and K. Inomata, App. Phys. Lett. **89** (2006) 252508

[120] *Effect of Annealing on $Co_2FeAl_{0.5}Si_{0.5}$ Thin Films: A Magneto-Optical and X-Ray Absorption Study*, S. Trudel, G. Wolf, J. Hamrle, B. Hillebrands, P. Klaer, M. Kallmayer, H-J. Elmers, H. Sukegawa, W. Wang, and K. Inomata, Phys. Rev. B **83** (2011) 104412

[121] *Realisation of Magnetically and Atomically Abrupt Half-Metal/Semiconductor Interface: $Co_2FeSi_{0.5}Al_{0.5}$/Ge(111)*, Z. Nedelkoski, B. Kuerbanjiang, S.E. Glover, A.M. Sanchez, D. Kepaptsoglou, A. Ghasemi, C.W. Burrows, S. Yamada, K. Hamaya, Q.M. Ramasse, P.J. Hasnip, T. Hase, G.R. Bell, A. Hirohata, and V.K. Lazarov, Sci. Rep. **6** (2016) 37282

[122] *Co_2FeAl Heusler Thin Films Grown on Si and MgO Substrates: Annealing Temperature Effect,* M. Belmeguenai, H. Tuzcuoglu, M.S. Gabor, T. Petrisor Jr., C. Tiusan, F. Zighem, S.M. Chérif, and P. Moc h, J. Appl. Phys, **11** (2014) , 043918

[123] *Temperature-Dependent Gilbert Damping of Co_2FeAl Thin Films with Different Degree of Atomic Order*, A. Kumar, F. Pan, S. Husain, S. Akansel, R. Brucas, L. Bergqvist, S. Chaudhary, and P. Svedlindh, Phys. Rev. B **96** (2017) 224425[124] *The Basics of Crystallography and Diffraction* (2nd Edition), C. Hammond, Oxford University Press (2003)

[125] *X-Ray Thin Film Measurment Techniques: V. X-Ray Reflectivity Measurement*, M. Yasaka, Rigaku Journal **26** *2* (2010)

[126] *Elements of X-Ray Diffraction* (2nd Edition), B.D. Cullity, Addison-Wesley Publishing (1978)

[127] *Grazing Incidence X-Ray Diffraction*, P. Dutta, Current Science **78** *12* (2000)

[128] *X-Ray Thin Film Measurement Techniques*, K. Inaba, Rigaku Journal **24** *1* (2008)

[129] *Thin-Film Characterisation by Grazing Incidence X-Ray Diffraction and Multiple Beam Interference*, S-L. Chang, J. Phys. Chem. Solids **62** (2001) pp.1765-1775

[130] *In-Plane X-Ray Diffraction for Characterization of Monolayer and Few-Layer Transition Metal Dichalcogenide Films*, M. Chubarov, T.H. Choudhury, X. Zhang and J.M. Redwing, Nanotechnology **29** (2018) 055706

[131] *X-Ray Diffraction Analysis of Cubic Zincblende III-Nitrides*, M. Frentrup, L.Y. Lee, S-L. Sahonta, M.J. Kappers, F. Massabuau, Priti Gupta, R.A. Oliver, C.J. Humphreys and D.J. Wallis, J. Phys D: Appl. Phys **50** *43* (2017)

[132] *Introduction to X-Ray Analysis Using the Diffraction Method*, H. Toraya, Rigaku Journal **32** *2* (2016)

[133] *INDX, X-Ray Diffraction Powder Pattern Indexing, Trial Unit Cell Testing*, R.B. Roof, Organisation for Economic Co-Operation and Development, Nuclear Energy Agency, **41** *26* (1989)

[134] *The use of X-ray Diffraction Rocking Curve Methodology for Assessment of the c-axis Orientation in Bi-Sr-Ca-Cu-O Superconducting Thin Films*, T.N. Blanton, M. Lelental and C.L. Barnes, Physica C **184** (1991) pp.119-126

[135] *A rigorous comparison of X-ray diffraction thickness measurement techniques using silicon-on-insulator thin films*, A.J. Ying, C.E. Murray and I.C. Noyan, J. Appl. Cryst. **42** *3* (2009) pp.401-410

[136] *The Scherrer Equation and the Dynamical Theory of X-ray Diffraction*, F.T.L. Muniz, M.A.R. Miranda, C. Morilla dos Santos and J.M. Sasaki, Acta. Cryst. A **72**, (2016) pp.385-390

[137] *Thin Film and Surface Characterization by Specular X-Ray Reflectivity*, E. Chason and T.M. Mayer, Crit. Rev. Solid State Mat. **22** *1* (1997)

[138] *X-Ray and Neutron Reflectivity for the Investigation of Polymers,* T.P. Russell, Mater. Sci. Rep. **5** *4* (1990) pp.171-271

[139] *Surface Studies of Solids by Total Reflection of X-Rays*, L.G. Parratt, Phys. Rev. **95** (1954)

[140] *X-ray and neutron scattering from rough surfaces*, S. K. Sinha, E. B. Sirota, S. Garoff, and H. B. Stanley, Phys. Rev. B **38** (1988)

[141] *Structural Characterisation of Thin Films by X-Ray Reflectivity*, I. Kojima and B. Lee, The RIgaku Journal **16** 2 (1999)

[142] *Structural Analysis of Cubic GaN through X-Ray Pole Figure Generation*, K. Balakrishnan, G. Feuillet, K. Ohta, H. Hamaguchi, H. Okumura and S. Yoshida, Jpn. J. Appl. Phys. **36** (1997) 6221

[143] *X-Ray Thin Film Measurement Techniques: VII. Pole Figure Measurement*, K. Nagao and E. Kagami, Rigaku Journal **27** *2* 2011

[144] *Z-Contrast Stem for Materials Science*, S.J. Pennycook, Ultramicroscopy **30** (1989) pp.58-69

[145] *Thermal Diffuse Scattering in Transmission Electron Microscopy*, B.D. Forbes, A.J. D'Alfonso, S.D. Findlay, D. Van Dyck, J.M. LeBeau, S. Stemmer and L.J. Allen, Ultramicroscopy **111** (2011) pp.1670–1680

[146] *Atomic-Resolution Incoherent High-Angle Annular Dark Field STEM Images of Si(011)*, K. Watanabe, T. Yamazaki, Y. Kikuchi, Y. Kotaka, M. Kawasaki, I. Hashimoto, and M. Shiojiri, Phys. Rev. B. **63** (2001) 085316

[147] *Energy-Filtering Transmission Electron Microscopy*, L. Reimer, Adv. Electr. Elec. Phys. **81** (1991) pp.43-126

[148] *Fundamentals of Electron Energy Loss Spectroscopy*, F. Hofer, F.P. Schmidt, W. Grogger and G. Kothleitner, IOP Conf. Series: Mat. Sci. Eng. **109** (2016) 012007

[149] *Electron Energy-Loss Spectroscopy in the TEM*, R.F. Egerton, Rep. Prog. Phys. **72** (2009) 016502

[150] *Selected Area Electron Diffraction and its Use in Structure Determination*, W.F. Tivol, Micro. Today **18** *4* (2010)

[151] *Electron Diffraction Using Transmission Electron Microscopy*, L.A. Bendersky and F.W. Gayle, J. res. Nat. Inst. Stand. Technol. **106** *6* (2001) pp.997-1012

[152] *Progress in the Preparation of Cross-Sectional TEM Specimens by Ion-Beam Thinning*, A. Strecker, U. Bäder, M. Kelsch, U. Salzberger, M. Sycha, M. Gao, G. Richter and K. van Benthem, Zeit. Metall. **94** *3* (2003)

[153] *Versatile and Sensitive Vibrating-Sample Magnetometer*, S. Foner, Rev. Sci. Instr. **30** *7* (1959)

[154] *Detection of Magnetic Moment in Thin Films with a Home-Made Vibrating Sample Magnetometer*, D. Jordán, D. González-Chávez, D. Laura, L.M. León Hilario, E. Monteblanco, A. Gutarra and L..Avilés-Félix, J. Magn. Mag. Mat. **456** (2018) pp.56-61

[155] *The Relationship Between Field-Cooled and Zero-Field-Cooled Susceptibilities of Some Ordered Magnetic Systems*, P.A. Joy, P.S. Anil Kumar and S.K. Date, J. Phys. Cond. Mat. **10** *48* (1998)

[156] *Theoretical Studies of the Field-Cooled and Zero-Field Cooled Magnetization of Interacting Fine Particles*, R.W. Chantrell, N.S. Walmsley, J. Gore and M. Maylin, J. Appl. Phys. **85** *8* (1999)

[157] *Finite Size Effects in the Verwey Transition of Magnetite Thin Films, A.M. Bataille, E. Vincent, S. Gota and M. Gautier-Soyer,* arXiv:cond-mat/0610291

[158] *Microstructure, Magnetic and Magneto-Transport Properties of Polycrystalline Fe_3O_4 Films*, twW.B. Mi, J.J. Shen, E.Y. Jiang, H.L. Bai, Acta Mater. **55** (2007) pp.1919–1926

[159] *Magnetic Field Dependence of Blocking Temperature in Oleic Acid Functionalized Iron Oxide Nanoparticles*, S. Tanwar, V.P.S. Awana, S.P. Singh and R. Pasricha, J. Supercond. Nov. Mag. **25** *6* (2012) pp.2041-2045

[160] *Mechanism for Superparamagnetic Behavior in Epitaxial Fe_3O_4 Films,* W. Eerenstein, T. Hibma and S. Celotto, Phys. Rev. B **70** (2004) 184404

[161] *Tuning the Magnetic Properties of Nanoparticles,* A.G. Kolhatkar, A.C. Jamison, D. Litvinov, R.C. Willson and T.R. Lee, Int. J. Mol. Sci. **14** 8 (2013) pp.15977–16009.

[162] *The SQUID Handbook Vol. 1: Fundamentals and Technology of SQUIDs and SQUID Systems* (1st Edition), J. Clarke and A.I. Braginski, Wiley-VCH Verlag GmbH & Co (2004)

[163] *Microwave Electronics: Measurement and Materials Characterization* (1st Edition), L.F. Chen, C. K. ng, C. P. Neo, V. V. Varadan and V. K. Varadan, John Wiley and Sons (2004)

[164] *Radio Frequency Integrated Design*, J. Rodgers and C. Plett (1st Edition), Artech House (2003)

[165] *Magnetostrictive Thin Films for Microwave Spintronics*, D.E. Parkes, L.R. Shelford, P. Wadley, V. Holý, M. Wang, A T. Hindmarch, G. van der Laan, R.P. Campion, K.W. Edmonds, S.A. Cavill and A.W. Rushforth, Sci. Rep. **3** (2013)

[166] *Ferromagnetic Resonance Linewidth in Metallic Thin Films: Comparison of Measurement Methods,* S.S. Kalarickal, P. Krivosik, M. Wu, C.E. Patton, M.L. Schneider, P. Kabos, T.J. Silva and *J.P.* Nibarger, J. Appl. Phys. **99** (2006) 093909

[167] *Fundamentals of Vector Network Analysis* (4th Edition), M. Hiebel, Rohde & Schwarz GmbH & Co. KG (2008)

[168] *Introduction to: Broadband FMR Spectroscopy: Application Note 1087-201* (Rev. A0), Quantum Design, www.qdusa.com/sitedocs/appNotes/general/1087-201.pdf (2017)

[169] *A New Highly Sensitive Broadband Ferromagnetic Resonance Measurement System With Lock-in Detection*, S. Beguhn, Z. Zhou, S. Rand, X. Yang, J. Lou and N.X. Sun, J. Appl. Phys. **111** (2012) 07A503

[170] *Broadband Stripline Ferromagnetic Resonance Spectroscopy of Ferromagnetic Films, Multilayers and Nanostructures*, I.S. Maksymov and M. Kostylev, Physica E, **69** (2015)

[171] *K- and L-edge X-ray Absorption Spectroscopy (XAS) and Resonant Inelastic X-ray Scattering (RIXS) Determination of Differential Orbital Covalency (DOC) of Transition Metal Sites*, M.L. Baker, M.W. Mara, J.J. Yan, K.O. Hodgson, B. Hedman, and E. Solomon, Coord. Chem. Rev. **345** (2017) pp.182–208

[172] *High-Resolution X-Ray Emission and X-Ray Absorption Spectroscopy*, F. de Groot, Chem. Rev. **101** (2001) pp.1779-1808

[173] *Core Level Spectroscopy of Solids* (1st Edition), F. de Groot and A. KotaniCRC Press (2008)

[174] *X-Ray Magnetic Circular Dichroism - A Versatile Tool to Study Magnetism*, G. van der Laan and A.I. Figueroa, Coord. Chem. Rev. **277-278** (2014) pp. 95-129

[175] *Bulk Sensitive X-Ray Absorption Spectroscopy Free of Self-Absorption Effects*, A. J. Achkar, T.Z. Regier, H. Wadati, Y.J. Kim, H. Zhang and D.G. Hawthorn, Phys. Rev. B **83** (2011) 081106(R)

[176] *Dips and Peaks in Fluorescence Yield XAS are due to State-Dependent Decay*, F.M.F de Groot, Nat. Chem. **4** (2012) 766

[177] *Applications of Soft X-Ray Magnetic Dichroism*, G. van Der Laan, J. Phys.: Conf. Ser. **430** (2013) 012127

[178] *Recent Advances in Circular and Linear X-Ray Magnetic Dichroism: Experiment and Theory*, G. van der Laan, Synchr. Rad. News **26** *6* (2013) pp.6-11

[179] *Strong Magnetic X-Ray Dichroism in 2p Absorption Spectra of 3d Transition Metal Ions*, G. van der Laan and B.T. Thole, Phys. Rev. B **43** (1991) pp. 13401 – 13411

[180] *Optimized End Station and Operating Protocols for Reflection Extended X-Ray Absorption Fine Structure (ReflEXAFS) Investigations of Surface Structure at the European Synchrotron Radiation Facility Beamline BM29*, V. López-Flores, S. Ansell, D.T. Bowron, S. Díaz-Moreno, S. Ramos and A. Muñoz-Páez, Rev. Sci. Instr. **78** (2007) 013109

[181] *Setup for Optimized Grazing Incidence X-Ray Absorption Experiments on Thin Films on Substrates*, C. Maurizioa, M. Rovezzi, F. Bardellib, H.G. Paisc and F. D'Acapito, Rev. Sci. Instr. **80** (2009) 063904

[182] *Soft X-Ray Magnetic Circular Dichroism Study on Gd-Doped EuO Thin Films*, H. Ott, S.J. Heise, R. Sutarto, Z. Hu, C.F. Chang, H.H. Hsieh, H.J. Lin, C.T. Chen and L.H. Tjeng, Phys. Rev. B **73** (2006) 094407

[183] *Synchrotron Light: From Basics to Coherence and Coherence-Related Applications*, G. Margaritondp, Y. Hwu and G. Tromba, Synchrotron Radiation: Methodologies and Applications edited by Mobilio and Vlaic (SIF Bologna) (2003) pp.25-53

[184] *'How Does A Synchrotron Radiation Source Work?*', DESY Synchrotron source website, http://photon-science.desy.de/research/students__teaching/primers/synchrotron_radiation/index_eng.html

[185] *X-Ray Circular Dichroism as a Probe of Orbital Magnetization*, B.T. Thole, P. Carra, F. Sette, and G. van der Laan, Phys. Rev. Lett. **68** (1992) 1943

[186] *X-Ray Circular Dichroism and Local Magnetic Fields*, P. Carra, B.T. Thole, M. Altarelli and X. Wang, Phys. Rev. Lett. **70** (1993) 694

[187] *Experimental Confirmation of the X-Ray Magnetic Circular Dichroism Sum Rules for Iron and Cobalt*, C.T. Chen, Y.U. Idzerda, H-J. Lin, N.V. Smith, G. Meigs, E. Chaban, G.H. Ho, E. Pellegrin, and F. Sette, Phys. Rev. Lett. **75** (1995) 152

[188] *Ferromagnetic Moment and Antiferromagnetic Coupling in (Ga,Mn)As Thin Films*, K.W. Edmonds, N.R.S. Farley, T.K. Johal, G. van der Laan, R.P. Campion, B.L. Gallagher and C.T. Foxon, Phys. Rev. B **71** (2005) 064418

[189] *Sum Rule Practice*, G. van der Laan, J. Synch. Rad. **6** (1999) pp.694-695

{190] *The Theory of Atomic Structure and Spectra* (1st Edition), R.D. Cowan, University of California Press (1981)

[191] *Approximate Relativistic Corrections to Atomic Radial Wave Functions*, R.D. Cowan and D.C. Griffin, J. Opt. Soc, Am. **66** *10* (1976) pp.1010-1014

[192] *The CTM4XAS program for EELS and XAS spectral shape analysis of transition metal L edges*, E. Stavitski and F. M. F. de Groot, Micron **41** (2010) pp.687-694

[193] *Broadband Ferromagnetic Resonance System and Methods for Ultrathin Magnetic Films*, E. Montoya, T. McKinnon, A. Zamani, E. Girt and B. Heinrich, J. Mag. Magn. Mater. **356** (2014) pp12-20

[194] *Design of High Power Electromagnets*, Y.Ishikawa and S. Chikazumi, Jpn. J. Appl. Phys. **1** *3* (1962)

[195] *Coplanar Waveguide: A Surface Strip Transmission Line Suitable for Nonreciprocal Gyromagnetic Device Applications*, C.P. Wen, IEEE Transactions on Microwave Theory and Techniques, **17** *12* (1969)

[196] *The Analysis of Impedance Matching Problem in RF Circuit Design*, B. Mindan and L. Hong, 2010 International Forum on Information Technology and Applications **3** (2010)

[197] *Impact of Ground Via Placement in Grounded Coplanar Waveguide Interconnects*, A. Sain and K.L. Melde, IEEE Transactions on Components, Packaging and Manufacturing Technology **6** *1* (2016)

[198] *On the Use of Vias in Conductor-Backed Coplanar Circuits*, W.H. Hadyl, IEEE Transactions on Microwave Theory and Techniques **50** *6* (2002)

[199] *High- Q Tunable Microwave Cavity Resonators and Filters Using SOI-Based RF MEMS Tuners*, X. Liu, L.P.B. Katehi, W.J. Chappel and D. Peroulis, J. Microelec. Syst. **19** *4* (2010) pp774-784

[200] *Ferromagnetic Resonance Study of Polycrystalline $Fe_{1-x}V_x$ Alloy Thin Films*, J.M.I Beaujour, A.D. Kent, D.W. Abraham and J.Z. Sun, J. Appl. Phys. **103** 07B519 (2008)

[201] *Spin Torque Ferromagnetic Resonance with Magnetic Field Modulation*, A.M. Gonçalves, I. Barsukov, Y-J. Chen, L. Yang, J.A. Katine, and I.N. Krivorotov Appl. Phys. Lett. **103** (2013) 172406

[202] *Magnetostatic Modes in Ferromagnetic Resonance*, L.R. Walker, Phys. Rev. **105** *2* (1957)

[203] *Ferromagnetic Resonance: Theory and Application* (1st Edition), O. Yalçin, InTech Publishing (2013)

[204] *Model SR830 DSP Lock-In Amplifier* (Revision 2.5), Stanford Research Systems (2011)

[205] *Experimental Investigation of Temperature-Dependent Gilbert Damping in Permalloy Thin Films*, Y. Zhao, Q. Song, S-H. Yang, T. Su, W. Yuan, S. S. P. Parkin, J. Shi and W. Han, Nat. Sci. Rep. **6** (2016) 22890

[206] *Permalloy Thin Films on MgO(001): Epitaxial growth and Physical Properties*, F. Michelini, L. Ressier, J. Degauque, P. Baulès, A. R. Fert, J. P. Peyrade and J. F. Bobo, J. App. Phys. **92** *12* (2002) 7337

[207] *Voltage-Induced Strain Control of the Magnetic Anisotropy in a Ni Thin Film on Flexible Substrate*, F. Zighem, D. Faurie, S. Mercone, M. Belmeguenai and H. Haddadi, J. Appl. Phys. **114** (2013) 073904

[208] *Microstructure and Magnetic Properties of Strained Fe_3O_4 Films*, Y.Z. Chen, J.R. Sun, Y.N. Han, X.Y. Yie, J. Shen, C.B. Rong, S.L. He and B.G. Shen, J. Appl. Phys **103** (2008) 07D703

[209] *Size Dependence of Metal-Insulator Transition in Stoichiometric Fe_3O_4 Nanocrystals*, J. Lee, S.G. Kwon, J-G. Park and T. Hyeon, Nano. Lett. **15** (2015) pp.4337-4342

[210] *Magnetic Anomalies in Single Crystal Fe_3O_4 Thin Films*, D.T. Margulies, F.T. Parker and A.E. Berkowitz, J. Appl. Phys. **75** (1994) 6097

[211] *Anomalous Strain Relaxation Behaviour of Fe_3O_4/MgO (100) Heteroepitaxial System Grown Using Molecular Beam Epitaxy*, S.K. Arora, R.G.S. Sofin, I.V. Shvets and M. Luysberg, J. Appl. Phys. **100** (2006) 073908

[212] *Atomic Structure and Composition of the Yttria-Stabilised Zirconia (111) Surface*, V. Vonk, N. Khorshidi, A. Stierle and H. Dosch, Surface Science **612** (2013) pp.69-75University of Tennessee (2002)

[213] *Preparation and Properties of Y_2O_3-Doped ZrO2 Thin Films by the Sol-Gel Process,* J-S. Lee, T. Matsubara, T. Sei and T. Tsuchiya, J. Mater. Sci. **32** (1997) pp.5249-5256

[214] *Yttria-Stabilized Zirconia Thin Films by Pulsed Laser Deposition: Microstructural and Compositional Control*, S. Heiroth, T. Lippert, A. Wokaun, M. Dobeli, J.L.M. Rupp, B. Scherrer and L.J. Gauckler, J. Euro. Cer. Soc. **30** (2012) pp. 489-495

[215] *Y:ZrO2 – YSZ for Research and Development* (Crystec Materials Datasheet), CrysTec GmbH, found online at www.crystec.de/daten/ysz.pdf

[216] *Magnetic Properties of Nanoparticle Systems of Fe, Co, Ni, and FePt, Created by Ion Implantation (*PhD, Thesis), K.D. Sorge, University of Tennessee (2002)

[217] *Skull Melter Growth of Magnetite (Fe_30_4)*, H.R. Harrison and R. Aragón, Mater. Res. Bull. **13** (1978) pp.1097-1104

[218] *Heat Capacity and Entropy of Nonstoichiometric Magnetite $Fe_{3(1-\delta)}0_4$: The Thermodynamic Nature of the Verwey Transition*, J.P. Shepherd, J.W. Koenitzer, R. Aragón, J. Spalek and J.M. Honig, Phys. Rev. B. **43** *10*, (1991) pp.8461-8471

[219] *The System Iron-Oxygen II. Equilibrium and Thermodynamics of Liquid Oxide and Other Phases,* L.S. Darken and R.W. Gurry, J. Am. Chem. Soc. **68** *5* (1946) pp.798–816

[220] *X-ray Data Booklet* (3rd Edition), A. Thompson, I. Lindau, D. Attwood, Y. Liu, E. Gullikson, P. Pianetta, M. Howells, A. Robinson, K-J Kim, J. Scofield, J. Kirz, J. Underwood, J. Kortright, G. Williams and H. Winick, Lawrence Berkley National Laboratory (2009)

[221] *Magnetocrystalline Anisotropy of Magnetite*, R. Řezníček, V. Chlan, H. Štěpánková, P. Novák and M. Maryško, J. Phys. Cond. Mat. **24** (2012) 055501[222] *Magnetic Anisotropy of Ultrathin Fe Films Grown on Vicinal Si (111)*, H-L. Liu, W. He, Q. Wu, J. Ye, X-Q. Zhang, H-T. Yang, and Z-H. Cheng, AIP Advances **3** (2013) 062101

[223] *Determination of Magnetic Anisotropy Constants in Fe Ultrathin Film on Vicinal Si(111) by Anisotropic Magnetoresistance*, J. Ye, W. He, Q. Wu, H-L. Liu, Z-Y. Chen and Z-H. Cheng, Sci. Rep. **3** (2013) 2148

[224] *Surface-Step-Induced Magnetic Anisotropy in Thin Epitaxial Fe Films on W(001)*, J. Chen and J.L. Erskine, Phys. Rev. Lett. **68** *8* (1992) pp.1212-1215

[225] *Interface Magnetic and Optical Anisotropy of Ultrathin Co Films Grown on a Vicinal Si Substrate*, A. Stupakiewicz, A. Kirilyuk, A. Fleurence, R. Gieniusz, T. Maroutian, P. Beauvillain, A. Maziewski, and Th. Rasing, Phys. Rev. B. **80** (2009) 094423

[226] *Ferromagnetic Resonance Linewidth Mechanisms in Polycrystalline Ferrites: Role of Grain-to-Grain and Grain-Boundary Two-Magnon Scattering Processes*, S.S. Kalarickal, N. Mo, P. Krivosik and c.E. Patton, Phys. rev. B **79** (2009) 094427

[227] *Two Magnon Scattering in Ultrathin Ferromagnets: The Case Where the Magnetization is Out of Plane*, P. Landeros, R.E. Arias, and D.L. Mills, Phys. Rev. B **77** (2008) 214405

[228] *High-Spin Polarization of Heusler Alloys*, B. Hillebrands and C. Felser, J. Phys. D: Appl. Phys. **39** *5* (2006)

[229] *Heusler Compounds—A Material Class With Exceptional Properties*, T. Graf, S.S.P. Parkin and C. Felser, IEEE Trans. Mag. **47** *2* (2011) pp.367-373

[230] *Symmetry-Induced Magnetic Anisotropy in Fe Films Grown on Stepped Ag(001)*, R. K. Kawakami, E. J. Escorcia-Aparicio and Z. Q. Qiu, Phys. Rev. Lett. **77** *12* (1996)

[231] *Damping Constants for Permalloy Single-Crystal Thin Films,* K. Kobayashi, N. Inaba, N. Fujita, Y. Sudo, T. Tanaka, M. Ohtake, M. Futamoto and F. Kirino, IEEE Trans. Magn. **45** *6* (2009)

[232] *Growth of Co2FeAl Heusler Alloy Thin Films on Si(100) Having Very Small Gilbert Damping by Ion Beam Sputtering,* S. Husain, S. Akansel, A. Kumar, P. Svedlindh and S. Chaudhary, Sci. Rep. **6** (2016)

[233] *Magnetic Damping Constant in Co-Based Full Heusler Alloy Epitaxial Films*, M. Oogane, T. Kubota, H. Naganuma and Y. Ando, J. Phys. D: Appl. Phys. **48** *16* (2015)

[234] *Exchange Bias Induced at a Co2FeAl0.5Si0.5/Cr Interface*, C.N.T. Yu, A.J. Vick, N. Inami, K. Ono, W. Frost and A. Hirohata, J. Phys. D: Appl. Phys. **50** (2017) 125004

[235] *Ferromagnetic Resonance of Fe(111) Thin Films and Fe(111)/Cu(111) Multilayers*, S.M. Rezende, J.A.S. Moura, F.M. de Aguiar and W.H. Schreiner, Phys. Rev. B. **49** *21* (1994)

[236] *Magnetization Dynamics in an Exchange-Coupled NiFe/CoFe Bilayer Studied by X-Ray Detected Ferromagnetic Resonance*, G.B.G Stenning, L.R. Shelford, S.A. Cavill, F. Hoffmann, M. Haertinger, T. Hesjedal, G. Woltersdorf, G. J. Bowden, S.A. Gregory and C.H. Back, New J. Phys. **17** (2015) 013019

[237] *Time-Resolved X-Ray Detected Ferromagnetic Resonance of Spin Currents*, G. van der Laan, J. Electron Spec. and Related Phenomena **220** (2017) pp.137-146